Novel Flow Processes towards Water Soluble CdX Quantum Dots

Guillaume Petit

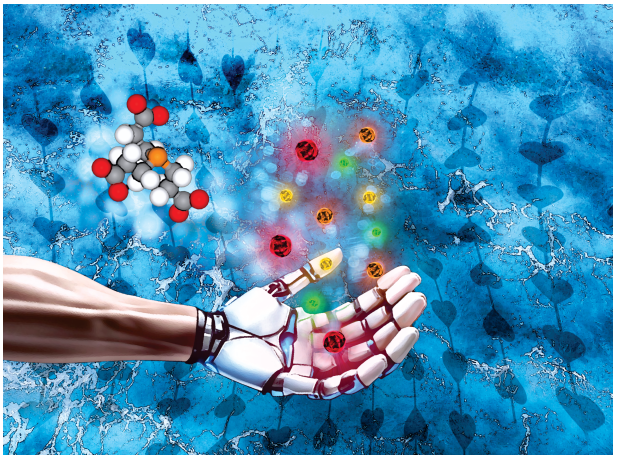

Faculty of Sciences from Liège University

Department of Chemistry, MolSys Research Unit

Thesis submitted in fulfilment of the requirements for the degree of Doctor of Philosophy in Sciences

Under the supervision of Prof. Jean-Christophe M. Monbaliu

Academic year 2025-2026

"Man muss noch Chaos in sich haben, um einen tanzenden Stern gebären zu können."

"One must still have chaos in oneself to be able to give birth to a dancing star."

Friedrich Nietzsche
"Also sprach Zarathustra", 1883–1885

Abstract

The profound impact of Quantum Dots (QDs) on both the scientific community and high-tech daily applications echoes in the 2023 Nobel Prize. QDs are a diverse class of nanoscale semiconductors with transformative applications deeply rooted in the digital era and for medical applications. Challenging conventional preparations and optimizing their synthesis is therefore crucial for advancing next-generation technologies, particularly under scalable and sustainable conditions.

This thesis presents an innovative approach to synthesizing chalcogenide precursors and their application in the continuous-flow production of CdX (X = S, Se, Te) QDs in water. Tris(2-carboxyethyl)phosphine (TCEP) is identified as a novel, highly efficient, and water-soluble chalcogenide transfer agent, enabling the controlled formation of CdX QDs in an aqueous medium. A comprehensive study of critical process parameters and reaction kinetics is conducted to optimize their preparation under continuous-flow conditions.

The research explores the seamless integration of TCEP conversion into TCEP=X (X = S, Se, Te) species within a continuous-flow setup and their subsequent use in CdX QD formation. Experimental conditions are systematically optimized for high-quality QD synthesis under both microfluidic and mesofluidic regimes. Furthermore, an in-depth mechanistic investigation into QD formation is provided, addressing key chemical transformations and nucleation-growth dynamics.

The thesis concludes with efforts toward the biofunctionalization of aqueous QDs using modified biotin, highlighting their potential for biomedical applications. Future perspectives on biofunctionalization strategies and their broader implications are also discussed.

Acknowledgements

I would like to express my gratitude to my PhD advisor, Prof. Jean-Christophe M. Monbaliu for giving me the opportunity to pursue a PhD cursus under his guidance, support and commitment through this research program.

I thank Dr. Thomas Noblet for his guidance as members of my PhD committee. I also extend special thanks to Prof. Laurent Dreesen who, in addition to his role on the committee, led the project QD3Drops, which framed and supported the present thesis.

I would like to thank Prof. Souhir Boujday, Prof. Séverine Le Gac, Dr. Guillaume Gauron, Prof. Laurent Dreesen, Prof. Bernard Leyh and Dr. Cédric Malherbe for their expertise on the evaluation of this PhD dissertation.

I would like to acknowledge Milhad Abolhassani for fruitful discussions on microfluidic design and process optimization, which played a key role in the emergence of the dynamic flow experiment approach described in Chapter 5.

I would like to thank all the scientists who, each within their own field of expertise, contributed to shaping this work. In particular, I would like to thank: Dr. P. Compère for the endless sessions in the microscopy lab, Prof. C. Damblon for the time spent to develop these exotic NMR methods, Prof. B. Leyh for the long talks about kinetics/math, Dr. C. Malherbe for sharing his passion for Raman Spectoscopy and introduced me to deeper data treatment, Prof. B. Vertruyen for the stimulating discussions on XRD and their applied data treatment, and all those who, in one way or another, contributed to making this work possible.

A thesis is never purely an individual endeavour, and I would like to thank all my colleagues who, through insightful discussions, moments of complicity, or both, helped me get through the more difficult times. A special thought goes to the successive generations of the "North" office members, who made this office a pleasant place to work. They are too many to name individually, but I hope they will recognize themselves.

This work was supported by the Wallonia within the framework of the program "Win2Wal" (QD3Drops, project n° 1810126). The University of Liège is acknowledged as well for its financial support.

Finally, I would like to express my deep gratitude to my family, my friends and everyone who supported and encouraged me throughout this process. Their support means a lot to me and helped me get through these years, despite my frequent absence.

And to conclude, my deepest apologies to you, who endured my years of absence, frequent bad moods, and lack of energy, yet remained strong throughout.

Declaration of Authorship

I, Guillaume Petit, declare that this PhD thesis titled, “Novel Flow Processes towards Water Soluble CdX Quantum Dots” and the work presented in this thesis is solely my own. I confirm that:

- This work was done wholly or mainly while in candidature for a PhD degree at the University of Liège.
- Where any part of this thesis has been previously published, this has been clearly stated.
- Where I have consulted the published work of others, this is always clearly attributed.
- Where I have quoted from the work of others, the source is always given. With the exception of such quotations, this thesis is entirely my own work.
- Where the thesis is based on work done by myself jointly with others, this has been clearly stated.
- I have acknowledged all main sources of help.

Contents

Acronyms

AIC Akaike information criterion. 169, 174, 180, 295, 297, 300

BET Brunauer, Emmett and Teller theory. 145

BIC Bayesian information criterion. 169, 174, 180, 295, 297, 300

BPR Back Pressure Regulator. 67, 98

BR Batch reactor. 52

CAGR Compound annual growth rate. 23

CFD Computational Fluid Dynamic. 56, 63

CNT Classical Nucleation Theory. 37, 47, 72, 157

CSSNCs Core–shell Semiconducting Nanocrystals. 34, 36, 72, 93, 98

CSTR Continuously Stirred Tank Reactor. 52–56, 58–60, 70, 71, 315

DET Dimensionless effective time. 174, 176–178, 181–185, 188, 191–194, 197, 299

DFE Dynamic Flow Experiments. 68, 221

DFT Density Functional Theory. 162

DoE Design of Experiments. 68, 119, 120, 122, 123, 217, 220

EDX Energy-Dispersive X-ray. 186–189, 211, 276, 318

ERT Effective residence time. 168, 170, 172, 222, 296, 297, 300, 321

FRET Förster Resonance Energy Transfer. 21, 25, 231, 312

FW mechanism Finke-Watzky mechanism. 47, 157, 169, 170, 174, 175, 210, 222, 224, 295, 298, 322, 323

FWHM Full Width at Half Maximum. 33, 43, 72, 170, 172, 184–187, 189, 194, 195, 197, 208, 317, 318, 323

HRTEM High-resolution transmission electron microscopy. 134, 137, 186–189, 211, 316, 318

HSAB Hard and soft acids and bases. 130, 158, 160

HTF Heat Transfer Fluid. 56, 58

ISC inter system crossing. 25

LED light-emitting diode. 25

ML Machine Learning. 71, 219

P-XRD powder X-ray diffraction. 134, 135, 137, 316

P/V ratio peak to valley ratio. 170, 177–179, 182, 184, 192, 299, 317, 318, 321

PAT Process Analytical Technology. 60, 67, 219

PBM Population Balance Models Learning. 222, 224

PBS Phosphate Buffer Saline. 230, 307, 308, 324

PFTR Plug Flow Tubular Reactor. 53–56, 58–62, 70, 71, 315

PLQY Photoluminescence Quantum Yield. 34, 72, 75, 79, 93, 100, 168, 172, 173, 193–195, 197, 213, 221, 318

PLS Partial Least Squares. 301

QDs Quantum Dots. 21–23, 25, 28, 71, 75, 77, 79, 98–100, 119, 120, 156, 161, 163, 165, 166, 168, 176, 179, 183, 185, 316

STY space-time yield. 131, 132

VIP Variable Importance in Projection. 301

XPS X-ray photoelectrons spectroscopy. 206, 207, 209, 276, 303, 318

Molecules Acronyms

$(BDMS)_2Te$ Bis(tert-butyldimethylsilyl)tellurium. 76, 77, 84

$(TMS)_2Se$ Bis(trimethylsilyl)selenide. 76, 77, 84

$(TMS)_2S$ Bis(trimethylsilyl)sulfide. 76, 77, 84

2-DET 2-(dimethylamino)ethanethiol. 92, 96

2-MA 2-Mercaptoethylamine. 96

2-ME 2-Mercaptoethanol. 92, 96

3-MPA 3-Mercaptopropionic acid. 92, 96, 159, 161–165, 178, 179, 206, 213, 230, 233, 293, 294, 296, 298, 299, 307, 308, 317, 321

3-PPA 3-Phosphopropionic acid. 159–161, 317

AA Allylamine. 86

Asc Ac Ascorbic acid. 97

BP Benzophenone. 86

$Cd(Me)_2$ Dimethylcadmium. 75, 77, 79, 99

Cit Sodium citrate. 96

DDA Dodecylamine. 86

DDT 1-dodecanethiol. 77, 86

DMOA N,N-dimethyl-oleoyl amide. 86

DMP 2,3-dimercapto-1-propanol. 96

DOA Dioctylamine. 85

DTA Dowtherm A. 85

DTBT 2,2′-dithiobisbenzothiazole. 86

DX Decyl xanthate. 87

EX Ethyl xanthate. 87

HDA Hexadecylamine. 75, 85

HDX Hexadecyl xanthate. 87

HH Hexadecyl hexadecanoate. 87

HPA Hexylphosphonic acid. 85

L−Cy L-Cysteine. 96

LA Lauric acid. 75, 85

MA Myristic acid. 87

MSA Mercaptosuccinic acid. 97

N_2H_4 Hydrazine. 97

NDSU N,N-dimethylselenourea. 90, 97

OAM Oleylamine. 86

OA Oleic acid. 85

ODA Octadecylamine. 87

ODE Octadecene. 75, 76, 85

ODPA Octadecylphosphonic acid. 87

OD Octadecane. 87

PAA Phosphoacetic acid. 160, 161

PFA Phosphonoformic acid. 160

PVA Polyvinyl alcohol. 92, 97

SA Stearic acid. 75, 85

SPP Sodium polyphosphate. 88, 92, 97

SeU Selenourea. 90, 97

T_{66} Therminol 66. 86

TBPSe Tributylphosphine selenide. 84

TBP Tributylphosphine. 76, 84

TCEP Tris(2-carboxyethyl)phosphine. 119, 120, 156, 217–219

TDPA Tetradecylphosphonic acid. 85

TGA Thioglycolic acid. 92, 96

TGL 1-Thioglycerol. 96

TMPPA Bis-(2,2,4-trimethylpentyl)phosphinic acid. 86

TOPO Trioctylphosphine oxide. 75, 84

TOPSe Trioctylphosphine selenide. 84

TOPS Trioctylphosphine sulfide. 84

TOPTe Trioctylphosphine telluride. 84

TOP Trioctylphosphine. 76, 84

TTDS Tetraethylthiuram disulfides. 86

TU Thiourea. 90, 96, 220

$ZnEt_2$ Diethylzinc. 85

Chapter 1

General introduction

1.1 Preface

This introduction chapter, dedicated to Quantum Dots (QDs) synthesis, aims to provide the reader with a comprehensive and didactic overview of the key concept developed in experimental chapters.

This project was initially part of a broader research program (QD3Drops project), which aimed the development of a genetic diseases sensor. The detection principle relied on Förster Resonance Energy Transfer (FRET). In this context, the QDs formation lies on aqueous synthesis, as it offers significant advantages for subsequent bio-functionalization. Consequently, the focus of this introduction progressively shifts from general considerations to aqueous QD synthesis under continuous conditions.

In this perspective, the introduction is structured as follow:

- **Section 2: Description** of the QDs, their general properties, and their range of application.
- **Section 3: Market and applications** to complete the overview on overall interest as well as application for the technology.
- **Section 4: Origin of Fluorescence** provides an overview of the physics concepts that induce the QDs fluorescence, quantitative modelization with the exception to these models as well as the solution to overcome them.
- **Section 5: QDs formation** focuses in details on the crystals formation though the various phases of the process. Bases on these description two models global mechanism are presented an conclude on the methods to stabilize nanocrystals and their morphology.

- **Section 6: Reactor technology** provide an overview of the less known continuous reactors converging into microfluidic systems. The section then focuses on the key characteristics of the microfluidic reactors under various point of view (*e.g.*, fluid dynamic, heat transfer, mixing, concatenation and many more.)
- **Section 7: CdX QDs synthesis** provides an exhaustive review on the state of art for QDs synthsis, focusing on the precursors developed since their discovery, both in organic and aqueous matrices conclude by the synthesis applied to microfluidic taking advantage of section 6.
- **Section 8: Project motivation** highlight the weaknesses in QDs aqueous synthesis and proposes an innovative strategy to overcome them.

1.2 Description

QDs are nanoscale semiconductor crystals with unique size-dependent optical and electronic properties. This main feature arises from the interplay of two key characteristics: their nanometric dimensions, which induce quantum confinement effects, and the semiconducting nature of their constituent materials, which govern their optoelectronic behaviour.

QDs were first discovered in the early 1980s, when Ekimov demonstrated size-dependent emission in semiconductor-doped glasses. [1] Independently, Brus observed a similar phenomenon in colloidal solutions [2] and developed the eponymous equation to describe the relationship between QD size and electronic properties. [3] Later, Bawendi revolutionized QDs synthesis by introducing advanced precursor chemistry and high-temperature injection techniques, leading to high-quality, nearly monodisperse QDs with superior optical properties. [4, 5]

The main reason for this sustained interest for the QDs comes from the tunability of their properties. Indeed, their optoelectronic properties (*i.e.* the properties involving interaction with light and electrical signals) can be adjusted by modifying both the particle size, typically from 1.5 nm to 10 nm, and the nature of the bulk material (semiconductor). This unique conjunction of properties make them suitable for a broad range utilisations due to their spectral emission, from UV to NIR, [6] as shown in Figure 1.1.

This range of size can be accessed from two approaches: (a) top down (mechanical way) and (b) bottom up (chemical way). [8, 9] For practical reasons, most of the current processes to access QDs involve a bottom up approach. In practice, the monomeric units are synthesized in soluble phase, in the presence of a ligand. This ligand acts as a stabilizing agent, binding to the surface of forming nanoparticles and controlling their solubility. As

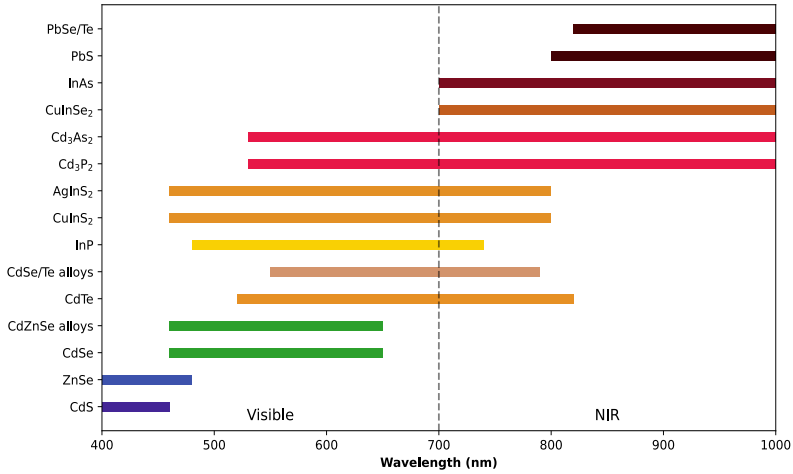

Figure 1.1. QDs spectral ranges of emission for accessible for various types of semiconductor nanoparticles. [7]

the precursor concentration surpasses the nucleation threshold, particle formation begins, and the ligand remains adsorbed on the surface, preventing aggregation. These surface ligands play a critical role in preserving the nanoparticles' optical properties, solubility, and size distribution overtime.

1.3 Market and Applications

Since their discovery in the early 1980s, the QDs have benefited of an ever renewed interest, especially in the current context of digitalization. This increasing interest is illustrated in Figure 1.2 by plotting the number of patent publication featuring the keys words "quantum dots" overtime. Indeed, the total number of granted and applied patents increases from 653 in 2000 to 31.443 in 2024. Among the top applicants for patents in the field are major technology companies such as Samsung, AT&T, LG Display, Apple Inc., IBM, and Huawei, alongside leading academic institutions like the University of California and the Massachusetts Institute of Technology (MIT). [10]

The industry's enthusiasm for this technology is reflected in market metrics: in 2023, the QD market was valued at approximately USD 5.69 billion and is projected to reach USD 16.59 billion by 2030, with a Compound annual growth rate (CAGR) of 16.5%. [11] Among the materials used to synthesize QDs, cadmium-based QDs (*e.g.*, CdS, CdSe, CdTe) have been overly represented due to their exceptional optical properties. [11] However, concerns regarding the toxicity of cadmium have led to increased research and development of cadmium-free alternatives for safer and more environmentally friendly applications. [12]

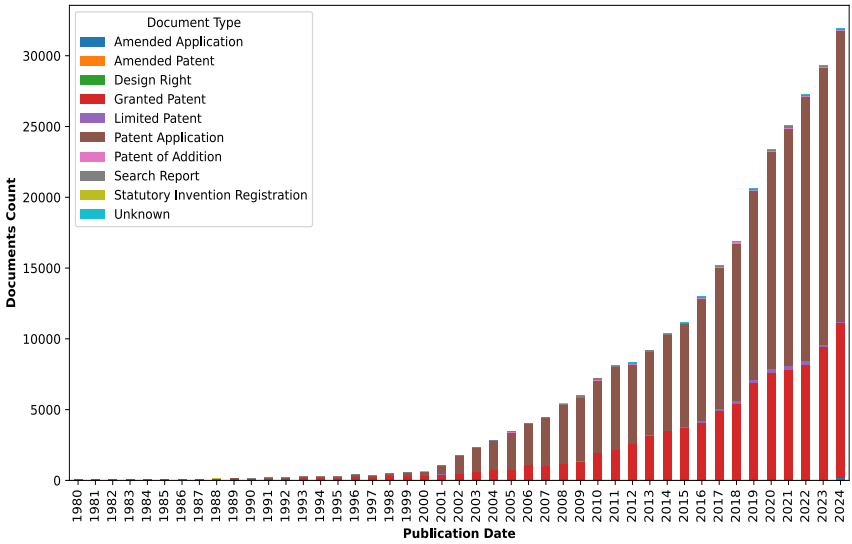

Figure 1.2. QDs synthesis patent analysis from their discovery to date. [10]

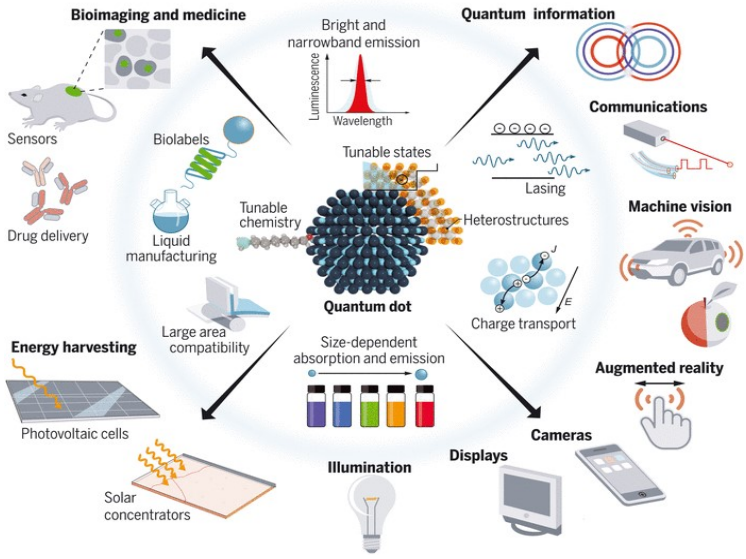

Figure 1.3. Overview of the QDs application. Illustration from [13].

QDs have a wide range of applications, particularly in emerging technologies (as summarized in Figure 1.3). They are used in photovoltaic devices such as quantum dot-sensitized solar cells, [14, 15] as light sources in light-emitting diode (LED) for enhanced color purity and efficiency and QLED display monitors, or even as laser sources. [16, 17] They also serve in photodetection for cameras and sensors, [18, 19] photocatalysis for radical generation in redox reactions, [20, 21] as well as in bio-imaging (bio-labeling) and medicine, notably for drug delivery. [22, 23]

Among these various fields, bio-related applications are of particular interest in the present work. In the frame of the current project, which aims to develop biosensors for genetic diseases, the focus is placed on bio-applications based on FRET. This distance-dependent energy transfer mechanism relies on non-radiative energy transfer between a donor and an acceptor species. In the presence of the target compound, two populations of QDs embedded in the matrix are brought into close proximity, enabling energy transfer and resulting in the quenching of the emission of the smallest QDs. [24, 25] This approach has demonstrated high sensitivity [26] and is readily adaptable to biomolecule detection. [27, 28]

1.4 Origin of the QDs fluorescence

Fluorescence is the process in which a molecule, after absorbing an electromagnetic wave (photon), enters an excited electronic state. Upon relaxation, it emits a photon at a longer wavelength (lower energy) due to partial energy dissipation before emission. The phenomenon of absorption and emission of photons happen at specific wavelengths, quantified level of energy. The amount of energy corresponding to these transitions depends on the molecule involved.

The interplay of various phenomenona involving the absorption or the emission of photons can be effectively visualized using a Jablonski diagram, as shown in Figure 1.4. [29] In this diagram, singlet electronic states are denoted by the letter S (*e.g.*, S_0, S_1, S_2), while triplet states are represented by T. When a material absorbs energy, it transitions from ground state (S_0) to an excited singlet state (S_1, S_2). The transition to a fundamental state can occur through various ways:

- **Fluorescence:** The excited molecule relaxes to a lower electronic state and emits a photon at a longer wavelength (lower energy) than the absorbed one. This energy shift is known as the Stokes shift.
- **Phosphorescence:** In some cases, the molecule undergoes inter system crossing (ISC) to a triplet state (T_1), followed by delayed photon emission.

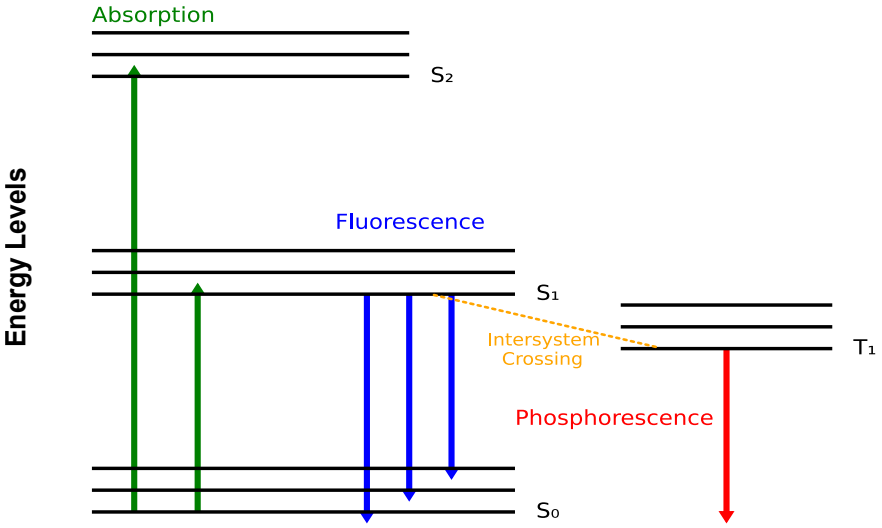

Figure 1.4. Jablonski diagram of photonic effects, adapted from [29].

- **Non-radiative decay:** The excited molecule can also return to the ground state through vibrational relaxation or other non-emissive pathways, dissipating energy as heat rather than light (not shown in Figure 1.4).

1.4.1 Band Theory

In their solid form, the materials can be classified into three different categories, based on their electrical conductivity: insulators, semiconductors and conductors. This classification is determined by the electronic band structure, specifically the valence and conduction bands. [30]

The valence band consists of energy levels occupied by electrons that are bound to atoms, restricting their movement. In contrast, the conduction band contains electrons that are free to move, enabling the material to conduct an electric current. If these two bands do not overlap, the energy gap is known as a band gap (E_g). [31] This property is characteristic of each material, as illustrated in Figure 1.5:

a) **Conductors:** They are characterized by a band gap of 0 eV or nearly zero, allowing free electron movement between the conduction and valence bands.

b) **Insulators:** They have a large band gap, typically greater than 4 eV, preventing electron flow under normal conditions.

c) **Semiconductors:** They possess an intermediate band gap, usually between 0.1 eV and 4 eV, enabling controlled conductivity.

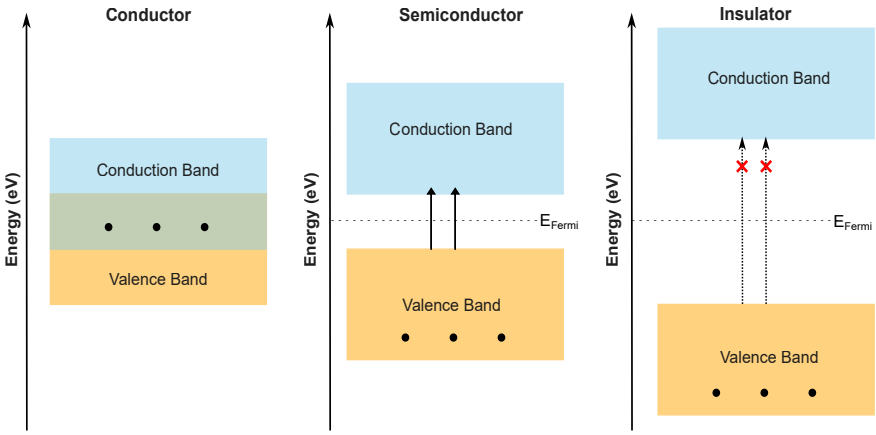

Figure 1.5. Discretization of the materials based on their band gap properties.

The values reported for the band gap (E_g) in Figure 1.5 are primarily for informational purposes. Their value is temperature-dependent, affecting charge carrier mobility within the material. A commonly used model to estimate $E_g(T)$ for type II-VI QDs is the Bose-Einstein equation, which explicitly accounts for electron-phonon interactions. However, alternative approaches such as the Varshni equation or empirical models are also frequently employed, depending on material properties. [32]

In most cases, thermal effects generally lead to a decrease in the band gap due to electron-phonon interactions and lattice expansion. However, exceptions exist, particularly in certain narrow-band gap, disordered, or low-temperature systems.

As mentioned earlier, in conductors, charge carriers (electrons) are free to move within the material. However, in semiconductors at their fundamental (intrinsic) state, no free charge carriers are present in the conduction band. If the amount of energy available (under thermal or photo form) is larger or equal to the band gap, an electron (e^-) is promoted from the valence band to the conduction band. This process generates an exciton (*i.e.*, a combination of an electron (e^-) and a hole (h^+)), considered as quasiparticle. The electron in the conduction band and the hole in the valence band act as charge carriers, allowing electrical conduction under specific conditions. There is therefore coexistence of two charge carrier species, of opposite polarities, in a close environment.

1.4.2 Electron-hole Confinement

As depicted in the previous section, in semiconductors, the formation of an exciton corresponds to the creation of a quasiparticle composed of an electron and and a hole with opposite charges. Due to their opposite charges, there is a strong Coulomb attraction between them.

For an exciton to exist, there must be a physical separation between the electron and the hole, known as the exciton Bohr radius, which is specific to each material. To calculate the Bohr radius, in a semiconductor, the Bohr radius formula is adapted from hydrogen to exciton, under the denomination of a_B^*. The modified Bohr radius formula for exciton is given by Equation 1.1.

$$a_B^* = \frac{4\pi\epsilon_0\epsilon_r\hbar^2}{\left(\frac{m_e^* m_h^*}{m_e^* + m_h^*}\right)e^2} \tag{1.1}$$

Where:

- $\mathbf{a_B^*}$: Excitonic Bohr radius [m],
- $\epsilon_\mathbf{0}$: Permittivity of free space [F.m^{-1}],
- $\epsilon_\mathbf{r}$: Relative permittivity of the material [unitless],
- $\boldsymbol{\hbar}$: Reduced Planck's constant [J.s],
- $\mathbf{m_e^*}$: Effective electron mass [kg],
- $\mathbf{m_h^*}$: Effective hole mass [kg],
- $\mathbf{e}$: Electron charge [Coulombs].

In the case of QDs, the particles size becomes comparable to or smaller than the exciton Bohr radius (a_B^*). This results in quantum confinement, where the wavefunction of the electron and hole is spatially restricted, leading to an increase in their kinetic energy and a modification of the Coulomb interaction. Consequently, the total energy depends of the sum of the kinetic and potential energies (E_c and V_r respectively), formally: $E_{tot} \sim E_c + V(r)$. [33] These models will be more extensively discussed in section 1.4.3.

The quantum confinement can be classified into three distinct regimes based on the competition between the kinetic energy and the attractive exciton potential. This classification is determined by a dimensionless parameter, referred to as the confinement parameter (λ) which is calculated using Equation 1.2. [34]

$$\lambda = \frac{r}{a_B^*} \tag{1.2}$$

Where:

- $\boldsymbol{\lambda}$: Confinement parameter [dimensionless],
- $\mathbf{r}$: Radius of the QDs [m],
- $\mathbf{a_B^*}$: Excitonic Bohr radius [m].

  - $\boldsymbol{\lambda \gg 1}$**: Weak confinement:** The size of the quantum dot has practically no effect on the band gap, and it is close to the bulk material ($\boldsymbol{\Delta E \simeq E_g}$).
  - $\boldsymbol{\lambda \approx 1}$**: Intermediate confinement:** The contributions of both kinetic and potential energies are comparable. The confinement has a weak effect on the energy ($\boldsymbol{\Delta E \approx E_g}$).
  - $\boldsymbol{\lambda \ll 1}$**: Strong confinement:** Both contributions are significantly influenced by confinement, with a particularly strong effect on the kinetic energy ($\boldsymbol{\Delta E > E_g}$).

In addition to its effect on the band gap, quantum confinement has another important consequence on the behaviour of quantum dots: it causes the energy levels to become discretized. This means that as the size of the QDs decreases, the quantization of the energy levels becomes more pronounced. Both effects due to electron-hole confinement are shown in Figure 1.6.

The discretization of the energy levels of the quantum dots can be explained by an analogy with quantum molecular orbitals. Semiconductor crystallites can be seen as sp^3 hybridized structures where the orbitals form bonds between neighbouring atoms, analogous to sets of σ and σ^* orbitals. The growth of three dimensional crystallites leads to the formation molecular-like orbitals extending across the entire crystal. In this analogy, the set of σ orbitals corresponds to the valence band, while the σ^* orbitals form the conduction band. As a corollary of this model, when the crystallites size is reduced to the nanoscale, the energy difference between these molecular-like orbitals increases due to quantum confinement. This leads to the discretization of energy levels, meaning that instead of continuous bands, quantum dots exhibit discrete electronic states. In this model, the highest occupied molecular orbital in the σ (HOMO) set corresponds to the top of the valence band, and the lowest unoccupied molecular orbital in the σ^* (LUMO) set corresponds to the bottom of the conduction band. [35]

As shown in Equation 1.2, the quantum confinement is a phenomenon that occurs when the size of a material is reduced below the exciton Bohr radius in

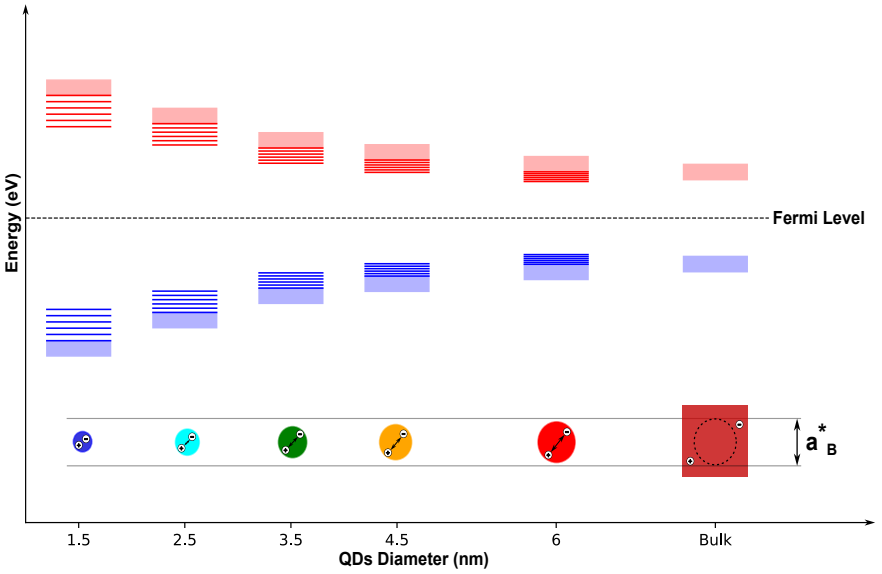

Figure 1.6. Confinement effect on the band gap and the discretization of the quantum dots as function of particle size.

one or more dimensions. [30] Depending on the extent of confinement, four distinct cases can be identified, as summarized in Figure 1.7:

- **No confinement:** When the crystal size is larger than the exciton Bohr radius, the material behaves like its bulk counterpart, and the band gap remains unchanged.
- **Quantum well:** Confinement occurs in only one dimension, while charge carriers remain free to move in the other two dimensions. This results in a planar structure, often used in thin films and heterostructures.
- **Quantum wire:** Confinement happens in two dimensions, leaving free movement along one axis. The material has a wire-like shape.
- **Quantum dots:** Confinement occurs in all three dimensions, forming a spherical nanosized particle qualified as 0D material, commonly named quantum dot.

In the frame of the current work, mostly the case of quantum dots (0D materials) will be discussed.

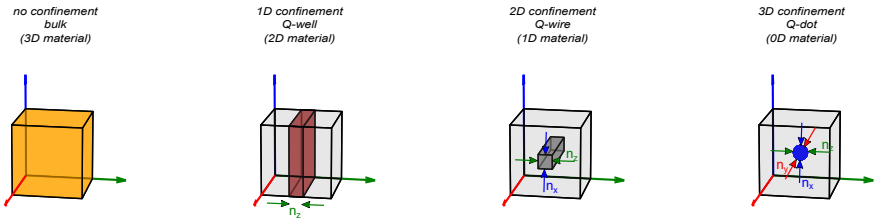

Figure 1.7. Quantum confinement dimension effect adapted from [30].

1.4.3 The Efros model and its development into the Brus equation

Following the identification of quantum confinement in CdS crystallites dispersed in an aqueous phase, [2] scientists developed analytical expressions to predict the evolution of the band gap as a function of the confinement regime. In 1982, Efros *et al.* introduced a model to predict the band gap of quantum dots for both strong and intermediate confinement regimes, [36] as shown in Equation 1.3.

$$E(r) = E_g + \frac{\hbar^2 \pi^2}{2r^2}\left(\frac{1}{m_e} + \frac{1}{m_h}\right) - \frac{\beta e^2}{4\pi\epsilon_0\epsilon_r r} \tag{1.3}$$

Where:

- $\mathbf{E(r)}$: Excitation energy as a function of radius r [J],
- $\mathbf{E_g}$: Bulk band gap energy of the material [J],
- $\boldsymbol{\hbar}$: Reduced Planck's constant [J.s],
- $\mathbf{m_e}$: Electron mass [kg],
- $\mathbf{m_h}$: Hole mass [kg],
- $\boldsymbol{\beta}$: Parameters that reflect the defect and irregularities in the material [dimensionless],
- $\mathbf{e}$: Electron charge [Coulombs],
- $\boldsymbol{\epsilon_0}$: Permittivity of free space [F.m^{-1}],
- $\boldsymbol{\epsilon_r}$: Relative permittivity of the material [dimensionless],
- $\mathbf{r}$: Radius of the nanoparticle [m].

The Efros-Shklovskii equation is actually the sum of three terms:

- E_g: The band gap energy of the considered semiconductor.
- $\frac{\hbar^2\pi^2}{2r^2}\left(\frac{1}{m_e}+\frac{1}{m_h}\right)$: Corresponds to the kinetic energy of the exciton (E_c). This term is obtained by solving the Schrödinger equation in the case of a particle of mass m, in a spherical box of radius R, in a fundamental mode (n=1). [37]
- $\frac{\beta e^2}{4\pi\epsilon_0\epsilon_r r}$: Is the Coulombian contribution for the attractive interaction between the electron (e^-) and the hole (h^+), corresponding to the potential V(r), discussed in section 1.4.2.

Building upon the work of Efros *et al.*, Brus popularized an alternative form of Equation 1.3 by experimentally determining the β parameter as 1.8. This value holds true in the regime of strong quantum confinement. [3] The corresponding expression is given in Equation 1.4.

$$E(r) = E_g + \frac{\hbar^2\pi^2}{2r^2}\left(\frac{1}{m_e}+\frac{1}{m_h}\right) - \frac{1.8e^2}{4\pi\epsilon_0\epsilon_r r} \tag{1.4}$$

This formulation is the most commonly used, but additional terms can be added for more accurate modelling.

In the Equation 1.4, the quantum dots radius has a double, opposite, influence on the band gap. First, $\frac{1}{r^2}$ which increases the band gap due to the quantum confinement and $-\frac{1}{r}$, reducing the band gap because of the Coulomb attraction between the electron and the hole. The overall effect can be visualized in Figure 1.5.

1.4.4 Surface Defect Influences

The band theory applied to semiconductor, along with quantum confinement effects, enables accurate predictions of the band gap of quantum dots using the Brus Equation (1.4). However, these models have limitations for ultrasmall QDs (smaller than 2 nm). At such small dimensions, surface defects may become significant, leading to deviations from theoretical predictions. These defects can lead to two major consequences:

- Stabilization (or pinning) of the particles emission
- Formation of mid-gap electronic sates

These states introduce additional energy levels within the band gap, altering the optoelectronic properties of quantum dots and potentially reducing their emission efficiency. [38, 39]

1.4.4.1 Pinned emission

The limitation to the expansion of the band gap, illustrated in Figure 1.8, finds its origin in a double phenomena.

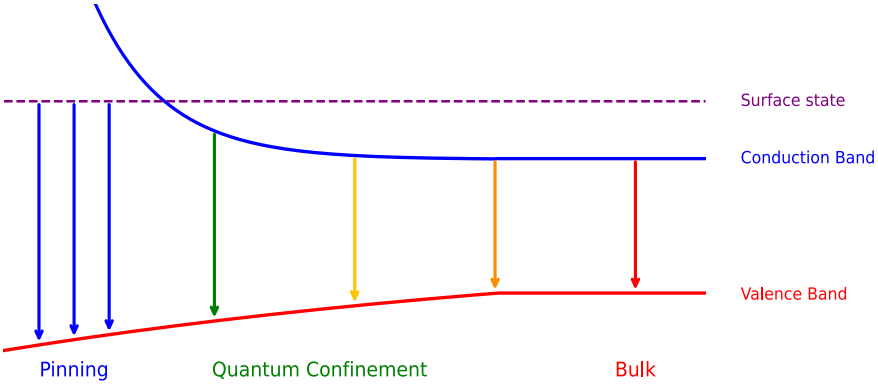

Figure 1.8. Pinning of the QDs emission.

Firstly, in some cases, a rearrangement of the nanoparticles surface can occur without disrupting the crystal lattice. This process leads to relaxed and unrelaxed configurations of the particles. This phenomenon can shift the relative position of the HOMO and LUMO of the clusters, commonly referred to as "self-healing", by reducing surface traps and stabilizing the electronic structure of the particles. [40] Secondly, for ultrasmall particles, Coulomb confinement can become dominant over the kinetic energy of the charge carriers, favouring the formation of a Wigner phase, in which electrons organize into a crystalline-like structure due to strong repulsive interactions. [41]

1.4.4.2 Mid-gap states formation

In addition to the pinning effect, a red shift in the emission spectrum (*i.e.* the formation of mid-gap states) is often observed, generally combined with an increased of the peak Full Width at Half Maximum (FWHM), like summarized in Figure 1.9. This phenomenon occurs when surface molecules contain unsaturated (dangling) bonds, creating electronic states at lower energy levels. [42] Additionally, charge transfer at the interface between the particle and the surface ligands or the solvent can further stabilize these mid-gap states. [43–45]

The formation of mid-gap energy states can be partially mitigated by passivating the surface of quantum dots. This can be achieved either by adding ligands that bond to unsaturated surface sites, thus minimizing surface

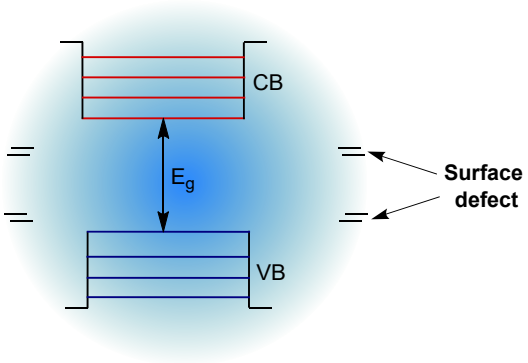

Figure 1.9. Realistic band gap energy diagram including mid-gap energy level (trap states).

defects, or by growing a shell around the QD core, forming a core–shell heterostructure.

1.4.5 Core–shell Nanocrystals and Heterostructures

The synthesis of Core–shell Semiconducting Nanocrystals (CSSNCs) involves a multi-step process in which several layers are grown on the QD core. This strategy can be used to improve the Photoluminescence Quantum Yield (PLQY) by reducing the probability of exciton trapping at surface defects, to tune the optoelectronic properties of the nanocrystals, and to enhance their chemical and photostability.

The effect of shell growth primarily depends on the relative positions of the electronic energy levels of the core and shell materials. For type II–VI semiconductors, these levels are summarized in Figure 1.10. The energy levels are given relative to the vacuum level (0 eV): the conduction band minimum corresponds to the negative electron affinity ($-\chi$), while the valence band maximum is defined as $-\chi - E_{\text{gap}}$. The corresponding values are listed in Table 1.1. [47]

For the type II–VI semiconductors summarized in Figure 1.10 and Table 1.1, the bandgap decreases with increasing chalcogen size (*e.g.*, S > Se > Te) for a given cation. Additionally, comparing different cations shows that zinc-based QDs exhibit a larger bandgap than cadmium-based ones.

As mentioned above, the choice of materials leads to three main types of core–shell CSSNCs, as illustrated in Figure 1.11:

- **Type I CSSNCs**: This is the most common type of core–shell structure. The core has a smaller bandgap than the shell, so the exciton remains

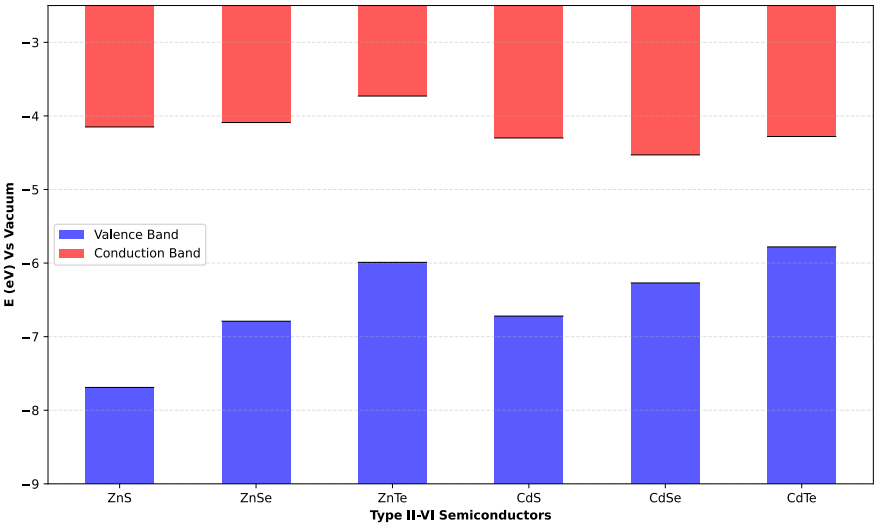

Figure 1.10. Electronic energy levels of the type II–VI semiconductors, based on valence band offsets reported in the reference [46].

Table 1.1. Material parameters of type II-VI bulk semiconductors, data compiled from [46, 47]. [1]: Two lattice parameters are listed due to the Wurtzite crystal structure, whereas the other compounds crystallize in the Zinc Blende structure.

Material	**E_{gap} [eV]**	**Electronic affinity χ [eV]**	**Lattice parameter [Å]**	**Density [kg.m^{-3}]**
ZnS	3.54	4.15	5.41	4090
ZnSe	2.70	4.09	5.668	5266
ZnTe	2.26	3.73	6.104	5636
CdS	2.42	4.30	4.136/6.714[1]	4820
CdSe	1.74	4.53	4.3/7.01[1]	5810
CdTe	1.50	4.28	6.482	5870

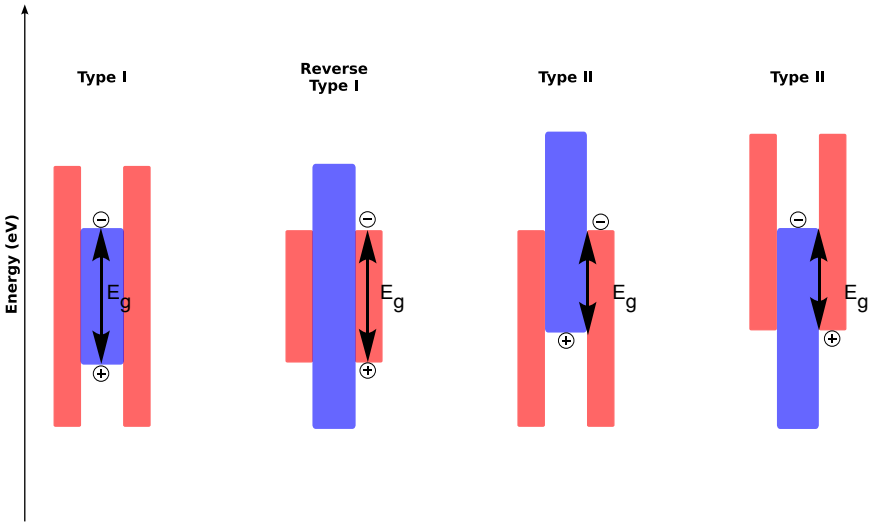

Figure 1.11. Schematic illustration of energy-level alignment in various core/shell structures. The top and bottom edges of each rectangle represent the positions of the conduction and valence band edges for the core (blue) and shell materials (red), respectively, adapted from [47].

confined within the core, isolated from surface defects that are passivated by the shell. Common examples include CdSe/CdS, CdSe/ZnS, among many others. [47]

- **Reverse Type I CSSNCs**: In this case, the shell has a smaller bandgap than the core, causing the exciton to be confined in the shell. This configuration allows better control over the spatial distribution of charge carriers. Examples include CdS/CdSe, ZnSe/CdSe, along with many others. [47]
- **Type II CSSNCs**: The band alignment depends on the relative positions of the core and shell energy levels. The electron and hole are spatially separated, with the electron confined in the material with the lower conduction band and the hole in the material with the higher valence band. An example is ZnTe/CdX (X = S, Se, Te). [48]

To achieve improved synthesis of core–shell nanocrystals, it is preferable to use materials with closely matched lattice parameters. For example, in the case of CdSe passivation, ZnS is often used. However, its lattice mismatch is greater than that of CdS (*i.e.*, the difference in lattice constants between two materials that can induce strain and defects at the core–shell interface when the mismatch is large). For this reason, CdSe is commonly passivated using a core–shell–shell structure (*e.g.*, CdSe/CdS/ZnS). [49]

1.5 QDs Formation

This section will focus exclusively on the bottom-up approach to quantum dot synthesis. Their formation occurs according to three main stages: (a) pre-nucleation, (b) nucleation, and (c) growth, eventually accompanied by Ostwald ripening. A qualitative understanding of these overall processes can be gained through the LaMer or the Finke-Watzky mechanisms, which will be discussed in the sections 1.5.5 and 1.5.6.

1.5.1 Pre-nucleation or Phase I

At the origin of every bottom up approach, there is a pre-nucleation phase or phase I. Indeed, the particle formation is primarily governed by the monomer concentration and more precisely its concentration regarding to the solubility threshold.

Since the entire process of quantum dot formation depends on the monomer concentration, precise control of the kinetic parameters is required to maintain the monomer concentration in solution above the solubility threshold. This parameter is critical for controlling the subsequent nucleation and growth steps.

In most cases, as shown in Figure 1.1, the monomeric units forming QDs consist of heteroatomic molecules produced through chemical reactions. The precise control of these monomeric units formation can therefore be particularly challenging.

1.5.2 Nucleation or Phase II

This section focuses on the homogeneous Classical Nucleation Theory (CNT), phenomenon that occurs during the formation of soluble QDs. The nucleation process is driven by changes in Gibbs free energy (ΔG). During supersaturation, dispersed monomers spontaneously assemble into nanocrystals. However, for these nuclei to become stable, their size must surpass an activation barrier ($\Delta G^{\ddagger}$).

The general expression for the formation of a spherical nucleus containing n monomers is given by Equation 1.5. The driving forces behind nucleation can be divided into two main contributions: the gain in chemical energy (released through bond formation within the crystal) and the increase in surface energy. [50]

$$\Delta G = n(\mu_c - \mu_l) + 4\pi r^2 \sigma \tag{1.5}$$

Where:

- $\boldsymbol{\Delta G}$: Gibbs free energy [J],
- $\mathbf{n}$: Number of monomeric building blocks [units],
- $\boldsymbol{\mu_c}$: Chemical potential of crystal phase [J.mol^{-1}],
- $\boldsymbol{\mu_l}$: Chemical potential of liquid phase [J.mol^{-1}],
- $\mathbf{r}$: Nucleus radius [m],
- $\boldsymbol{\sigma}$: Surface tension [N.m^{-1}].

To express directly the Gibbs free energy variation as function of the particle radius, the Equation 1.5 is often rewritten by posing:

$$\Delta G_v = \frac{\Delta \mu}{\Omega} \tag{1.6}$$

Where:

- $\boldsymbol{\Delta G_v}$: Gibbs free energy per unit volume [J.m^{-3}],
- $\boldsymbol{\Omega}$: New phase molar volume [m^3.mol^{-1}].

and:

$$n = \frac{\left(\frac{4\pi r^3}{3}\right)}{\Omega} \tag{1.7}$$

The combination of Equation 1.6 and Equation 1.7 leads to the Equation 1.8.

$$n(\mu_c - \mu_l) = \frac{4}{3}\pi r^3 \Delta G_v \tag{1.8}$$

The final expression is given by Equation 1.9. In this form, the variations in Gibbs free energy are directly expressed as a function of particle radius. It appears as a sum of two terms: the volume term $\frac{4}{3}\pi r^3 \Delta G_v$ and the surface term $4\pi r^2 \sigma$.

$$\Delta G(r) = \frac{4}{3}\pi r^3 \Delta G_v + 4\pi r^2 \sigma \tag{1.9}$$

Where:

- $\boldsymbol{\Delta G(r)}$: Gibbs free energy as a radius function [J],
- $\mathbf{r}$: Nucleus radius [m],
- $\boldsymbol{\Delta G_v}$: Gibbs free energy per unit volume [J.m^{-3}],
- $\boldsymbol{\sigma}$: Surface tension [N.m^{-1}].

In this form, the critical radius (r*), at which the nanocrystal spontaneously assembles, can be determined. Beyond this point, the system thermodynamically evolves towards larger particles. This expression is obtained by identifying the maximum of the $\Delta G(r)$ function using Equation 1.9.

$$\left|\frac{dG}{dr}\right|_{r=r^*} = 0 \tag{1.10}$$

It leads that the critical radius of nanocrystal (r*) is defined by Equation 1.11.

$$r^* = \frac{2\sigma}{|\Delta G_v|} \tag{1.11}$$

The injection of the critical radius (r*) expression in Equation 1.11 allows to calculate the nucleation activation barrier ($\Delta G^{\ddagger}$), leading to Equation 1.12.

$$\Delta G^{\ddagger} = \frac{16\pi\sigma^3}{3(\Delta G_v)^2} \tag{1.12}$$

Figure 1.12 provides a clear summary of the mathematical development of the nucleation phenomenon, showing the variation of Gibbs free energy as a function of particle radius. The contributions of the terms introduced in Equation 1.9 are represented: volume (red curve), surface (black curve), and their sum (green curve). At small radii, the surface term dominates, making small nuclei unstable. Once the critical radius (r*) is reached, the volume contribution takes over, promoting the growth of the newly formed nuclei.

Note that Equation 1.9 represents an ideal case. In the presence of ions and ligands, a polar layer may form, or complexation of the reactive species can occur. These effects may lead to deviations from the ideal case. Therefore, it is sometimes necessary to add a third term to Equation 1.9, called the ion interaction energy term (F_{ions}). In practice, this term is computed as a volume integral of three contributions: electrostatic interactions, solvation

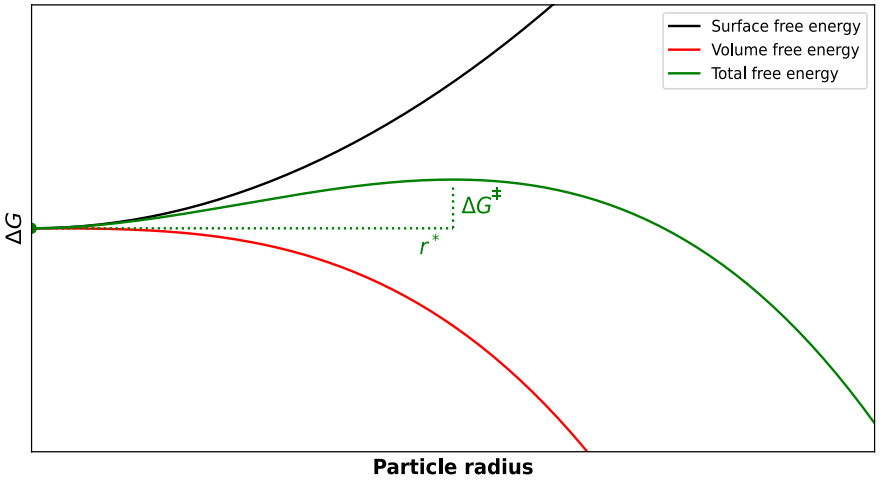

Figure 1.12. Gibbs free energy (ΔG) variation with particle growth.

energy, and entropy. It is challenging to calculate F_{ions} and it is often required to proceed through numerical simulations. [51]

Finally, the nucleation rate (J) can be determined using an Arrhenius-type expression, as shown in Equation 1.13. [52] It explicitly depends on the activation barrier and temperature. The pre-exponential factor is influenced by the number of nucleation sites, the attachment rate to the nucleus, and the probability that the radius reaches its critical value (r*). [53, 54]

$$J = A.\exp\left(-\frac{\Delta G^{\ddagger}}{k_B T}\right) \tag{1.13}$$

Where:

- $\boldsymbol{J}$: Nucleation rate [s^{-1}],
- **A**: Pre-exponential term [dimensionless],
- $\boldsymbol{\Delta G^{\ddagger}}$: Nucleation activation barrier [J],
- $\mathbf{k_B}$: Boltzmann constant [$J.K^{-1}$],
- **T**: Absolute temperature [K].

The nucleation activation barrier ($\Delta G^{\ddagger}$) being determined by mean of Equation 1.12, its expression is replaced in Equation 1.13, leading to the Equation 1.14.

$$J = A.\exp\left(-\frac{16\pi\sigma^3}{3k_BT(\Delta G_v)^2}\right) \tag{1.14}$$

Where:

- $\boldsymbol{J}$: Nucleation rate [s^{-1}],
- $\mathbf{A}$: Pre-exponential term [s^{-1}],
- $\boldsymbol{\sigma}$: Surface tension [$N.m^{-1}$],
- $\mathbf{k_B}$: Boltzmann constant [$J.K^{-1}$],
- $\mathbf{T}$: Absolute temperature [K],
- $\boldsymbol{\Delta G_v}$: Gibbs free energy per unit volume [$J.m^{-3}$].

The discussion above focuses exclusively on homogeneous nucleation, which competes with heterogeneous nucleation processes. As the name suggests, heterogeneous nucleation occurs on pre-existing nucleation sites, such as impurities or the reactor surface, and is generally favoured over homogeneous nucleation due to its lower activation barrier. The relationship between the two activation barriers is given by Equation 1.15, which shows that the heterogeneous nucleation barrier is reduced relative to the homogeneous one by a geometrical factor dependent on the contact angle between the liquid and the solid. [53]

$$\Delta G^{\ddagger}_{\text{het}} = \Delta G^{\ddagger}_{\text{homo}}, f(\theta) \tag{1.15}$$

Where:

- $\boldsymbol{\Delta G^{\ddagger}_{het}}$: Heterogeneous nucleation activation barrier [J],
- $\boldsymbol{\Delta G^{\ddagger}_{homo}}$: Homogeneous nucleation activation barrier [J],
- $\boldsymbol{f(\theta)}$: Geometrical reduction factor for heterogeneous nucleation [dimensionless].

The geometrical factor $f(\theta)$ corresponds to the ratio between the volume of a spherical cap formed during heterogeneous nucleation on a solid substrate and the volume of a complete spherical nucleus formed during homogeneous nucleation. This factor quantifies the reduction of the nucleation energy barrier induced by the presence of a solid surface and is given by Equation 1.16.

$$f(\theta) = \frac{1}{2} - \frac{3}{4}\cos\theta + \frac{1}{4}\cos^3\theta \tag{1.16}$$

Where:

- $\boldsymbol{f(\theta)}$: Geometrical reduction factor [dimensionless],
- $\boldsymbol{\theta}$: Contact angle between the liquid phase and the nucleation site, determined by Young's equation [radians].

Equation 1.16 implies that for $\theta \in [0, \pi]$, $f(\theta) \leq 1$, with equality only in the limiting case of a non-wetting substrate. Consequently, the activation energy barrier for heterogeneous nucleation is always lower than or equal to that for homogeneous nucleation. As a result, the free energy barrier for homogeneous nucleation ($\Delta G^{\ddagger}_{\text{homo}}$) is greater than or equal to that for heterogeneous nucleation ($\Delta G^{\ddagger}_{\text{het}}$).

Therefore, optimizing experimental conditions to favour homogeneous nucleation (*e.g.*, high supersaturation, reactor wall properties, reagent purity) is essential to minimize the impact of heterogeneous nucleation. [54]

1.5.3 Growth or Phase III

As the monomer concentration decreases below the minimum nucleation concentration while remaining above the solubility threshold, nucleation ceases and the excess monomers contribute to particle growth. The general expression describing particle growth is given by Equation 1.17.

$$\frac{dr}{dt} = \frac{\dot{n}}{4\pi r^2 \rho_m} \tag{1.17}$$

Where:

- $\mathbf{r}$: Particle radius [m],
- $\mathbf{t}$: Time [s],
- $\dot{\mathbf{n}}$: Monomer flux [$\text{mol} \cdot \text{s}^{-1}$],
- $\rho_{\mathbf{m}}$: Molar density of the solid phase [mol.m^{-3}].

The diffusive flux of material arriving at the particle surface is governed by Fick's law, as expressed in Equation 1.18.

$$\dot{n} = 4\pi r D(C_\infty - C_i) \tag{1.18}$$

Where:

- **D**: diffusion coefficient $[\mathrm{m}^2 \cdot \mathrm{s}^{-1}]$,
- $\mathbf{C_\infty}$: monomer concentration in the bulk solution $[\mathrm{mol} \cdot \mathrm{L}^{-1}]$,
- $\mathbf{C_i}$: monomer concentration at the particle interface $[\mathrm{mol} \cdot \mathrm{L}^{-1}]$.

Substituting Equation 1.18 into Equation 1.17 leads to the general growth law for quantum dots:

$$\frac{dr}{dt} = \frac{D(C_\infty - C_i)}{r\rho_m} \tag{1.19}$$

Integration of Equation 1.19 yields:

$$r(t) = \sqrt{r^{*2} + \frac{2D(C_\infty - C_i)}{\rho_m} t} \tag{1.20}$$

Equation 1.20 is valid from the formation of stable particles (*i.e.*, particles larger than the critical radius r^*) until another process becomes rate-limiting or until the concentration gradient vanishes ($C_\infty - C_i \leq 0$). This diffusion-limited growth regime is characterized by a $r \sim t^{1/2}$ dependence and is typically associated with particle size broadening, *i.e.*, an increase in the particle FWHM, see Figure 1.13.

1.5.4 Ostwald Ripening

As the reaction proceeds, the monomer concentration in solution eventually decreases below the solubility threshold, and particle growth becomes governed by curvature-induced solubility effects described by the Gibbs–Thomson relation (Equation 1.21). In this regime, the system minimizes its total surface energy through the dissolution of smaller particles and the growth of larger ones, a process commonly referred to Ostwald ripening. [55]

$$C_{eq}(r) = C_{eq}(\infty) \exp\left(\frac{2\sigma V_m}{r k_B T}\right) \tag{1.21}$$

Where:

- $\mathbf{C_{eq}(r)}$: Equilibrium monomer concentration at the surface of a particle of radius r [mol $\cdot$ L^{-1}],
- $\mathbf{C_{eq}(\infty)}$: Equilibrium monomer concentration at a planar interface [mol $\cdot$ L^{-1}],
- $\boldsymbol{\sigma}$:Surface tension [N $\cdot$ m^{-1}],
- $\mathbf{V_m}$: Molar volume [m^3 $\cdot$ mol^{-1}],
- $\mathbf{r}$: Particle radius [m],
- $\mathbf{k_B}$: Boltzmann constant [J $\cdot$ K^{-1}],
- $\mathbf{T}$: Absolute temperature [K].

The Gibbs–Thomson equation predicts that, at equilibrium, the monomer concentration surrounding smaller particles is higher than that around larger ones. Consequently, smaller particles tend to dissolve, releasing monomeric units that diffuse through the solution and contribute to the growth of larger particles.

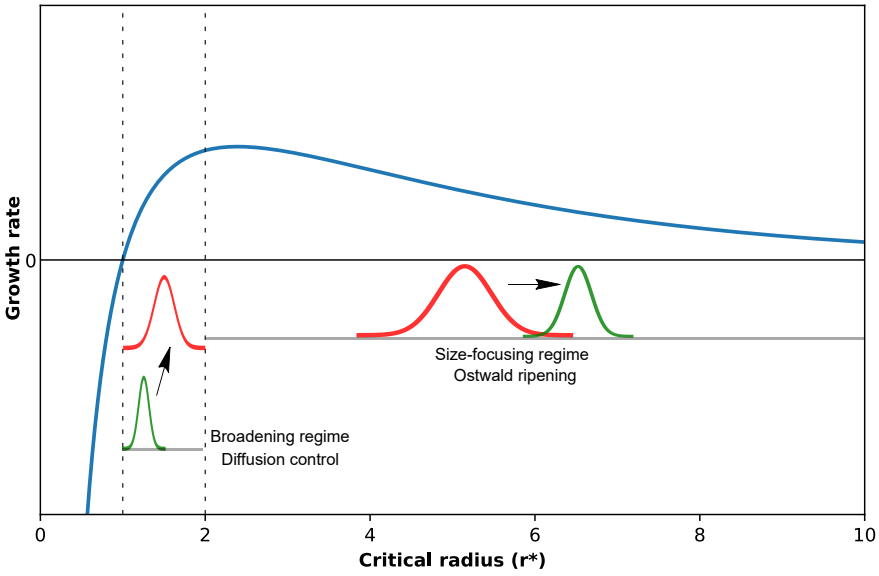

Figure 1.13. Evolution of quantum dot growth regimes as a function of particle radius relative to the critical radius r^*.

Among the various attempts to quantitatively describe Ostwald ripening, Lifshitz and Slyozov proposed a diffusion-limited model in which the temporal evolution of the average particle radius is given by Equation 1.22. [56]

$$\langle r \rangle^3 - \langle r \rangle_0^3 = \frac{8\sigma C_{eq} V_m^2 D}{9RT}, t \tag{1.22}$$

Where:

- $\langle \mathbf{r} \rangle$: Average particle radius [m],
- $\langle \mathbf{r} \rangle_\mathbf{0}$: Initial average particle radius [m],
- $\boldsymbol{\sigma}$: Surface tension [$\mathrm{N \cdot m^{-1}}$],
- $\mathbf{C_{eq}}$: Equilibrium monomer concentration at the particle interface [$\mathrm{mol \cdot L^{-1}}$],
- $\mathbf{V_m}$: Molar volume [$\mathrm{m^3 \cdot mol^{-1}}$],
- $\mathbf{D}$: Diffusion coefficient [$\mathrm{m^2 \cdot s^{-1}}$],
- $\mathbf{R}$: Gas constant [$\mathrm{J \cdot mol^{-1} \cdot K^{-1}}$],
- $\mathbf{T}$: Absolute temperature [K],
- $\mathbf{t}$: Time [s].

In this framework, Equation 1.22 predicts a growth law of the form $\langle r \rangle \sim t^{1/3}$. Depending on the experimental conditions, Ostwald ripening may lead either to a transient size focusing or to a broadening of the particle size distribution. [57, 58]

The transition between growth regimes is illustrated in Figure 1.13. Initially, particle growth is dominated by high supersaturation and diffusion-limited monomer supply. Once the solubility threshold is crossed, the system enters the Ostwald ripening regime, where smaller particles dissolve and feed the growth of larger ones. Surface ligands can significantly slow down this process by stabilizing the particle surface, thereby enhancing colloidal stability and allowing partial control over long-term size evolution.

1.5.5 LaMer Mechanism

Originally proposed by LaMer in 1952, this model provides a conceptual framework for understanding homogeneous nucleation across a wide spectrum of fields, from colloid chemistry to metallurgy. [59] It describes how a new condensed phase emerges from a supersaturated homogeneous medium.

In the context of quantum dots, the system evolves from dissolved monomeric species toward a solid nanocrystalline phase, as illustrated in Figure 1.14. The mechanism is classically divided into three stages. In Phase I,

monomers are produced (typically through a chemical reaction) and gradually accumulate in the liquid phase. When the monomer concentration reaches the critical supersaturation threshold, spontaneous homogeneous nucleation takes place (Phase II). During this burst nucleation event, a large number of nuclei form over a very short period while the monomer concentration drops rapidly below the nucleation threshold. Beyond this point, no new nuclei can form.

Under LaMer conditions, the particle concentration during the nucleation stage can be roughly estimated by:

$$\frac{d[\mathrm{M}]}{dt} = -k_1[\mathrm{M}] \tag{1.23}$$

Where:

- $[\mathbf{M}]$ = Monomer concentration [mol.L^{-1}],
- $\mathbf{t}$ = Time [s],
- $\mathbf{k_1}$ = Kinetic constant for precursor degradation [variable],

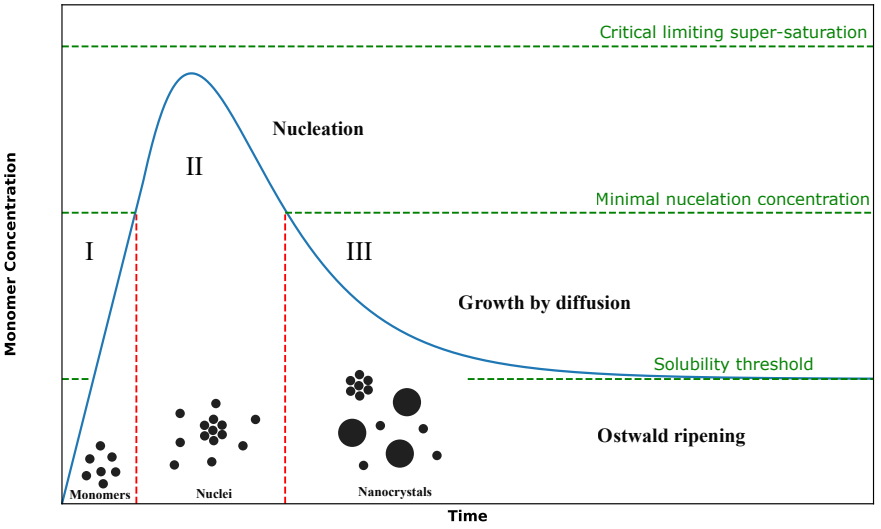

Figure 1.14. Scheme of the LaMer mechanism.

In Phase III, as long as the monomer concentration remains above the solubility limit, the existing nuclei continue to grow by monomer addition. Once the concentration falls below this limit, further growth may occur through Ostwald ripening. A more detailed description of these growth regimes is provided in the following sections.

1.5.6 Finke-Watzky Mechanism

The Finke-Watzky mechanism (FW mechanism) mechanism was introduced in 1997 by Watzky *et al.* in the context of catalytic nanoparticle formation, but it is now widely recognized as a more general and flexible description of nucleation and growth phenomena. [60] It can be viewed as a generalization of the ideal LaMer model.

Whereas LaMer assumes a burst, instantaneous, and purely homogeneous nucleation event followed by growth, the FW mechanism abandoned these constraints. In particular, it better describes systems with slow kinetics or high activation barriers, for which nucleation is not instantaneous. As shown in Figure 1.15, the time evolution of particle concentration displays an initial lag phase, during which no detectable nanoparticles are formed. Nucleation then begins and proceeds according to CNT, producing the first nanoparticles.

The FW mechanism expresses the rate of nanoparticle formation as the combination of two parallel pathways:

$$\frac{d[\mathrm{M}]}{dt} = -k_1[\mathrm{M}] - k_2[\mathrm{M}][\mathrm{QD}] \tag{1.24}$$

Where:

- $[\mathbf{M}]$ = Monomer concentration [mol.L^{-1}],
- $\mathbf{t}$ = Time [s],
- $\mathbf{k_1}$ = Kinetic constant for precursor degradation [variable],
- $\mathbf{k_2}$ = Kinetic constant for the autocatalytic reaction [variable],
- $[\mathbf{QD}]$ = Quantum dot concentration [mol.L^{-1}].

Once the first nuclei are formed, their surfaces catalyze further precursor conversion. This leads to an autocatalytic growth pathway (k_2), which is typically faster and more efficient than the homogeneous pathway described by k_1. As a result, new nuclei may continue to form throughout the reaction, producing the characteristic sigmoidal particle concentration curve. [61]

1.5.7 QD Surface Passivation

As shown in Equation 1.9 and Figure 1.12, from a thermodynamic point of view, once the critical radius (r^*) is exceeded, further particle growth becomes energetically favourable. Surface ligands play a key role in moderating this process. By reducing the interfacial tension (σ) at the crystal–solvent

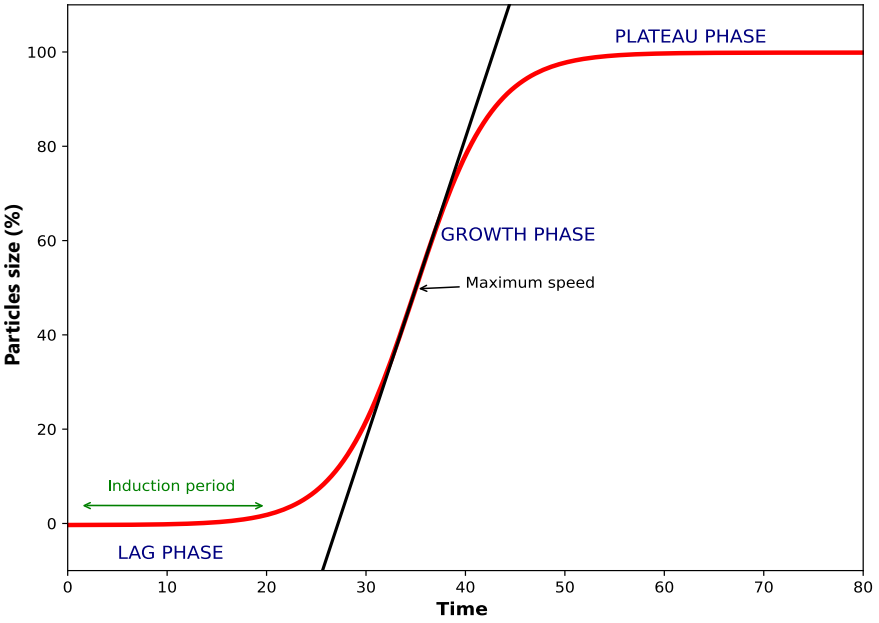

Figure 1.15. General representation of the Finke–Watzky mechanism, showing the sigmoidal evolution of particle concentration as a function of time. Figure adapted from [61].

interface, ligands decrease the thermodynamic driving force for nucleation and growth. This can lead to a quasi-equilibrium state in which growth significantly slows down or becomes kinetically limited, not due to monomer depletion but because the surface becomes energetically saturated.

These ligands bind to the nanocrystal surface, providing steric and, in some cases, electrostatic stabilization. They also contribute to passivating surface defects, as discussed in Section 1.4.4.

In surface chemistry, [62–67] ligands are commonly classified into three major types based on their binding modes, as depicted in Figure 1.16. This classification is determined by their chemical functionality and the nature of their interaction with the QD surface:

- **L-type ligands**: Neutral two-electron donors that possess a lone electron pair, which forms a dative bond with a surface metal atom (*e.g.*, :PR_3, :NH_2R, :OPR_3).
- **X-type ligands**: Functional groups that possess an odd number of valence electrons in their neutral form and require one electron from the crystal surface to form a two-electron covalent bond (*e.g.*, -O_2CR, -SR, -O(OH)POR).

- **Z-type ligands**: Ligands that possess an even number of valence electrons in their neutral form and act as electron acceptors, forming a coordinate covalent bond by accepting a pair of electrons from the crystal surface, typically metal-based Lewis acids (*e.g.*, $Cd(O_2CR)_2$, $Cd(SR)_2$, $CdCl_2$, $Cd(OPR_3)_2$).

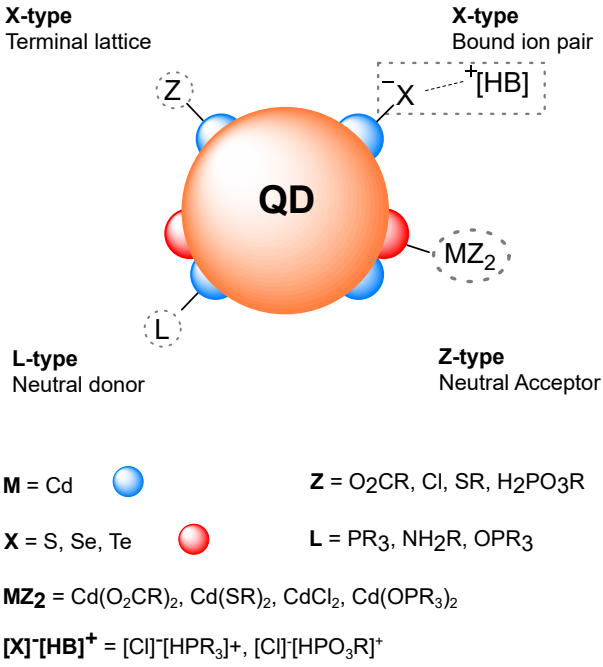

Figure 1.16. Illustration of the different coordination types of the cadmium-chacogenide QDs surface with ligands, adapted from [64].

In practical reaction conditions, the QD surface is often covered by a mixture of ligand types. The nature of the ligands, their concentration, and the timing of their introduction during synthesis depend heavily on the intended outcome. Several strategies can be adopted depending on the desired particle properties:

- Use of weakly binding ligands during growth, which allows larger particle formation, followed by introduction of strongly binding ligands to halt growth and stabilize the surface.
- Use of moderate-affinity ligands throughout, which facilitates post-synthetic ligand exchange to tune solubility or surface functionality.
- Early introduction of X-type ligands, which strongly bind to the surface and limit particle growth, resulting in smaller QDs sizes.

A concise overview of ligand classes and their binding characteristics is provided in Table 1.2, helping to rationalize the chemist's choices.

Table 1.2. Summary of ligand types, their chemical nature, interaction types with surfaces, and relative bond strengths.

Ligand type	Ligand nature	Interaction type	Relative bond strength
X-type	Anionic ligand (Lewis base)	Ionic or polarized covalent bond	Strong
L-type	Neutral donor ligand (Lewis base)	Covalent dative bond (σ-donation)	Moderate
Z-type	Neutral acceptor ligand (Lewis acid)	Back-donation or metal-to-ligand π-backbonding	Variable (often weak to moderate)

The impact of ligands on quantum dot nucleation, growth, and surface stabilization cannot be fully decoupled from the physical conditions under which the synthesis occurs. Temperature gradients, mixing efficiency, and precursor delivery rates all modulate the outcome of surface–ligand interactions.

1.5.8 Quantum Dots Morphology

As depicted in Figure 1.7, quantum confinement can occur over different dimensionalities, leading to a wide range of optoelectronic properties. These properties depend primarily on the synthesis pathway. In Section 1.5.3, it is assumed that, during the growth phase, all sites where monomeric units are deposited are equivalent. However, the parameters $C_{eq}(\infty)$ (equilibrium concentration on a planar surface) and σ (surface tension), as defined in Equation 1.21, are not necessarily identical across all crystallographic surfaces, which can result in nanocrystals with diverse morphologies. [68] Depending on facet availability, the growing crystal can evolve into either an isotropic structure (*e.g.*, 0D confinement) or an anisotropic one (*e.g.*, 1D or 2D confinement).

From a thermodynamic perspective, the Curie–Gibbs–Wulff theorem states that not all facets of a growing crystal are equivalent, thereby influencing its final morphology. [57] As discussed in Section 1.5.7 and shown in Table 1.2, the bond strength between the surface and the ligand can either promote the addition of monomeric units or inhibit growth on a given facet. During the growth phase, the dynamics of ligand binding and exchange at the synthesis temperature modulate these facet-dependent energies, thereby coupling surface chemistry to crystal shape evolution. [69] This interplay primarily

affects the surface tension term σ in the thermodynamic description of morphology. [40, 70]

In addition to these surface-related effects, the concentration of available monomers also governs the growth regime and thus the resulting shape. It plays a significant role in determining $C_{eq}(\infty)$ [71]:

- **Low monomer concentration:** isotropic nanocrystal growth, typically exhibiting 0D confinement.
- **Intermediate monomer concentration:** anisotropic growth, often resulting in rod-like structures (1D confinement).
- **High monomer concentration:** strongly anisotropic growth, potentially forming tetrapods.

More generally, when nanoparticles exceed a size of approximately 10 nm, anisotropic growth is often favoured under typical synthetic conditions, thereby impacting the emission properties of the resulting quantum dots.

1.6 Reactors Technologies

This section is primarily based on the lectures given by *Sophie Liégeois* within the framework of the *"Génie Chimique 4, Réacteurs Chimiques"* course at Meurice Institut during the 2017–2018 academic year as well as the reference book "Fogler, H. S. (2016). Elements of Chemical Reaction Engineering (5^{th} ed.)" [72]

1.6.1 Reactors Overview

The reactor is at the heart of chemical processes, where reagents are converted into the desired products while optimizing conversion efficiency, product selectivity, and reaction rates. Over time, various reactor types have been developed to improve both conversion efficiency and selectivity. Inside the reactor, many parameters, such as heat and mass transfer, residence time, and temperature control, can significantly influence the reaction outcome. Therefore, it is crucial to judiciously select the most suitable reactor type based on factors such as reaction kinetics, heat and mass transfer characteristics, and energy efficiency. [73]

Three main types of reactors have been developed, each with its distinct operational advantages and limitations. The comparison between them is often based on the time reaction (t for batch) or mean residence time ($\boldsymbol{\tau}$ for

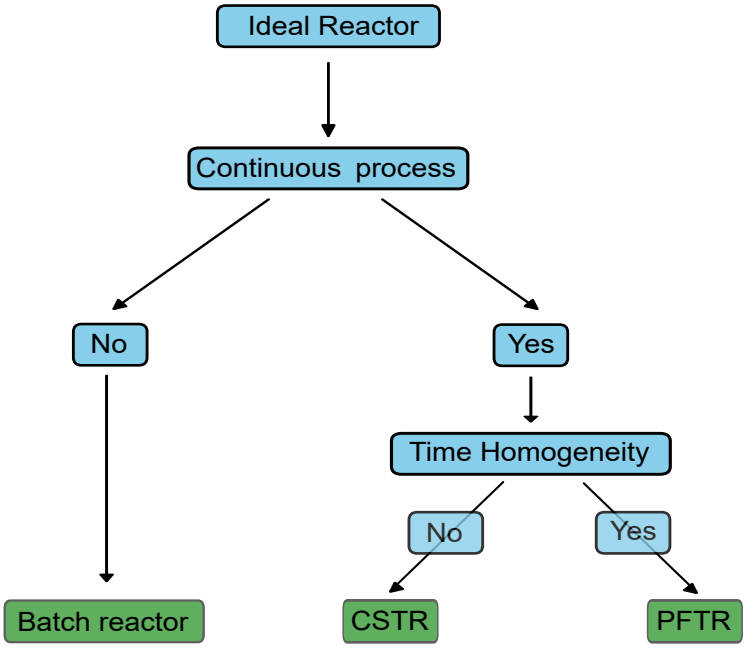

Figure 1.17. Reactor choice decision tree

continuous reactors, *e.g.*, $\tau = \frac{V}{V'}$, where V = reactor volume, V' = Flow rate) required to reach a given conversion (X). [74] Their main characteristics and design equations are summarized below:

a) Batch reactor (BR)

They are widely used, especially in laboratory settings for R&D and in industries such as pharmaceuticals and fine chemicals. In an ideal case, they are perfectly mixed, ensuring uniform composition throughout the reactor. The concentrations of the chemical species are unsteady and change over time, as the conversion of reagents to products increases. However, they operate in a discontinuous manner, requiring filling, reaction, and emptying steps.

$$t_{batch} = -\int_{C_{A0}}^{C_{Af}} \frac{dC_A}{-r_A(C_A)} \tag{1.25}$$

b) Continuously Stirred Tank Reactor (CSTR)

Very much alike batch reactors, CSTRs are tank reactors that are ideally perfectly mixed. However, unlike batch reactors, they operate with a continuous inflow and outflow of reactants and products. This

continuous operation allows them to reach and maintain a steady-state regime under ideal conditions.

$$\tau_{CSTR} = \frac{C_{A0} - C_{Af}}{-r_A(C_{Af})} \tag{1.26}$$

c) Plug Flow Tubular Reactor (PFTR)

This type of reactor consists of a tubular geometry in which steady-state conditions are maintained, while concentration and temperature vary along the reactor length. It also operates continuously and, under ideal conditions, assumes no axial mixing and perfect radial mixing.

$$\tau_{PFTR} = -\int_{C_{A0}}^{C_{Af}} \frac{dC_A}{-r_A(C_A)} \tag{1.27}$$

Where:

- $\boldsymbol{\tau}$: The mean residence time [s],
- $\mathbf{C_A}$: The concentration of species A [mol.L^{-1}],
- $\mathbf{r_A}$: The reaction rate of species A [mol.L^{-1}.s^{-1}].

As a corollary to these design equations, the relevant reaction kinetics parameters must be known in order to select the most suitable reactor. As a first approach to selecting the appropriate reactor technology for a given reaction, a simplified decision tree is presented in Figure 1.17. For practical reasons, continuous reactors are preferred over batch reactors whenever possible because their systems are more stable over time, allowing better control of operating conditions and thus a more homogeneous production.

1.6.2 Continuous Reactors

Both CSTR and PFTR operate in continuous mode, transforming reagents over time. At steady state, the inlet flow rate (V'$_{in}$) equals the outlet flow rate (V'$_{out}$), as illustrated in Figure 1.18. This implies that the system is considered ideal, with no accumulation of compounds within the reactor.

Despite this common characteristic, each reactor has its own operational properties. The following subsection compares ideal CSTR and PFTR reactors based on the mean residence time (τ) required to achieve a given conversion degree (X), the breakthrough curves F(t), and thermal exchanges.

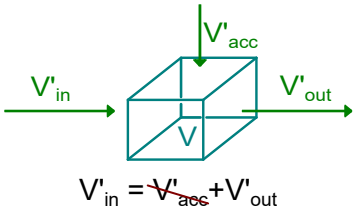

Figure 1.18. Volumetric balance inside a continuous flow reactor at steady state

1) Comparison of the mean residence time through Levenspiel diagram

The Levenspiel diagram consists of a plot with the compound concentration on the x-axis (abscissa) and r^{-1} on the y-axis (ordinate). Therefore, the reaction kinetics must be known beforehand.

In this diagram, the inverse of the reaction rate is plotted against the compound concentration. This representation makes it possible to visualize the mean residence time (τ) required to achieve the desired compound concentration (C_A).

Indeed, Equations 1.26 and 1.27 define the area corresponding to τ in Figure 1.17, for both reactor types.

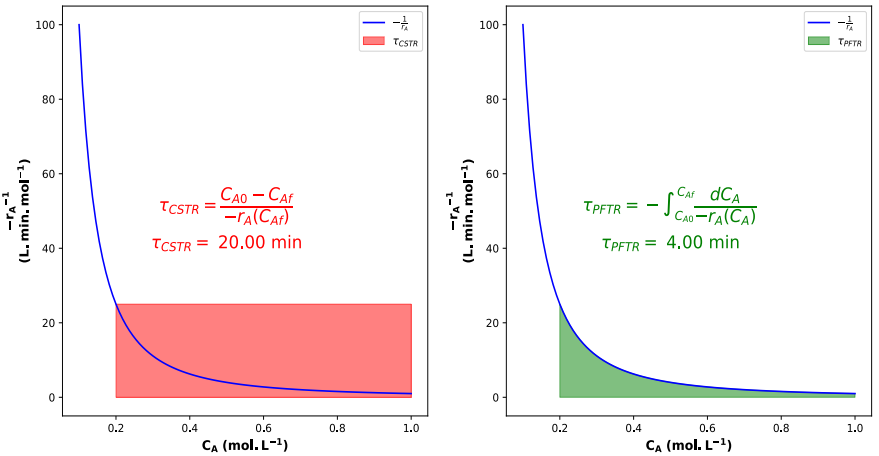

Figure 1.19. Comparison of the mean residence time τ for ideals CSTR and PFTR to reach a C_{A_f} starting from C_{A_0}. In the example presented above: $r_a = -kC_A^2$, where k = 1 $L.mol^{-1}.min^{-1}$.

The example illustrated in Figure 1.19 shows a second-order reaction where reagent A is converted into another product. The initial concentration is $C_{A_0} = 1\ mol.L^{-1}$ and the expected final concentration is $C_{A_f} = 0.2\ mol.L^{-1}$. In both cases, the kinetic constant is k = 1 $L.mol^{-1}.min^{-1}$.

The results show that in the CSTR $\tau = 20$ min, whereas in the PFTR $\tau = 4$ min. This means that to achieve the same conversion, the PFTR requires five times less time than the CSTR.

2) Comparison of the breakthrough curves ($F(t)$)

The breakthrough curves ($F(t)$) provide a useful criterion for estimating the response time of a continuous reactor to a step injection, mathematically represented by a Heaviside function $H(t)$. This situation often occurs when introducing a new reagent into the reactor.

This response curve is calculated using Equation 1.28, and an example of the response curves for both reactor types is presented in Figure 1.20. [75]

$$F(t) = \int_{t_0}^{t_i} E(t)dt \tag{1.28}$$

Where:

- $\boldsymbol{F(t)}$: The breakthrough curve [dimensionless],
- $\boldsymbol{E(t)}$: The residence time distribution [s^{-1}].

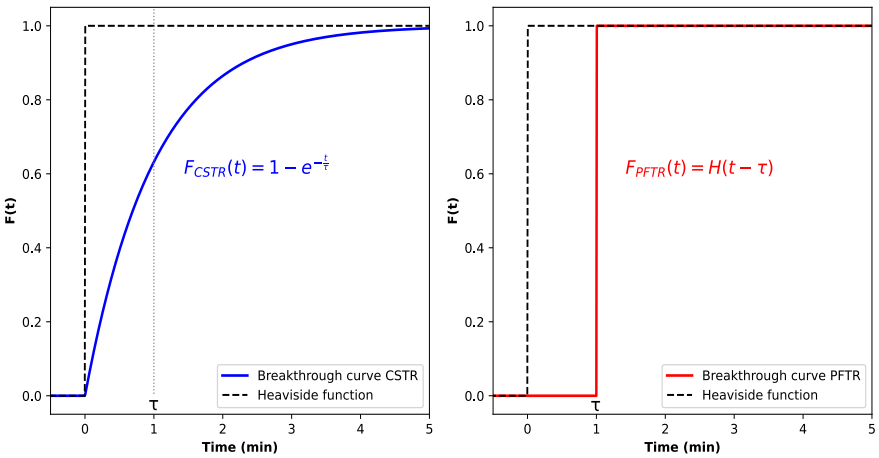

Figure 1.20. Comparison of the breakthrough curves ($F(t)$) for ideal CSTR and PFTR in response to a Heaviside function; in this example $\tau = 1$ min.

The breakthrough curve, illustrating the response time at the outlet of both the CSTR and PFTR to a step injection of a tracer compound, is presented in Figure 1.20. In this example, the mean residence time has been fixed to 1 min.

In the case of the CSTR, the curve takes the form of an exponential growth function, tending toward a horizontal asymptote of 1 as time

$\rightarrow \infty$. At $\tau = 1$ min close to 60% of the outlet flow is composed of the tracer. Therefore, it is necessary to wait several τ's to reach steady state.

However, in the case of the an ideal PFTR, since the flow is a plug flow, at $\tau = 1$ min, the outlet flow reaches 100% tracer concentration. The time required to reach steady state in the case of a PFTR is much shorter than for a CSTR.

3) Comparison of the thermal transfer

In most cases, to keep at constant temperature a reactor, a Heat Transfer Fluid (HTF) circulates around the reactor, transferring heat toward it. This heat transfer typically occurs at an interface (often solid/fluid, *i.e.*, at the wall of the reactor) through a phenomenon called convection (*i.e.*, the combination of **con**duction and ad**vection**. The general expression used to quantify the heat flux by convection is summarized in Equation 1.29.

$$Q = h \cdot \Omega \cdot (T_s - T_{fl}) \tag{1.29}$$

Where:

- $\boldsymbol{Q}$: Heat transfer [W],
- $\mathbf{h}$: Heat transfer coefficient by convection [$\mathrm{W.m^{-2}.K^{-1}}$],
- $\boldsymbol{\Omega}$: Exchange surface [$\mathrm{m^2}$],
- $\mathbf{T_{s,fl}}$: Temperature difference between the solid and the fluid [K].

In most cases, convection around the reactor is driven by mass transfer of the HTF. The study of the temperature evolution in such a system is often very challenging, as it leads to differential equations that are difficult to solve. One solution is to solve these equations numerically, which opens the field to Computational Fluid Dynamic (CFD). However, there is an empirical alternative involving dimensionless numbers. In the case of forced convection, the empirical correlation is given by an expression of the form Equation 1.30, derived using the Buckingham theorem.

$$Nu = k \cdot Re^m Pr^n \tag{1.30}$$

Where:

- $\boldsymbol{k, m, n}$: Constants depending on the geometry, flow regime, etc.

The **Nusselt number (Nu)** is a dimensionless number that characterizes the ratio of convective to conductive heat transfer at a boundary. It is defined as:

$$Nu = \frac{hL_c}{\lambda} \tag{1.31}$$

Where:

- **h**: Convective heat transfer coefficient [W.m^{-2}.K^{-1}],
- $\mathbf{L_c}$: Characteristic length [m],
- $\boldsymbol{\lambda}$: Thermal conductivity of the fluid [W.m^{-1}.K^{-1}].

A higher Nusselt number indicates a dominant convective heat transfer mechanism.

The **Reynolds number (Re)** is a dimensionless quantity that determines the flow regime of a fluid. It is given by:

$$Re = \frac{\rho v L_c}{\mu} \tag{1.32}$$

Where:

- $\boldsymbol{\rho}$: Fluid density [kg.m^{-3}],
- **v**: Average velocity of the fluid [m.s^{-1}],
- $\mathbf{L_c}$: Characteristic length [m],
- $\boldsymbol{\mu}$: Dynamic viscosity [Pa.s].

The flow regime of a fluid is classified, according to the numerical value of Re:

- $Re < 2300$: **Laminar flow** (smooth and orderly).
- $2300 < Re < 10^4$: **Transitional flow** (mix of laminar and turbulent behaviour).
- $Re > 10^4$: **Turbulent flow** (chaotic and highly mixing).

The **Prandtl number (Pr)** is a dimensionless number that represents the ratio between momentum diffusivity (viscous effects) and thermal diffusivity. It is given by:

$$Pr = \frac{\mu c_p}{\lambda} \tag{1.33}$$

Where:

- $\boldsymbol{\mu}$: Dynamic viscosity [Pa.s],
- $\mathbf{c_p}$: Specific heat capacity at constant pressure [J.kg^{-1}.K^{-1}],
- $\boldsymbol{\lambda}$: Thermal conductivity of the fluid [W.m^{-1}.K^{-1}].

In order to illustrate the difference in thermal transfer between a CSTR and a PFTR, a concrete example is shown in Figure 1.20. In this case study, a 1 L reactor is immersed in a HTF at 80 °C, with (V'in) = (V'out) = 75 $mL.min^{-1}$, and the fluid involved is water. The purpose of the exercise is to determine the time required to reach 80 °C. The reactor properties are as follows:

- PFTR: internal diameter = 50 cm, Re_{PFTR} = 1909, for laminar flow, in a pipe, Nu = 3.66, leading to a h_{PFTR} = 43.92 $W.m^{-2}.K^{-1}$.

- CSTR: geometry = spherical, mixing rotor at 300 rpm paddle diameter = 3 cm. Re_{CSTR} is estimated to 14137, Pr = 7 (assumed constant). For these conditions, the Ranz-Marshall correlation was used (*i.e.*, for Equation 1.30, k = 2, m = 0.5, n = 0.33). This resolution led to h_{CSTR} = 825.5 $W.m^{-2}.K^{-1}$.
- Calculation note: The values reported above are calculated under the assumption that the reactor wall remains at a constant temperature (hypothesis valid only for highly conductive walls) and that heat transfer occurs only at the reactor-liquid interface. For a more accurate heat transfer calculation, two additional steps must be considered: the convective heat transfer from the HTF to the reactor wall (using the same process as in Equation 1.30) and the thermal conductivity of the reactor material (λ).

The comparison of the heat transfer coefficient (h) is already telling: 825 $W.m^{-2}.K^{-1}$ for the CSTR vs 44 $W.m^{-2}.K^{-1}$ for the PFTR. This significant difference can be clearly visualized in Figure 1.19: The CSTR reaches fastly the set temperature in approximately 1 min while the PFTR takes about 4 min. These results are mainly explained by the turbulence in the respective reactors: Re_{CSTR} = 14137 compared to Re_{PFTR} = 1909. This indicates that, because the flow regime in the PFTR is laminar, it results to a weak axial thermal dispersion.

4) Global conclusions for continuous reactors

The conclusions of the discussion to compare the CSTR and PFTR are summarized in Table 1.3.

This comparison highlights that both technologies have their advantages and drawbacks. However, it appears that the PFTR offers more benefits

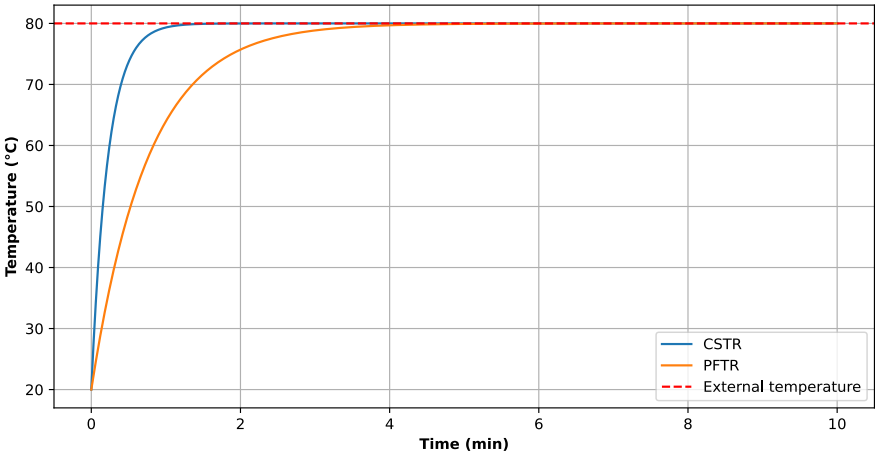

Figure 1.21. Exemple of thermal behaviour of the CSTR vs PFTR to reach 80 °C starting from 20 °C

Table 1.3. Comparison between ideal CSTR and PFTR based on τ, thermal behaviour, and fluid dynamics.

Criterion	CSTR	PFTR
τ in Levenspiel's diagram	Rectangular shape with larger surface than the one between r_a^{-1} and 0	Closely follows the r_a^{-1} curve and minimizes τ
Fluid dynamics	Complete macroscopic mixing, large residence time dispersion	Laminar flow, limited axial dispersion
Thermal behaviour	Uniform temperature, efficient heat transfer	Axial temperature gradients, heat transfer limited by geometry

than the CSTR, except in terms of thermal exchange. This could pose a challenge in the context of this project, as a rapid drop to the temperature set point is crucial for achieving efficient super-saturation. The key factor limiting heat exchange is the pipe diameter. In this context, the emergence of microfluidic reactors could provide a promising compromise, allowing the advantages of the PFTR while also leveraging the benefits of microfluidics.

1.6.3 Microfluidic Reactors

Over the past two decades, the reliance on traditional glass batch reactors has gradually shifted towards a new generation of reactors: continuous flow reactors. In addition to inheriting the intrinsic advantages of PFTR (as discussed above), scaling down further enhances mass and heat transfer due to an improved surface-to-volume ratio compared to macrofluidic systems. Furthermore, these reactors effectively integrate both technology and chemistry, opening new avenues for innovation. A key benefit is their seamless integration with ancillary technologies, such as advanced automation and Process Analytical Technology (PAT). [76] Besides their inherent advantages, continuous flow reactors also present limitations, such as handling solids or highly viscous liquids.

It is important, when discussing scaling down, to clearly distinguish between microfluidic and mesofluidic systems. In the case of microfluidics, the pipe dimensions typically range from 250 μm to 750 μm in internal diameter, while in mesofluidics, the range is from 1 mm to several cm. [77] The following section will focus solely on microfluidics, providing an overview of how microscale technologies can enhance chemistry research, applications, and safety.

1) Thermal Perspective

As discussed in Section 1.6.2, PFTR reactors offer a broad range of advantages: continuous operation, shorter mean residence time (τ), and reduced flow dispersion. However, their geometry often results in low Reynolds numbers (*e.g.*, laminar flow regime), leading to stratified fluid streamlines. The fully developed expression for temperature evolution along a pipe reactor is given in Equation 1.34.

$$\frac{\partial T}{\partial z} = \mathrm{Re} \cdot \mathrm{Pr} \cdot \frac{R}{r \cdot \left(1 - \left(\frac{r}{R}\right)^2\right)} \cdot \frac{\partial}{\partial r}\left(r \frac{\partial T}{\partial r}\right) \tag{1.34}$$

Where:

- $\boldsymbol{T}$: Temperature [K],
- $\boldsymbol{z}$: Axial position [m],
- $\boldsymbol{Re}$: Reynolds number [dimensionless],
- $\boldsymbol{Pr}$: Prandtl number [dimensionless],
- $\boldsymbol{R}$: Pipe radius [m],
- $\boldsymbol{r}$: Radial position in the pipe [m].

As shown in this equation, the pipe radius plays a crucial role in convective heat transfer, especially under laminar flow conditions. Reducing the internal diameter (*i.d.*) of a PFTR from the macroscopic to the microscopic scale (typically below 750 μm) significantly enhances heat transfer efficiency by increasing the surface-area-to-volume ratio. This transition mitigates the main limitation of traditional pipe reactors and enables more effective thermal control in continuous processes.

2) Inherent Safety

In addition to the intrinsic benefits of PFTR in microfluidics, such as precise residence time control, optimized fluid dynamics, and efficient thermal regulation, microfluidic reactors offer significant inherent safety advantages due to their small scale and unique operating principles.

- **Low internal volume:**
  - Continuous operation allows a given production rate to be achieved with significantly smaller reactor volumes.
  - Smaller reactor volumes ensure that, in processes involving hazardous substances, only limited quantities of chemicals are present at any given time.
  - As fewer chemicals are in contact at any given time, the risk of runaway reactions is significantly reduced.
- **Fast thermal exchanges:**
  - High heat dissipation due to the important surface:volume ratio. This is critical for exothermic reactions. As shown in Equation 1.34, the reduced thermal gradient across the microchannels enhances heat transfer, preventing thermal runaway.
  - Additionally, the convective heat transfer coefficient (h) is increased in microfluidic systems (see Equation 1.31), as the Nusselt number remains constant in laminar flow. The small characteristic length (L_c) combined with tunable reactor materials (λ) further optimizes thermal control.

- **Reduced risk of contamination and side reactions:**
  - The continuous flow reactors are compact and enclosed systems reducing the potential exposure to chemical contaminants.
  - The precise flow control allows a strict control on the local stoichiometry avoiding unwanted side reactions.
- **Minimal waste generation and safer handling:**
  - Since the reactor's volumes are smaller, the amount of reagent and product is reduced. Leading to less hazardous waste to manage.
  - Because the chemicals used are enclosed, it is safer to handle and dispose the dangerous chemicals
- **Scalability and modularity:**
  - The modular approach used to design continuous processes allows a more easy scaling-up of the separated steps.
  - The modular construction of these systems makes individual modules easier to isolate and shut down in case of runaway reactions, like shown in Figure 1.23.

3) Selectivity Enhancement

One of the key challenges for 21st-century chemists is to improve the sustainability of chemical processes. In this context, replacing batch reactors with microfluidic reactors offers significant advantages. The precise thermal control in microfluidic systems minimizes temperature gradients within the reactor, keeping the process closer to the set point.

This is particularly beneficial in competitive reactions, where fine thermal regulation selectively favours one reaction pathway over another, thereby enhancing process selectivity and overall yield, as illustrated in Figure 1.22. [79]

4) Static Micromixers

From this point onward, the discussion shifts away from the flow dynamics within the pipe reactor itself and instead focuses on the upstream mixing of reactant feeds, a crucial step prior to their introduction into the reactor. As illustrated in Figure 1.17, in the case of an ideal PFTR, the flow regime is laminar, with limited radial diffusion of chemical species. Since most chemical reactions involve at least two reactant streams, proper mixing of these feeds is essential before they enter the reactor. This requirement becomes particularly critical in microfluidics, where precise control over local stoichiometry, often far superior to that achievable in batch processes, can have a significant impact on reaction selectivity.

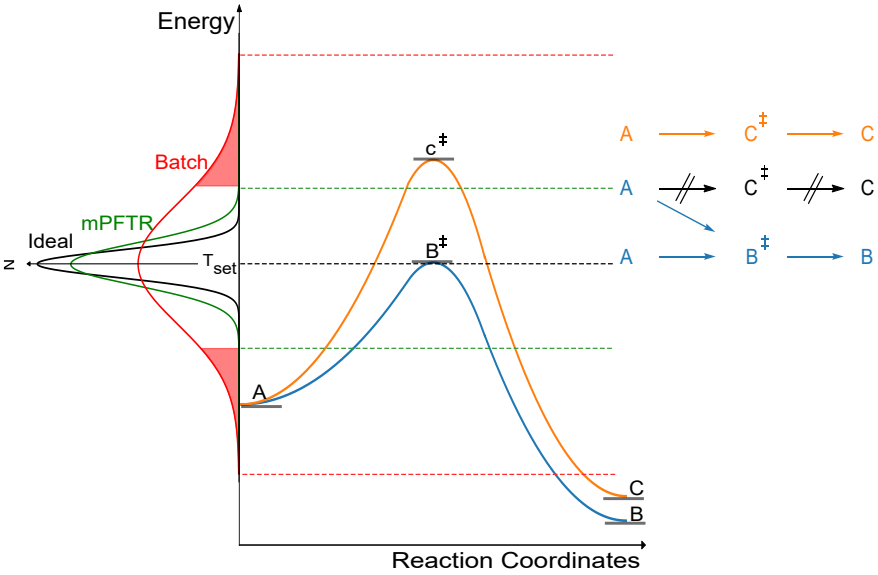

Figure 1.22. Illustration of the selectivity improvement by using microfluidic PFTR (mPFTR), due to the reduction of the temperature distribution. Illustration adapted from [78].

In this context, various types of passive and active mixers have been developed to enhance mixing efficiency in microfluidic systems. In this section, only liquid/liquid mixing will be considered. [80] The most commonly used passive mixers, often regarded as the gold standard in microfluidics, are the T-mixer, the Y-mixer, the arrowhead mixer and helical mixer. [81]

The main parameters influencing flow patterns and, therefore, mixing homogeneity, are the flow rates, the mixer geometry, the viscosity of the liquids, and the temperature. However, unlike the flow in the reactor channel itself, it is often difficult to directly assess the mixing efficiency within the mixer. The most reliable approaches are either experimental, through flow tests using a tracer and an output detector (*e.g.*, Villermaux–Dushman Test) [83, 84] or theoretical, based on finite element simulations using CFD modeling (Comsol or Openfoam). In most cases, simple passive mixers do not allow for complete mixing due to the dominance of laminar flow and the limited contribution of diffusion at small scales. To address this, the addition of embedded obstacles and/or specific structural elements within the channel is often necessary to enhance mixing performance. [82, 85–87]

An alternative to using additional obstacles after the mixer is to simply coil the reactor into a small loop, thereby favouring the formation of internal vortices induced by the centrifugal force resulting from the flow

Table 1.4. Types of Passive Mixers in Microfluidics

Mixer Type	Advantages	Disadvantages	Ref
T-Mixer	Simple design, low pressure drop	Incomplete mixing for highly viscous fluids, limited by low Reynolds number (laminar flow)	[80, 82]
Y-Mixer	Less pressure drop compared to other mixers, suitable for mixing at low flow rates	Not suitable for very high flow rates, limited performance in complex fluid dynamics	[80]
Arrowhead Mixer	High mixing efficiency at low flow rates, simple geometry for integration into microfluidic systems	Requires more complex fabrication, may not work well with highly viscous fluids	[81]
Helical Mixer	Efficient mixing for a wide range of flow conditions, continuous mixing over long distances	Higher pressure drop compared to simple mixers, complex fabrication and higher fabrication cost	[80]

rate. The intensity of the generated vortices is quantified by the **Dean number (De)**, a dimensionless quantity. [74, 88, 89]

This value is calculated as follows:

$$De = Re\sqrt{\frac{D}{R}} \tag{1.35}$$

Where:

- **De**: Dean number [dimensionless],
- **Re**: Reynolds number [dimensionless],
- **D**: Hydraulic diameter [m],
- **R**: Curvature radius [m].

An illustrative calculation of the Dean vortex generated in a microfluidic pipe (750 μm in diameter), coiled into a 10 cm diameter loop, is provided in Figure 1.22.

Under microfluidic conditions, the flow behaviour depends strongly on the Dean number: for De < 5, the flow remains almost purely axial; between 5 and 20, weak secondary vortices appear, allowing

limited transverse spreading; in the range 20–100, Dean vortices are well developed, offering a good compromise between mixing efficiency and flow stability; finally, for De > 100, strong secondary flows dominate, promoting efficient mixing but potentially inducing particle migration or inertial separation effects.

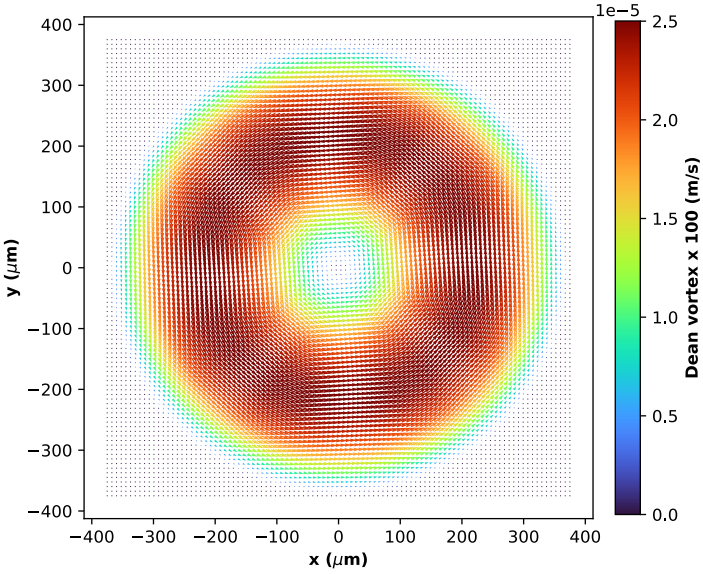

Figure 1.23. Illustration of the Dean vortex inside a tube with 750 μm inner diameter (*i.d.*), which is a common dimension at lab scale, curved into a 10 cm diameter loop, crossed by a water flow of 500 $\mu L.min^{-1}$. Note that the vortex speeds have been scaled by a factor of 100 to improve the visual clarity.

In the example illustrated in Figure 1.23, the flow is characterized by a Reynolds number of **Re** = 14.15 and a Dean number of **De** = 1.73. These values indicate a laminar regime, with only minimal Dean-induced recirculation, leading to slight broadening of the particle front rather than significant transversal mixing.

While such secondary flows may enhance downstream particle distribution, the core mixing performance of the reactor is still primarily governed by the upstream flow characteristics. Both experimental and computational approaches to assess mixing remain time-consuming. As a result, researchers often rely on dimensionless numbers such as the Reynolds number (Equation 1.32) or the **Peclet number (Pe)** to estimate mixing efficiency. [80] The Peclet number expresses the ratio of advection to diffusion and helps identify the dominant transport mechanism: Pe $\ll$ 1 implies diffusion-dominated transport, while Pe $\gg$ 1 indicates advection-dominated flow. It is defined as:

$$Pe = \frac{vL_c}{D_{ab}} \tag{1.36}$$

Where:

- $\mathbf{v}$: Average velocity of the fluid [m.s^{-1}],
- $\mathbf{L_c}$: Characteristic length [m],
- $\mathbf{D_{ab}}$: Diffusion coefficient [m^2.s^{-1}].

However, the relevance of such dimensionless numbers remains limited, as they were primarily developed to describe fluid behaviour in simple pipe flows, and not for complex microstructured geometries. The information they provide should therefore be considered with caution, particularly when applied to micromixer design and analysis.

Another dimensionless number that can be used indirectly to evaluate mixing performance is the **Damköhler number (Da)**. It represents the ratio between the characteristic reaction rate and the characteristic diffusion rate. Depending on its value, it provides insight into the limiting mechanism of the process: for $Da \geq 1$, the conversion is primarily limited by mixing, whereas for $Da \leq 1$, the reaction rate itself is the limiting factor.

$$Da = \frac{k_r C_0^{n-1} L_c^2}{4 D_{ab}} \tag{1.37}$$

Where:

- $\mathbf{k_r}$: Kinetic rate constant [variable],
- $\mathbf{n}$: Reaction order [dimensionless],
- $\mathbf{C_0}$: Initial concentration [mol.L^{-1}],
- $\mathbf{L_c}$: Characteristic length [m],
- $\mathbf{D_{ab}}$: Diffusion coefficient [m^2.s^{-1}].

The estimation of the Damköhler number, downstream, provides valuable insight into whether the overall process suffers from inadequate mixing. [81]

From a global perspective, the mixing step upstream of a microfluidic reactor is crucial. Depending on the reaction under consideration, different technologies can be employed, whether a homogeneous stream is required or, conversely, a slow diffusion at the stream interface is desired. In any case, depending on the mixing requirements, a preliminary study, either experimental or via CFD simulations, should be conducted to identify the most suitable mixer for the reaction.

5) Integration of Complex Systems

Over the past decades, microfluidic reactors have undergone significant development and have found an increasing number of applications. This sustained interest has driven the flow chemistry community to continuously implement new tools, making flow-based processes increasingly attractive.

In the following section, recent advances and trends are discussed, based on several comprehensive reviews from the literature, [77, 90, 91] which served as primary sources of information.

One of the key advantages of switching to flow chemistry is the possibility of reaction telescoping, a strategy that enables either the direct quenching of highly toxic intermediates or the seamless integration of multiple reaction steps into a single continuous process, thereby protecting air-sensitive compounds. A realistic example of a telescoped process involving the formation of a harmful intermediate is presented in Figure 1.24, illustrating how telescoping can enhance process safety.

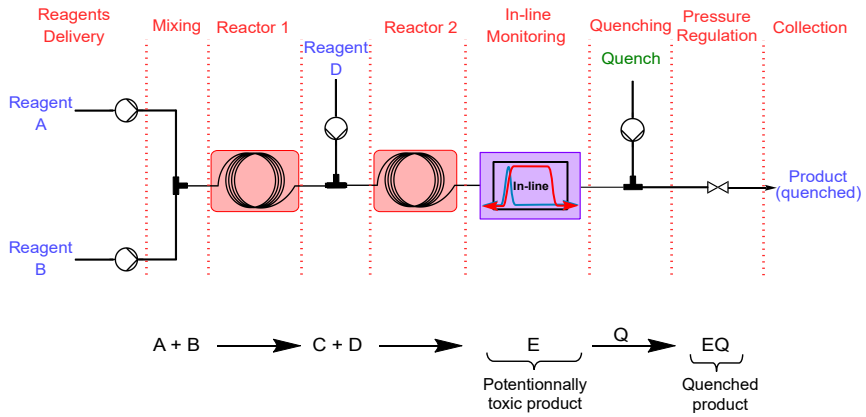

Figure 1.24. Example of a telescoped process in which a potentially toxic compound **E** is formed by the reaction of **A** and **B**, yielding intermediate **C**. This intermediate then reacts with **D** to produce **E**. In-line monitoring (PAT) enables the quantification of **E**, which is subsequently quenched by **Q**, resulting in the formation of **EQ**, a harmless compound.

In addition to reaction sequencing, various tools have been developed to broaden the scope of flow chemistry applications. Among these, Back Pressure Regulator (BPR) are essential devices that enable high-pressure reactions in a straightforward and controlled manner.

Three main types of BPRs can be distinguished:

(**I**) **Spring-based regulators**, which allow fluid flow only when the pressure exceeds the spring force.

(**II**) **Tesla valves**, passive devices with no moving parts. [92]

(**III**) **Membrane-based systems**, which require a gas cylinder and a pressure regulator to set and control system pressure. This configuration can also be operated remotely.

Advancements in flow technology have also driven innovations in pumping systems. In microfluidics, pumps are generally categorized into three main types:

- **Syringe pumps** offer high precision and can operate at elevated pressures, but they are limited by the small reagent volumes they can handle.
- **HPLC pumps** provide accurate control over a broad range of flow rates and support larger volumes. However, they are sensitive to fluid viscosity and the presence of solids, which may cause blockages or malfunctions. Pulsations during operation may also occur.
- **Peristaltic pumps** are suitable for large flow rates and heterogeneous feeds but are constrained by a limited pressure range.

Additionally, a variety of sensors (*e.g.*, temperature and pressure) and spectroscopic techniques, including UV/Vis, NIR, photoluminescence, IR, Raman, and NMR, have been integrated to monitor reaction conditions. These devices can be remotely controlled via computer, allowing real-time monitoring and assessment throughout the process.

Ultimately, this approach has enabled fully automated systems capable of completing an entire (Design of Experiments (DoE)) cycle in a single run. When combined with artificial intelligence, such systems open the door to self-optimizing processes, autonomously adjusting parameters to maximize performance. [93] A key recent development involves Dynamic Flow Experiments (DFE), which accelerate data generation and intensification, thereby expediting material discovery. [94]

6) Non-Idealities in Continuous Flow Reactors

a) Laminar flow regime

The breakthrough curve $F(t)$ presented in Figure 1.20 represents the ideal case for a plug flow reactor and therefore represents an ideal plug flow behaviour. However, in practice, the flow regime is laminar, leading to a parabolic velocity profile. To illustrate the non-ideal nature of the breakthrough curve in a microfluidic reactor, an example is shown in Figure 1.25.

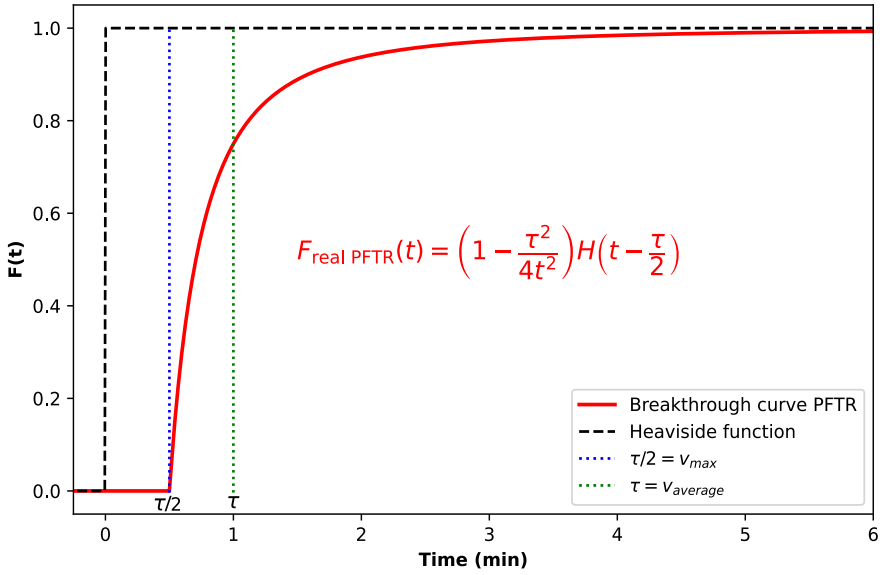

Figure 1.25. Illustration of a realistic breakthrough curve in a microfluidic reactor.

In this illustration, the curve shows that due to the parabolic velocity profile, the maximum velocity v_{max} occurs at the center of the section, causing the tracer to move faster than the residence time τ. After one equivalent residence time, around 70 % of the outlet flow is composed of the tracer. Several residence times (τ) are needed to obtain pure tracer in the outlet flow.

b) Axial dispersion

In addition to the parabolic velocity profile, microfluidic reactors have a second drawback: the axial dispersion, due to the Fick's Law. The balance equation of the infinitesimal concentration variation can be written, leading to breakthrough curve presented in the Equation 1.38.

$$F(t) = \frac{1}{2}\left[\text{erf}\left(\sqrt{\frac{\text{Bo}}{4}\left(\frac{t}{\tau} - 1\right)}\right) + \text{erf}\left(\sqrt{\frac{\text{Bo}}{4}}\right)\right] \tag{1.38}$$

In this equation, the **Bodenstein number (Bo)** is introduced as a dimensionless quantity that characterizes the tendency of the flow to move through the reactor or to diffuse randomly. It is given by:

$$Bo = \frac{vL}{D_{ab}} \tag{1.39}$$

Where:

- **v**: Average velocity of the fluid [m.s^{-1}],
- **L**: Reactor length [m],
- **D_{ab}**: Diffusion coefficient [m^2.s^{-1}].

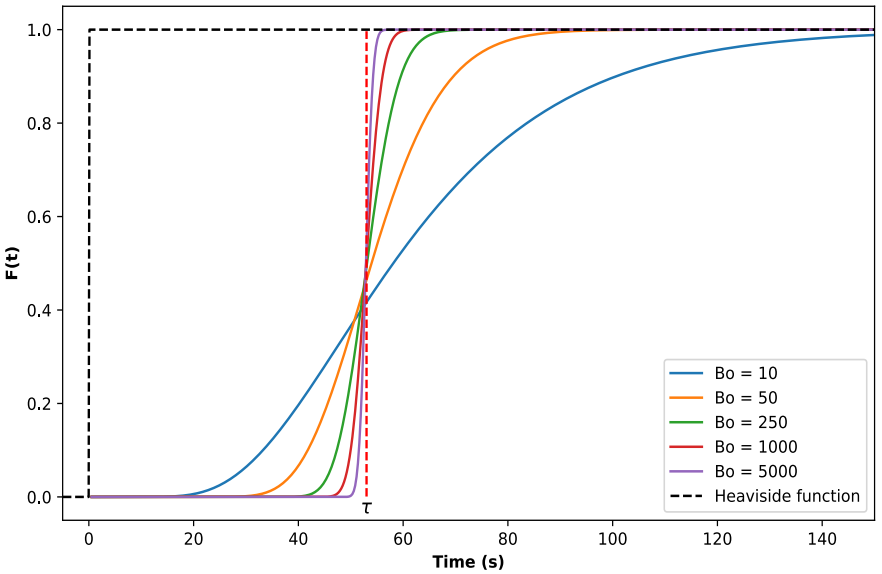

Figure 1.26. Illustration of the impact of the axial dispersion (through the Bodenstein number) into the breakthrough curve in a microfluidic reactor.

This integral form cannot be solved analytically and must therefore be evaluated numerically. In the following example, the Equation 1.38 is solved for a microchannel (*i.d.* = 750 μm), flow rate = 500 $\mu L.min^{-1}$. The Bodenstein value ranges through the diffusion coefficient. The result is shown in Figure 1.26.

Based on the curves plotted in Figure 1.26, the Bodenstein number can be described as follows:

- $Bo \to 0$: $D_{ab} \to \infty$ — The reactor tends to behave like an ideal CSTR.
- $Bo \to \infty$: $D_{ab} \to 0$ — The reactor tends to behave like an ideal PFTR.

Therefore, it is crucial to carefully select the flow velocity and diffusion coefficient to optimize the performance of microfluidic reactors. This ensures that the flow conditions align with the ideal behaviour, minimizing axial species dispersion and maximizing efficient transport within the reactor.

7) Conclusion on Microfluidic Reactors Technology

As discussed throughout this section, PFTR technologies offer intrinsic advantages over conventional batch and CSTR systems. They enable continuous operation with improved control over residence time distribution and reaction kinetics. Furthermore, they provide a better mean residence time to reach a given conversion rate.

However, traditional macroscale PFTR are often limited by poor heat transfer properties. The transition to microfluidic PFTR overcomes these limitations, enabling efficient thermal management, enhanced safety, and precise control of reaction parameters. Additionally, microfluidic platforms offer great versatility, allowing for the integration of complex reaction sequences (telescoped reactions), *in-line* sensing, and remote control of flow rates and pressures.

Combined with automated control systems, these features facilitate rapid process optimization, and in some cases, self-optimizing synthesis using Machine Learning (ML).

Nevertheless, microfluidic systems are not without limitations. A significant gap often remains between theoretical models and practical operation, particularly regarding mixing efficiency, velocity profiles, and axial dispersion. Moreover, microscale dimensions introduce specific challenges, such as managing highly viscous fluids (which induce pressure drops and exacerbate axial dispersion) or handling solid particles (risking channel clogging).

Finally, microfluidic technologies require substantial investments, not only in equipment but also in human resources, necessitating multidisciplinary teams for design, operation, and maintenance.

1.7 CdX QDs Synthesis

Preface

The content of this section was later expanded into a Perspective published in *JACS Au*:

Campalani, C., Petit, G., & Monbaliu, J.-C. M. (2025). Aqueous Continuous Flow Synthesis of Cadmium Chalcogenide Quantum Dots: Opportunities and Challenges. *JACS Au*, 6(1), 2025, 38–58. DOI: 10.1021/jacsau.5c01449. [95]

This section is primarily devoted to illustrating the versatility of chemical strategies developed for the synthesis of QDs in both organic and aqueous

solvents. A brief subsection dedicated to microfluidic applications is presented at the end of Section 1.7.

As most of the chemical innovations have already been introduced in Section 1.7.2, the objective here is rather to illustrate the principles described in Section 1.6.3, and more specifically Subsection **5) Integration of Complex Systems**, through concatenated approaches enabling the formation of complex structures (*i.e.*, CSSNCs).

1.7.1 Introduction

As mentioned in Section 1.2, among the various types of quantum dots illustrated in Figure 1.1, cadmium-based quantum dots (*e.g.*, CdS, CdSe, and CdTe), which belong to the II-VI semiconductor family, remain among the most widely produced, despite concerns over their toxicity. [12] These QDs are primarily favoured for their broad emission spectra and excellent optical properties, such as high PLQY and narrow FWHM.

From a chemical standpoint, synthesizing these materials is, in principle, as simple as reacting Cd^{2+} with X^{2-} (where X = S, Se, or Te) in the presence of ligands. However, challenges arise when soluble precursors are required in the chosen reaction medium, whether organic or aqueous. Finally, controlling the reaction kinetics, first step of the LaMer mechanism, is essential to control the overall process: the CNT and the following steps of growth process, to achieve the formation of the QDs with the desired properties, as described in Section 1.5.

The following sections provide a non-exhaustive overview of key advances in the bottom-up approaches developed for the synthesis of high-quality cadmium chalcogenide QDs (*i.e.*, CdX, where X = S, Se, or Te).

1.7.2 Batch Applications

As mentioned above, four components are required to achieve the synthesis of cadmium chalcogenide QDs: the cadmium and chalcogenide precursors, the ligand(s), and the solvent. In some cases, the solvent can also acts as a ligand. The solvent also governs the accessible synthesis methods and the nature of the molecules used to carry the atomic precursors.

The batch synthesis of quantum dots can be broadly categorized into three main families, based on the precursor addition sequence and the heating strategy:

- **Solvothermal methods**: This approach involves mixing the precursors at room temperature, followed by a gradual increase in temperature

that leads to the formation of monomeric units. This category includes the hydrothermal technique as a sub-type. [96, 97]

- **Microwave-assisted methods**: Similar to solvothermal synthesis, this technique also involves mixing the precursors at room temperature, but the heating is achieved via microwave irradiation, allowing for a rapid and uniform temperature increase. [98, 99]
- **Hot-injection methods**: In this method, the solvent and/or a thermally stable precursor is preheated to a high temperature, followed by the rapid injection of the remaining precursor(s). [45]

However, none of the techniques described above is perfect, and a summary of their strengths and weaknesses is provided in Table 1.5.

Table 1.5. Overview of the main bottom-up synthesis strategies for cadmium-based quantum dots, highlighting the pros and cons for each method.

Criteria	**Solvothermal**	**Microwave-assisted**	**Hot-injection**
Temperature	Medium	Medium	High
Duration	Long	Very short	Very short
Size control	Moderate	Variable	Excellent
Key advantage	Simplicity	Fast heating, efficient	Highly monodisperse QDs
Limitations	Poor control, long duration	Low reproducibility, specific setup	Chemical complexity, organic solvents

In practice, the most commonly used techniques are the solvothermal and hot-injection methods. The solvothermal approach is appreciated for its simplicity, flexibility, and compatibility with aqueous media, making it particularly suitable for biomedical applications such as bioimaging (see Figure 1.1). In such contexts, it avoids the additional ligand exchange step required when QDs are synthesized in organic solvents, which can be time-consuming and affect their surface and optical properties, as discussed in Section 1.4.4.

The hot-injection method, on the other hand, is widely employed for producing high-quality, monodisperse QDs, though it is limited by its low compatibility with aqueous precursors, which are often unstable at the required temperatures.

Microwave-assisted synthesis remains relatively uncommon, primarily due to reproducibility issues and the need for specialized equipment. For these reasons, this technique will not be covered further in the present review.

Here below, the literature review focuses on the synthesis of cadmium-chalcogenide QDs using both hot-injection and solvothermal methods. Due to their thermal requirements, solvothermal method is generally more suited for aqueous precursors (note that hydrothermal synthesis at higher temperatures than 100 °C requires autoclave batch reactors), whereas organic solvents are typically preferred for hot-injection approaches. An illustration of an experimental batch setup is shown in Figure 1.27.

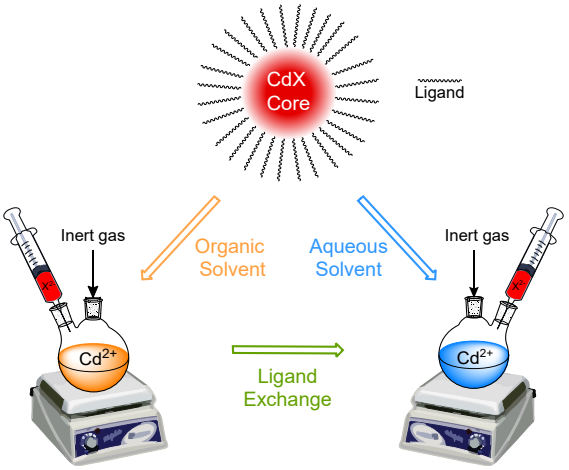

Figure 1.27. Typical batch synthesis process for CdX QDs (where X = S, Se, or Te) in both organic and aqueous solvents as well as a downstream ligand exchange.

Beyond thermal consideration, another major difference between aqueous and organic syntheses lies in the solubility of the involved species. In both systems, the precursors and ligand(s) must be ideally soluble in the chosen solvent, which in turn dictates the solubility of the resulting QDs in their synthesis medium. While this solvent-specific solubility is often beneficial during synthesis, it can limit downstream processing or application. To address this, ligand exchange strategies have been developed to modify the surface chemistry and tune the solubility of QDs for diverse environments and functionalities. [100–102]

Since the solvent influences both the choice of precursors and ligands, the following state of the art will be organized according to the solvent type used: the organic synthesis (*e.g.*, hot-injection and solvothermal) and the aqueous synthesis.

1.7.2.1 Organic solvent protocols

The pioneering work in QD synthesis using organic solvents involved the development of a hot-injection protocol by Bawendi et al. [4] in 1993, which remained the gold standard for quantum dot synthesis until the early 2000s. In this method, a cadmium or chalcogen precursor is rapidly injected into a hot solution containing the complementary precursor in the presence of a stabilizing agent. Significant improvements were later achieved by adding a shell to the CdX core, which greatly enhanced the PLQY. [103]

1) Solvent

Quantum dot synthesis in organic media is typically carried out under harsh conditions, with temperatures sometimes reaching up to 350 °C for hot-injection protocols. As a result, this method almost invariably relies on high-boiling-point organic solvents such as Octadecene (ODE), Trioctylphosphine oxide (TOPO), Lauric acid (LA), Stearic acid (SA), and Hexadecylamine (HDA), among others. These solvents share a key characteristic: they are non-polar or only weakly polar, a property that strongly influences the choice of both precursors and ligands. In some cases, the ligand itself may also act as the solvent.

2) Cadmium precursors

The primary commercially available cadmium source for organic synthesis is Dimethylcadmium ($Cd(Me)_2$). However, its high toxicity and pyrophoric nature make its use dangerous. In addition to these safety concerns, it has been shown that under the high-temperature conditions of the hot-injection method, $Cd(Me)_2$ can decompose in the presence of TOPO, forming an insoluble metallic precipitate [104].

For these reasons, Peng et al. [105] shifted toward safer and more controllable alternatives, notably by generating cadmium carboxylates, phosphonates, and phosphine complexes *in situ*. This was achieved through high-temperature reactions (typically above 150 °C) of primary cadmium sources with carboxylic acids, phosphonic acids, phosphines, xanthate salts, or mixtures thereof, as illustrated in Figure 1.28. Common cadmium precursors used for this purpose include CdO, $Cd(OAc)_2$, $CdCl_2$, $Cd(NO_3)_2$, and $CdCO_3$.

These new precursors, however, are less reactive than $Cd(Me)_2$, making burst nucleation more difficult to achieve and thus reducing the reproducibility of small QDs formation. The bond strength between ligands and cadmium strongly influences the reaction rate and, consequently, the size distribution.

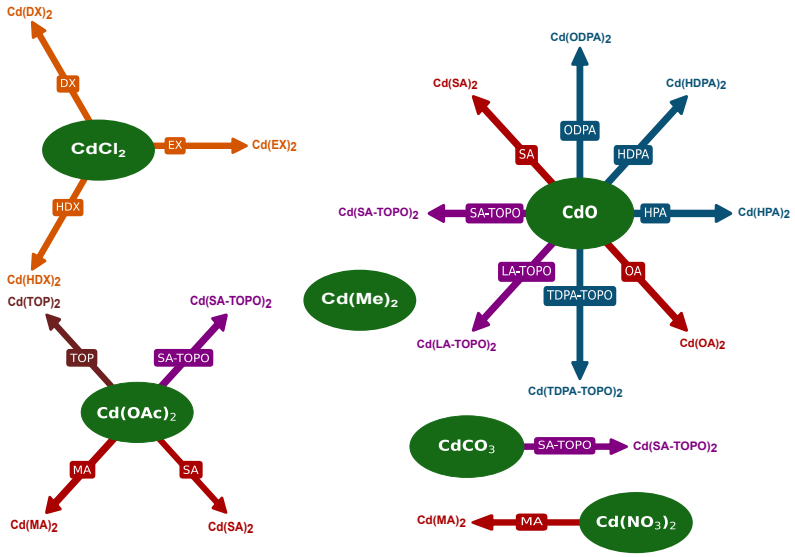

Figure 1.28. Common commercial cadmium sources (green ellipses) used to generate various Cd^{2+} precursors: **blue arrow** = phosphonate precursors, **red arrow** = carboxylate precursors, **orange arrow** = xanthate precursors, **purple arrow** = mixed carboxylate–phosphonate precursors, and **brown arrow** = phosphine precursors.

3) Chalcogen precursors

For the preparation of chalcogen sources, three main strategies are typically used to obtain X^{2-} species (where X = S, Se, or Te):

a) Silylated chalcogenides

The first approach involves using commercially available silylated chalcogenide compounds such as Bis(trimethylsilyl)sulfide ($(TMS)_2S$), Bis(trimethylsilyl)selenide ($(TMS)_2Se$), or Bis(tert-butyldimethylsilyl) tellurium ($(BDMS)_2Te$). However, the use of these reagents has declined over time due to their high reactivity and poor controllability, leading to a preference for phosphine-based sources.

b) Phosphine-mediated reduction *in-situ*

In this widely adopted method, the chalcogenide precursor is generated *in situ* by reducing elemental chalcogen with an organo-soluble phosphine (*e.g.*, Trioctylphosphine (TOP) or Tributylphosphine (TBP)).

c) Thermal activation of elemental chalcogen

For sulfur and selenium, another approach involves heating the elemental chalcogen in a non-reductive solvent (such as ODE,

paraffin, or similar) at temperatures above their melting points (115 °C for sulfur and 221 °C for selenium). Under these conditions, the chalcogen becomes more reactive, possibly via dismutation or thermal activation, leading to the formation of X^{2-} species.

An overview of these strategies is provided in Table 1.6.

Table 1.6. Overview of the main approaches used to obtain reactive chalcogen sources for hot-injection quantum dot synthesis.[1] Tellurium has a melting point of 450 °C, making it impractical to use in molten form.

Chalcogen	Commercial source	Reduction *in situ*	Thermal activation *in situ*
Sulfur	$(TMS)_2S$	$:PR_3 + S \xrightarrow[\text{solvent}]{\Delta} SPR_3$	$S_{(s)} \xrightarrow[\text{solvent}]{\Delta} S_{(l)}$
Selenium	$(TMS)_2Se$	$:PR_3 + Se \xrightarrow[\text{solvent}]{\Delta} SePR_3$	$Se_{(s)} \xrightarrow[\text{solvent}]{\Delta} Se_{(l)}$
Tellurium	$(BDMS)_2Te$	$:PR_3 + Te \xrightarrow[\text{solvent}]{\Delta} TePR_3$	Not accessible[1]

Additionally, gaseous precursors such as H_2S are sometimes used, particularly for shelling CdSe or CdTe cores with CdS or ZnS layers. However, they are less common for core synthesis, mainly because mass transfer is too slow for efficient nucleation, making them more suited to growth phases.

Another, less common, alternative is to use cadmium complexes that already contain the chalcogen source, such as cadmium xanthates (*e.g.*, $Cd(EX)_2$, $Cd(DX)_2$, $Cd(HDX)_2$). This approach is mostly found in solvothermal protocols. [106, 107]

4) Ligands

As discussed in Section 1.5.7, the ligands used to stabilize the CdX QDs must possess a functional group capable of interacting with the nanoparticle surface, while also containing a non-polar moiety to ensure solubility in the reaction medium. Typical ligands for this process are amphiphilic compounds. Their polar head groups vary depending on the intended application, and are often L-type or Z-type ligands, which provide moderate binding and can be replaced by stronger-binding ligands (such as 1-dodecanethiol (DDT)) or exchanged later to tailor surface properties, by ligand exchange, like shown in Figure 1.27.

In addition to deliberately added ligands, some precursors or their by-products can act as surface stabilizers. First generation metal and chalcogen precursors (*e.g.*, $Cd(Me)_2$, silylated chalcogenides) tend to yield volatile by products, whereas second generation systems leave

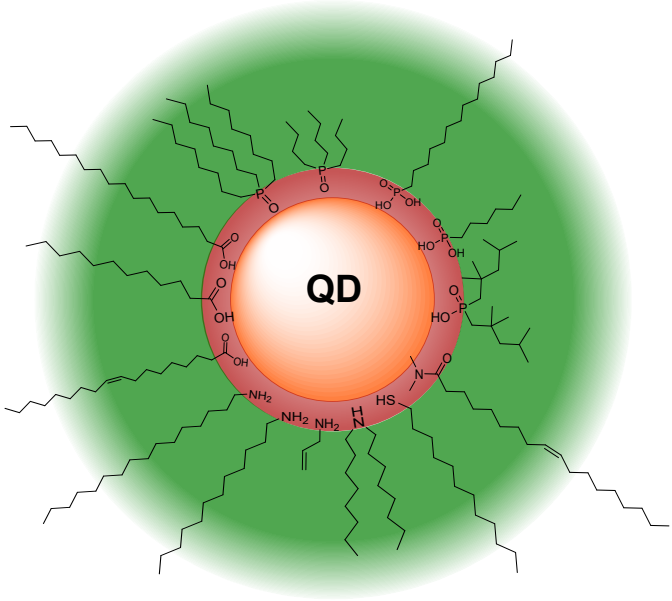

Figure 1.29. Illustration of cadmium chalcogenide QDs stabilization via organic synthesis. The amphiphilic molecules orient their polar heads toward the red shell surrounding the quantum dot, while their non-polar components extend into the green area, interacting with the organic solvent.

non volatile species, such as cadmium carboxylates or phosphonates, that remain bound to the QDs surface. Phosphine-based chalcogen precursors, after delivering the chalcogen atom, can oxidize to L- type ligands whose binding efficiency depends on steric factors such as the Tolman cone angle. [67]

In practice, a mixture of ligand species almost always caps the QD surface, and the composition of this ligand shell strongly affects both the photoluminescence and the crystalline structure of the nanocrystals. [108]

5) General considerations on hot-injection

Early publications on hot-injection protocols typically reported the synthesis of single-core QDs stabilized by moderate-interaction ligands, leading to poor surface passivation. This often resulted in either low PLQY or complete absence of emission. Nonetheless, these methods allowed access to a broad size range.

The subsequent introduction of a ZnS shell-growth step dramatically improved PLQY, often approaching or even exceeding 100 %, while preserving size tunability.

With the replacement of $Cd(Me)_2$ by cadmium carboxylates, phosphonates, and phosphine complexes again reduces the PLQY, even though broad size control was maintained. As before, overcoating with ZnS restored high quantum yields. Further optimization was achieved by ensuring crystal lattice matching in core/shell/shell architectures (Section 1.4.5), which minimized interfacial defects.

Establishing direct correlations between thermal history and final QD properties remains challenging, as each synthesis involves a unique combination of precursors, ligands, solvents, thermal profile, and residence time, leading research groups to develop tailored optimization strategies.

6) General considerations on solvothermal synthesis

Organic solvothermal synthesis generally uses the same types of precursors as hot-injection, but proceeds at lower temperatures over longer reaction times (a few hours instead of minutes).

These reactions often employ more reactive or single-source precursors, and the resulting QDs tend to have larger average core sizes than their hot-injection counterparts. However, PLQY is usually lower, with a typical ceiling around 65 %, likely due to less effective passivation during slow growth and competition between growth and nucleation.

Table 1.7 reviews the advances in organic synthesis achieved through both hot-injection (orange rows) and solvothermal (light-orange rows) methods, summarizing the precursor sources, ligands, solvents, synthesis temperatures, and, when available, the size range and quantum yields obtained. All acronyms used, along with their corresponding names and structures, are summarized in Figure 1.30.

Table 1.7. Review of organic processes for CdX(–shell) QDs. n.a.: Not available information, [1]: Qualified as a nucleating agent, [2]: Capping agent added after QD purification (quench step), [3]: Secondary ligand, [4]: Common data for [109], [5]: TMPPA is used either to control the nucleation rate [110] or to influence the crystalline structure [111], [6]: Olive oil is a mixture mostly composed of OA, its composition may vary, and other fatty acids present can act as stabilizing agents, [7]: $Cd(OA)_2$ heated at 310 °C for 30 min to generate Cd_0 nanoparticles prior to the addition of TOPTe.

Core	Cd & Chalcogen Sources	Ligands	Solvent	Temp (°C)	Size (nm)	QY (%)	Ref.
CdS	$Cd(Me)_2$/TOP + $(TMS)_2S$	TOP, TOPO	TOP, TOPO	320-100	1.2 (100 °C)	n.a.	[4]
	$Cd(HPA)_2$+TOPS	HPA	TOPO	250-300	n.a.	n.a.	[105]
	$Cd(TDPA)_2$+TOPS	TDPA	TOPO	250-300	n.a.	n.a.	[105]
	$Cd(OA)_2$+ODE–S	OA	ODE	300-250	2-5.3	n.a.	[112]
	$Cd(OAM)_2$ + OAM–S	OAM	OAM	90-160	5.1	0.43	[113]
	$Cd(MA)_2$ + S	TTDS/ DTBT [1]	ODE	200-240	3.8	12	[114]
CdS/ ZnS	$Cd(HDX)_2$+ $Zn(HDX)_2$	HDA	HDA	70-140	3.5-5.2	2-13.9	[106]
	$Cd(HDX)_2$+ $Zn(HDX)_2$	HDA	HDA	70-140	3.5-5.2	2-13.9	[106]
	$Cd(EX)_2$+ $Zn(EX)_2$	HDA	HDA	70-140	3.7-4.3	1-16	[107]
	$Cd(DX)_2$+ $Zn(DX)_2$	HDA	HDA	70-140	3.7-4.3	1-16	[107]
	$Cd(HDX)_2$+ $Zn(HDX)_2$	HDA	HDA	70-140	3.7-4.3	1-16	[107]
CdSe	$Cd(Me)_2$/TOP + TOPSe	TOP, TOPO	TOP, TOPO	300, 230-260	1.2-11.5	9.6	[4]

Continued on next page

Continued from previous page

Core	Cd & Chalcogen Sources	Ligands	Solvent	Temp (°C)	Size (nm)	QY (%)	Ref.
CdSe	$Cd(Me)_2$/TOP +$(TMS)_2Se$	TOP, TOPO	TOP, TOPO	320-100	1.2 (100 °C)	n.a.	[4]
	$Cd(Me)_2$+$(TBP)_2Se$	TBP, TOPO	TBP, TOPO	350-300	0.93 - 3.35	n.a.	[115]
	$Cd(HPA)_2$+TOPSe	HPA	TOPO	250-300	n.a.	n.a.	[105]
	$Cd(TDPA)_2$+TOPSe	TDPA	TOPO	250-300	n.a.	n.a.	[105]
	$Cd(SA/TOPO)_2$+ TOPSe	SA/ TOPO	SA/ TOPO	300	1.5-25[4]	20-30[4]	[109]
	$Cd(SA)_2$+TOPSe	SA	SA	200-320	2-25	n.a.	[109]
	$Cd(LA/TOPO)_2$+ TOPSe	LA/ TOPO	LA/ TOPO	200-320[4]	1.5-25[4]	20-30[4]	[109]
	$Cd(TOPO)_2$+ TOPSe	TOPO	TOPO	200-320[4]	1.5-25[4]	20-30[4]	[109]
	$Cd(TDPA/TOPO)_2$+ TOPSe	TDPA/ TOPO	TDPA/ TOPO	200-320[4]	1.5-25[4]	20-30[4]	[109]
	$Cd(DDA/TOPO)_2$+ TOPSe	DDA, TOPO	DDA, TOPO	220-200	n.a.	n.a.	[109]
	$Cd(SA)_2$+TBPSe	TOPO, HDA, DOA	TOPO, HDA, DOA	320-290	6-9	62-100	[116]
	$Cd(OA)_2$+TOPSe	OA	ODE	275-265	0.8-2.2	n.a.	[117]
	$Cd(OA)_2$+ (TOP/ODE)Se	OA/ TMPPA[5]	ODE	300-230	3.1-3.8	5-10	[111]
	$Cd(MA)_2$+ODE−Se	OA	ODE	210-220	2-4.5	30-40	[118]
	$Cd(SA)_2$+TOPSe	HH, BP	HDA, OD	340-270	2.6-5.9	n.a.	[119]
	$Cd(OA)_2$+TOPSe	OA/ TMPPA[5]	ODE	315-190	2.4-7	n.a.	[110]
	$Cd(OA)_2$ + TOPSe	OA	Phenyl ether	110-170	1.8-2.7	n.a.	[120]

Continued on next page

Continued from previous page

Core	Cd & Chalcogen Sources	Ligands	Solvent	Temp (°C)	Size (nm)	QY (%)	Ref.
CdSe/CdS	$Cd(Me)_2$+TOPSe/ $Cd(Me)_2$+$(TMS)_2S$	TOP, TOPO/ TOP, TOPO	TOP, TOPO/ TOP, TOPO	360-290/ 180	CdSe core: 3.35-3.5	n.a.	[121]
	$Cd(TOP)_2$+TOPSe/ H_2S	HDA/ TOPO/ TOP/ TDPA	HDA/ TOPO/ TOP/ TDPA	300-260/ 140-50	CdSe core: 2.5-5	50-85	[122]
	$Cd(Me)_2$+TOPSe/ $Cd(Me)_2$+$(TMS)_2S$	HDA/ TOPO/ TOP	HDA/ TOPO/ TOP	300/140-90	CdSe core: 3.4	73	[122]
	$Cd(OA)_2$+TOPSe/ $Cd(OA)_2$+TOPS	OA	TOPO, ODE, DTA, T66	250-150, 120	3.5-5.2	3.3-15.9	[123]
CdSe/ZnS	$Cd(Me)_2$+TOPSe/ $ZnEt_2$+$(TMS)_2S$	TOP, TOPO/ TOP, TOPO	TOP, TOPO/ TOP, TOPO	360-290/ 140-220	CdSe core: 2.3-5.5	15-50	[121]
	$Cd(Me)_2$+TOPSe/ $ZnEt_2$+$(TMS)_2S$	HDA, TOP, TOPO/ TOPO, HDA/ DDA^2, AA^2	HDA, TOP, TOPO/ TOPO, HDA	300, 250-310/ 220	CdSe core: 4.5-5	12-66	[124]
CdSe/ZnSe	$Cd(Me)_2$+TOPSe/ $ZnEt_2$+TOPSe	TOPO, TOP / TOP,	TOPO, TOP/ TOP	230/ 150	2-6.8	1->100	[103]
Cd (Se,Te	$Cd(HPA-TOPO)_2$+ TOP(Se/Te)	OA	ODE	300	2.7-8.6	25-60	[125]
CdSe/CdS/ZnS	$Cd(TOP)_2$+TOPSe, H_2S/ $ZnEt_2$+$(TMS)_2S$	HDA, TOPO, TOP	HDA, TOPO, TOP/ HDA, TOPO, TOP, hexane	300/ 140-90/ 210	3.2/ 1.2	n.a.	[49]

Continued on next page

Continued from previous page

Core	Cd & Chalcogen Sources	Ligands	Solvent	Temp (°C)	Size (nm)	QY (%)	Ref.
CdSe/ ZnSe/ ZnS	$Cd(Me)_2$+TOPSe/ $ZnEt_2$+TOPSe/ $ZnEt_2$+$(TMS)_2S$	HDA, TOPO, TOP	HDA, TOPO, TOP/ HDA, TOPO, TOP, hexane	200-320/ 190/ 200-220	3.6	70-85	[49]
CdTe	$Cd(Me)_2$/TOP + TOPTe	TOP, TOPO	TOP, TOPO	240, 190-220	n.a.	n.a.	[4]
	$Cd(Me)_2$/TOP +$(BDMS)_2$Te	TOP, TOPO	TOP, TOPO	320-100	1.2 (100 °C)	n.a.	[4]
	$Cd(HPA)_2$+TOPTe	HPA	TOPO	270-250	2-8	> 20	[105]
	$Cd(TDPA)_2$+TOPTe	TDPA	TOPO	270-250	2-8	> 20	[105]
	$Cd(Me)_2$ + TOPTe	DDA	DDA	150-220	2.5-7	35-65	[126]
	$Cd(ODPA)_2$+TBPTe	no additional	ODE	240	n.a.	n.a.	[118]
	$Cd(OA)_2$/Cd_0 [7]+ TOPTe	OA	ODE	310-260	3-3.8	0-80	[127]

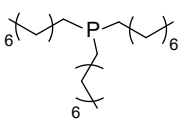

1. Trioctylphosphine (TOP)

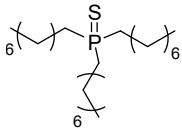

2. Trioctylphosphine sulfide (TOPS)

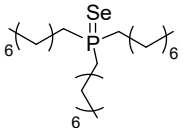

3. Trioctylphosphine selenide (TOPSe)

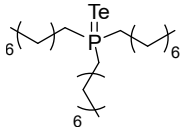

4. Trioctylphosphine telluride (TOPTe)

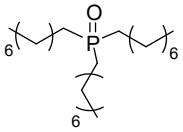

5. Trioctylphosphine oxide (TOPO)

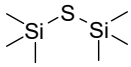

6. Bis(trimethylsilyl)sulfide ($(TMS)_2S$)

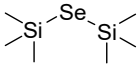

7. Bis(trimethylsilyl)selenide ($(TMS)_2Se$)

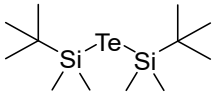

8. Bis(tert-butyldimethylsilyl) tellurium ($(BDMS)_2Te$)

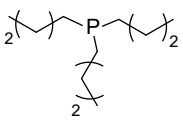

9. Tributylphosphine (TBP)

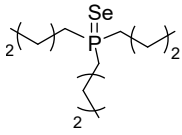

10. Tributylphosphine selenide (TBPSe)

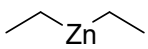

11. Diethylzinc ($ZnEt_2$)

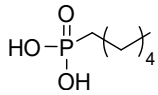

12. Hexylphosphonic acid (HPA)

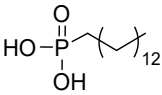

13. Tetradecylphosphonic acid (TDPA)

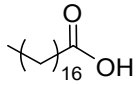

14. Stearic acid (SA)

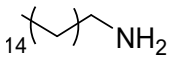

15. Hexadecylamine (HDA)

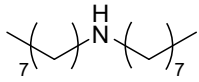

16. Dioctylamine (DOA)

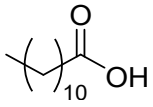

17. Lauric acid (LA)

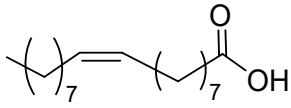

18. Oleic acid (OA)

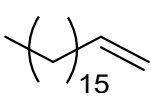

19. Octadecene (ODE)

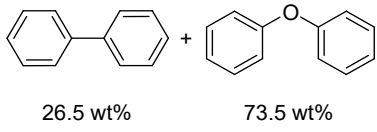

20. Dowtherm A (DTA)

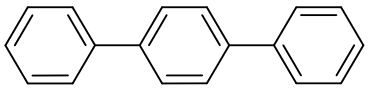

21. Therminol 66 (T66)

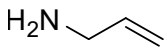

22. Allylamine (AA)

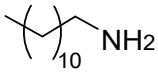

23. Dodecylamine (DDA)

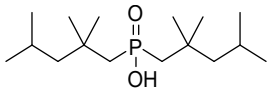

24. Bis-(2,2,4-trimethylpentyl)phosphinic acid (TMPPA)

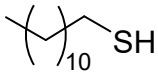

25. 1-dodecanethiol (DDT)

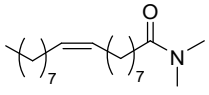

26. N,N-dimethyl-oleoyl amide (DMOA)

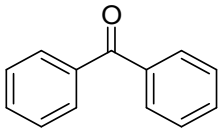

27. Benzophenone (BP)

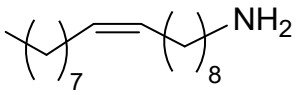

28. Oleylamine (OAM)

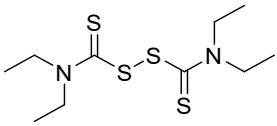

29. Tetraethylthiuram disulfides (TTDS)

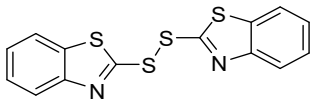

30. 2,2′-dithiobisbenzothiazole (DTBT)

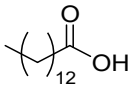

31. Myristic acid (MA)

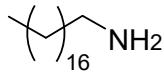

32. Octadecylamine (ODA)

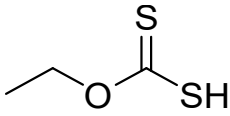

33. Ethyl xanthate (EX)

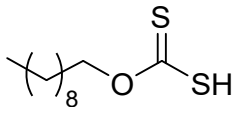

34. Decyl xanthate (DX)

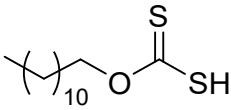

35. Hexadecyl xanthate (HDX)

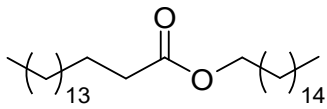

36. Hexadecyl hexadecanoate (HH)

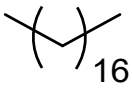

37. Octadecane (OD)

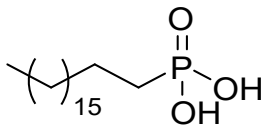

38. Octadecylphosphonic acid (ODPA)

Figure 1.30. Structures and full names of the compounds corresponding to the acronyms used in Table 1.7.

1.7.2.2 Aqueous protocols

The aqueous synthesis of CdX quantum dots has its rises in the early 1980s, when CdS precipitation was first achieved on colloidal silica, which acted as both stabilizer and support.[128] However, these early attempts did not produce nanocrystals small enough to display quantum confinement effects. Progress came with the use of water soluble copolymers such as styrene/maleic acid [129] and Sodium polyphosphate (SPP), [130] which enabled the observation of significant blue-shifts relative to bulk CdS.

These pioneering works, typically performed near neutral pH, largely focused on CdS. During the 1990s, the introduction of diverse precursors and stabilizers broadened the accessible cadmium-based cores and improved size distribution control, setting the stage for more advanced aqueous protocols.

1) Solvent

In aqueous protocols, the solvent is invariably water, which must be of the highest possible purity to avoid contamination from soluble impurities that could interfere with nucleation and growth. The use of double-distilled or ultra pure water is therefore strongly recommended.

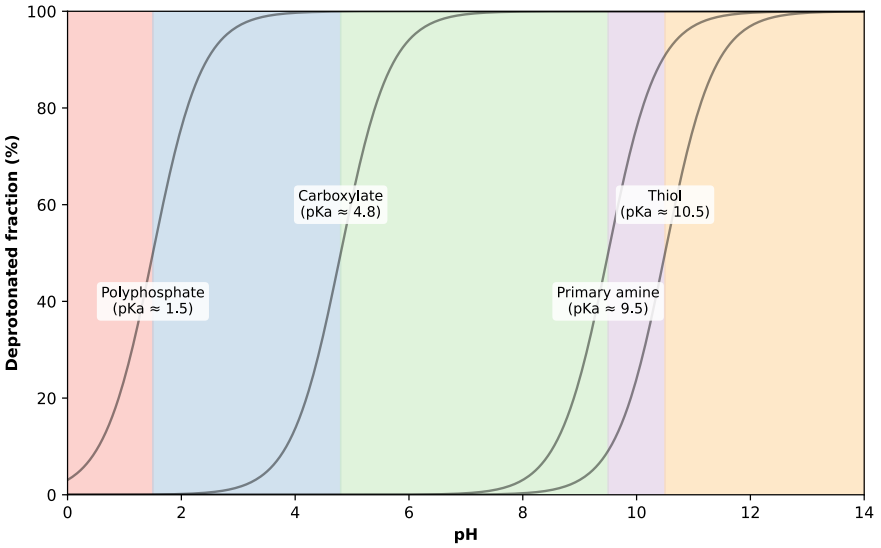

Figure 1.31. Illustration of the resulting form of the stabilizing agent as function of the reaction medium pH.

A key distinction of aqueous synthesis, compared to organic routes, is the need to carefully control the solvent pH, typically in the range of 7 to 12. The desired value is generally obtained by the cautious addition

of NaOH, although the use of buffered systems (*e.g.*, phosphate, Tris) has occasionally been reported. These buffers, however, often lead to poor size control and optical properties. This will not be further considered in this review.

In practice, the selected pH represents a compromise: it must ensure the deprotonation of stabilizing ligands for efficient surface coordination, enhance precursor reactivity, and at the same time limit unwanted side reactions, their protonation state is illustrated in Figure 1.31. This delicate balance highlights the central role of pH control in aqueous CdX quantum dot synthesis. [130]

2) Cadmium precurors

In contrast to organic-phase syntheses, where cadmium precursors often require pretreatment or custom preparation, aqueous syntheses can be used directly in their commercial form, as inorganic cadmium salts such as $Cd(CH_3COO)_2$, $CdCl_2$, $Cd(ClO_4)_2$, $Cd(NO_3)_2$, or $CdSO_4$. These salts are typically obtained in hydrated form and should be stored in a desiccator to preserve their stability.

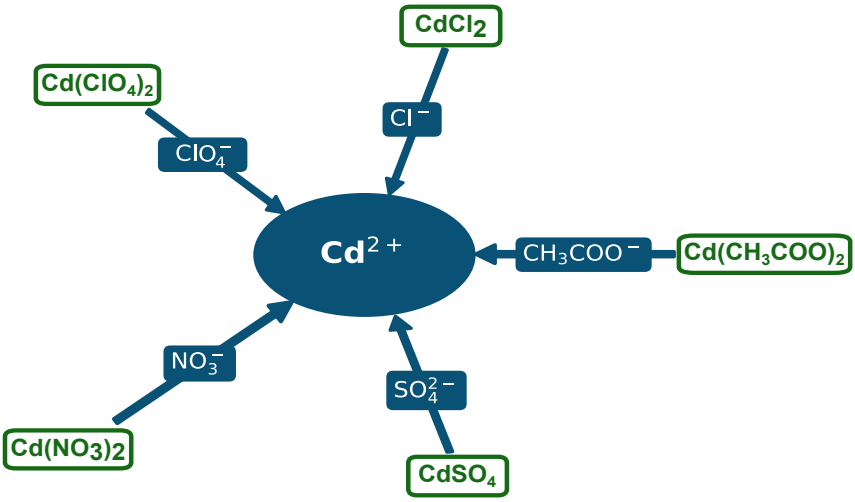

Figure 1.32. Main commercial cadmium sources (green box), soluble in water, leading to Cd^{2+} ions, usable for QDs synthesis and their counteranion in the blue arrow.

Their high water solubility makes them convenient precursors. Upon dissolution, these salts furnish free Cd^{2+} ions in solution, as shown in Figure 1.32. Under alkaline conditions, however, Cd^{2+} tends to form insoluble $Cd(OH)_2$, leading to precipitation during pH adjustment with NaOH. To prevent this undesired process, cadmium salts are usually

dissolved in the presence of strongly binding ligands (often thiolates), after which the pH of the solution can be safely adjusted.

The influence of the counteranion on cadmium specification and reactivity will be discussed later in the section dedicated to ligands.

3) Chalcogen precurors

The chalcogen precursors represent the most challenging part for the aqueous synthesis, except for the sulfur sources, commercially available, the selenium and tellurium precursors must be, in most of the cases, freshly prepared prior to the synthesis. The discussion will be therefore split in two parts: the commercially available precursors and the *in situ* preparations. These paths are summarized in Tables 1.8 and 1.9.

a) Commercial source

Only sulfur and selenium precursors are commercially available, with sulfur offering a wider range of options. Salts containing sulfur in its reduced form (S^{2-}), such as Na_2S, are air stable and provide highly reactive sulfide ions. Thiourea (TU) is another common choice, its lower reactivity compared to Na_2S makes it attractive for more controlled crystal growth.[131] Finally, thiolates, which are often used to stabilize cadmium precursors under basic conditions, can also act as sulfur donors under harsher conditions. This property can be exploited during the annealing phase, to improve the core crystallinity and surface passivation.

Selenium sources are more limited, essentially to two organoselenium compounds with moderate reactivity: N,N-dimethylselenourea (NDSU) and Selenourea (SeU).

Table 1.8. Overview of the commercially available chalcogen precursors for aqueous quantum dot synthesis. Corresponding structure and full name of the acronyms are available in Table 1.31.

Chalcogen	Commercial source
Sulfur	Na_2S, TU, Thiolates
Selenium	NDSU, SeU

In contrast, no tellurium precursors are commercially available, and their reactive forms must be generated *in-situ*, as discussed in the following section.

b) *In-situ* preparation

Most *in-situ* preparations are necessary to obtain unstable or highly reactive chalcogen precursors. Among the hydrogen chalcogenides,

only H_2S is commercially available. For laboratory use, however, it is preferable to generate it directly within the reactor to avoid handling this hazardous gas. The selenium and tellurium counterparts, H_2Se and H_2Te, are obtained by the same route. In practice, aluminium chalcogenides (Al_2X_3, with X = S, Se, Te) are hydrolyzed with aqueous sulfuric acid, releasing the volatile H_2X species. Although highly reactive, this approach suffers from poor solubility and mass transfer of the gas into aqueous solution. H_2X can be either bubbled directly into the cadmium precursor solution (with the exhaust stream carefully neutralized in a NaOH trap), or first absorbed in basic solution to generate soluble salts such as Na_2Se or NaHTe.

These latter compounds can also be obtained by complete reduction of their corresponding oxyanions (Na_2SeO_3 or Na_2TeO_3), in which the oxidation state decreases from +4 to –2. This reduction can be achieved using strong reductants such as $NaBH_4$, hydrazine, or Na_2SO_3 (the last two reported only for selenium). Hydrazine reduction produces highly unstable selenide species that either react rapidly with Cd^{2+} or form Na_2Se by binding sodium ions. The resulting Na_2Se or NaHTe solutions exhibit very high reactivity toward CdX nanocrystal formation.

Finally, milder reducing agents such as ascorbic acid can partially reduce Na_2SeO_3 or Na_2TeO_3, switching the oxidation state from +4 to 0. This process generates colloidal Se_0 or Te_0 nanoparticles, which are less reactive precursors. They can nevertheless be activated by thermal treatment or undergo dismutation reactions to provide reactive chalcogen species for CdX nucleation.

Table 1.9. Overview of the main approaches used to obtain reactive chalcogen sources for aqueous quantum dot synthesis. n.r.: Not reported; [1]: complete reduction from +4 to –2 with $NaBH_4$, hydrazine, or Na_2SO_3; [2]: partial reduction from +4 to 0 using weaker reductants, followed by thermal activation or dismutation.

Chalcogen	Acid hydrolysis	Reduction[1]	Partial reduction[2]
Sulfur	$Al_2S_3 \xrightarrow[H_2O]{H_2SO_4} 3\,H_2S$	n.r.	n.r.
Selenium	$Al_2Se_3 \xrightarrow[H_2O]{H_2SO_4} 3\,H_2Se$	$Na_2SeO_3 \xrightarrow[H_2O]{Red} Na_2Se$	$Na_2SeO_3 \xrightarrow[H_2O]{Red} Se_{(0)}$
Tellurium	$Al_2Te_3 \xrightarrow[H_2O]{H_2SO_4} 3\,H_2Te$	$Na_2TeO_3 \xrightarrow[H_2O]{Red} NaHTe$	$Na_2TeO_3 \xrightarrow[H_2O]{Red} Te_{(0)}$

A general consideration when selecting chalcogen precursors is the balance between precursor reactivity and reaction temperature. In aqueous phase, highly reactive species can undergo oxidation by the solvent itself at elevated temperatures, which renders them ineffective for CdX QD formation.

4) Ligands

As mentioned in the solvent discussion, the reaction medium is typically basic, pH 7 to 12, which favours the precipitation of $Cd(OH)_2$. Strongly binding ligands are therefore required to stabilize surface Cd^{2+} ions. X-type ligands such as thiolates, phosphates, or deprotonated alcohols are preferred. Neutral donors (L-type), such as non-deprotonated alcohols or amines, can also bind but usually provide weaker passivation and may not prevent the $Cd(OH)_2$ formation.

Unlike in organic synthesis, ligands must be water-soluble. Hydrophobic amphiphiles (long-chain thiols or amines) are thus not compatible. Instead, multifunctional hydrophilic ligands are commonly employed: thiolates compounds with a second function carboxylic acid (Thioglycolic acid (TGA) or 3-Mercaptopropionic acid (3-MPA)), amines (2-Mercaptoethanol (2-ME), 2-(dimethylamino)ethanethiol (2-DET)), among other.

Hydrosoluble polymers such as SPP or Polyvinyl alcohol (PVA) can also act as weak coordinating ligands (L- or pseudo X-type) and provide additional steric stabilization in aqueous dispersions.

Table 1.10. Summary of ligands and counter-ions used in aqueous synthesis of CdX quantum dots.

Type	Examples	Role in CdX QDs
X-type ligands	Thiolates (TGA, 3-MPA, 2-ME, 2-DET)	Strong binding to Cd^{2+}, stabilize surface sites and prevent $Cd(OH)_2$ precipitation, affect nucleation and growth
Weak L / Pseudo-X ligands	PVA, SPP (hydrosoluble polymers)	Provide steric stabilization in aqueous media, weak coordination
Counter-ions	CH_3COO^-, Cl^-, ClO_4^-, NO_3^-, SO_4^{2-}	Can occupy residual coordination sites on Cd^{2+}, affect nucleation and growth

Finally, the counter-anion of the cadmium salts (*e.g.*, CH_3COO^-, Cl^-, ClO_4^-, NO_3^-, SO_4^{2-}) also contributes to surface passivation. Acetate and chloride ions coordinate strongly to Cd^{2+} compared to nitrate, sulfate, or perchlorate, thereby influencing nucleation and growth. The counter-anion contribution is further discussed more in detail in Section 3.1.2.

5) General consideration on aqueous synthesis

Aqueous CdX QD protocols generally yield smaller core particles compared to their organic counterparts. Indeed, the literature summarized in Tables 1.7 and 1.11 show that the reported organic made core size are often start at 3 nm diameter while aqueous ones are closer to 2 nm. This difference introduces more surface defects (see Section 1.4.4 to the pinned emission) for aqueous made QDs than their organic counterpart.

As a result, their PLQY remains modest, typically below 60 % and rarely exceeding 53.3 %. Among the aqueous protocols review, the CdTe core exhibit the most important PLQY. This results in the absence of self-healing emission due to the use of thiol stabilizing agent. [45] A generic method to solve this issue is the use of CSSNCs described in Section 1.4.5. However, only a few protocols have reported core–shell QDs in aqueous medium, in batch, and the improvements in photoluminescence are often limited.

The small core size can be explained by the low reactivity of cadmium precursors in aqueous media, as they are stabilized by thiolate ligands. The Cd–S bond is particularly strong, requiring higher thermal activation energy for monomer formation, which in turn results in slower growth kinetics and longer reaction times.

Synthesis is usually carried out under reflux at ∼100 °C, although lower temperatures can be employed when highly reactive precursors are used. Some research groups have even developed hot-injection protocols in water, reaching up to 240 °C, which require the use of autoclave reactors. [132, 133]

Table 1.11 reviews recent advances in aqueous synthesis, summarizing precursor sources, ligands, pH, synthesis temperatures, and, when available, the size ranges and quantum yields obtained. All acronyms used, together with their corresponding names and chemical structures, are summarized in Figure 1.33.

Table 1.11. Review of hydrothermal processes for CdX QDs. n.a.: Not available information, [1]: Under nanoparticles form, obtain by ascorbic acid reduction of X(IV), X_0 is then activated by dismutation or thermal activation, [2]: Solution basified by addition of ammonia [3]: Obtained by hydrazine reduction, highly unstable either reacts fastly with Cd^{2+} either captures two Na^+ in reaction medium.

Core	Cd & Chalcogen Sources	Ligands	pH	Temp (°C)	Size (nm)	QY (%)	Ref.
CdS	$Cd(ClO_4)_2$+ Na_2S	ClO_4^-	7.2	25	n.a.	n.a.	[128]

Continued on next page

Continued from previous page

Core	Cd & Chalcogen Sources	Ligands	pH	Temp (°C)	Size (nm)	QY (%)	Ref.
CdS	$Cd(TGL)_2$+ H_2S	TGL	11.2	100	1.3-3.9	n.a.	[130]
	$Cd(SPP)$+ H_2S	SPP	11.5	100	1.3-3.9	n.a.	[130]
	$Cd(MPA)_2$+ TU	MPA	8-12	100	2.4-3.5	<2-20	[131]
CdS/ ZnS	$Cd(MPA)_2$+ TU, $Zn(MPA)_2$	MPA	10.3	100	CdS core: 3.1, CdS/ ZnS: 3.6	22-23	[131]
CdSe	$Cd(2\text{-}MA)_2$+ NaHSe	2-MA	11.2	100	1.4-2.2	<0.1	[134]
	$Cd(TGL)_2$+ NaHSe	TGL	11.2	100	1.4-2.2	<0.1	[134]
	$Cd(TGA)_2$+ NaHSe	TGA	11.2	100	2.1-3.2	<0.1	[134]
	$Cd(TGA)_2$+ Na_2SeSO_3	TGA	11	90	2	n.a.	[135]
	$Cd(MPA)_2$+ Na_2Se	MPA	9.3	100	<2	up to 3	[136]
	Cd(Cit)+ NDSU	Cit	7-11	240-200	3.5-5	<0.1-5.7	[137]
	$Cd(MPA)_2$+ Na_2Se	MPA	9-10	100	1.58-3.42	12-43	[138]
	$Cd(L-Cy)_2$+ Se_0 [1]	L−Cy	7-11	80	5	up to 22	[139]
	$Cd(MSA)_2$+ Se_0 [1]	TGA	11.8	100	up to 2.9	1.9-22.7	[140]
	Cd/PVA+ SeU	TGA	n.a. [2]	80	6	n.a.	[141]
	$Cd(TGA)_2$+ Se^{2-} [3]	TGA	8.5-11	100	1.77-1.93	n.a.	[142]
CdTe	$Cd(TGA)_2$+H_2Te	TGA	11.2	100	1-2	2-47	[143]
	$Cd(2\text{-}ME)_2$+H_2Te	2-ME	11.2-11.8	100	1-2	<1	[144]

Continued on next page

Continued from previous page

Core	Cd & Chalcogen Sources	Ligands	pH	Temp (°C)	Size (nm)	QY (%)	Ref.
CdTe	$Cd(TGL)_2$+H_2Te	TGL	11.2-11.8	100	n.a.	3	[144]
	$Cd(TGL/DMP)_2$+H_2Te	TGL/ DMI	11.2-11.8	100	n.a.	6	[144]
	$Cd(TGA)_2$+H_2Te	TGA	11.2-11.8	100	n.a.	6	[144]
	$Cd(2\text{-}MA)_2$+H_2Te	2-MA	5.6-5.9	100	n.a.	10	[144]
	$Cd(L-Cy)_2$+H_2Te	2-MA	11.2-11.8	100	n.a.	10	[144]
	$Cd(2\text{-}DET)_2$+H_2Te	2-DET	5-6	100	n.a.	30	[144]
	$Cd(TGA)_2$+NaHTe	TGA	9	180-100	2-4	2-35	[145]
	$Cd(MPA)_2$+NaHTe	MPA	9	180-100	2-4	2-35	[145]
	$Cd(TGL)_2$+NaHTe	TGL	9	180-100	2-4	2-35	[145]
	$Cd(TGA)_2$+NaHTe	TGA	11.2-11.8	100-200	2-6	27.4	[132]
	$Cd(2\text{-}MA)_2$+NaHTe	2-MA	5-9	240-140	2-4	5-19.7	[133]
	$Cd(MPA)_2$+NaHTe	MPA/Cit	10.5	100	3.1-6.41	n.a.	[146]
	$Cd(TGA)_2$+NaHTe	TGA/Cit	10.5	100	3.1-6.41	n.a.	[146]
	$Cd(TGA)_2$+Te_0 [1]	TGA	10.5	100	2.1-2.7	5.4-53.3	[147]
CdTe/ CdSe	$Cd(MPA)_2$+NaHTe, $Cd(MPA)_2$+Na_2Se	MPA/Cit	10.5	100, 150	CdTe core: 6.41, CdTe/ CdSe: 7.17-8.19	44.2	[146]

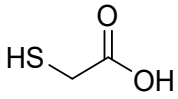

1. Thioglycolic acid (TGA)

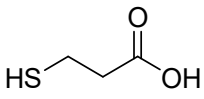

2. 3-Mercaptopropionic acid (3-MPA)

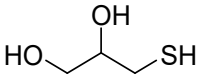

3. 1-Thioglycerol (TGL)

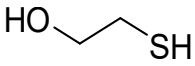

4. 2-Mercaptoethanol (2-ME)

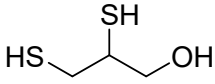

5. 2,3-dimercapto-1-propanol (DMP)

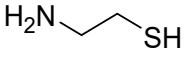

6. 2-Mercaptoethylamine (2-MA)

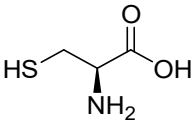

7. L-Cysteine (L−Cy)

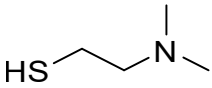

8. 2-(dimethylamino)ethanethiol (2-DET)

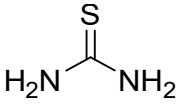

9. Thiourea (TU)

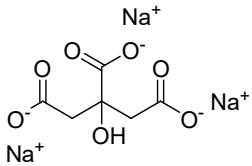

10. Sodium citrate (Cit)

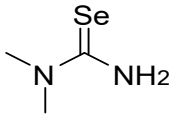

11. N,N-dimethylselenourea (NDSU)

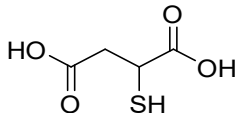

12. Mercaptosuccinic acid (MSA)

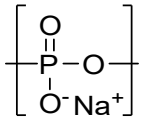

13. Sodium polyphosphate (SPP)

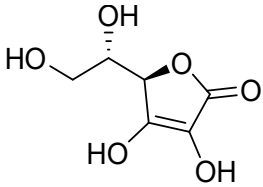

14. Ascorbic acid (Asc Ac)

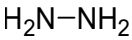

15. Hydrazine (N_2H_4)

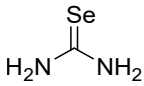

16. Selenourea (SeU)

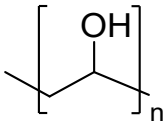

17. Polyvinyl alcohol (PVA)

Figure 1.33. Structures and full names of the compounds corresponding to the acronyms used in Table 1.11.

1.7.3 Microfluidic Applications

In parallel of the advances made in batch reactor, the emergence of microfluidic technologies in the early 2000s established a new foundation for customizable and scalable production of high-quality quantum dots (QDs). Continuous micro- and mesofluidic approaches have demonstrated clear advantages in this context, including improved reaction control, enhanced reproducibility, and straightforward scalability. [148]

Thanks to precise control over reaction parameters including heat transfer, mixing efficiency and residence time, see Section 1.6.3, the Chemistry and Chemical Engineering communities have progressively embraced microfluidic synthesis routes. [149, 150] As discussed in Section 1.7.2, all critical parameters for the successful QDs preparation, can be more effectively controlled through microfluidic processes. [151–154]

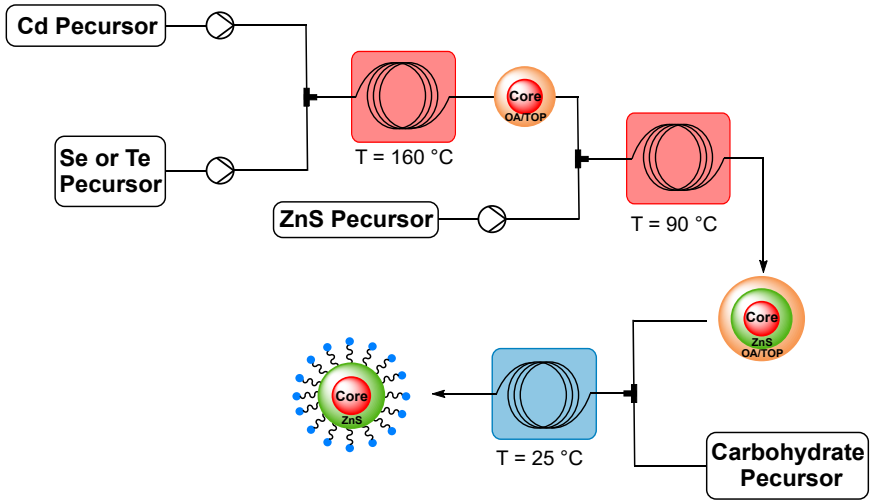

Figure 1.34. Illustration of concatenated formation of CdSe/ZnS or CdTe/ZnS QDs process followed by a ligand-exchange with sulfur functionalized carbohydrate, adapted from [155].

Among nanosized semiconductors, type II–VI QDs, and more specifically cadmium chalcogenide QDs (*i.e.*, CdX where X = S, Se, or Te), have been extensively studied. [156] Their hot-injection synthesis is particularly amenable to translation into flow conditions, as rapid thermal exchange enables sharper temperature gradients than those achievable with solvothermal methods. Microfluidics allow the straightforward implementation of concatenated reactions, which is especially useful for CSSNCs synthesis, as illustrated in Figure 1.34. Segmented-flow reactions can also be generated, influencing the fluid dynamics within the segments/droplets and avoiding axial dispersion. [157] Furthermore, the introduction of a BPR downstream facilitates high-

pressure syntheses, including hydrothermal conditions, within microfluidic platforms.

Furthermore, the synthesis of CdX QDs involves the use of harmful reagents. Microfluidics is employed to reduce the risks by limiting the amount of reagent reacting at a given moment. Additionally, the reagents are usually pumped from a closed container, preventing the operator from coming into contact with these chemicals.

Most of the microfluidic protocols involve the use of a soluble chalcogen transfer agent as well as stabilizing agents. Various types of chalcogen sources, highlighted in Subsection 1.7.2.1, have been transposed in microfluidic, such as trioctylphosphochalcogenides [4, 153, 155, 158–161], tributylphosphochalcogenides [152, 162] or those chelated by the solvent itself (such as octadecene [158]).

Similarly, the cadmium precursors followed the same trend as observed in batch: early syntheses were carried out using $Cd(Me)_2$. Subsequently, the precursors evolved toward less toxic compounds, prepared *ex situ*, as presented in Figure 1.28. Representative synthetic protocols under flow conditions for the preparation of QDs are illustrated in the right panel of Figure 1.35.

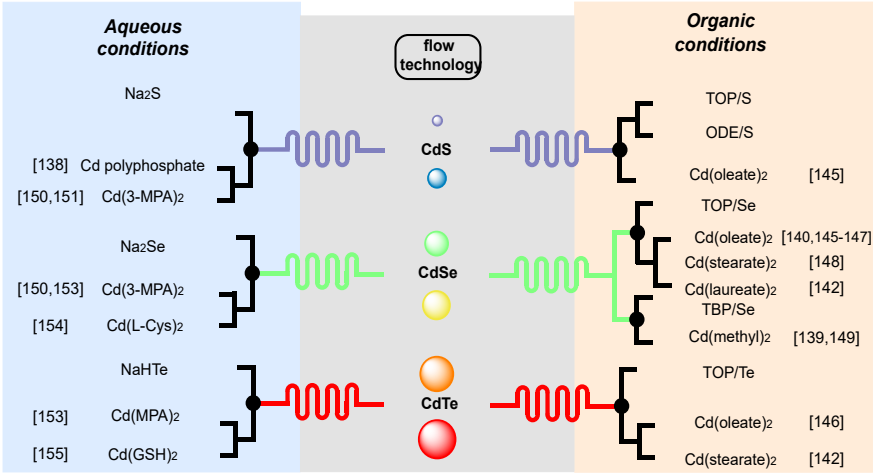

Figure 1.35. Protocols from the prior Art for accessing QDs with flow processes. For each chalcogen (S, Se, Te), the precursors are summarized according to the reaction medium (aqueous/organic).

As mentioned in Subsection 1.7.2.2, one of the main challenges in synthesizing QDs in water lies in preparing a suitable reduced chalcogen source, which is essential for initiating the transfer to the cadmium precursor and producing QDs. Most reported protocols involve homogeneous chalcogenide precursors prepared *ex situ* in batch, as depicted in the third column of Table 1.9, which may be prone to decomposition. Commercial sulfur precursors have also been employed. Typically, these protocols rely on the reduction of

native chalcogens with ionic reductants such as $NaBH_4$, yielding air-sensitive ionic chalcogenides like Na_2S [151, 163, 164], Na_2Se [165–167], or NaHTe. [166, 168]

The cadmium sources used under flow conditions are the same as those employed in batch (see Figure 1.32 and Section 2 in Subsection 1.7.2.2). Representative synthetic protocols for QD preparation under flow conditions are illustrated in the left panel of Figure 1.35.

Moreover, reports on the aqueous preparation of QDs in flow often lack photoluminescence data, [169] suggesting that the resulting optical properties are poorer or, at best, comparable to those obtained in batch.

1.8 Project Motivations

The review presented in Section 1.7 highlighted a gap between aqueous and organic syntheses in terms of accessible size range and PLQY. As mentioned in Section 1.2 and 1.7 the ligands play a key role in the QDs synthesis but also in their potential use. Indeed, their nature depends primary on the solvent chosen for the synthesis. The quantum dots obtained in organic solvents often exhibit superior emission properties and greater versatility. Such organic-soluble particles are suitable for most quantum dot applications and have low impact on electronic uses (*e.g.*, solar cells, communications, displays). However, it impacts the applications of QDs for bio-application, where their water solubility properties are required.

Currently, two main strategies allow the production of water-soluble QDs (see Figure 1.27 and 1.34, by an organic synthesis followed by ligand exchange, which is an additional step that decreases the PLQY and the overall particles properties. [170, 171]. The second approach aims to a direct aqueous synthesis. Both approaches usually lead to lower emission performance than their organic counterpart and thus to less sensitive bio-labels. The ideal solution would be to by-pass the ligand-exchange step by developing an improved aqueous synthesis method capable of achieving PLQY comparable to organic routes.

In this perspective, the review revealed that most of the drawbacks of aqueous processes come from poor control over precursor reactivity. Cadmium precursors tend to be insufficiently reactive, whereas chalcogen precursors are often too reactive. The ambition of the present project is therefore to identify a moderately reactive chalcogen precursor and to implement it within a synthesis setup that offers greater flexibility for controlling nanoparticle formation.

Indeed, the models discussed in Section 1.5 emphasis the importance of controlling the saturation levels of monomeric building blocs. This goal can be achieved only by a fine tuning of the experimental conditions (*e.g.*,

residence time, temperature, local stoichiometry). It is expected that resort to microfluidic technologies, that benefit from the advantages describes in Section 1.6, will help to bridge the gap traditionally observed between organic and aqueous synthesis protocols.

In addition to the fine tuning of the reaction parameters through microfluidics, a novel water-soluble chalcogen agent is sought. Indeed, one of the key to control the reaction kinetics and, consequently the degree of supersaturation, lies in moderating the reactivity of the precursors. This allow a broader parameter space and therefore a finer control over the reaction tunability.

References

[1] A. I. Ekimov and A. A. Onushchenko. "Quantum Size Effect in Three-Dimensional Microscopic Semiconductor Crystals". In: *JETP Letters* 34.6 (1981), pp. 363–366. ISSN: 01631829. DOI: 10.1134/S0021364023130040.

[2] R. Rossetti, S. Nakahara, and L. E. Brus. "Quantum size effects in the redox potentials, resonance Raman spectra, and electronic spectra of CdS crystallites in aqueous solution". In: *The Journal of Chemical Physics* 79.2 (1983), pp. 1086–1088. ISSN: 00219606. DOI: 10.1063/1.445834.

[3] Louis Brus. "Electron – electron and electron-hole interactions in small semiconductor crystallites : The size dependence of the lowest excited electronic state". In: *J. Chem. Phys.* 80 (1984), p. 4403. DOI: 10.1063/1.447218.

[4] C. B. Murray, D. J. Norris, and M. G. Bawendi. "Synthesis and Characterization of Nearly Monodisperse CdE (E = S, Se, Te) Semiconductor Nanocrystallites". In: *Journal of the American Chemical Society* 115.19 (1993), pp. 8706–8715. ISSN: 15205126. DOI: 10.1021/ja00072a025.

[5] B. O. Dabbousi et al. "(CdSe)ZnS core-shell quantum dots: Synthesis and characterization of a size series of highly luminescent nanocrystallites". In: *Journal of Physical Chemistry B* 101.46 (1997), pp. 9463–9475. ISSN: 15206106. DOI: 10.1021/jp971091y.

[6] Tyler Maxwell et al. "Quantum dots". In: *Nanoparticles for Biomedical Applications: Fundamental Concepts, Biological Interactions and Clinical Applications*. Elsevier, Jan. 2019, pp. 243–265. ISBN: 9780128166628. DOI: 10.1016/B978-0-12-816662-8.00015-1.

[7] Cécile Philippot and Peter Reiss. "Synthesis of inorganic nanocrystals for biological fluorescence imaging". In: *Frontiers of Nanoscience*. Vol. 4. Elsevier Ltd, 2012, pp. 81–114. DOI: 10.1016/B978-0-12-415769-9.00003-0.

[8] D. Sumanth Kumar, B. Jai Kumar, and H. M. Mahesh. "Quantum Nanostructures (QDs): An Overview". In: *Synthesis of Inorganic Nanomaterials: Advances and Key Technologies*. Elsevier, Jan. 2018, pp. 59–88. ISBN: 9780081019757. DOI: 10.1016/B978-0-08-101975-7.00003-8.

[9] Humaira Arshad, Abdul Majid, and Muhammad Azmat Ullah Khan. "Quantum Dots: Synthesis, Properties, and Applications". In: *Quantum Dots for Plant Systems*. Cham: Springer International Publishing, 2022, pp. 11–45. ISBN: 978-3-031-10216-5. DOI: 10.1007/978-3-031-10216-5_2.

[10] Lens.org. *Quantum Dots Patent Search*. https://www.lens.org/lens/search/patent/analysis?q=quantum%20dots&p=0&n=10&s=_score&d=%2B&f=false&e=false&l=en&authorField=author&dateFilterField=publishedDate&orderBy=%2B_score&presentation=false&preview=false&stemmed=true&useAuthorId=false&publishedDate.from=1980-01-01&publishedDate.to=2025-01-01. Accessed: 2025-01-13.

[11] Maximize Market Research. *Quantum Dots (QD) Market: Industry Trends and Forecast 2024*. https://www.maximizemarketresearch.com/market-report/quantum-dots-qd-market/11730/. Accessed: 2024-03-19. 2024.

[12] Carlotta Campalani and Jean Christophe M. Monbaliu. "Towards sustainable quantum dots: Regulatory framework, toxicity and emerging strategies". In: *Materials Science and Engineering R: Reports* 163 (Apr. 2025). ISSN: 0927796X. DOI: 10.1016/j.mser.2025.100940.

[13] "Semiconductor quantum dots: Technological progress and future challenges". In: *Science* 373 (6555 Aug. 2021). ISSN: 10959203. DOI: 10.1126/science.aaz8541.

[14] Sisi Liu et al. "Efficient quantum dot infrared solar cells with enhanced low-energy photon conversion via optical engineering". In: *Nano Research* 16 (2023), pp. 2392–2398. DOI: 10.1007/s12274-022-4906-1.

[15] Long Hu et al. "Flexible and efficient perovskite quantum dot solar cells via hybrid interfacial architecture". In: *Nature Communications* 12.1 (2021), pp. 1–9. ISSN: 20411723. DOI: 10.1038/s41467-020-20749-1. URL: 10.1038/s41467-020-20749-1.

[16] Weiran Cao et al. "Highly stable QLEDs with improved hole injection via quantum dot structure tailoring". In: *Nature Communications* 9.1 (2018), pp. 2–7. ISSN: 20411723. DOI: 10.1038/s41467-018-04986-z. URL: http://dx.doi.org/10.1038/s41467-018-04986-z.

[17] Lee Suhyeon et al. "Quantum-dot and organic hybrid light-emitting diodes employing a blue common layer for simple fabrication of full-color displays". In: *Nano Research* 15.7 (2022), pp. 6477–6482. DOI: 10.1007/s12274-022-4204-y.

[18] Sungho Park et al. "Improving the photodetection and stability of a visible-light QDs/ZnO phototransistorviaan Al2O3additional layer". In: *Journal of Materials Chemistry C* 9.7 (2021), pp. 2550–2560. ISSN: 20507526. DOI: 10.1039/d0tc05626j.

[19] Jari Leemans et al. "Colloidal III–V Quantum Dot Photodiodes for Short-Wave Infrared Photodetection". In: *Advanced Science* 9.17 (2022), pp. 1–8. ISSN: 21983844. DOI: 10.1002/advs.202200844.

[20] Carlotta Campalani et al. "Continuous Flow Photooxidative Degradation of Azo Dyes with Biomass-Derived Carbon Dots". In: *ChemPhotoChem* 7.5 (2023), pp. 1–8. ISSN: 23670932. DOI: 10.1002/cptc.202200234.

[21] Xuejiao Wu et al. “Ligand-Controlled Photocatalysis of CdS Quantum Dots for Lignin Valorization under Visible Light”. In: *ACS Catalysis* 9.9 (2019), pp. 8443–8451. ISSN: 21555435. DOI: 10.1021/acscatal.9b02171.

[22] Debasis Bera et al. “Quantum dots and their multimodal applications: A review”. In: *Materials* 3.4 (2010), pp. 2260–2345. ISSN: 19961944. DOI: 10.3390/ma3042260.

[23] Asha Kumari et al. “Proficient surface modification of CdSe quantum dots for highly luminescent and biocompatible probes for bioimaging: A comparative experimental investigation”. In: *Journal of Luminescence* 199.January (2018), pp. 174–182. ISSN: 00222313. DOI: 10.1016/j.jlumin.2018.03.032.

[24] Manuela Lunz et al. “Förster resonant energy transfer in quantum dot layers”. In: *Superlattices and Microstructures* 47 (1 Jan. 2010), pp. 98–102. ISSN: 07496036. DOI: 10.1016/j.spmi.2009.06.011.

[25] Julie Hottechamps et al. “All-quantum dot based Förster resonant energy transfer: key parameters for high-efficiency biosensing”. In: *Nanoscale* 15 (6 Dec. 2022), pp. 2614–2623. ISSN: 20403372. DOI: 10.1039/d2nr06161a.

[26] M. Lismont et al. “Fiber based optofluidic biosensors”. In: *Applied Physics Letters* 105 (13 Sept. 2014), p. 133701. ISSN: 00036951. DOI: 10.1063/1.4896767.

[27] Xavier Michalet et al. “Molecules Single Properties of Fluorescent Semiconductor Nanocrystals and their Application to Biological Labeling”. In: *Single Mol* 2 (4 Dec. 2001), pp. 261–276. ISSN: 1438-5171. DOI: 10.1002/1438-5171(200112)2:4<261::AID-SIMO261>3.0.CO;2-P.

[28] Paul Alivisatos. *The use of nanocrystals in biological detection*. Jan. 2004. DOI: 10.1038/nbt927.

[29] H. H. Jaffe and Albert L. Miller. “The fates of electronic excitation energy”. In: *Journal of Chemical Education* 43 (9 Sept. 1966), pp. 469–473. ISSN: 0021-9584. DOI: 10.1021/ed043p469.

[30] A P Alivisatos. “Perspectives on the Physical Chemistry of Semiconductor Nanocrystals”. In: *The Journal of Physical Chemistry* 100 (31 Mar. 1996), pp. 13226–13239. DOI: 10.1021/jp9535506.

[31] C Kittel. *Introduction to Solid State Physics*. 8th ed. Wiley, 2004, pp. 190–193. ISBN: 978-0-471-41526-8.

[32] J. Bhosale et al. “Temperature dependence of band gaps in semiconductors: Electron-phonon interaction”. In: *Physical Review B - Condensed Matter and Materials Physics* 86 (19 Nov. 2012). ISSN: 10980121. DOI: 10.1103/PhysRevB.86.195208.

[33] H. I. Ikeri, A. I. Onyia, and O. J. Vwavware. "The Dependence of Confinement Energy on the Size of Quantum Dots". In: *International Journal of Scientific Research in Physics and Applied Sciences* 7 (2 Apr. 2019), pp. 27–30. DOI: 10.26438/ijsrpas/v7i2.2730.

[34] L Bányai and S. W. Koch. "Chapter 3: Quantum confinement regimes". In: *Semiconductor Quantum Dots*. Vol. 2. World scientific, May 1993, pp. 37–62. ISBN: 978-981-4354-41-7. DOI: 10.1142/9789814354417_0003.

[35] Moungi G Bawendi, Michael L Steigerwald, and Louis E Brus. "The quantum mechanics of larger semiconductor clusters ("Quantum Dots")". In: *Annu. Rev. Phys. Chem* 41 (1990), pp. 477–496. DOI: 10.1146/annurev.pc.41.100190.002401.

[36] Alexander L. Efros and Alexei L. Efros. "Interband Light Absorption in Semiconductor Spheres". In: *Soviet Physics - Semiconductors* 16 (7 July 1982), pp. 772–775. URL: https://www.researchgate.net/publication/279890805.

[37] L Bányai and S. W. Koch. "Chapter 2: Quantum confinement regimes". In: *Semiconductor Quantum Dots*. Vol. 2. World scientific, May 1993, pp. 7–36. ISBN: 978-981-4354-41-7. DOI: 10.1142/9789814354417_0002.

[38] Sameer Sapra et al. "Bright white-light emission from semiconductor nanocrystals: By chance and by design". In: *Advanced Materials* 19 (4 Feb. 2007), pp. 569–572. ISSN: 09359648. DOI: 10.1002/adma.200602267.

[39] Michael J. Bowers, James R. McBride, and Sandra J. Rosenthal. "White-light emission from magic-sized cadmium selenide nanocrystals". In: *Journal of the American Chemical Society* 127 (44 Nov. 2005), pp. 15378–15379. ISSN: 00027863. DOI: 10.1021/ja055470d.

[40] Aaron Puzder et al. "Self-healing of CdSe nanocrystals: First-principles calculations". In: *Physical Review Letters* 92 (21 May 2004). ISSN: 00319007. DOI: 10.1103/PhysRevLett.92.217401.

[41] Dinh Duy Vu and S. Das Sarma. "Collective ground states in small lattices of coupled quantum dots". In: *Physical Review Research* 2 (2 Apr. 2020). ISSN: 26431564. DOI: 10.1103/PhysRevResearch.2.023060.

[42] Szymon Godlewski et al. "Interaction of a conjugated polyaromatic molecule with a single dangling bond quantum dot on a hydrogenated semiconductor". In: *Physical Chemistry Chemical Physics* 18 (5 2016), pp. 3854–3861. ISSN: 14639076. DOI: 10.1039/c5cp07307c.

[43] Svetlana V. Kilina, Patrick K. Tamukong, and Dmitri S. Kilin. "Surface Chemistry of Semiconducting Quantum Dots: Theoretical Perspectives". In: *Accounts of Chemical Research* 49 (10 Oct. 2016), pp. 2127–2135. ISSN: 15204898. DOI: 10.1021/acs.accounts.6b00196.

[44] Albert D. Dukes et al. “Pinned emission from ultrasmall cadmium selenide nanocrystals”. In: *Journal of Chemical Physics* 129 (12 2008). ISSN: 00219606. DOI: 10.1063/1.2983632.

[45] Sander F. Wuister, Celso De Mello Donegá, and Andries Meijerink. “Influence of thiol capping on the exciton luminescence and decay kinetics of CdTe and CdSe quantum dots”. In: *Journal of Physical Chemistry B* 108 (45 Nov. 2004), pp. 17393–17397. ISSN: 15206106. DOI: 10.1021/jp047078c.

[46] Su Huai Wei and Alex Zunger. “Calculated natural band offsets of all II-VI and III-V semiconductors: Chemical trends and the role of cation d orbitals”. In: *Applied Physics Letters* 72 (16 Apr. 1998), pp. 2011–2013. ISSN: 00036951. DOI: 10.1063/1.121249.

[47] Peter Reiss, Myriam Protière, and Liang Li. “Core/shell semiconductor nanocrystals”. In: *Small* 5 (2 Jan. 2009), pp. 154–168. ISSN: 16136810. DOI: 10.1002/smll.200800841.

[48] Renguo Xie, Xinhua Zhong, and Thomas Basche. “Synthesis, characterization, and spectroscopy of type-II core/shell semiconductor nanocrystals with ZnTe cores”. In: *Advanced Materials* 17 (22 Nov. 2005), pp. 2741–2745. ISSN: 09359648. DOI: 10.1002/adma.200501029.

[49] Dmitri V. Talapin et al. “CdSe/CdS/ZnS and CdSe/ZnSe/ZnS core-shell-shell nanocrystals”. In: *Journal of Physical Chemistry B* 108 (49 Dec. 2004), pp. 18826–18831. ISSN: 15206106. DOI: 10.1021/jp046481g.

[50] David W Oxtoby. “Homogeneous nucleation: theory and experiment”. In: *J. Phys.: Condens. Matter* 4 (1992), pp. 7627–7650. DOI: 10.1088/0953-8984/4/38/001. URL: http://iopscience.iop.org/0953-8984/4/38/001.

[51] Roni Kroll and Yoav Tsori. “The effect of ion solvation on ion-induced nucleation—A generalized Thomson model”. In: *Physics of Fluids* 36 (12 Dec. 2024). ISSN: 10897666. DOI: 10.1063/5.0243822.

[52] Dmitri V. Talapin et al. “Evolution of an ensemble of nanoparticles in a colloidal solution: Theoretical study”. In: *Journal of Physical Chemistry B* 105 (49 Dec. 2001), pp. 12278–12285. ISSN: 10895647. DOI: 10.1021/jp012229m.

[53] X. Y. Liu. “Heterogeneous nucleation or homogeneous nucleation?” In: *Journal of Chemical Physics* 112 (22 2000), pp. 9949–9955. ISSN: 00219606. DOI: 10.1063/1.481644.

[54] Richard P. Sear. “Nucleation: Theory and applications to protein solutions and colloidal suspensions”. In: *Journal of Physics Condensed Matter* 19 (3 Jan. 2007). ISSN: 09538984. DOI: 10.1088/0953-8984/19/3/033101.

[55] A Baldan. "Progress in Ostwald ripening theories and their applications to nickel-base superalloys Part I: Ostwald ripening theories". In: *Journal of Materials Science* 37 (2002), pp. 2171–2202. DOI: 10.1023/A:1015388912729.

[56] I M Lifshitz and V V Slyozov. "The kinetics of precipitation from supersaturated solid solution". In: *J. Phys. Chem. Solids* 19 (1961), pp. 35–50. DOI: 10.1016/0022-3697(61)90054-3.

[57] Tadao Sugimoto. "Preparation of Monodispersed colloidal particles". In: *Advances in Colloid and Interface Science* 28 (1987), pp. 65–108. ISSN: 1873-3727. DOI: 10.1016/0001-8686(87)80009-X.

[58] Xiaogang Peng, J. Wickham, and A. P. Alivisatos. "Kinetics of II-VI and III-V Colloidal Semiconductor Nanocrystal Growth "Focusing" of Size Distributions". In: *Journal of the American Chemical Society* 120 (21 May 1998), pp. 5343–5344. ISSN: 1520-5126. DOI: 10.1021/ja9805425.

[59] Victor K. La Mer. "Nucleation in Phase Transitions". In: *Industrial & Engineering Chemistry* 44 (6 1952), pp. 1270–1277. DOI: 10.1021/ie50510a027.

[60] Murielle A Watzky and Richard G Finke. "Transition Metal Nanocluster Formation Kinetic and Mechanistic Studies. A New Mechanism When Hydrogen Is the Reductant: Slow, Continuous Nucleation and Fast Autocatalytic Surface Growth". In: *Journal of the American Chemical Society* 119 (43 Oct. 1997), pp. 10382–10400. DOI: 10.1021/ja9705102.

[61] Lucian Bentea, Murielle A. Watzky, and Richard G. Finke. "Sigmoidal Nucleation and Growth Curves Across Nature Fit by the Finke-Watzky Model of Slow Continuous Nucleation and Autocatalytic Growth: Explicit Formulas for the Lag and Growth Times Plus Other Key Insights". In: *Journal of Physical Chemistry C* 121 (9 Mar. 2017), pp. 5302–5312. ISSN: 19327455. DOI: 10.1021/acs.jpcc.6b12021.

[62] Alexander H. Ip et al. "Hybrid passivated colloidal quantum dot solids". In: *Nature Nanotechnology* 7 (9 2012), pp. 577–582. ISSN: 17483395. DOI: 10.1038/nnano.2012.127.

[63] Matthew J. Greaney et al. "Controlling the trap state landscape of colloidal CdSe nanocrystals with cadmium halide ligands". In: *Chemistry of Materials* 27 (3 Feb. 2015), pp. 744–756. ISSN: 15205002. DOI: 10.1021/cm503529j.

[64] Jonathan Owen. "The coordination chemistry of nanocrystal surfaces". In: *Science* 347 (6222 Feb. 2015), pp. 615–616. ISSN: 10959203. DOI: 10.1126/science.1259924.

[65] Michael A. Boles et al. "The surface science of nanocrystals". In: *Nature Materials* 15 (2 Jan. 2016), pp. 141–153. ISSN: 14764660. DOI: 10.1038/nmat4526.

[66] Katrien De Keukeleere et al. “Stabilization of Colloidal Ti, Zr, and Hf Oxide Nanocrystals by Protonated Tri-n-octylphosphine Oxide (TOPO) and Its Decomposition Products”. In: *Chemistry of Materials* 29 (23 Dec. 2017), pp. 10233–10242. ISSN: 15205002. DOI: 10.1021/acs.chemmater.7b04580.

[67] Jonathan De Roo. “The Surface Chemistry of Colloidal Nanocrystals Capped by Organic Ligands”. In: *Chemistry of Materials* 35 (10 May 2023), pp. 3781–3792. ISSN: 15205002. DOI: 10.1021/acs.chemmater.3c00638.

[68] W. William Yu, Y. Andrew Wang, and Xiaogang Peng. “Formation and Stability of Size-, Shape-, and Structure-Controlled CdTe Nanocrystals: Ligand Effects on Monomers and Nanocrystals”. In: *Chemistry of Materials* 15 (22 Nov. 2003), pp. 4300–4308. ISSN: 08974756. DOI: 10.1021/cm034729t.

[69] Narayan Pradhan et al. “Surface ligand dynamics in growth of nanocrystals”. In: *Journal of the American Chemical Society* 129 (30 Aug. 2007), pp. 9500–9509. ISSN: 00027863. DOI: 10.1021/ja0725089.

[70] Emile Drijvers et al. “Revisited Wurtzite CdSe Synthesis: A Gateway for the Versatile Flash Synthesis of Multishell Quantum Dots and Rods”. In: *Chemistry of Materials* 28 (20 Oct. 2016), pp. 7311–7323. ISSN: 15205002. DOI: 10.1021/acs.chemmater.6b02666.

[71] Xiaogang Peng. “Mechanisms for the Shape-Control and Shape-Evolution of Colloidal Semiconductor Nanocrystals”. In: *Advanced Materials* 15 (5 Mar. 2003), pp. 459–463. ISSN: 09359648. DOI: 10.1002/adma.200390107.

[72] H Scott Fogler. *Elements of Chemical Reaction Engineering*. 5th. Prentice Hall, 2016, pp. 1–958. ISBN: 9780133887518. URL: https://madar-ju.com/storage/images/files/file_1738588074Np08H.pdf.

[73] Gary L Foutch and Arland H Johannes. “Reactors in Process Engineering”. In: *Encyclopedia of Physical Science and Technology*. Ed. by Robert A. Meyers. 3rd ed. Academic Press, 2001, pp. 23–43. ISBN: 978-0-12-227410-7. DOI: 10.1016/B0-12-227410-5/00654-2.

[74] Chuntian Hu. “Reactor design and selection for effective continuous manufacturing of pharmaceuticals”. In: *Journal of Flow Chemistry* 11 (3 Sept. 2021), pp. 243–263. ISSN: 20630212. DOI: 10.1007/s41981-021-00164-3.

[75] Nikolay Cherkasov et al. “Continuous stirred tank reactors in fine chemical synthesis for efficient mixing, solids-handling, and rapid scale-up”. In: *Reaction Chemistry and Engineering* 8 (2 Oct. 2022), pp. 266–277. ISSN: 20589883. DOI: 10.1039/d2re00232a.

[76] Andrea W. Chow. “Lab-on-a-Chip: Opportunities for Chemical Engineering”. In: *AIChE journal* 48 (8 Aug. 2002), pp. 1590–1595. DOI: 10.1002/aic.690480802.

[77] Matthew B. Plutschack et al. “The Hitchhiker’s Guide to Flow Chemistry”. In: *Chemical Reviews* 117 (18 Sept. 2017), pp. 11796–11893. ISSN: 15206890. DOI: 10.1021/acs.chemrev.7b00183.

[78] Jacques Pelleter and Fabrice Renaud. “Facile, fast and safe process development of nitration and bromination reactions using continuous flow reactors”. In: *Organic Process Research and Development* 13 (4 July 2009), pp. 698–705. ISSN: 10836160. DOI: 10.1021/op8002695.

[79] Thomas Schwalbe, Volker Autze, and Gregor Wille. “Chemical Synthesis in Microreactors”. In: *CHIMIA* 56 (11 2002), pp. 636–646. ISSN: 0009-4293. DOI: 10.2533/000942902777679984.

[80] Volker Hessel, Holger Löwe, and Friedhelm Schönfeld. “Micromixers - A review on passive and active mixing principles”. In: *Chemical Engineering Science* 60 (8-9 Apr. 2005), pp. 2479–2501. ISSN: 00092509. DOI: 10.1016/j.ces.2004.11.033.

[81] Sebastian Schwolow et al. “Application-oriented analysis of mixing performance in microreactors”. In: *Organic Process Research and Development* 16 (9 Sept. 2012), pp. 1513–1522. ISSN: 10836160. DOI: 10.1021/op300107z.

[82] Mubashshir Ahmad Ansari, Kwang Yong Kim, and Sun Min Kim. “Numerical and experimental study on mixing performances of simple and vortex micro T-mixers”. In: *Micromachines* 9 (5 Apr. 2018). ISSN: 2072666X. DOI: 10.3390/mi9050204.

[83] Pierrette Guichardon, Carlos Baqueiro, and Nelson Ibaseta. “Villermaux–Dushman Test of Micromixing Characterization Revisited: Kinetic Effects of Acid Choice and Ionic Strength”. In: *Industrial and Engineering Chemistry Research* 60 (50 Dec. 2021), pp. 18268–18282. ISSN: 15205045. DOI: 10.1021/acs.iecr.1c03208.

[84] Torben Frey et al. “Local analysis of micro mixing for the Villermaux-Dushman protocol by using the imaging UV-Vis spectroscopy”. In: *Chemical Engineering Research and Design* 205 (May 2024), pp. 822–829. ISSN: 02638762. DOI: 10.1016/j.cherd.2024.04.049.

[85] Baggie W. Nyande, Kiran Mathew Thomas, and Richard Lakerveld. “CFD Analysis of a Kenics Static Mixer with a Low Pressure Drop under Laminar Flow Conditions”. In: *Industrial and Engineering Chemistry Research* 60 (14 Apr. 2021), pp. 5264–5277. ISSN: 15205045. DOI: 10.1021/acs.iecr.1c00135.

[86] T. Tajik Ghanbari et al. “Mixing performance improvement of T-shaped micromixer using novel structural design of channel and obstacles”. In: *Physics of Fluids* 35 (12 Dec. 2023). ISSN: 10897666. DOI: 10.1063/5.0177344.

[87] Arabdha Bhattacharya et al. “Mixing performance of T-shaped wavy-walled micromixers with embedded obstacles”. In: *Physics of Fluids* 36 (3 Mar. 2024). ISSN: 10897666. DOI: 10.1063/5.0194724.

[88] William. Reginald. Dean. "Note on the Motion of Fluid in a Curved Pipe". In: *Philosophical Magazine* 4 (1927), pp. 208–223. DOI: 10.1080/14786440708564324.

[89] Ke Jun Wu, Geoffroy Michet De Varine Bohan, and Laura Torrente-Murciano. "Synthesis of narrow sized silver nanoparticles in the absence of capping ligands in helical microreactors". In: *Reaction Chemistry and Engineering* 2 (2 Apr. 2017), pp. 116–128. ISSN: 20589883. DOI: 10.1039/c6re00202a.

[90] Klavs F. Jensen. "Flow chemistry—Microreaction technology comes of age". In: *AIChE Journal* 63 (3 Mar. 2017), pp. 858–869. ISSN: 15475905. DOI: 10.1002/aic.15642.

[91] Volker Hessel et al. "Sustainability of flow chemistry and microreaction technology". In: *Green Chemistry* (July 2024). ISSN: 14639270. DOI: 10.1039/d4gc01882f.

[92] Chien Chong Hong, Jin Woo Choi, and Chong H. Ahn. "A novel in-plane passive microfluidic mixer with modified Tesla structures". In: *Lab on a Chip* 4 (2 2004), pp. 109–113. ISSN: 14730197. DOI: 10.1039/b305892a.

[93] Kameel Abdel-Latif et al. "Self-Driven Multistep Quantum Dot Synthesis Enabled by Autonomous Robotic Experimentation in Flow". In: *Advanced Intelligent Systems* 3 (2 Feb. 2021). ISSN: 2640-4567. DOI: 10.1002/aisy.202000245.

[94] Fernando Delgado-Licona et al. "Flow-driven data intensification to accelerate autonomous inorganic materials discovery". In: *Nature Chemical Engineering* (July 2025). ISSN: 2948-1198. DOI: 10.1038/s44286-025-00249-z.

[95] Carlotta Campalani, Guillaume Petit, and Jean-Christophe M. Monbaliu. "Aqueous Continuous Flow Synthesis of Cadmium Chalcogenide Quantum Dots: Opportunities and Challenges". In: *JACS Au* 6 (1 Dec. 2025), pp. 38–58. ISSN: 2691-3704. DOI: 10.1021/jacsau.5c01449.

[96] Juandria V. Williams et al. "Hydrothermal synthesis of CdSe nanoparticles". In: *Industrial and Engineering Chemistry Research* 46 (13 June 2007), pp. 4358–4362. ISSN: 08885885. DOI: 10.1021/ie061413x.

[97] Jidong Wang, Jizu Zhai, and Shumin Han. "Non-injection one-pot preparation strategy for multiple families of magic-sized CdTe quantum dots with bright bandgap photoemission". In: *Chemical Engineering Journal* 215-216 (Jan. 2013), pp. 23–28. ISSN: 13858947. DOI: 10.1016/j.cej.2012.10.092.

[98] Mojtaba Mirhosseini Moghaddam et al. "Microwave-assisted synthesis of CdSe quantum dots: Can the electromagnetic field influence the formation and quality of the resulting nanocrystals?" In: *Nanoscale* 4 (23 Dec. 2012), pp. 7435–7442. ISSN: 20403364. DOI: 10.1039/c2nr32441e.

[99] R. K. Singh et al. “Progress in microwave-assisted synthesis of quantum dots (graphene/carbon/semiconducting) for bioapplications: a review”. In: *Materials Today Chemistry* 12 (June 2019), pp. 282–314. ISSN: 24685194. DOI: 10.1016/j.mtchem.2019.03.001.

[100] Jonathan S. Owen et al. “Reaction chemistry and ligand exchange at cadmium-selenide nanocrystal surfaces”. In: *Journal of the American Chemical Society* 130 (37 Sept. 2008), pp. 12279–12281. ISSN: 00027863. DOI: 10.1021/ja804414f.

[101] Yi Shen et al. “Purification of quantum dots by gel permeation chromatography and the Eeffect of excess ligands on shell growth and ligand exchange”. In: *Chemistry of Materials* 25 (14 July 2013), pp. 2838–2848. ISSN: 08974756. DOI: 10.1021/cm4012734.

[102] Yi Shen et al. “Gel permeation chromatography as a multifunctional processor for nanocrystal purification and on-column ligand exchange chemistry”. In: *Chemical Science* 7 (9 May 2016), pp. 5671–5679. ISSN: 20416539. DOI: 10.1039/c6sc01301e.

[103] Michal Danek et al. “Synthesis of Luminescent Thin-Film CdSe/ZnSe Quantum Dot Composites Using CdSe Quantum Dots Passivated with an Overlayer of ZnSe”. In: *Chemistry of Materials* 8 (1 Jan. 1996), pp. 173–180. ISSN: 0897-4756. DOI: 10.1021/cm9503137.

[104] Xiaogang Peng, Zuoyan Peng, and Lianhua Qu. “Synthesis of colloidal metal chalcogenide nanocrystals”. European pat. EP1337695B1. The Board of Trustees of the University of Arkansas. European Patent EP1337695B1. Aug. 20, 2003. URL: https://patents.google.com/patent/EP1337695B1/en.

[105] Z. A. Peng and X. Peng. “Formation of high-quality CdTe, CdSe, and CdS nanocrystals using CdO as precursor”. In: *Journal of the American Chemical Society* 123 (1 Jan. 2001), pp. 183–184. ISSN: 00027863. DOI: 10.1021/ja003633m.

[106] Narayan Pradhan and Shlomo Efrima. “Single-precursor, one-pot versatile synthesis under near ambient conditions of tunable, single and dual band fluorescing metal sulfide nanoparticles”. In: *Journal of the American Chemical Society* 125 (8 Feb. 2003), pp. 2050–2051. ISSN: 00027863. DOI: 10.1021/ja028887h.

[107] Narayan Pradhan, Beni Katz, and Shlomo Efrima. “Synthesis of High-Quality Metal Sulfide Nanoparticles from Alkyl Xanthate Single Precursors in Alkylamine Solvents”. In: *Journal of Physical Chemistry B* 107 (50 Dec. 2003), pp. 13843–13854. ISSN: 15206106. DOI: 10.1021/jp0357951.

[108] Mona B. Mohamed et al. “Synthesis of high quality zinc blende CdSe nanocrystals”. In: *Journal of Physical Chemistry B* 109 (21 June 2005), pp. 10533–10537. ISSN: 15206106. DOI: 10.1021/jp051123e.

[109] Lianhua Qu, Z. Adam Peng, and Xiaogang Peng. “Alternative Routes toward High Quality CdSe Nanocrystals”. In: *Nano Letters* 1 (6 June 2001), pp. 333–337. ISSN: 15306984. DOI: 10.1021/nl0155532.

[110] Joel Van Embden and Paul Mulvaney. "Nucleation and growth of CdSe nanocrystals in a binary ligand system". In: *Langmuir* 21 (22 Oct. 2005), pp. 10226–10233. ISSN: 07437463. DOI: 10.1021/la0510811.

[111] Jacek Jasieniak et al. "Phosphine-free synthesis of CdSe nanocrystals". In: *Journal of Physical Chemistry B* 109 (44 Nov. 2005), pp. 20665–20668. ISSN: 15206106. DOI: 10.1021/jp054289o.

[112] W. William Yu and Xiaogang Peng. "Formation of high-quality CdS and other II-VI semiconductor nanocrystals in noncoordinating solvents: Tunable reactivity of monomers". In: *Angewandte Chemie - International Edition* 41 (13 July 2002), pp. 2368–2371. ISSN: 14337851. DOI: 10.1002/1521-3773(20020703)41:13<2368::AID-ANIE2368>3.0.CO;2-G.

[113] Jin Joo et al. "Generalized and facile synthesis of semiconducting metal sulfide nanocrystals". In: *Journal of the American Chemical Society* 125 (36 Sept. 2003), pp. 11100–11105. ISSN: 00027863. DOI: 10.1021/ja0357902.

[114] Y. Charles Cao and Jianhui Wang. "One-pot synthesis of high-quality zinc-blende CdS nanocrystals". In: *Journal of the American Chemical Society* 126 (44 Nov. 2004), pp. 14336–14337. ISSN: 00027863. DOI: 10.1021/ja0459678.

[115] J E Bowen Katari, V L Colvin, and A P Alivisatos. "X-ray Photoelectron Spectroscopy of CdSe Nanocrystals with Applications to Studies of the Nanocrystal Sllrface". In: *J. Phys. Chem* 98 (15 Feb. 1994), pp. 4109–4117. DOI: 10.1021/j100066a034.

[116] Lianhua Qu and Xiaogang Peng. "Control of photoluminescence properties of CdSe nanocrystals in growth". In: *Journal of the American Chemical Society* 124 (9 Mar. 2002), pp. 2049–2055. ISSN: 00027863. DOI: 10.1021/ja017002j.

[117] Craig R. Bullen and Paul Mulvaney. "Nucleation and growth kinetics of CdSe nanocrystals in octadecene". In: *Nano Letters* 4 (12 Dec. 2004), pp. 2303–2307. ISSN: 15306984. DOI: 10.1021/nl0496724.

[118] Yongan Andrew Yang et al. "Synthesis of CdSe and CdTe nanocrystals without precursor injection". In: *Angewandte Chemie - International Edition* 44 (41 Oct. 2005), pp. 6712–6715. ISSN: 14337851. DOI: 10.1002/anie.200502279.

[119] Dengguo Wu, Martin E. Kordesch, and P. Van Gregory Patten. "A new class of capping ligands for CdSe nanocrystal synthesis". In: *Chemistry of Materials* 17 (25 Dec. 2005), pp. 6436–6441. ISSN: 08974756. DOI: 10.1021/cm050799j.

[120] Rong He and Hongchen Gu. "Synthesis and characterization of mondispersed CdSe nanocrystals at lower temperature". In: *Colloids and Surfaces A: Physicochemical and Engineering Aspects* 272 (1-2 Jan. 2006), pp. 111–116. ISSN: 09277757. DOI: 10.1016/j.colsurfa.2005.07.017.

[121] B. O. Dabbousi et al. "(CdSe)ZnS core-shell quantum dots: Synthesis and characterization of a size series of highly luminescent nanocrystallites". In: *Journal of Physical Chemistry B* 101 (46 June 1997), pp. 9463–9475. ISSN: 15206106. DOI: 10.1021/jp971091y.

[122] Ivo Mekis et al. "One-pot synthesis of highly luminescent CdSe/CdS core-shell nanocrystals via organometallic and "greener" chemical approaches". In: *Journal of Physical Chemistry B* 107 (30 July 2003), pp. 7454–7462. ISSN: 15206106. DOI: 10.1021/jp0278364.

[123] Subashini Asokan et al. "The use of heat transfer fluids in the synthesis of high-quality CdSe quantum dots, core/shell quantum dots, and quantum rods". In: *Nanotechnology* 16 (10 Oct. 2005), pp. 2000–2011. ISSN: 09574484. DOI: 10.1088/0957-4484/16/10/004.

[124] Dmitri V. Talapin et al. "Highly Luminescent Monodisperse CdSe and CdSe/ZnS Nanocrystals Synthesized in a Hexadecylamine-Trioctylphosphine Oxide-Trioctylphospine Mixture". In: *Nano Letters* 1 (4 Apr. 2001), pp. 207–211. ISSN: 15306984. DOI: 10.1021/nl0155126.

[125] Robert E. Bailey and Shuming Nie. "Alloyed semiconductor quantum dots: Tuning the optical properties without changing the particle size". In: *Journal of the American Chemical Society* 125 (23 June 2003), pp. 7100–7106. ISSN: 00027863. DOI: 10.1021/ja035000o.

[126] Dmitri V. Talapin et al. "A novel organometallic synthesis of highly luminescent CdTe nanocrystals". In: *Journal of Physical Chemistry B* 105 (12 Mar. 2001), pp. 2260–2263. ISSN: 15206106. DOI: 10.1021/jp003177o.

[127] Viki Kloper et al. "The growth of colloidal cadmium telluride nanocrystal quantum dots in the presence of Cd0 nanoparticles". In: *Journal of Physical Chemistry C* 111 (28 July 2007), pp. 10336–10341. ISSN: 19327447. DOI: 10.1021/jp0708906.

[128] A Henglein. "Photo-Degradation and Fluorescence of Colloidal-Cadmium Sulfide in Aqueous Solution". In: *Berichte der Bunsengesellschaft für physikalische Chemie* 86 (4 Apr. 1982), pp. 301–305. ISSN: 00059021. DOI: 10.1002/bbpc.19820860409. URL: https://onlinelibrary.wiley.com/doi/10.1002/bbpc.19820860409.

[129] R. Rossetti, S. Nakahara, and L. E. Brus. "Quantum size effects in the redox potentials, resonance Raman spectra, and electronic spectra of CdS crystallites in aqueous solution". In: *The Journal of Chemical Physics* 79 (2 1983), pp. 1086–1088. ISSN: 00219606. DOI: 10.1063/1.445834.

[130] T Vossmeyer et al. "CdS Nanoclusters: Synthesis, Characterization, Size Dependent Oscillator Strength, Temperature Shift of the Excitonic Transition Energy, and Reversible Absorbance Shift". In: *J. Phys. Chem* 98 (31 Aug. 1994), pp. 7665–7673. ISSN: 1089-5639. DOI: 10.1021/j100082a044.

[131] Abdelhay Aboulaich et al. “One-pot noninjection route to CdS quantum dots via hydrothermal synthesis”. In: *ACS Applied Materials and Interfaces* 4 (5 May 2012), pp. 2561–2569. ISSN: 19448244. DOI: 10.1021/am300232z.

[132] Mengying Li et al. “Hydrothermal synthesis of highly luminescent CdTe quantum dots by adjusting precursors’ concentration and their conjunction with BSA as biological fluorescent probes”. In: *Talanta* 72 (1 Apr. 2007), pp. 89–94. ISSN: 00399140. DOI: 10.1016/j.talanta.2006.09.028.

[133] Wei hai Yang et al. “Hydrothermal synthesis for high-quality CdTe quantum dots capped by cysteamine”. In: *Materials Letters* 62 (17-18 June 2008), pp. 2564–2566. ISSN: 0167577X. DOI: 10.1016/j.matlet.2007.12.049.

[134] Andrey L. Rogach et al. “Synthesis and characterization of a size series of extremely small thiol-stabilized CdSe nanocrystals”. In: *Journal of Physical Chemistry B* 103 (16 Apr. 1999), pp. 3065–3069. ISSN: 15206106. DOI: 10.1021/jp984833b.

[135] He you Han, Zong hai Sheng, and Jian gong Liang. “A novel method for the preparation of water-soluble and small-size CdSe quantum dots”. In: *Materials Letters* 60 (29-30 Dec. 2006), pp. 3782–3785. ISSN: 0167577X. DOI: 10.1016/j.matlet.2006.03.113.

[136] Xianfeng Chen et al. “A one-step aqueous synthetic route to extremely small CdSe nanoparticles”. In: *Journal of Colloid and Interface Science* 319 (1 Mar. 2008), pp. 140–143. ISSN: 00219797. DOI: 10.1016/j.jcis.2007.11.043.

[137] Juandria V. Williams, Nicholas A. Kotov, and Phillip E. Savage. “Materials and interfaces a rapid hot-injection method for the improved hydrothermal synthesis of CdSe nanoparticles”. In: *Industrial and Engineering Chemistry Research* 48 (9 May 2009), pp. 4316–4321. ISSN: 08885885. DOI: 10.1021/ie8007067.

[138] M. N. Kalasad, M. K. Rabinal, and B. G. Mulimani. “Ambient synthesis and characterization of high-quality CdSe quantum dots by an aqueous route”. In: *Langmuir* 25 (21 Nov. 2009), pp. 12729–12735. ISSN: 07437463. DOI: 10.1021/la901798y.

[139] Rongfang Wang et al. “Synthesis of color-tunable CdSe nanocrystals via a green synthetic method”. In: *IEEE Photonics Technology Letters* 26 (12 June 2014), pp. 1196–1198. ISSN: 10411135. DOI: 10.1109/LPT.2014.2318723.

[140] Yilin Wang et al. “Simple synthesis of luminescent CdSe quantum dots from ascorbic acid and selenium dioxide”. In: *Luminescence* 30 (8 Dec. 2015), pp. 1375–1379. ISSN: 15227243. DOI: 10.1002/bio.2909.

[141] Zubair M.S.H. Khan, Hana Khan, and M. Zulfequar. “CdSe quantum dots using selenourea as selenium source in polymer matrix”. In: *Journal of Materials Science: Materials in Electronics* 28 (19 Oct. 2017), pp. 14638–14645. ISSN: 1573482X. DOI: 10.1007/s10854-017-7328-1.

[142] Rongfang Wang et al. “One-Step Synthesis of CdSe Quantum Dots by Using Hydrazine Hydrate Reduction of Selenium Dioxide”. In: *Australian Journal of Chemistry* 71 (7 2018), pp. 524–526. ISSN: 14450038. DOI: 10.1071/CH18100.

[143] Dmitri V. Talapin et al. “Dynamic distribution of growth rates within the ensembles of colloidal II-VI and III-V semiconductor nanocrystals as a factor governing their photoluminescence efficiency”. In: *Journal of the American Chemical Society* 124 (20 May 2002), pp. 5782–5790. ISSN: 00027863. DOI: 10.1021/ja0123599.

[144] Nikolai Gaponik et al. “Thiol-capping of CdTe nanocrystals: An alternative to organometallic synthetic routes”. In: *Journal of Physical Chemistry B* 106 (29 July 2002), pp. 7177–7185. ISSN: 10895647. DOI: 10.1021/jp025541k.

[145] Hao Zhang et al. “Hydrothermal Synthesis for High-Quality CdTe Nanocrystals”. In: *Advanced Materials* 15 (20 Oct. 2003), pp. 1712–1715. ISSN: 09359648. DOI: 10.1002/adma.200305653.

[146] Jing Wang and Heyou Han. “Hydrothermal synthesis of high-quality type-II CdTe/CdSe quantum dots with near-infrared fluorescence”. In: *Journal of Colloid and Interface Science* 351 (1 Nov. 2010), pp. 83–87. ISSN: 00219797. DOI: 10.1016/j.jcis.2010.07.025.

[147] Xian Xie et al. “Aqueous synthesis of luminescent cadmium telluride quantum dots using ascorbic acid as the reducing agent”. In: *Micro and Nano Letters* 9 (7 2014), pp. 478–481. ISSN: 17500443. DOI: 10.1049/mnl.2014.0084.

[148] Liang Jun Pan et al. “Controllable synthesis of nanocrystals in droplet reactors”. In: *Lab on a Chip* 18 (1 2018), pp. 41–56. ISSN: 14730189. DOI: 10.1039/c7lc00800g.

[149] Mara Guidi, Peter H. Seeberger, and Kerry Gilmore. “How to approach flow chemistry”. In: *Chemical Society Reviews* 49 (24 2020), pp. 8910–8932. ISSN: 14604744. DOI: 10.1039/c9cs00832b.

[150] Luca Capaldo, Zhenghui Wen, and Timothy Noël. “A field guide to flow chemistry for synthetic organic chemists”. In: *Chemical Science* (2023), pp. 4230–4247. ISSN: 20416539. DOI: 10.1039/d3sc00992k.

[151] Joshua B. Edel et al. “Microfluidic routes to the controlled production of nanoparticles”. In: *Chemical Communications* 2 (10 2002), pp. 1136–1137. ISSN: 1364548X. DOI: 10.1039/b202998g.

[152] Emory M. Chan, Richard A. Mathies, and A. Paul Alivisatos. “Size-controlled growth of CdSe nanocrystals in microfluidic reactors”. In: *Nano Letters* 3 (2 2003), pp. 199–201. ISSN: 15306984. DOI: 10.1021/nl0259481.

[153] Brian K.H. Yen et al. “A Continuous-Flow Microcapillary Reactor for the Preparation of a Size Series of CdSe Nanocrystals”. In: *Advanced Materials* 15 (21 2003), pp. 1858–1862. ISSN: 09359648. DOI: 10.1002/adma.200305162.

[154] Samuel Marre et al. “Supercritical continuous-microflow synthesis of narrow size distribution quantum dots”. In: *Advanced Materials* 20 (24 2008), pp. 4830–4834. ISSN: 09359648. DOI: 10.1002/adma.200801579.

[155] Raghavendra Kikkeri et al. “Synthesis of carbohydrate-functionalized quantum dots in microreactors”. In: *Angewandte Chemie - International Edition* 49 (11 Mar. 2010), pp. 2054–2057. ISSN: 14337851. DOI: 10.1002/anie.200905053.

[156] Yuan Pu et al. “Colloidal Synthesis of Semiconductor Quantum Dots toward Large-Scale Production: A Review”. In: *Industrial and Engineering Chemistry Research* 57 (6 2018), pp. 1790–1802. ISSN: 15205045. DOI: 10.1021/acs.iecr.7b04836.

[157] Emory M. Chan, A. Paul Alivisatos, and Richard A. Mathies. “High-temperature microfluidic synthesis of CdSe nanocrystals in nanoliter droplets”. In: *Journal of the American Chemical Society* 127 (40 Oct. 2005), pp. 13854–13861. ISSN: 00027863. DOI: 10.1021/ja051381p.

[158] Matt S. Naughton et al. “High temperature continuous flow synthesis of CdSe/CdS/ZnS, CdS/ZnS, and CdSeS/ZnS nanocrystals”. In: *Nanoscale* 7 (38 2015), pp. 15895–15903. ISSN: 20403372. DOI: 10.1039/c5nr04510j.

[159] Milad Abolhasani et al. “Oscillatory Microprocessor for Growth and in Situ Characterization of Semiconductor Nanocrystals”. In: *Chemistry of Materials* 27 (17 2015), pp. 6131–6138. ISSN: 15205002. DOI: 10.1021/acs.chemmater.5b02821.

[160] Ayumi Toyota et al. “Combinatorial synthesis of CdSe nanoparticles using microreactors”. In: *Journal of Physical Chemistry C* 114 (17 2010), pp. 7527–7534. ISSN: 19327447. DOI: 10.1021/jp911876s.

[161] Hiroyuki Nakamura et al. “Application of a microfluidic reaction system for CdSe nanocrystal preparation: Their growth kinetics and photoluminescence analysis”. In: *Lab on a Chip* 4 (3 2004), pp. 237–240. ISSN: 14730197. DOI: 10.1039/b310915a.

[162] Manabu Kawa et al. “Large-scale production of CdSe nanocrystal by a continuous flow reactor”. In: *Journal of Nanoparticle Research* 5 (1-2 2003), pp. 81–85. ISSN: 13880764. DOI: 10.1023/A:1024434502893.

[163] Ilya Shestopalov, Joshua D. Tice, and Rustem F. Ismagilov. “Multi-step synthesis of nanoparticles performed on millisecond time scale in a microfluidic droplet-based system”. In: *Lab on a Chip* 4 (4 2004), pp. 316–321. ISSN: 14730197. DOI: 10.1039/b403378g.

[164] Jing Dai et al. “Particle size controlled synthesis of CdS nanoparticles on a microfluidic chip”. In: *Chemical Engineering Journal* 280 (2015), pp. 385–390. ISSN: 13858947. DOI: 10.1016/j.cej.2015.06.005.

[165] Xiangliang Yang et al. “A modified method to prepare diselenides by the reaction of selenium with sodium borohydride”. In: *Journal of Chemical Research - Part S* (4 2002), pp. 160–161. ISSN: 03082342. DOI: 10.3184/030823402103171726.

[166] Gauthier Emonds-alt et al. “Exploring the Fundamentals of Microreactor Technology with Multidisciplinary Lab Experiments Combining the Synthesis and Characterization of Inorganic Nanoparticles”. In: *Journal of chemical education* 94 (2017), pp. 775–780. DOI: 10.1021/acs.jchemed.6b00899.

[167] R. C. Mbwahnche et al. “Segmented flow reactor for synthesis of quantum dot nanocrystals and plasmonic nanoparticles”. In: *Journal of Physics: Conference Series* 741 (1 2016), pp. 1–6. ISSN: 17426596. DOI: 10.1088/1742-6596/741/1/012026.

[168] Dipika Das and Raj Kumar Dutta. “Structure-optical property correlation in CdTe/CdS core-shell quantum dots and their effects on Cu2+ sensing mechanisms”. In: *Journal of Photochemistry and Photobiology A: Chemistry* 400 (2020), p. 112709. DOI: 10.1016/j.jphotochem.2020.112709.

[169] Subbiramaniyan Kubendhiran et al. “Microfluidic Synthesis of Semiconducting Colloidal Quantum Dots and Their Applications”. In: *ACS Applied Nano Materials* 2 (4 2019), pp. 1773–1790. ISSN: 25740970. DOI: 10.1021/acsanm.9b00456.

[170] Boon Kin Pong, Bernhardt L. Trout, and Jim Yang Lee. “Modified ligand-exchange for efficient solubilization of CdSe/ZnS quantum dots in water: A procedure guided by computational studies”. In: *Langmuir* 24 (10 May 2008), pp. 5270–5276. ISSN: 07437463. DOI: 10.1021/la703431j.

[171] David R. Baker and Prashant V. Kamat. “Tuning the emission of CdSe quantum dots by controlled trap enhancement”. In: *Langmuir* 26 (13 July 2010), pp. 11272–11276. ISSN: 07437463. DOI: 10.1021/la100580g.

Chapter 2

Innovative Chalcogenide Transfer Agent for Improved Aqueous Quantum Dot Synthesis

2.1 Preface

An innovative approach to chalcogenide precursor synthesis and their subsequent use for the production of CdX (X = S, Se, Te) quantum dots QDs in water under scalable and intensified continuous flow conditions is introduced. Herein, Tris(2-carboxyethyl)phosphine (TCEP) is identified as a novel, efficient and water-soluble vehicle for chalcogenide transfer to form CdX QDs under aqueous conditions. A comprehensive exploration of critical process parameters, including pH, chalcogen excess, and residence time, utilizing a DoE approach is reported. Reaction kinetics are investigated in real-time using a combination of *in situ* Raman spectroscopy and *in-line* ^{31}P-NMR spectroscopy. The conversion of TCEP into TCEP=X (X = S, Se, Te) species is seamlessly adapted to continuous flow conditions. TCEP=X precursors are subsequently employed in the synthesis of CdX QDs.

2.2 General information

This chapter is a modified version of a published paper in *Chemical Science*:

Petit, G., Malherbe, C., Bianchi, P., & Monbaliu, J. C. M. "An innovative chalcogenide transfer agent for improved aqueous quantum dot synthesis". In: *Chemical Science* 15(33), 2024, 13148–13159. ISSN: 20416539. DOI: 10.1039/d4sc01135j.

Authors contributions

GP designed and performed the experiments, analysed the results, and wrote the first draft of the manuscript and Supporting Information. CM designed the Raman *in-line* batch experiments, provided technical assistance for the data treatment and the kinetic model and proofread the manuscript. PB designed and performed a preliminary study on the preparation of TCEP=Se, analyzed the data and contributed to the redaction of the manuscript. JCMM designed the concepts, supervised the research, and wrote the manuscript.

Acknowledgements

This work was supported by the Service Public de Wallonie (Win2Wal 2018 Program, QD_3Drops Project). Computational resources were provided by the "Consortium des Équipements de Calcul Intensif" (CÉCI), funded by the "Fonds de la Recherche Scientifique de Belgique" (F.R.S.-FNRS) under Grant No. 2.5020.11a and by the Walloon Region. The authors also thank Marc Winter and Dr. Guillaume Gauron (Corning SAS) for their technical support and the loan of the pilot scale mesofluidic equipment. The TEM pictures were realized at the CAREM microscopy facility of the University of Liège. The authors also acknowledge Prof. B. Leyh (ULiège) for stimulating discussions on kinetics and Prof. B. Vertruyen (ULiège) for acquiring the Powder X-ray Diffraction data, Dr. P. Compère (ULiège) for the HRTEM data.

2.3 Modified version of the article

2.3.1 Introduction

As mentioned in Section 1.8, the current work aims to synthesize CdX QDs (where X = S, Se, or Te) in aqueous media through microfluidics, with emission properties approaching those obtained in organic processes. In this perspective, the first step identified is the development of a novel chalcogenide transfer agent with moderated reactivity, enabling improved control over QD formation.

Building on unmet needs for the scalable aqueous preparation of QDs and drawing on established expertise in flow chemistry, [1–6] a concrete solution was pursued to develop a robust and innovative water-soluble chalcogenide source. TCEP has emerged as a highly effective water-soluble vehicle for reduced chalcogens, enabling the preparation of CdX (where X = S, Se, or Te) QDs.

The impact of various parameters such as pH, chalcogen excess, and residence time on the conversion toward TCEP=X is explored through a DoE approach. The reduction kinetics and the formation of TCEP=X

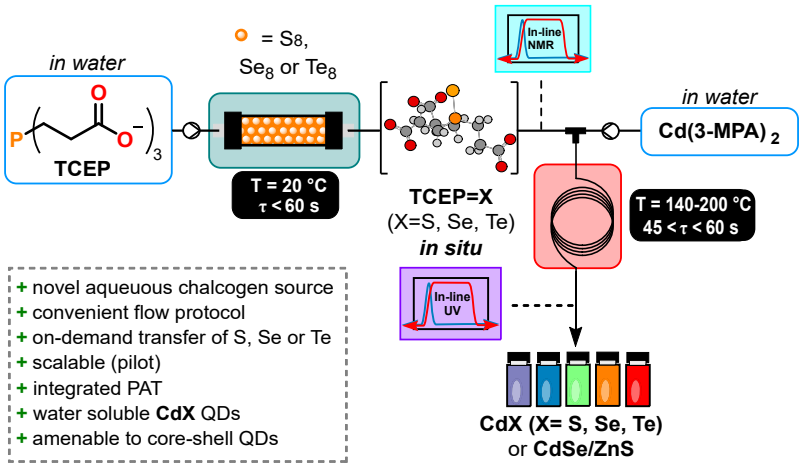

Figure 2.1. This work reports a fully concatenated flow process in water for accessing CdX (where X = S, Se, Te) QDs.

species are studied via *in situ* Raman spectroscopy. This reaction is then successfully adapted to continuous flow conditions with *in-line* low field ^{31}P-NMR monitoring. Subsequently, these novel water-soluble chalcogenide precursors are assessed for the synthesis of CdX QDs, like shown in figure 2.1.

2.3.2 Results and discussion

2.3.2.1 Optimization of the preparation of TCEP=X

Since its initial description by Whitesides, [7] in 1991, TCEP has found widespread synthetic utilities for reducing disulfide bonds in biochemistry, peptide chemistry and desulfurization/deselenization reactions. [8–15] Subsequently, TCEP's utility was broadened to the reduction of various organic functional groups [16, 17] and for the coordination of metal cations. [18] The use of TCEP in QDs synthesis, however, still remains undocumented. The initial phase of the project therefore aimed to demonstrate the adaptability of TCEP for reducing three key chalcogens (sulfur, selenium and tellurium) under aqueous conditions.

Preliminary experiments highlighted a stronger resistance towards air oxidation compared to common sodium-based chalcogenide precursors subsubsection 6.1.4.4. Early trials also emphasized a substantial effect of the pH on the outcomes. Indeed, TCEP is a phosphine compound bearing up to 4 exchangeable protons: 3 on the carboxylic acid moieties (pKa = 2.99, 3.67, 4.36) and 1 on the phosphorus center itself (pKa = 7.66). [19] The latter proton plays the most influential role in modulating TCEP's reactivity. [18]

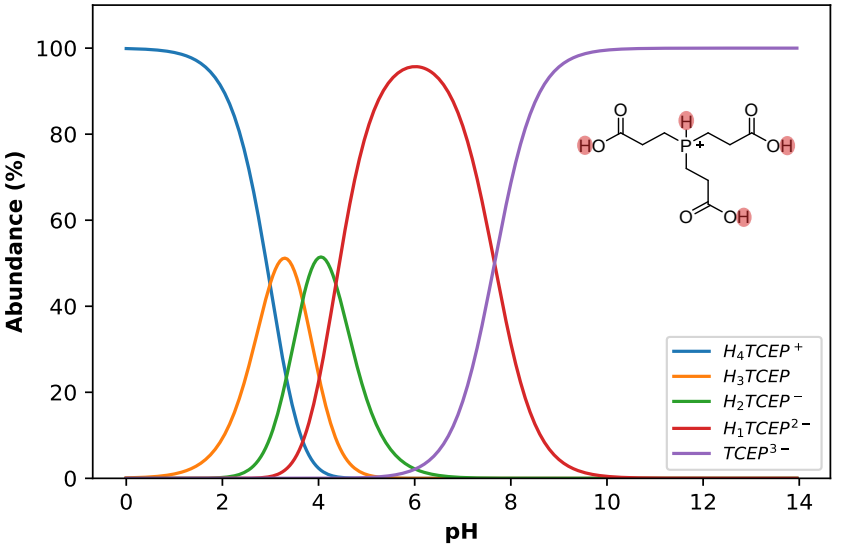

Figure 2.2. Calculation of the protonation distribution of TCEP species based on the pKa of the four pH active functions. Source from [19].

After the identification of the pH as the most critical parameter for the preparation of TCEP=X, a multifactorial optimization was initiated through a DoE, under batch conditions. The reaction between TCEP and elemental chalcogens is inherently heterogeneous, hence, apart from pH, 3 additional parameters are likely to influence the reaction: (a) the excess chalcogen, (b) the mixing efficiency and (c) the timeframe for the reaction.

The substantial impact of pH on TCEP's inherent features becomes evident when comparing the ^{31}P-NMR chemical shifts (2.3, blue spectra) of TCEP under acidic conditions (pH value from 5 to 7, δ = 17.5 ppm) and alkaline conditions (pH value from 8 to 11, δ = -20.6 ppm) and TCEP's protonation state particularly exerts a profound influence on the reduction of Te. For the latter, the acidic form of TCEP is unable to act as a reductant. 2.3 also presents the ^{31}P-NMR spectra for TCEP=O (δ = 56.9 ppm at pH = 2.5 and 58.9 ppm at pH = 11), TCEP=S (δ = 52.7 ppm), TCEP=Se (δ = 41.4 ppm) and TCEP=Te (δ = -6.8 ppm). The formation of TCEP=O as a side product is often observed when solutions of TCEP=X are exposed under aerobic conditions, especially at pH larger than 9. Therefore, to prevent the competing formation of TCEP=O, all reactions were carried out under an inert atmosphere.

The multifactorial optimization started with the synthesis of TCEP=S. A range of preliminary boundary conditions was selected, including pH values of 5 (representing a predominantly protonated form) and 11 (representing TCEP in its deprotonated form); an excess of chalcogen (S_8) ranging from 1.5 to 3 equivalents; stirring speed set between 700 to 900 rpm. Samples were

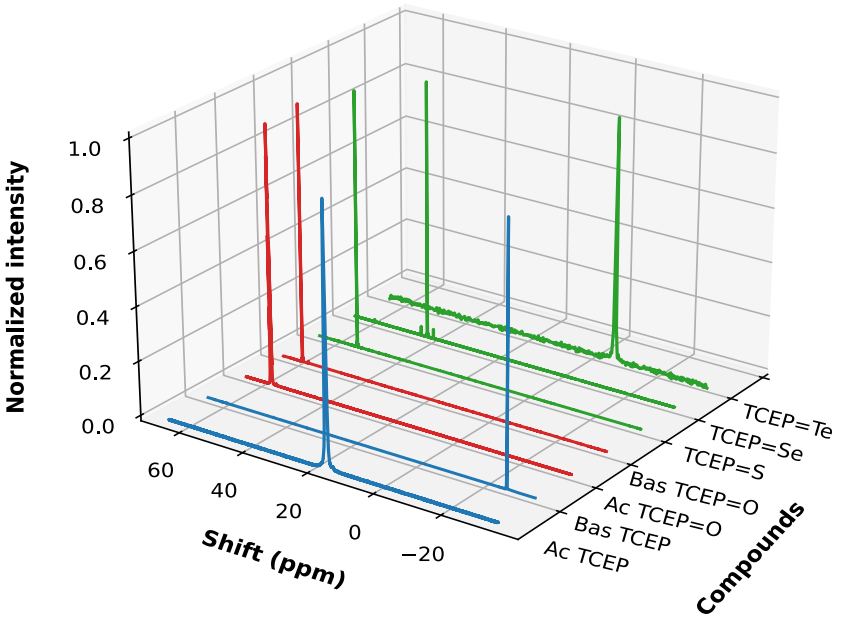

Figure 2.3. Chemical shifts for each TCEP derivative: blue = reagents (TCEP acid (Ac) and basic (B) forms), red = side product (TCEP=O acid (Ac) and basic (B) forms) and green = the products of interest (TCEP=S, TCEP=Se, TCEP=Te).

collected after 20, 40 and 60 min. Crude samples were directly analysed by high field ^{31}P-NMR, after the addition of deuterium oxide (50:50 crude/D_2O, in volume).

The preliminary set of results from the DoE was analysed through an effect plot, which summarizes the relative impact of each parameter on the conversion, see Figure 2.4a. A model was derived and is summarized as contour plots in Figure 2.4b. The effect plot shows that the most influential parameter to enhance conversion is the excess of chalcogen, contributing to 53.6%, followed by the reaction time to 26.9%. Interestingly, pH exhibits a quadratic effect. Indeed, it was expected that an increasing pH would only have a positive impact; however, this was not the case, since more alkaline conditions triggered a competitive phenomenon, *i.e.*, chalcogen polymerization. [20]

Mixing efficiency does not exert a significant direct impact with this range of rpm. However, when expressed as an interaction parameter, it shows a positive influence in conjunction with the reaction time. Moreover, pH and excess of S_8 are also associated with a positive interaction. The model resulting from these results (2.4b.) for sulfur reduction with TCEP toward TCEP=S anticipates full conversion with the simultaneous requirement for extended reaction times (>40 min), a large excess of sulfur (>2.5 eq) at

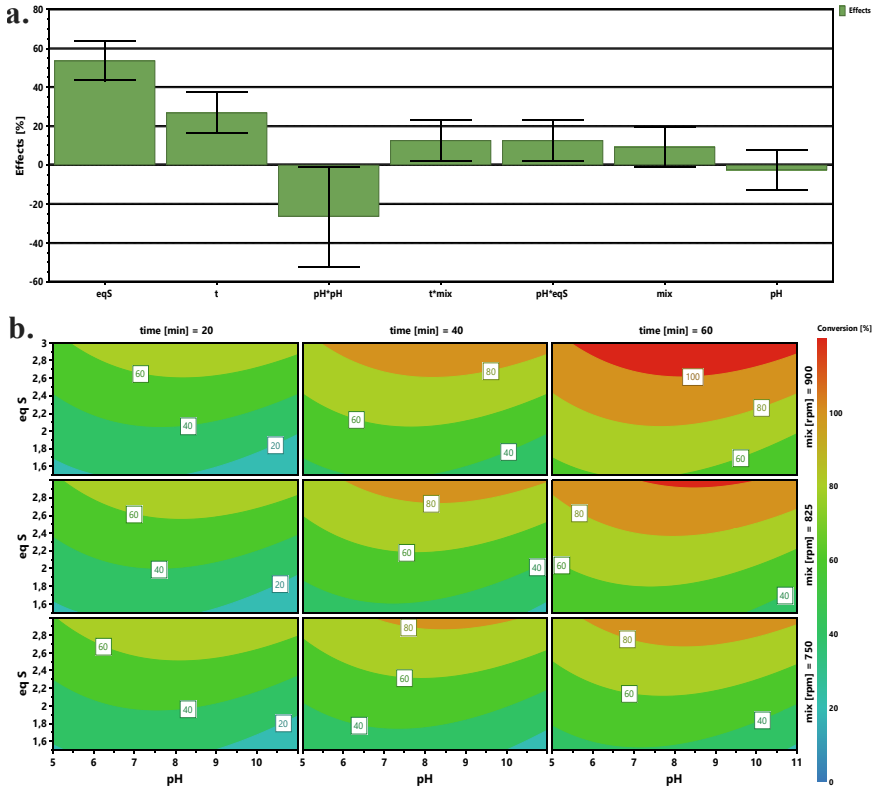

Figure 2.4. **a.** Plot of significant parameters influencing the formation of TCEP=S. **b.** Contour plot of the model developed here developed for the conversion into TCEP=S.

pH values between 7.5 and 9 (graphical determination), all under vigorous stirring.

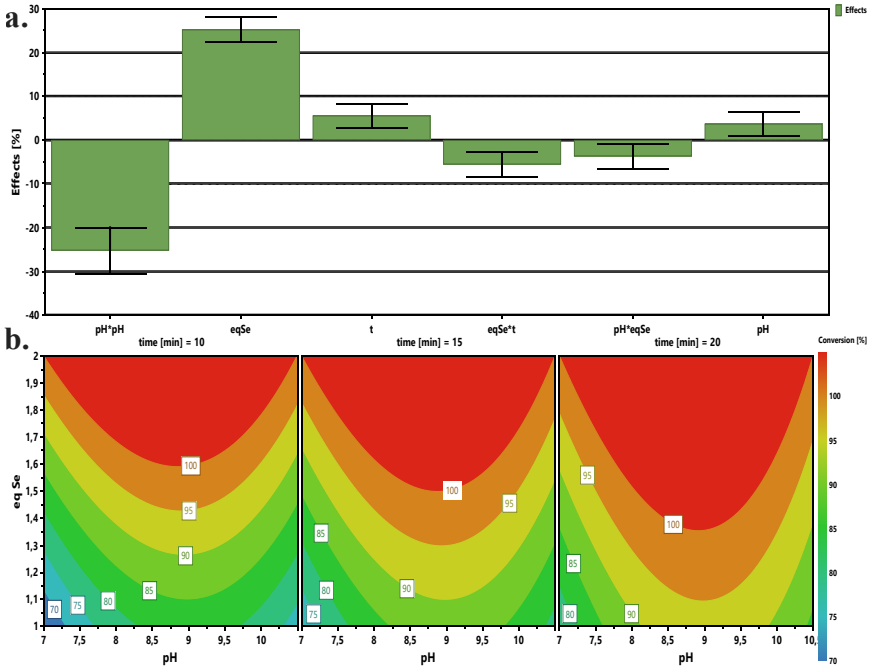

Figure 2.5. **a.** Plot of significant parameters influencing the formation of TCEP=Se. **b.** Contour plot of the model developed here developed for the conversion into TCEP=Se.

Similar behaviour can be drawn for the reduction of selenium with TCEP toward TCEP=Se, emphasizing a significant positive effect of the excess of Se_8, and a milder positive influence of the reaction time. For the preparation of TCEP=Se, the pH parameter exhibits a square term with an optimum between 8 and 9.5 (graphical determination). There are also two negative interaction parameters involving the excess Se_8 vs pH or reaction time (*i.e.*, pH.Eq and Eq.t, Figure 2.5a.). The model constructed for TCEP=Se predicts complete conversion within a short reaction time (10 min) and with a lower excess of selenium (up to 1.5 equiv.) (Figure 2.5b).

However, in the case of TCEP=Te, the optimization strategy needed adaptation. Firstly, as the protonated form of TCEP appeared incapable of reducing tellurium, TCEP in aqueous solution must be at a pH above 10 to react with Te_0. Secondly, due to the notably faster reduction rate for Te_0, the reaction with TCEP occurred within such a short time frame that ^{31}P-NMR reaction monitoring was not doable. Note that these preliminary observations were made by using 200 mesh tellurium. After several trials, -18 +60 mesh tellurium was preferred for easier monitoring. Instead, we selected *in situ* Raman spectroscopy (see Figure 2.6). This allowed for the assessment

of various parameters and their influence on the reaction initial rate (v_i), including the excess of tellurium, its granulometry and mixing efficiency.

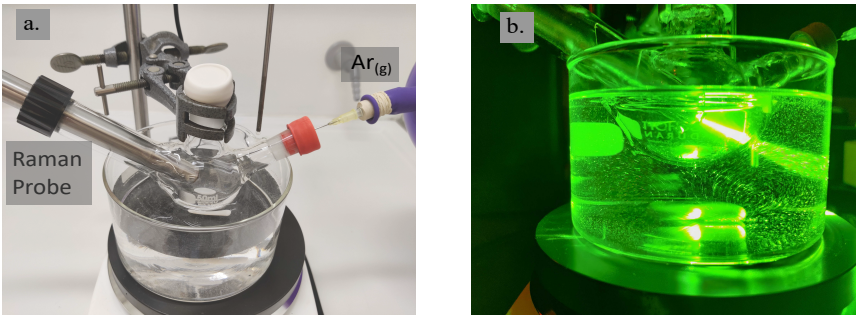

Figure 2.6. a. and b. Experimental setup with a modified three-necked bottomed flask allowing to insert an *in-line* Raman probe and flushing the flask with argon.

As illustrated in Figure 2.7 a, the mixing had only a minor effect on the reaction kinetics, with a mere 2.8% increase while transitioning from 500 to 750 rpm, which confirms the observation made on the effect diagram for TCEP=S formation. The excess of Te_8 had a positive effect on the reaction kinetics constant, accelerating it from 3.56 10^{-4} mol.L^{-1}.s^{-1} to 7.9 10^{-4} mol.L^{-1}.s^{-1} when the tellurium excess was increased (1.5 to 3 equiv.). In addition, the granulometry of tellurium had a profound impact on the reaction. When switching from -18+60 mesh to 200 mesh, *i.e.*, reducing the size of particles from 454.3 μm (equivalent diameter on volume) to 44 μm, the reaction proceeded 22.41 times faster (from 3.56 10^{-4} mol.L^{-1}.s^{-1} with particle sizes of 454.3 μm to 7.96 10^{-3} mol.L^{-1}.s^{-1} with particle sizes of 44 μm), as shown in Figure 2.7 b.

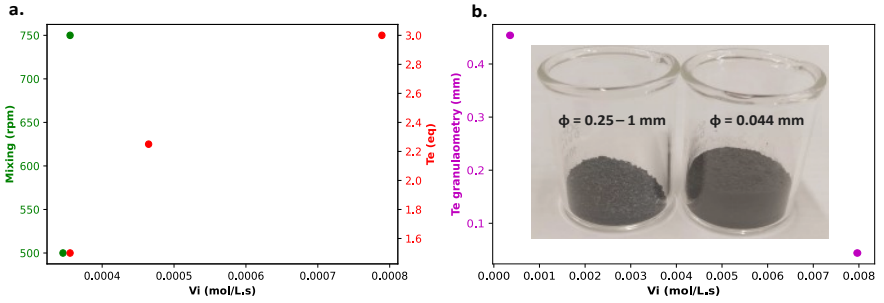

Figure 2.7. a. Influence of the mixing and tellurium excess on the initial reaction speed. **b.** Impact of the tellurium granulometry on the initial reaction speed.

To sum up the preliminary batch optimization, pH emerged as a critical factor for reaction rate, especially in the preparation of TCEP=Te. For sulfur and selenium, which exhibit quadratic behaviour, synthesis at the optimum pH, *i.e.* moderately basic, is also recommended. The quadratic behaviour of

the TCEP=S, Se formation is likely to be influenced by, at lower pH, the protonation rate of the TCEP and, at high pH, the formation of polymeric species. [20] Mixing effects were limited, and at speeds higher than 500 rpm, their influence became negligible. An excess of chalcogen had a positive impact on the preparation of all 3 compounds (TCEP=S, Se, Te). The effect of the granulometry, which was studied only for the preparation of TCEP=Te, clearly showed that smaller particles led to a drastic increase in kinetics, related to an increase in the surface area of the chalcogen. This is expected in a heterogeneous process where the rate-determining step involves homogeneous reagents (TCEP) and the chalcogen surface.

2.3.2.2 *In-situ* kinetics of chalcogens reduction by TCEP

Following preliminary optimization and multivariate analysis, a more refined kinetic study was conducted for the reduction of all chalcogens with TCEP. Prior to these experiments, a precise investigation of the optimum pH was conducted (Figure 2.22). These experiments aimed to determine the reaction mechanism, specific kinetics constants and apparent activation energies associated with the rate-limiting regime. Each substrate (TCEP=S, Se, Te) was subjected to the reaction at 30 °C, 40 °C and 50 °C, as well as 60 °C for Se and Te.

The reactions were monitored by in situ Raman spectroscopy following a protocol similar to Figure 2.6, with the time evolution of the Raman signal corresponding to the P=X (X=S, Se, Te) bond (P=Te: 376 cm^{-1}; P=Se: 428 cm^{-1}; P=S: 578 cm^{-1}). The results are plotted in Figure 2.8.

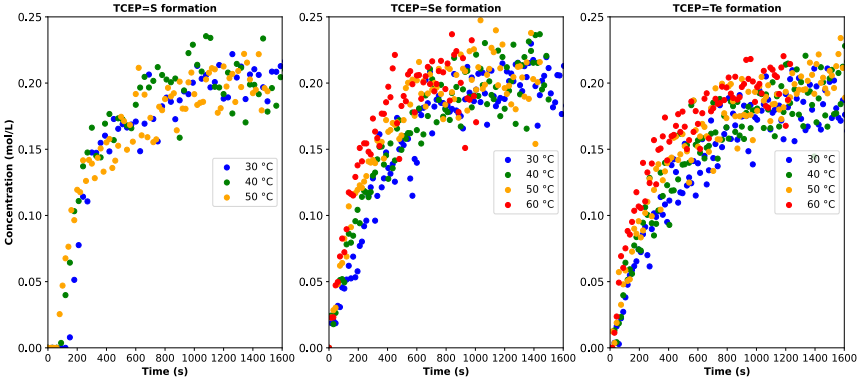

Figure 2.8. Crude data obtained during the kinetic monitoring, for each TCEP=X (X = S, Se, Te) derivative.

For each series, the temperature had a positive effect on the reaction kinetics. Similar trends were observed for the reduction of selenium and tellurium with TCEP: the reaction initiated rapidly and then slowed down

after reaching a concentration of 0.15 mol.L^{-1}. The reaction with S_8 followed a different pattern (Figures 2.24, 2.25). Initially, a complex, broad signal with characteristic peaks at 500 cm^{-1} and 825-870 cm^{-1} appeared, hypothesized to correspond to TCEP adsorbed on the surface of sulfur particles. This transient species eventually evolves into the expected product (TCEP=S).

The kinetic data were then used to establish the rate laws governing the preparation of TCEP=S, Se, Te. Various models were envisaged, accounting for the critical role of TCEP adsorption on the chalcogen surface (more details are provided in section 2.4.0.6). Despite their complexity, none of these models successfully fitted the kinetic data. Nonetheless, closer examination of the data indicated that the reaction slowed down more rapidly than predicted by the models. A plausible hypothesis to account for this deviation is a decrease in active site accessibility on the chalcogen's surface due to an increase in its porosity (Figure 2.9). This effect was integrated into the model as a decreasing exponential function (section 2.4.0.6).

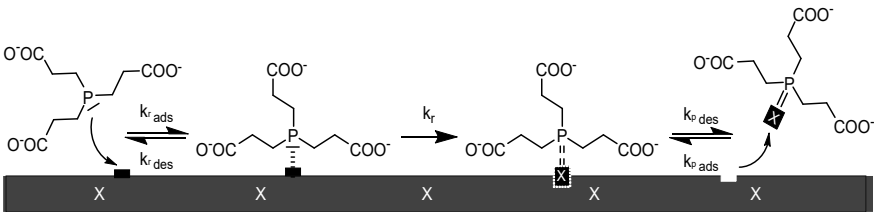

Figure 2.9. Hypothesized heterogeneous mechanism showing the interaction of TCEP on the surface of the elemental chalcogen.

Based on the hypothesized mechanism presented in figure 2.9, the equation 2.1 is presented to represent the chemical rate:

$$r(t) = k_r \frac{k_a C(t)}{1 + k_a C(t)} + f_{dea}(C(t)) \tag{2.1}$$

Where:

- $\mathbf{r(t)}$: Reaction rate [mol.L^{-1}.s^{-1}],
- $\mathbf{k_r}$: Reaction rate constant [mol.L^{-1}.s^{-1}],
- $\mathbf{k_a}$: Surface affinity constant [L.mol^{-1}],
- $\mathbf{C(t)}$: Concentration of TCEP [mol.L^{-1}],
- $\mathbf{f_{dea}(C(t))}$: Surface accessibility function [dimensionless].

The model in Equation 2.1 is composed of two term. The first term corresponds to a Langmuir-Hinshelwood-type mechanism describing the

interfacial reaction. The second term, f_{dea}, accounts for the progressive loss of accessible surface sites due to surface modification during the reaction.

Empirically, the surface accessibility function f_{dea} was determined as an exponential function of the TCEP concentration, as shown in Equation 2.2.

$$f_{dea}(C(t)) = \exp(-k_{dea}\, C(t)) \tag{2.2}$$

Where:

- $\mathbf{f_{dea}(C(t))}$: Surface accessibility function [dimensionless],
- $\mathbf{C(t)}$: Concentration of TCEP [mol.L^{-1}],
- $\mathbf{k_{dea}}$: Surface accessibility decay constant [L.mol^{-1}].

The Equation 1.1 being unsolvable by analytical methods, the equation 2.1 has been rearranged to take in account the surface accessibility function f_{dea}, yielding to the equation 2.3:

$$\frac{C(t)}{r(t)} = \frac{1}{k_r.k_a} + \frac{1}{k_r}.C(t) + e^{-k_{dea}.C(t)} \tag{2.3}$$

Where:

- $\mathbf{C(t)}$: Product concentration [mol.L^{-1}],
- $\mathbf{r(t)}$: Reaction rate [mol.L^{-1}.s^{-1}],
- $\mathbf{k_r}$: Reaction rate constant [mol.L^{-1}.s^{-1}],
- $\mathbf{k_a}$: Surface affinity constant [L.mol^{-1}],
- $\mathbf{k_{dea}}$: Deactivation constant of the chalcogen surface [L.mol^{-1}].

The revised kinetic model (equation 2.1) was effectively used to fit the experimental data using equation 2.3. With this approach, the kinetic constants were derived for the preparation of TCEP=S, Se, Te at 30 °C, 40 °C, 50 °C and 60 °C (the latter temperature was only considered for TCEP=Se, Te). These constants were next used to calculate the experimental activation energies for the rate-determining step of the 3 processes using Arrhenius' equation 2.4 (Figure 2.10).

$$\ln k_r = \ln A - \frac{E_a}{R} \cdot \frac{1}{T} \tag{2.4}$$

Where:

- $\mathbf{k_r}$: Reaction rate constant [mol.L^{-1}.s^{-1}],
- **A**: Pre-exponential factor [mol.L^{-1}.s^{-1}],
- $\mathbf{E_a}$: Activation energy [J.mol^{-1}],
- **R**: Gas constant [J.mol^{-1}.K^{-1}],
- **T**: Temperature [K].

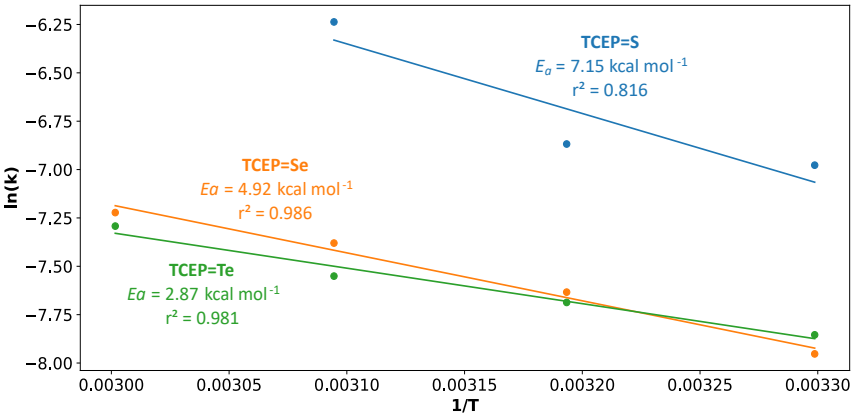

Figure 2.10. Experimental constant rates and Arrhenius fit for each TCEP=X derivative.

The values obtained for each species exhibited a periodic trend: TCEP=S (7.2 kcal.mol^{-1}) > TCEP=Se (4.9 kcal.mol^{-1}) > TCEP=Te (2.9 kcal.mol^{-1}). These observations align well with the ones collected during the batch optimization (full conversion was achieved faster with TCEP=Te > TCEP=Se > TCEP=S) and are consistent literature and with Hard and soft acids and bases (HSAB) considerations, where softer chalcogens exhibit lower activation barriers. [21]

2.3.2.3 Transposition in flow for the preparation of TCEP=X

Considering the compelling evidence that the reaction, proceeding via the adsorption of TCEP on the chalcogen particle surface, is dominated by surface accessibility, there are two potential options to enhance reaction kinetics: increasing the excess of chalcogen and/or reducing chalcogen particle size. These attributes can be effectively combined in a packed-bed flow configuration. Therefore, elemental chalcogen powder was considered as a packing material suitable for packed-bed tubular flow reactors. In this setup,

a feed solution of TCEP (0.2 M in water, pH = 10.7) is passed through the packed-bed column containing the elemental chalcogenides.

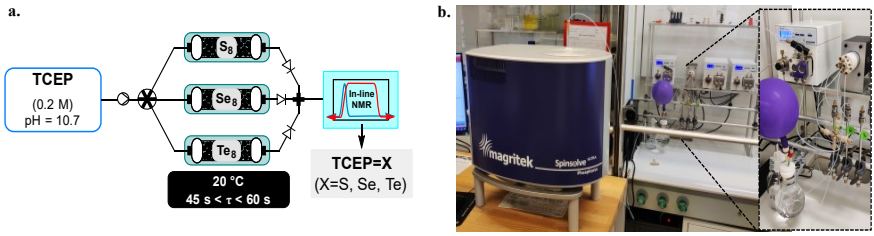

Figure 2.11. a. Simplified flow chart of the automated flow system featuring 3 packed-bed reactors (filled with sulfur, selenium, or tellurium) and operated in parallel. **b**. Photograph of the experimental device, emphasizing the *in-line* low field benchtop ^{31}P-NMR.

A versatile flow system was constructed, consisting of 3 columns (1/4" stainless steel, 150 mm length) operated in parallel, each filled with either sulfur, selenium, or tellurium, respectively (Figure 2.10 a, b). These 3 columns were connected upstream to a single feed solution of TCEP through an automated selection valve. The valve was remotely controlled to select the appropriate source of chalcogen, enabling on-demand preparation, at room temperature, of TCEP=S, TCEP=Se, and TCEP=Te. For each column, the porosity (ϵ) was estimated to be 0.287 (S_8), 0.098 (Se_8) and 0.434 (Te_8) (note that -18 +60 mesh tellurium was used), respectively. The downstream section of the flow setup featured a benchtop NMR operated in the ^{31}P-NMR mode to assess both productivity and stability (Figure 2.10 a, b).

For each chalcogen, a feed solution of TCEP (pH 10.7) was infused at flow rates ranging from 0.25 mL.min^{-1} to 2 mL.min^{-1}. Conversion and space-time yield (STY), (see section 6.1.5.1 for more details) were calculated to determine the productivity boundaries of the flow system. In the case of sulfur, full conversion to TCEP=S was maintained within the range of 0.25 mL.min^{-1} to 2 mL.min^{-1} (STY: 45.9 g.L^{-1}.min^{-1} with an estimated residence time of 0.354 min at 2 mL.min^{-1}). Similar results were observed for TCEP=Te (STY: 61.5 g.L^{-1}.min^{-1} and an estimated residence time of 0.534 min at 2 mL.min^{-1}).

For TCEP=Se, full conversion was observed up to 1 mL.min^{-1} (STY: 26.8 g.L^{-1}.min^{-1} and an estimated residence time of 0.242 min), as illustrated in Figure 2.12. These outcomes are particularly remarkable when compared to kinetic batch experiments, where full conversion required approximately 20, 23, and 26 min for sulfur, selenium, and tellurium, respectively. The substantial reduction in the time frame and the outstanding productivity metrics required to achieve full conversion emphasize the advantages of this flow setup for the reduction of chalcogens.

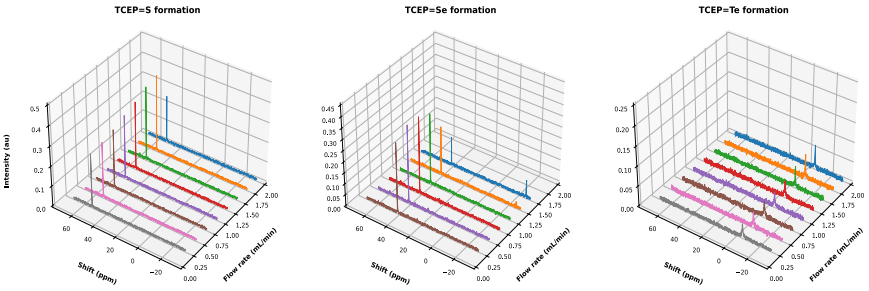

Figure 2.12. Reaction monitoring (^{31}P-NMR) for the production of TCEP=X (X=S, Se, Te), under various flow rate through the bed-packed reactor.

Continuous monitoring of TCEP=Te at a flow rate of 1.2 mL.min^{-1} was conducted and sustained full conversion for a total operation time of 200 min, notably in anticipation of scalability trials for CdTe QDs (see Section 6.1.5.2 and Figure 6.12).

To the best of the authors' knowledge, the in situ preparation of precursors upstream of QD synthesis has not yet been reported in the literature. A direct comparison with the current state of the art is therefore challenging.

One possible method for comparison is the STY, calculated without accounting the dead time between successive batch experiments. The estimated STY values for the batch formation of TCEP=S, TCEP=Se, and TCEP=Te are 2.82, 2.86, and 2.90 g.L^{-1}.min^{-1}, respectively.

Based on the estimated batch STY, the ratio STY_{micro}/STY_{batch} provides a useful metric to evaluate the improvement achieved through microfluidic transposition. The resulting values of 16.27, 9.35, and 21.14, highlight a significant intensification of the process.

In most of the studies reviewed in Section 1.7, the preliminary formation of the chalcogen precursor is not the primary focus and is rarely optimized. Consequently, STY values are generally not reported and are expected to remain close to the batch values estimated above (*e.g.*, close to 3 g.L^{-1}.min^{-1}).

2.3.2.4 Concatenation to downstream preparation of Quantum Dots

The direct concatenation of the upstream generator for TCEP=X with the downstream preparation of CdX significantly reduces the risk of precursor degradation and enhances the versatility of the flow setup 2.13. The aqueous protocol for CdX synthesis was adapted to accommodate our system, taking advantage of the distinctive features of the new chalcogenide precursor,

TCEP=X. Typically, these protocols involve a strongly basic solution (pH > 11) and cadmium mercaptopropionate Cd(3-MPA)$_2$ as cadmium precursor. [22]

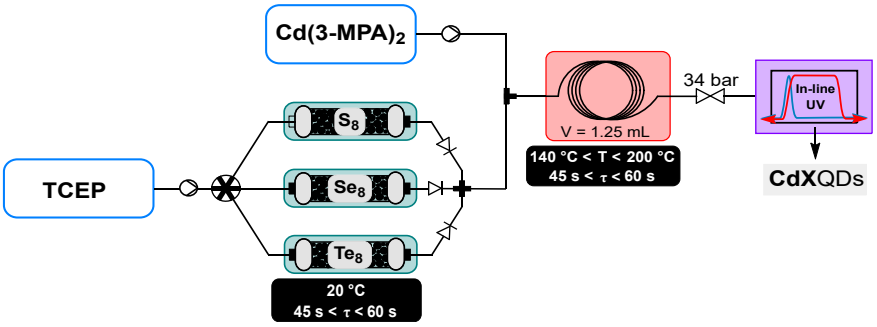

Figure 2.13. Simplified flow chart for the concatenated process towards CdS, CdSe and CdTe QDs.

In the proposed system, the TCEP=X generator (Figure 2.13) was inserted upstream of an additional static mixer. The latter allowed the stream of TCEP=X to be blended with a feed solution of Cd(3-MPA)$_2$. The resulting reaction mixture was then directed to a heated reaction coil for QD generation. The reactor effluent was thermally quenched and then connected to an *in-line* UV-VIS spectrometer for real-time reaction monitoring.

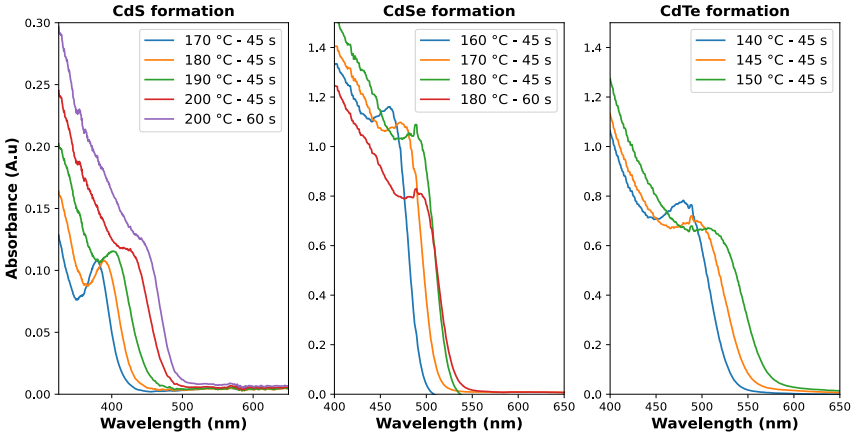

Figure 2.14. *In-line* monitoring with UV/Vis. (A.u. = Absorbance units), path length: CdS 0.5 mm, CdSe/Te: 10 mm

The results obtained during the synthesis are shown in Figure 2.14. Overall, these results demonstrate the effectiveness of fresh TCEP=X precursors as efficient chalcogenide carriers under aqueous conditions. They demonstrate the capability of TCEP=X to readily transfer chalcogen (X) to cadmium under relatively mild conditions. Furthermore, the findings highlight

that the reactivity of TCEP=X is significantly influenced by the nature of the chalcogen, establishing a reactivity hierarchy where softer chalcogens (TCEP=S < TCEP=Se < TCEP=Te) require lower process temperatures and shorter residence times.

2.3.2.5 Quantum Dots characterization

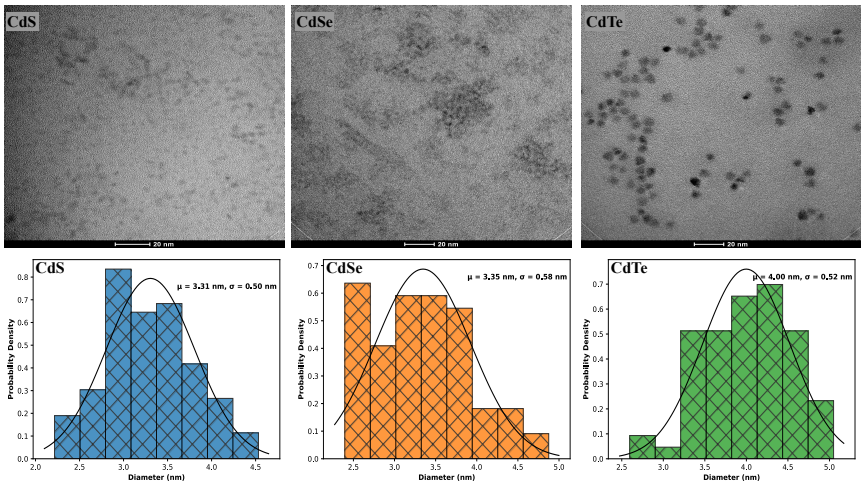

Figure 2.15. Characterizations of QDs after their production by High-resolution transmission electron microscopy (HRTEM) as well as their plot bar summarizing their size distribution.

HRTEM analyses were conducted to provide insights into the size and morphology of the QDs. The HRTEM images revealed that the particles exhibited a spherical morphology, with estimated particle sizes of 3.31 ± 0.50 nm for CdS, 3.35 ± 0.58 nm for CdSe, and 4.00± 0.52 nm for CdTe (Figure 2.15).

The normality of the size distribution shown in the second line of Figure 2.15 was estimated by means of a Shapiro-Wilk test, with the decision based on the resulting p-value. [23] For CdS (p-value = 0.666) and CdTe (p-value = 0.387), the distributions can be considered normal. In the case of CdSe, however, the p-value (0.053) is very close to the significance threshold and may be considered suspicious. From a physical point of view, this suggests that nucleation and growth coexist in the HRTEM sample, which deviates from the ideal LaMer mechanism.

Subsequently, powder X-ray diffraction (P-XRD) analyses were carried out on purified quantum dots, utilizing zero-background substrates. For all three samples (CdX, where X = S, Se, and Te), the XRD patterns matched those of reference samples, confirming the crystalline nature of the QDs (Figure 2.16).

These QDs exhibited a cubic crystal system. More details on the P-XRD tune cells are available in Figures 6.33, 6.35 and 6.37

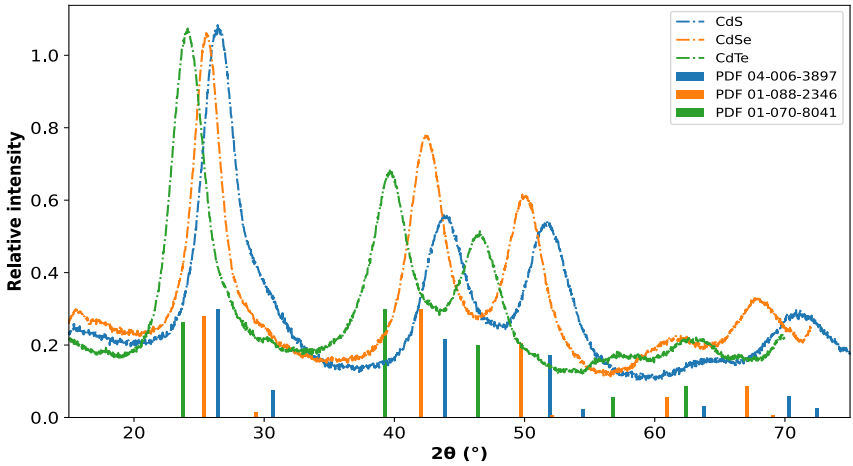

Figure 2.16. Characterizations of QDs after their production by Powder X-ray Diffraction analysis on QDs

2.3.2.6 Scalability trials with CdTe QDs

The synthesis of CdTe QDs required milder conditions, with temperatures ranging from 140 °C to 150 °C, and a similar residence time (45 s). The trends observed for CdTe paralleled those observed for CdSe: higher process temperatures led to a decrease in concentration and an increase in size. The new process offers several advantages over conventional methods. It allows for lower operating temperatures and the possibility to seamlessly integrate the precursor preparation with the QD synthesis within a mesofluidic synthesis. Specifically, the experimental conditions for the CdTe QDs (temperature 140-150 °C, residence time 42-52 s and pressure of 7 bar) are well suited for scalability trials in a mesofluidic reactor .

The mesofluidic setup is depicted in Figure 2.17 a,b and consists of 2 concatenated reactors. The first reactor is dedicated to producing TCEP=Te, building upon the packed-bed methodology. The second reactor is a commercial mesofluidic Corning® Advanced-Flow™ G1 SiC Reactor equipped with 6 Silicon Carbide fluidic modules connected in series (60 mL total internal volume) and concerns the formation of the CdTe QDs. Downstream operations include a cooling loop (thermal quench), a back pressure regulator, an *in-line* UV/Vis flow cell (5 mm optical pathway) and *off-line* ultrafiltration.

During the scale-up process using our fully integrated and continuous process, the total flow rate ranged from 70 to 86.2 mL.min^{-1}. Notably, the

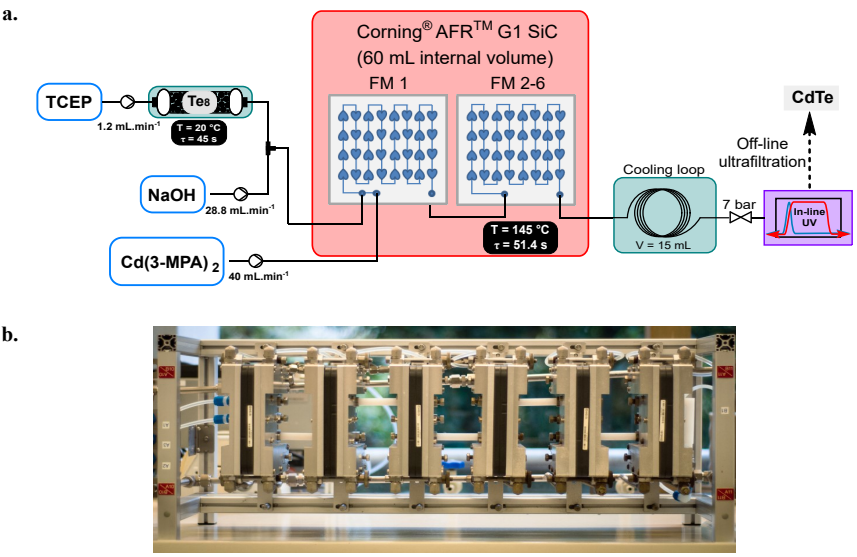

Figure 2.17. **a.** Simplified flow chart of the mesofluidic setup used for the scalability trials toward CdTe. **b.** Photograph of the experimental setup, featuring a Corning® Advanced-Flow Reactor™G1 SiC (60 mL of internal volume).

particles produced remained stable for at least five months, rendering them suitable for a wide range of industrial applications. [24] As the use of high flow rates comes inherently with an increase in size dispersion, a purification method was sought to keep the benefits of scale-up. Ultrafiltration of the sample collected downstream of the fluidic module was efficiently carried out on the CdTe QDs. The combination of two filters with various pore sizes (10 kDa and 30 kDa) reduced efficiently the width of the emission peak related to polydisperse QDs (Section 6.1.5.4). This method is therefore very convenient and ensures high quality for the samples collected (Figure 2.18).

2.3.3 Conclusions

This study introduces a novel water-soluble chalcogen vehicle which can be successfully transferred to a cadmium source, resulting in the formation of CdX (X = S, Se, Te) QDs in water. The preparation of TCEP=X (X = S, Se, Te) was optimized, with a focus on the influence of factors such as pH, chalcogen excess, mixing efficiency, and reagent granulometry, using a DoE approach. Following this optimization, in situ monitoring of the reaction was carried out at various temperatures using in-situ Raman spectroscopy. The kinetic data generated allowed for real-time observation of the formation of TCEP=X species and the identification of the reaction mechanism, which occurs at the surface of the chalcogen particles.

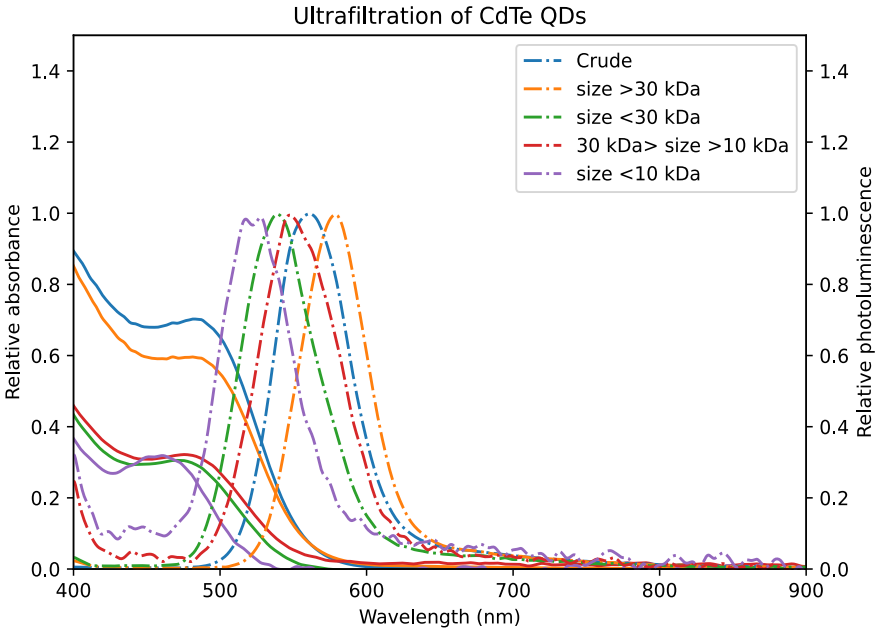

Figure 2.18. Comparison of samples prior and after ultrafiltration.

Over time, the reaction rate decreased due to surface degradation. Based on these observations, the process was successfully transposed in flow conditions using a packed-bed approach. Columns were filled with elemental chalcogens (S, Se, Te) and were operated in parallel for the on-demand production of the desired TCEP=X (X = S, Se, Te) precursors from the same feed of TCEP. Such an innovative approach achieved impressive productivity levels and was eventually amenable for pilot scale production. Following the successful transposition of precursor generation into a continuous flow system, this step was concatenated with the preparation of CdX (X = S, Se, Te) QDs. The resulting nanoparticles were characterized using HRTEM and P-XRD, revealing nanosized spherical shapes with a cubic crystal lattice structure. The entire process was transposed to pilot scale in a mesofluidic reactor and demonstrated for the production of CdTe QDs. The pilot scale setup produced up to 82.6 mL.min^{-1} of stable (>5 months) CdTe QDs. Ultrafiltration was successfully applied to minimize dispersity related to high flow rates. Such unprecedented processes under scalable flow conditions open new avenues for accessing aqueous QDs.

2.4 Complementary information

2.4.0.1 Stability study for TCEP=Te

The experimental details are available in Section 4.4.2. The samples were analyzed by 31P-NMR (162 MHz) and exhibited two peaks at δ = 58.7 ppm (TCEP=O) and δ = -4.88 ppm (TCEP=Te) after quantitative conversion of TCEP (δ = -26.27 ppm) with tellurium (Figure 2.19).

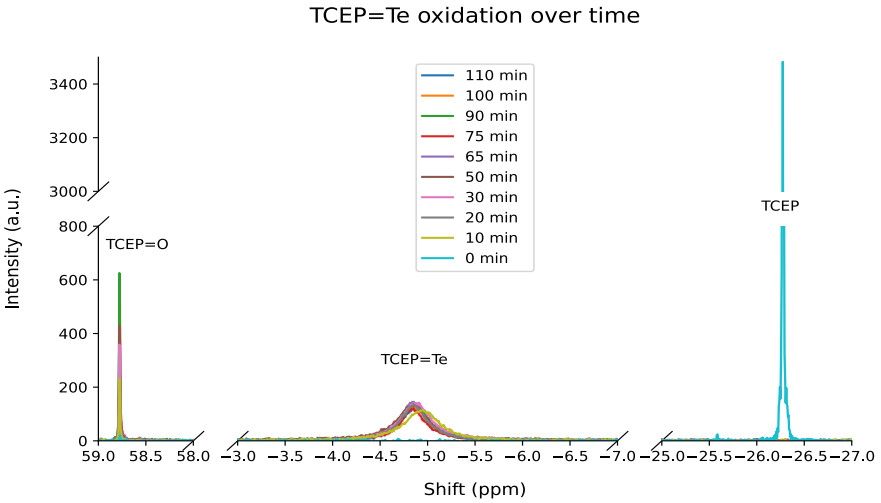

Figure 2.19. Crude results of TCEP=Te degradation (^{31}P-NMR, 162 MHz).

The ^{31}P-NMR peaks for TCEP=O and TCEP=Te were monitored and integrated over time, as depicted in Figure 2.20. As the conversion of TCEP=Te increased, the appearance of a layer of Te_0 was noticed.

The increase of TCEP=O over ~2 h emphasized the critical importance of degassing and maintaining solutions and working under argon to protect the integrity of TCEP=X (X=S, Se, Te).

2.4.0.2 Determination of the optimum pH

Figure 2.21 was obtained upon stacking the graphs from the pH optimization of TCEP=S, Se (section 1) and the deprotonation rate of the TCEP. An optimum pH appeared at 10.7, mostly due to TCEP=S formation's limitations.

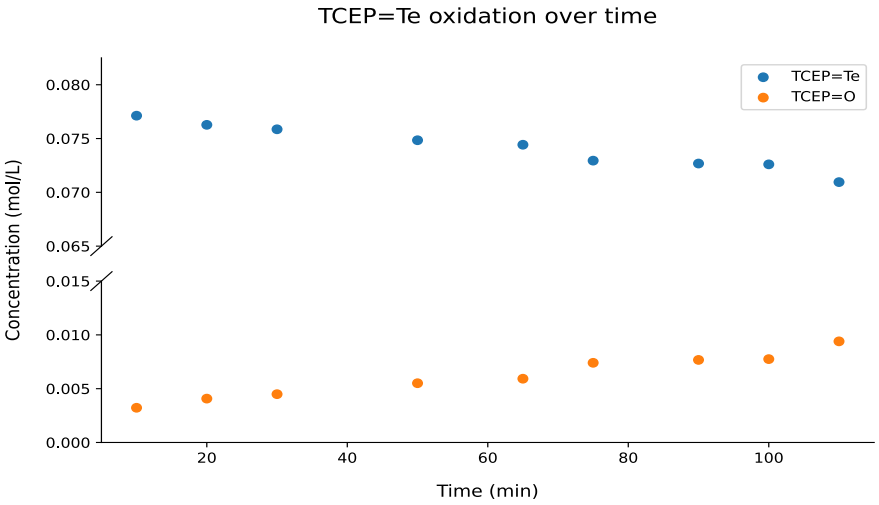

Figure 2.20. Oxidation rate of TCEP=Te towards TCEP=O

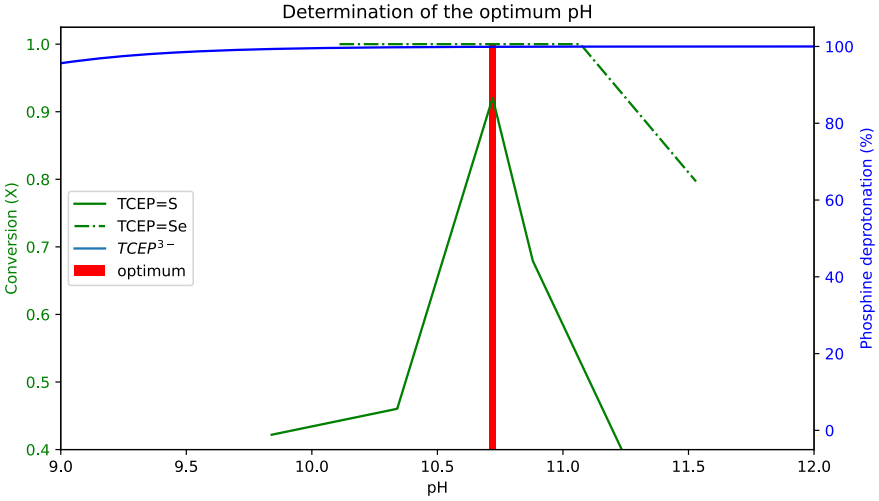

Figure 2.21. pH optimum for TCEP=X (X=S, Se, Te) formation

2.4.0.3 Raman monitoring for the formation of TCEP=S

The formation of TCEP=S was monitored in batch through Raman spectroscopy. The raw data were treated with a 6^{th} order polynomial Savitsky-Golay baseline correction and normalization of the intensity (based on the signal of water, assumed to remain constant, from 1635 cm^{-1} to 1655 cm^{-1}). Experimental data were then concatenated in a 3D matrix and plotted as a heatmap (Figure 2.22). From Figure 2.22, it became clear that 4 signals were evolving during the experiment at 875 cm^{-1} and 825 cm^{-1} (both signals seem to be related to an intermediate hypothesized as the adsorbed form TCEP on the sulfur surface) and 657 cm^{-1} (associated with the P-C bound, and thus the disappearance of TCEP) and 578 cm^{-1} (associated with the P=S bond and thus the appearance of TCEP=S).

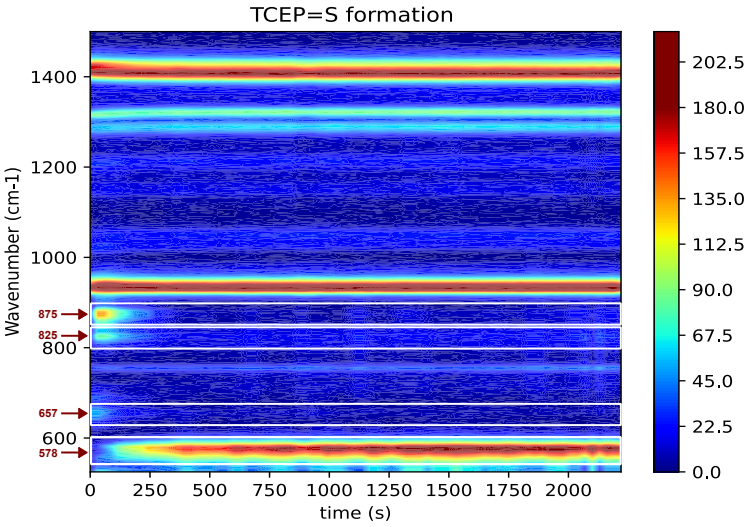

Figure 2.22. Heatmap for the formation of TCEP=S at 40 °C

Based on these observations, the intensity profile was extracted at 875 cm^{-1}, 657 cm^{-1} and 578 cm^{-1} (the intensities are obtained as the average on the 3 points closest to the maximum of height of the band). Then, based on the mass balance, the intensities are converted into a concentration profile (Figure 2.23).

2.4.0.4 Raman monitoring for the formation of TCEP=Se

The formation of TCEP=Se was monitored in batch through Raman spectroscopy. The raw data were treated with a 6^{th} order polynomial Savitsky-Golay baseline correction and normalization of the intensity (based on the signal of water, assumed to remain constant, from 1635 cm^{-1} to 1655 cm^{-1}). Experimental data were then concatenated in a 3D matrix and plotted

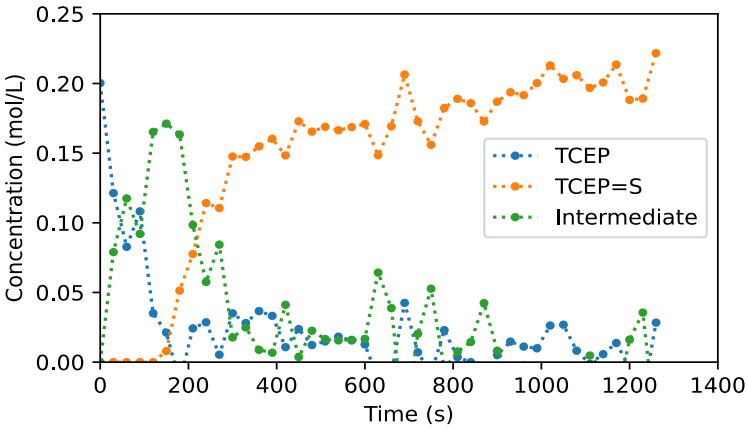

Figure 2.23. Concentration profiles for the formation of TCEP=S at 40 °C

as a heatmap (Figure 2.24). From Figure 2.24, it became clear that 3 signals were evolving during the experiment at 653 cm^{-1} (associated with the P-C bond, and thus the disappearance of TCEP) and at 428 cm^{-1} and 455 cm^{-1} (associated with the P=Se bond and thus the appearance of TCEP=Se).

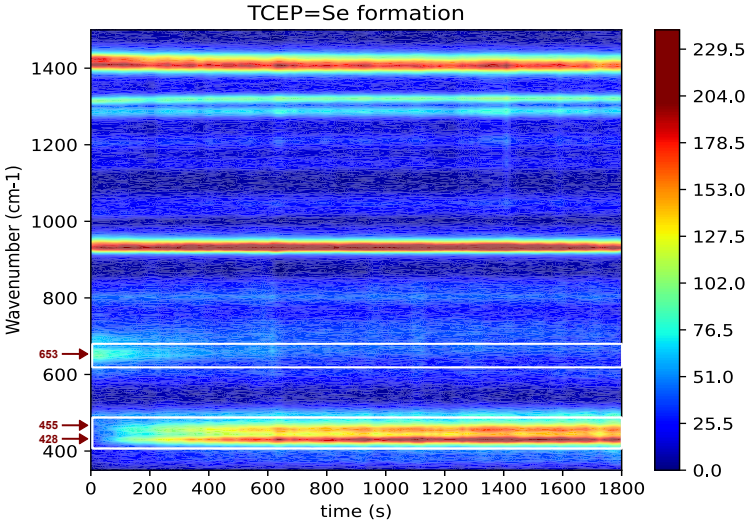

Figure 2.24. Heatmap for the formation of TCEP=Se at 40 °C

Based on these observations, the intensity profile was extracted at 653 cm^{-1} and 428 cm^{-1} (average on the 3 points closest to the maximum). Then, based on the mass balance, the intensities are converted into a concentration profile (Figure 2.25).

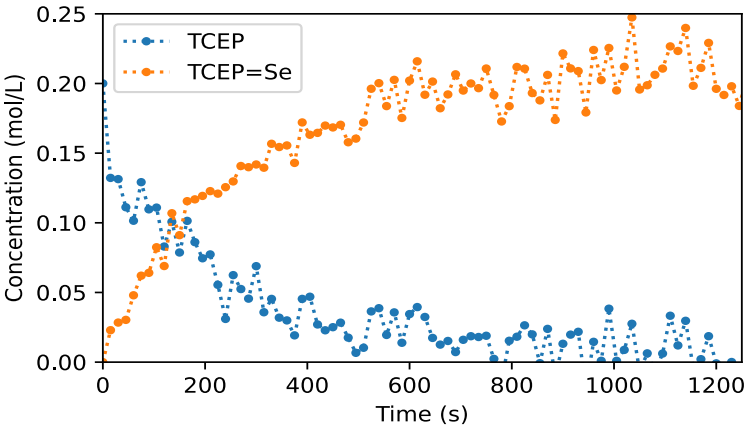

Figure 2.25. Concentration profiles for the formation of TCEP=Se at 40 °C

2.4.0.5 Raman monitoring for the formation of TCEP=Te

The formation of TCEP=Te was monitored in batch through Raman spectroscopy. The raw data were treated with a 6^{th} order polynomial Savitsky-Golay baseline correction and normalization of the intensity (based on the signal of water, assumed to remain constant, from 1635 cm^{-1} to 1655 cm^{-1}). Experimental data were then concatenated in a 3D matrix and plotted as a heatmap (Figure 2.26). From Figure 2.26, it became clear that 5 signals were evolving during the experiment at 494 cm^{-1} and 715 cm^{-1} (matrix effect, probably due to tellurium dioxide, [25]) 649 cm^{-1} (disappearance of the TCEP) and at 376 cm^{-1} and 418 cm^{-1} (associated with the P=Te bond and thus the appearance of TCEP=Te).

Based on these observations, the intensity profile was extracted at 649 cm^{-1} and 376 cm^{-1} (average on the 3 points closest to the maximum). Then, based on the mass balance, the intensities are converted into a concentration profile (Figure 2.26).

2.4.0.6 Establishment of a kinetic model

Three models were originally developed to fit the experimental data. For the discussion of the models, the following assumptions are made: (a) the reaction occurs at the interface between the chalcogen and the aqueous liquid phase when a phosphine molecule is adsorbed on the surface; and (b) the adsorption constant (k_{ads}) and the desorption constant (k_{des}) of TCEP are far more important than the constant rate (k_r), see figure 2.28.

With the previous assumptions, the general kinetic equation is:

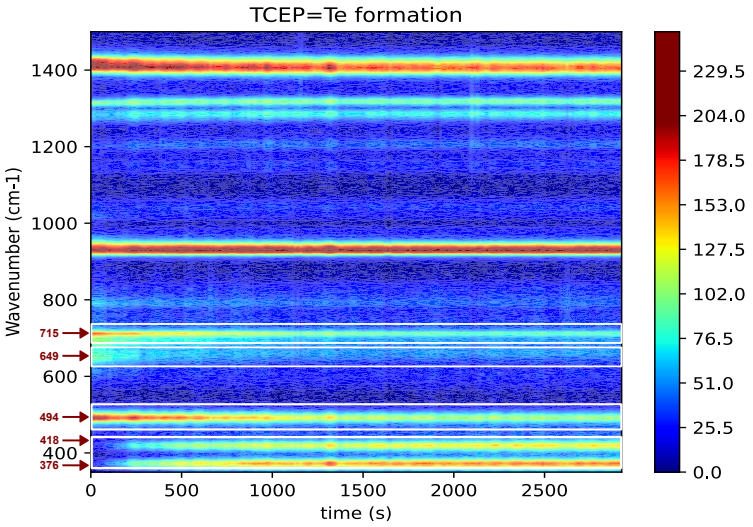

Figure 2.26. Heatmap for the formation of TCEP=Te at 40 °C

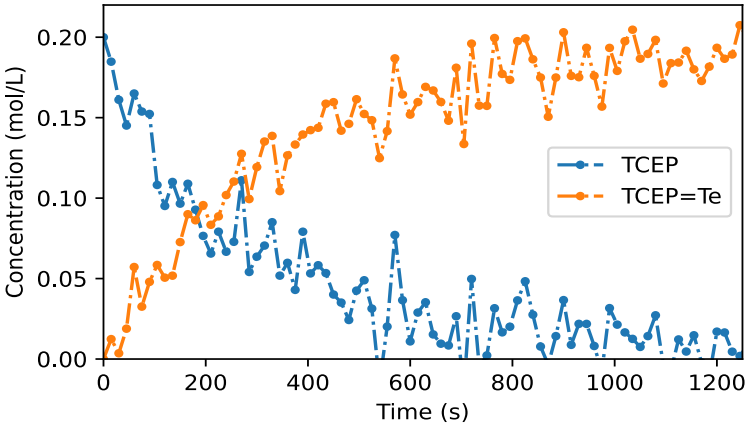

Figure 2.27. Concentration profiles for the formation of TCEP=Te at 40 °C

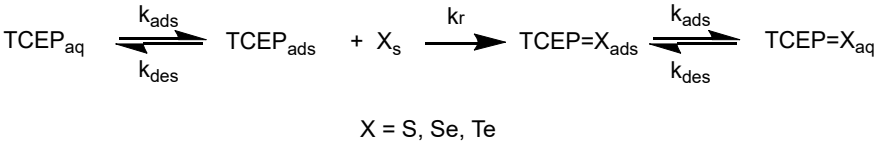

Figure 2.28. Fundamental step of TCEP=X formation

$$r(t) = -k_r.\theta_{TCEP}(t).\theta_x(t) \tag{2.5}$$

Where:

- $\mathbf{r(t)}$: Reaction rate [mol.L^{-1}.s^{-1}],
- $\mathbf{k_r}$: Reaction rate constant [variable],
- $\boldsymbol{\theta_{TCEP}(t)}$: Covering rate of TCEP [dimensionless],
- $\boldsymbol{\theta_x(t)}$: Covering rate of the chalcogen [dimensionless].

To solve the equation 2.5, three scenarios have been hypothesized:

1. In this scenario, since the powder is composed by the chalcogen, the assumption is made that the covering rate of chalcogen $\theta_x = 1$. Second assumption, the phosphine is adsorbed on the surface according to a Langmuir Isotherm. The kinetic equation then becomes:

$$r(t) = -k_r.\frac{k_a.C(t)}{1 + k_a.C(t)} \tag{2.6}$$

   Where:

   - $\mathbf{r(t)}$: Reaction rate [mol.L^{-1}.s^{-1}],
   - $\mathbf{k_r}$: Reaction rate constant [mol.L^{-1}.s^{-1}],
   - $\mathbf{k_a}$: Affinity constant of TCEP for the chalcogen surface [L.mol^{-1},
   - $\mathbf{C(t)}$: TCEP concentration [mol.L^{-1}].

2. The surface of the chalcogen is still saturated, but all sites are not equivalent. In this case, the hypothesis that $\theta_x = 1$ is not met, expressing the non-homogeneity of the sites on the surface. Here again, the assumption is made that the TCEP is adsorbed following a Langmuir Isotherm. Accordingly, the kinetic equation becomes as follows:

$$r(t) = -k_r.\frac{k_x.k_{TCEP}.C_x(t).C_{TCEP}(t)}{(1 + k_x.C_x(t) + k_{TCEP}.C_{TCEP}(t))^2} \tag{2.7}$$

   Where:

   - $\mathbf{r(t)}$: Reaction rate [mol.L^{-1}.s^{-1}],
   - $\mathbf{k_r}$: Reaction rate constant [mol.L^{-1}.s^{-1}],
   - $\mathbf{k_a}$: Affinity constant of TCEP for the chalcogen surface [L.mol^{-1}],

- **C(t)**: TCEP concentration [mol.L^{-1}].

The equation 2.7 can be rewrote as follow:

$$r(t) = -\frac{k_1 C_{TCEP}(t)}{(k_2 + k_3.C_{TCEP}(t))^2} \tag{2.8}$$

Where:

- **r(t)**: Reaction rate [mol.L^{-1}.s^{-1}],
- $\mathbf{k_1}$: $k_r \cdot k_x \cdot k_{TCEP} \cdot C_x(t)$ [variable],
- $\mathbf{k_2}$: $1 + k_x \cdot C_x(t)$ [dimensionless],
- $\mathbf{k_3}$: k_{TCEP} [variable].

3. In this scenario, the founding hypothesis is that the covering rate of chalcogen $\theta_x = 1$. But in this case, the phosphine adsorbs according to a Brunauer, Emmett and Teller theory (BET) isotherm, which leads to the following equation [26]:

$$r(t) = -k_r.\frac{k_s.C(t)}{(1 - k_l.C(t)).(1 - k_l.C(t) + k_s.C(t))} \tag{2.9}$$

Where:

- **r(t)**: Reaction rate [mol.L^{-1}.s^{-1}],
- $\mathbf{k_r}$: Reaction rate constant [variable],
- $\mathbf{k_s}$: Affinity constant of the first layer of TCEP adsorbed on the chalcogen [variable],
- $\mathbf{k_l}$: Affinity constant of the upper layers of TCEP [variable].

To efficiently segregate these three models, decision was made to compare them under the form $\frac{C_{TCEP}}{r(t)}$. Indeed, under this form, equation 2.6 becomes a straight line (equation 2.10, equation 2.8 becomes a parabola with all coefficients of the same sign (equation 2.11) and equation 2.9 becomes a parabola with variable sign coefficients (equation 2.12). These equations are summarized below:

$$\frac{C(t)}{r(t)} = -\frac{1}{k_r.k_a} - \frac{1}{k_r} - C(t) \tag{2.10}$$

$$\frac{C(t)}{r(t)} = -\frac{k_2^2}{k_1} - \frac{2.k_2.k_3}{k_1}.C(t) - \frac{k_3^2}{k_1}.C(t)^2 \tag{2.11}$$

$$\frac{C(t)}{r(t)} = -\frac{1}{k_r.k_s} + \frac{2.k_l - k_s}{k_r.k_s}.C(t) - \frac{k_l^2 - k_l.k_s}{k_r.k_s}.C(t)^2 \qquad (2.12)$$

Based on these assumptions, the expressions of $\frac{C(t)}{d(C(t))}$ f$(C(t))$ were plotted. The first observation is that the values of $\frac{C(t)}{d(C(t))}$ tend quickly towards a vertical asymptote. The first attempts to fit all the data with the three models failed. At best, if the fit is limited to lower conversion values *i.e.*, C $<$ 0.1 mol/L, the early stage of the reaction can be fitted with a relative success 2.29.

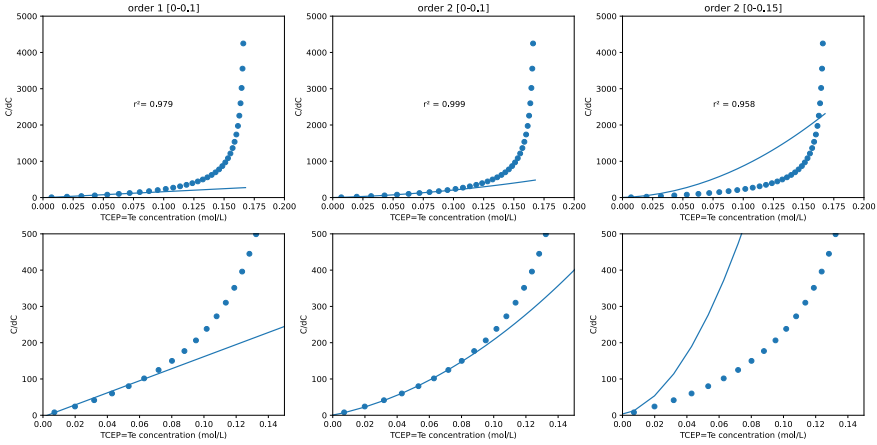

Figure 2.29. Trials to fit the $\frac{C(t)}{d(C(t))}$ f$(C(t))$ with first and second degree polynomials

The first row shows $\frac{C(t)}{d(C(t))}$ up to 5000, while the second row is limited to 500 to emphasize the fit quality in the early stages of the reaction. Generally speaking, the second-order polynomial fit (second and third columns) provides a better fit quality with a higher R^2. The first-order fit (first column) only fits a much earlier stage for the reaction.

With such poor fit quality, it became apparent that none of these models can explain the kinetics experimental data. These models work at best for the early stages of the experiments, then deviate significantly from the theoretical model. Such a deviation clearly emphasizes that the experimental kinetics slow down faster than what is predicted by all three models.

To take this observation into account, we hypothesized that surface deactivation was involved. Since deactivation is impossible strictly speaking with a reactive solid, it seemed more coherent to explain this reaction rate decrease with a decreasing surface accessibility. The latter probably arises because of an increase in surface roughness. Therefore, a decreasing exponential contribution was empirically added for establishing a new model 2.30.

$$r(t) = -k_r.\frac{k_a.C(t)}{1+k_a.C(t)} \qquad r(t) = -k_r.\frac{k_a.C(t)}{1+k_a.C(t)} - e^{-k_{dea}.C(t)}$$

Available sites f(time)

Langmuir adsoprtion
$\theta x = 1$

$$\frac{C(t)}{r(t)} = -\frac{1}{k_r.k_a} - \frac{1}{k_r} - C(t) \qquad \frac{C(t)}{r(t)} = -\frac{1}{k_r.k_a} - \frac{1}{k_r} - C(t) + e^{k_{dea}.C(t)}$$

Figure 2.30. Modification of a first-order kinetic with a decreasing surface availability

The experimental kinetics data were fitted with the revised model, as illustrated in Figure 2.31, with a significant improvement. The revised models cannot explain the decreasing rate for the late stages of the reaction but provided excellent regressions ($r^2 > 0.999$) up to 0.15 mol.L^{-1} (X = 0.75)

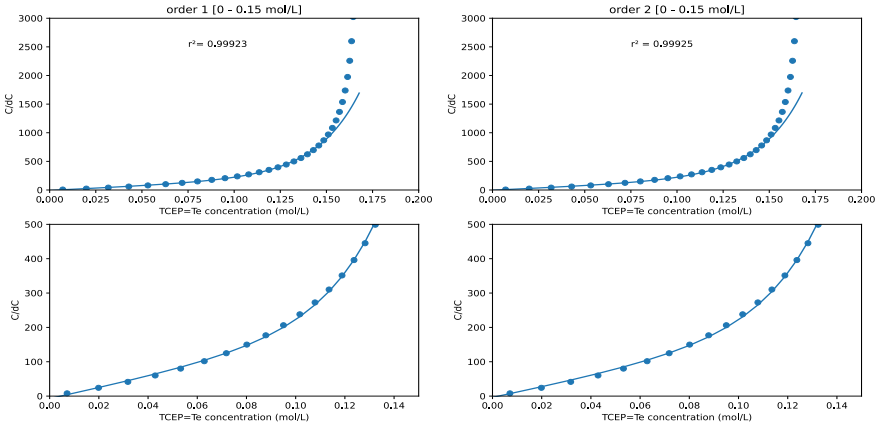

Figure 2.31. Modification of a first-order kinetic with a decreasing surface availability

The merits of the fits for 1st and 2nd order being very close to each other, we decided to fit all the experimental kinetics with the modified first-order law (equation 2.13).

$$\frac{C(t)}{r(t)} = -\frac{1}{k_r.k_a} - \frac{1}{k_r}.C(t) + e^{k_{dea}.C(t)} \tag{2.13}$$

Where:

- $\mathbf{r(t)}$: Reaction rate [mol.L^{-1}.s^{-1}],
- $\mathbf{k_r}$: Reaction rate constant [variable],
- $\mathbf{k_a}$: Affinity constant of TCEP [variable],

- $\mathbf{k_{dea}}$: Deactivation constant of the chalcogen surface [s^{-1}].

From there, k_r was extracted at each temperature and led to the experimental determination of the corresponding activation barriers for the formation of TCEP=X (X= S, Se, Te).

2.4.0.7 CdTe purification

1. Microfluidic samples

   Our TCEP-based process already produced CdTe QDs with interesting fluorescence properties (Figure 6.36). However, their emission peak was still rather broad and contained some surface defects. In order to improve their quality, a straightforward downstream purification step was developed. Downstream purification consists in a centrifugal filtration performed with two pore sizes (10 kDa (516-0230P) and 30 kDa (516-0232P), both purchased from VWR). 500 μL of crude sample were placed on the top of the filter membrane in an Eppendorf vial. The vials were then centrifugated at 10,000 rpm for 5 min. The filtrate was collected and the collected solid was resuspended with 500 μL of milliQ water. The corresponding post-treatment samples are illustrated in figure

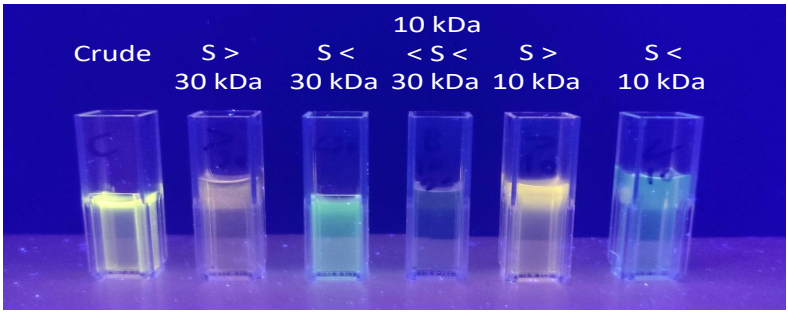

Figure 2.32. Picture under UV 365 nm light source of the purified samples.

The influence of the purification is already obvious under UV light: while the crude sample was yellow, filtration at 30 kDa produced green and brown samples and the filtration at 10 kDa gave orange and green samples. A combination of particles passing through the 30 kDa media but retained by the 10 kDa gave a yellowish sample.

These samples were then analyzed by fluorimetry and the normalized results are shown in figure

The filtration over 10 kDa allows to efficiently segregate the smaller particles from the crude. The membrane of 30 kDa split almost perfectly

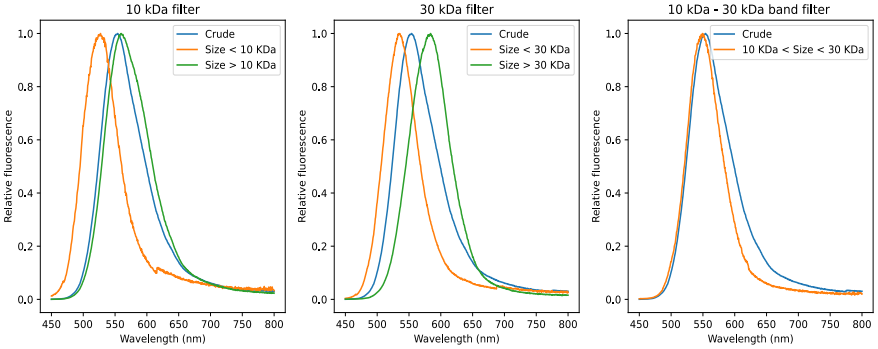

Figure 2.33. Left: filtration on the 10 kDa filter, middle: filtration over 30 kDa and on the right, sample after double filtration (30-10 kDa).

the crude in two halves. Finally, the use of the combined filters to obtain a bandpass-like filter reduces the emission band and further improves the optical purity of the CdTe QDs.

2. Mesofluidic samples

   According to the same protocol described in section 2.4.0.7, five samples, obtained from the scale up synthesis, were purified by ultra filtration on various pore size membranes (10 kDa or 30 kDa). The results of these purifications are shown in Figure 2.34, both the impact of peak position and FWHM are summarized.

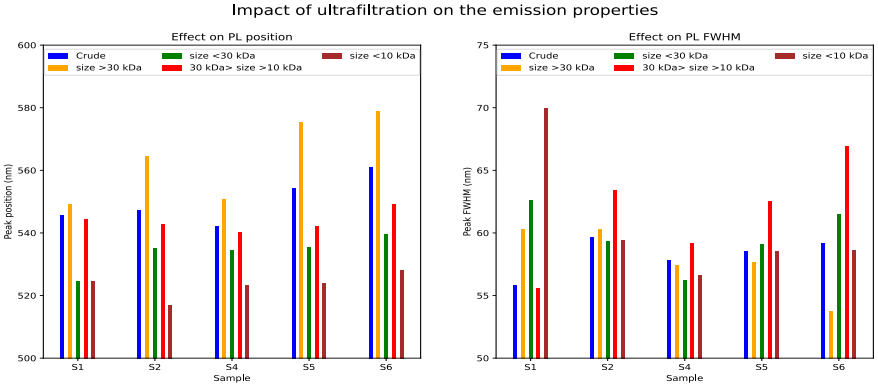

Figure 2.34. Evolution of the emission peak position (left) and of the full width half maximum (FWHM) of the samples produced during the scale up, highlightening the various phases isolated during the filtration steps.

Some observations can be made from these plots: the filtration of the crude mixture over the 30 kDa membrane splits the QDs population into two subsets with their peak position shifted below (filtrate) and above (filter cake) of the crude mixture. The same observation can be

done when the 30 kDa filtrate is passed through the 10 kDa media. About the FWHM, it seems there is no systematic pattern.

References

[1] Pauline Bianchi et al. "Metal-free synthesis of an estetrol key intermediate under intensified continuous flow conditions". In: *Reaction Chemistry and Engineering* 8 (7 2023), pp. 1565–1575. ISSN: 20589883. DOI: 10.1039/d3re00051f. URL: http://dx.doi.org/10.1039/D3RE00051F.

[2] Jean Christophe M. Monbaliu and Julien Legros. "Will the next generation of chemical plants be in miniaturized flow reactors?" In: *Lab on a Chip* 23 (5 2022), pp. 1349–1357. ISSN: 14730189. DOI: 10.1039/d2lc00796g.

[3] Romain Morodo et al. "Accelerating the end-to-end production of cyclic phosphate monomers with modular flow chemistry". In: *Chemical Science* 13 (36 2022), pp. 10699–10706. ISSN: 20416539. DOI: 10.1039/d2sc02891c.

[4] Diana V. Silva-Brenes et al. "Out-smarting smart drug modafinil through flow chemistry†". In: *Green Chemistry* 24 (5 2022), pp. 2094–2103. ISSN: 14639270. DOI: 10.1039/d1gc04666g.

[5] Yuesu Chen, Sébastien Renson, and Jean Christophe M. Monbaliu. "On Demand Flow Platform for the Generation of Anhydrous Dinitrogen Trioxide and Its Further Use in N-Nitrosative Reactions". In: *Angewandte Chemie - International Edition* 61 (41 2022), e202210146. ISSN: 15213773. DOI: 10.1002/anie.202210146.

[6] Pauline Bianchi, Guillaume Petit, and Jean Christophe M. Monbaliu. "Scalable and robust photochemical flow process towards small spherical gold nanoparticles". In: *Reaction Chemistry and Engineering* 5 (7 2020), pp. 1224–1236. ISSN: 20589883. DOI: 10.1039/d0re00092b.

[7] John A Burns et al. "Selective Reduction of Disulfides by Tris(2-carboxyethy1)phosphine". In: *J. Org. Chem* 56 (8 1991), pp. 2648–2650. DOI: 10.1021/jo00008a014.

[8] Nathalie Ollivier et al. "Accelerated microfluidic native chemical ligation at difficult amino acids toward cyclic peptides". In: *Nature Communications* 9 (1 2018), pp. 1–12. ISSN: 20411723. DOI: 10.1038/s41467-018-05264-8. URL: http://dx.doi.org/10.1038/s41467-018-05264-8.

[9] Vangelis Agouridas et al. "Native Chemical Ligation and Extended Methods: Mechanisms, Catalysis, Scope, and Limitations". In: *Chemical Reviews* 119 (12 2019), pp. 7328–7443. ISSN: 15206890. DOI: 10.1021/acs.chemrev.8b00712.

[10] Daniel J Cline et al. "New Water-Soluble Phosphines as Reductants of Peptide and Protein Disulfide Bonds : Reactivity and Membrane Permeability". In: *Biochemistry* 43 (48 2004), pp. 15195–15203. DOI: 10.1021/bi048329a.

[11] Phani Kumar et al. “Fluorescence-based detection of thiols in vitro and in vivo using dithiol probes”. In: *analytical biochemistry* 352 (2006), pp. 265–273. DOI: 10.1016/j.ab.2006.01.047.

[12] Christopher R Schlieve et al. “Synthesis and characterization of a novel class of reducing agents that are highly neuroprotective for retinal ganglion cells”. In: *Experimental Eye Research* 83 (2006), pp. 1252–1259. DOI: 10.1016/j.exer.2006.07.002.

[13] Jian-tao Ge et al. “Straightforward S - S Bond Formation via the Oxidation of S - Acetyl by Iodine in the Presence of N - Iodosuccinimide”. In: *J. Org. Chem.* 82 (2017), pp. 12613–12623. DOI: 10.1021/acs.joc.7b02367.

[14] Shahar Dery et al. “Insights into the deselenization of selenocysteine into alanine and serine”. In: *Chemical Science* 6 (2015), pp. 6207–6212. DOI: 10.1039/c5sc02528a.

[15] Nathalie Ollivier et al. “Selenopeptide Transamidation and Metathesis”. In: *Organic Letters* 16 (2014), pp. 4032–4035. DOI: 10.1021/ol501866j.

[16] Gwendoline Tallec et al. “Adequate Reducing Conditions Enable Conjugation of Oxidized Peptides to Polymers by One-Pot Thiol Click Chemistry”. In: *Bioconjugate Chemistry* 29 (11 2018), pp. 3866–3876. ISSN: 15204812. DOI: 10.1021/acs.bioconjchem.8b00684.

[17] Anne-marie Faucher and Chantal Grand-maître. “tris (2-Carboxyethyl) phosphine (TCEP) for the Reduction of Sulfoxides , Sulfonylchlorides , N - Oxides , and Azides”. In: *Synthetic Communications* 33 (20 2003), pp. 3503–3511. DOI: 10.1081/SCC-120024730.

[18] Artur Krezel et al. “Coordination Properties of Tris (2-carboxyethyl) phosphine , a Newly Introduced Thiol Reductant , and Its Oxide”. In: *Inorganic Chemistry* 42 (6 2003), pp. 1994–2003. DOI: 10.1021/ic025969y.

[19] J. Podlaha and J. Podlahová. “Compounds structurally related to complexone I. Tris(cabroxyethyl)phosphine”. In: *Collection of Czechoslovak Chemical Communications* 38 (6 1973), pp. 1730–1736. ISSN: 0010-0765. DOI: 10.1135/cccc19731730.

[20] Yoshihisa Iida et al. “Solubility of Selenium at High Ionic Strength under Anoxic Conditions”. In: *Journal of Nuclear Science and Technology* 47 (5 2010), pp. 431–438. DOI: 10.1080/18811248.2010.9711633.

[21] “Assessing Phosphine-Chalcogen Bond Energetics from Calculations”. In: *Organometallics* 34 (16 2015), pp. 4023–4031. ISSN: 15206041. DOI: 10.1021/acs.organomet.5b00428.

[22] Murthy A Vairavamurthy et al. “The interaction of hydrophilic thiols with cadmium: investigation with a simple model, 3-mercaptopropionic acid”. In: *Marine Chemistry* 70 (2000), pp. 181–189. ISSN: 0304-4203. DOI: 10.1016/S0304-4203(00)00023-2.

[23] Samuel Sanford Shapiro and Martin Wilk. "An analysis of variance test for normality (complete samples)". In: *Biometrika* 52 (3-4 Dec. 1965), pp. 591–611. ISSN: 1464-3510. DOI: 10.1093/biomet/52.3-4.591.

[24] Yuan Pu et al. "Colloidal Synthesis of Semiconductor Quantum Dots toward Large-Scale Production: A Review". In: *Industrial and Engineering Chemistry Research* 57 (6 2018), pp. 1790–1802. ISSN: 15205045. DOI: 10.1021/acs.iecr.7b04836.

[25] J. C. Champarnaud-Mesjard et al. "Crystal structure, Raman spectrum and lattice dynamics of a new metastable form of tellurium dioxide: γ-TeO2". In: *Journal of Physics and Chemistry of Solids* 61 (9 2000), pp. 1499–1507. ISSN: 00223697. DOI: 10.1016/S0022-3697(00)00012-3.

[26] "What is the correct form of BET isotherm for modeling liquid phase adsorption?" In: *Adsorption* 15 (1 2009), pp. 65–73. ISSN: 09295607. DOI: 10.1007/s10450-009-9151-3.

Chapter 3

QDs synthesis optimization

Preface

In Chapter 2, the results presented mainly demonstrate the efficiency of TCEP as chalcogen transport. Indeed, the trials performed illustrate the concept of chalcogen transfer with appropriate characterization (*e.g.*, UV/Vis, XRD and HRTEM). The emission properties shown by the resulting QDs are however poor and require an advanced systematic optimization process, appropriate for the TCEP=X derivatives.

In that perspective, the Chapter 3 is structured to provide a full overview of the parameters influencing the QDs formation, as described in Section 1.5, as summarized in Figure 3.1. To address these questions, the chapter begins with a justification of choice of reagents and the limitations they entail.

After marking the reagent nature and their range of values, the optimization of each core (*e.g.*, CdS, CdSe and CdTe) itself was carried out. For each system, the experimental parameters were varied and the data treatment aimed to predict the behaviour of QD formation with models as descriptive as possible to understand the mechanism of particle formation.

Based on the information extracted from the optimization phase, mechanistic insights were sought to determine the pathway of QD formation. The study covered the use of isotopic labelling, pH-metry, Raman monitoring and XPS surface analysis.

Finally, the Chapter 3 is currently under consideration for publication as a full paper.

Acknowledgements

This work was supported by the Service Public de Wallonie (Win2Wal 2018 Program, QD3Drops Project). The TEM pictures and EDX were realized at the CAREM microscopy facility of the University of Liège. The author acknowledge Dr. H. Hellwig for his help during the scalability trials, Dr. C. Campalani for her contribution during the pH-titration and Raman experiments, Dr. C. Malherbe for his help during the Raman *in-situ* batch experiments, Dr. P. Compère for the HRTEM/EDX data, Prof. S. Hermans and P. Eloy, from UCLouvain, for the XPS data acquisition and data treatment.

3.1 Parameters influencing QD formation

The versatility of TCEP as a chalcogen transfer reagent was proved in Chapter 2. Compared to conventional, water-soluble sodium chalcogenides, this new reagent exhibits greater air stability, as demonstrated in Figure 6.1. Moreover, the reduction step can be carried out in flow mode using a packed-bed column filled with elemental chalcogen. Beyond facilitating the transition from batch to flow, this approach improves process safety and reduces the risk of precursor degradation between their generation and subsequent use in concatenated processes.

Screening experiments based on the work of Emonds-Alt *et al.* [1] further confirmed, via UV/Vis analysis, that TCEP=X (with X = S, Se, Te) efficiently transfers the chalcogen to the cadmium source (see Figure 2.13). However, the resulting emission properties, not presented, remain poor, making it essential to optimize the experimental conditions in order to meet current standards for QDs emission performance.

3.1.1 Tunable parameters

In this section, the theoretical framework presented in Section 1.5 is connected to the experimental conditions illustrated in Figure 3.1. the main stages of the quantum dot formation mechanism are mapped onto the orange time line, and experimental parameters are highlighted in red boxes. Each stage is examined from a practical standpoint, linking theory to tunable factors.

- **Reaction rate**

  This initial phase governs the supply of freshly formed monomers for subsequent steps. This time step, almost invisible in the LaMer formalism, is explicitly captured in the Finke–Watzky pathway and is

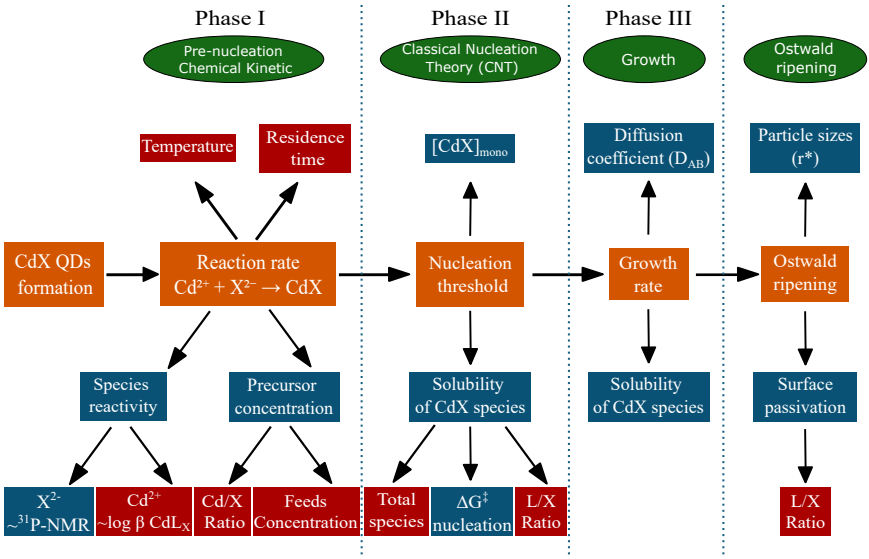

Figure 3.1. Schematic linking Section 1.5 to the experimental conditions for QDs formation. The main framework is shown in orange, tunable parameters in red, and uncontrolled ones in blue.

referred to as the induction period. The reaction rate depends on precursor concentration, temperature, residence time, and the intrinsic reactivity of the species. The chalcogen source exhibits a fixed reactivity (empirically correlated with the ^{31}P-NMR chemical shift: Te > Se > S > O), whereas the cadmium precursor reactivity can be tuned by modifying the chemical nature of its stabilizing ligand (roughly associated with log β).

- **Nucleation**

  Following the induction period, nucleation occurs only above a critical monomer concentration, which is directly linked to the reaction rate (phase I). In the LaMer formalism, it marks the beginning of the crystal growth and for FW mechanism it means the start of parallel reaction path with autocatalytic path. The nucleation threshold depends on monomer solubility and can be influenced experimentally through CNT parameters:

  – The nucleation activation barrier ($\Delta G^{\ddagger}$), governed by the Gibbs free energy per unit volume (ΔG_v, not directly controllable) and the surface tension σ, which can be adjusted via the ligand to precursor ratio (L/X).

  – The total species concentration, affecting ion interaction energies (F_{ions}).

- **Growth**

  The growth rate depends on the remaining monomer concentration and the diffusion coefficient (D_{ab}). In practice, phases II and III are difficult to separate experimentally because they are influenced by similar parameters. In the Finke–Watzky framework, no strict distinction is made between nucleation and growth, as both processes are assumed to proceed in parallel. The growth can be moderated by slowing the reaction rate after nucleation, either through controlled injection of additional precursors or by lowering the temperature, limiting supersaturation of monomeric units.

- **Ostwald ripening**

  Ostwald ripening occurs when the medium is depleted in precursors. Smaller particles, especially those below r^*, dissolve, while larger ones grow. This process is difficult to control; effective surface passivation, either via the L/X ratio during synthesis or through post-synthetic treatment, is the main strategy to mitigate it.

In the following sections, the influence of each experimental parameter (*e.g.*, red boxes in Figure 3.1) is reviewed to justify the choice of reagents as well as their reactivity limits.

3.1.2 Cadmium source

The selection of the cadmium source may seem trivial. However, a wise choice has an important impact on the emission properties of the final product, as well as on the growth rate.

The first requirement for the cadmium source is good water solubility. Most of the inorganic cadmium salts fulfil this condition. However, cadmium can easily form insoluble salts with many counter-ions, the most common being OH^-, which leads to $Cd(OH)_2$ precipitation.

In practice, no counter-ion from the cadmium source can fully prevent cadmium precipitation. Therefore, when the cadmium source is dissolved, an additional stabilizing agent is added to counterbalance the effect of OH^- ions (see Section 3.1.3). These stabilizers are typically X-type ligands (Table 1.2). At this stage, the initial counter-ions remain in the reaction medium.

During QD synthesis, these leftover ions play an important role in particle stabilization and surface passivation, as their affinity for cadmium affects surface–ion interactions. Two metrics can quantify these interactions: $\log\beta$ and HSAB theory. Cadmium is a soft acid, therefore, soft bases interact strongly with it. This latter parameter can be approximated by Mulliken electronegativity (χ), see Table 3.1. [4]

Table 3.1. Estimated bonding strength of various counter-ions with Cd^{2+}. n.a.: Not available, [1] data from [2], [2] data from [3].

Counter-ion	Log β[1]	χ Mulliken (eV)[2]
RS^-	n.a.	2.0 (approx.)
Cl^-	CdL: 1.42, CdL_2: 1.92	7.4
OAc^-	CdL: 1.00, CdL_2: 1.90	7.5
$NO_3{}^-$	n.a.	7.8 (approx.)
$SO_4{}^{2-}$	CdL: 0.85	8.0 (approx.)

The results indicate that thiolate functions bind strongly to cadmium atoms, making them excellent stabilizing agents. On the other hand, chloride and acetate ions present moderate logβ and χ values. These characteristics make them more suitable for CdX QD synthesis than nitrate or sulfate ions, which interact weakly with cadmium and do not contribute to surface passivation. [5]

Ultimately, $CdCl_2$ and $Cd(OAc)_2$ represent the best candidates, with similar potential interactions with cadmium. Among them, $Cd(OAc)_2$ was chosen because its methylene groups may be useful for further DOSY-NMR characterizations.

3.1.3 Cadmium - Stabilizing agent

The bibliographic review presented in Tables 1.7 and 1.11 shows that the most sustainable stabilizing agents are the X-types and more precisely phosphonate or thiol functional groups, which bind strongly to cadmium cations (Cd^{2+}). Based on this ligand screening, two stabilizing agents were selected: 3-Phosphopropionic acid (3-PPA) and 3-Mercaptopropionic acid (3-MPA). Both possess a propionate moiety, facilitating potential downstream biofunctionalization while ensuring the water solubility of the nanoparticles.

3.1.3.1 3-PPA

3-Phosphopropionic acid (3-PPA) is a bifunctional molecule containing both a carboxylic acid and a phosphonate group. Each group has its own pH-active center, with pKa values of 2.07, 4.56, and 7.31. The phosphonate group has two acidic protons (pKa 2.07 and 7.31), while the carboxylic acid has one (pKa 4.56). [6]

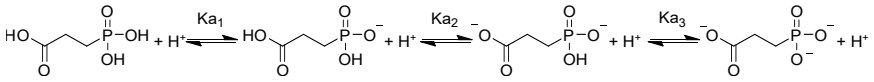

(3.1)

Figure 3.3 presents the species distribution as a function of pH. The first deprotonation occurs at the phosphonate, yielding an X-type ligand (see Table 1.2) well-suited for coordination with the soft Cd^{2+} ions. Subsequent deprotonation of the carboxylic acid provides an additional anionic site (also X-type) capable of coordinating cadmium. Finally, the second phosphonate proton is removed, producing the dianionic phosphonate species. While the increased negative charge enhances electrostatic attraction, the harder character of the dianion makes it less compatible with the soft Cd^{2+} according to HSAB principles. Thus, the overall interaction strength results from a balance between charge effects and acid–base softness/hardness.

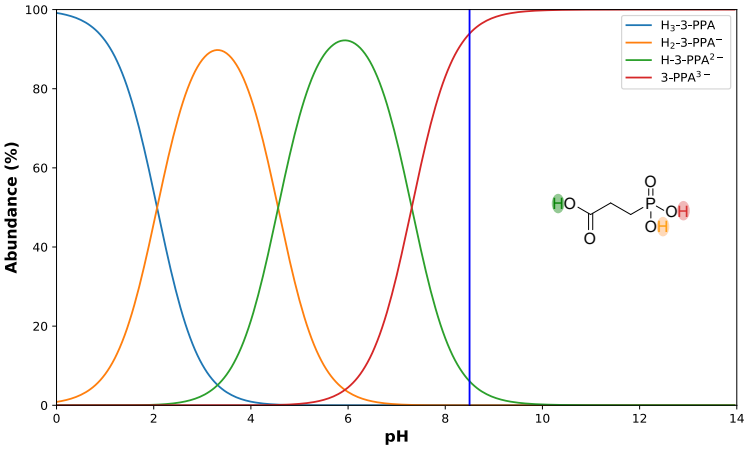

Figure 3.2. Species pH distribution of 3-Phosphopropionic acid (3-PPA).

In their study, Heubel *et al.* investigated the relationship between the protonation state of Phosphonoacetic acid (PAA) and its ^{31}P-NMR chemical shift (δ). The chemical shielding of the phosphorus nucleus can be related to the ligand ability to coordinate through an X-type bond. The resulting curve follows a parabolic trend, with a minimum corresponding to the fully deprotonated form of PAA (*i.e.*, phosphonate monoanion and carboxylate monoanion, net charge -2). [7] This behaviour is expected to apply similarly to 3-PPA, given the structural analogy.

Later, Farmer *et al.* conducted a study relative on the complexation properties of phosphonocarboxylic acids in aqueous media. [8] Their work focused on Phosphonoformic acid (PFA), PAA, and 3-PPA. Based on their measurements, 3-PPA was found to be the least efficient ligand for complexing Mg^{2+} and Ca^{2+}. Although no stability constants were reported for Cd-3-PPA

system, complexation data are available for cadmium with PAA, with log K_f = 3.9 (ML) and 1.9 (MHL). Given the functional similarity between 3-PPA and PAA, and the weak complexation observed for Mg^{2+} and Ca^{2+}, it is reasonable to expect that 3-PPA also exhibits relatively low affinity toward Cd^{2+}.

This observation was confirmed experimentally: mixtures of Cd^{2+} and 3-PPA did not withstand the addition of NaOH and rapidly precipitated as $Cd(OH)_2$. To prevent this undesired precipitation, the precursor solutions were prepared in the presence of a Tris buffer adjusted to pH = 8, which yielded stable mixtures. These buffered precursor solutions were subsequently used for the batch synthesis, as shown in Figure 3.3.

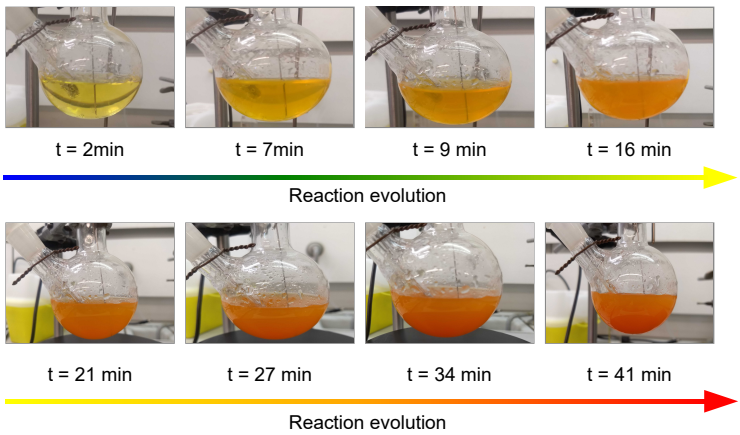

Figure 3.3. Batch synthesis of CdSe QDs stabilized by 3-PPA in presence of tris buffer.

The synthesis was initially expected to proceed at 65 °C. However, immediately after the addition of the TCEP=Se precursor, the reaction medium began to change color, indicating that nucleation had already started at room temperature. The experiment was monitored over time, but the spectral data proved unusable: in the absence of controlled thermal activation and quenching, the samples decomposed progressively, consistent with the visual evolution shown in Figure 3.3. These observations led us to discontinue the use of 3-PPA, as this stabilizing agent was not sufficiently strong to keep the forming QDs soluble under these conditions.

3.1.3.2 3-MPA

3-Mercaptopropionic acid (3-MPA) is a bifunctional molecule, containing both a carboxylic acid and a thiol group. Each has its own pH-active center with pKa values of 4.3 and 10.8, respectively. [9] The three resulting species

are presented in Equation 3.2, and their relative abundance as a function of pH is shown in Figure 3.4.

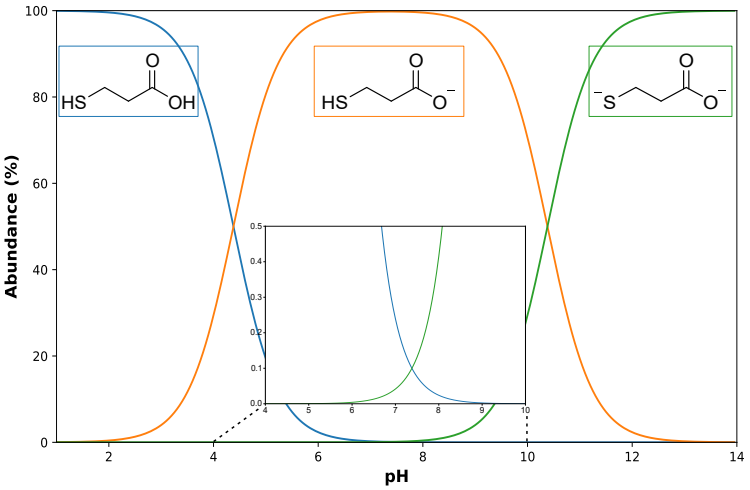

Figure 3.4. Species pH distribution of 3-MPA.

$$\mathrm{HS{-}(CH_2)_2{-}COOH} \overset{\mathrm{K_{a_1}}}{\rightleftharpoons} \mathrm{HS{-}(CH_2)_2{-}COO^-} + \mathrm{H^+} \overset{\mathrm{K_{a_2}}}{\rightleftharpoons} \mathrm{{}^-S{-}(CH_2)_2{-}COO^-} + \mathrm{H^+} \tag{3.2}$$

The protonation state of 3-MPA strongly influences its ability to act as a stabilizing agent. The fully protonated form cannot bind efficiently to the CdS surface. The first group to deprotonate is the carboxylic acid, forming a carboxylate (X-type ligand). The second is the thiol, yielding a thiolate, which is also an X-type ligand.

However, there is a significant difference in the Cd–ligand bond energy between the carboxylate and thiolate groups. Density Functional Theory (DFT) calculations estimate the Cd–O (carboxylate) bond energy to range from 0.25 to 1 eV, depending on the chelation mode, [10] and the Cd–S (thiolate) bond energy to range from 0.6 to 2.4 eV. [11]

These values were obtained through DFT simulations and may vary significantly with the solvent and the ions present in the medium (*e.g.*, the various X-type ligands illustrated in Figure 1.16). In practice, when the pH is sufficiently high, sulfur preferentially binds to cadmium atoms, replacing the carboxylate group.

Based on these considerations, assuming the pH is sufficiently high to form the thiolate form of 3-MPA, the following chelation equilibrium can be written:

$$\mathrm{Cd^{2+}} + \mathrm{{}^-S{-}(CH_2)_2{-}COO^-} \overset{\mathrm{K_{f_1}}}{\rightleftharpoons} \mathrm{[Cd{-}S{-}(CH_2)_2{-}COO]} \tag{3.3}$$

This allows us to write the first equilibrium expression (Equation 3.4), which can be simplified by substituting the concentration of RS^{2-} by the species from the second deprotonation step in Equation 3.2, leading to Equation 3.4:

$$K_{f_1} = \frac{[\text{Cd}-\text{SR}]}{[\text{Cd}^{2+}][\text{RS}^{2-}]} = \frac{[\text{Cd}-\text{SR}][\text{H}^+]}{[\text{Cd}^{2+}][\text{RSH}]K_{a_2}} \tag{3.4}$$

In the literature, the logarithm of the formation constant, $logK_{f_1}$, has been estimated as 8.8 at pH 7.5. [12] This monothiol complex is poorly soluble and forms a zwitterionic compound capable of cyclization through interaction with the carboxylate group. This cyclization is favoured due to formation of a stable six-membered ring, as shown in Figure 3.5.

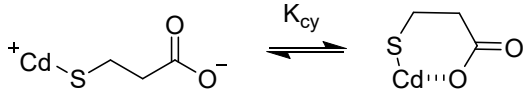

Figure 3.5. Monothiol-Cadmium complex cyclization due to carboxylate interaction.

In a second step, if free deprotonated 3-MPA molecules remain in the reaction medium, they can replace the carboxylate group in the cyclized form, leading to a 1:2 complex ($Cd(3\text{-}MPA)_2$), as shown by the chelation equilibrium in Equation 3.5.

$$[\text{Cd}-\text{S}-(\text{CH}_2)_2-\text{COO}] + {}^{-}\text{S}-(\text{CH}_2)_2-\text{COO}^- \overset{K_{f_2}}{\rightleftharpoons} [\text{Cd}-(\text{S}-(\text{CH}_2)_2-\text{COO})_2]^{2-} \tag{3.5}$$

Similarly to the 1:1 complex, the equilibrium expression can be written as in Equation 3.6. Once again, the term $[RS^{2-}]$ is replaced using the second deprotonation step from Equation 3.2.

$$K_{f_2} = \frac{[\text{Cd}(\text{SR})_2{}^{2-}]}{[\text{CdSR}][\text{RS}^{2-}]} = \frac{[\text{Cd}(\text{SR})_2{}^{2-}][\text{H}^+]}{[\text{CdSR}][\text{RSH}]K_{a_2}} \tag{3.6}$$

Experimentally, a value of $\log K_{f_2} = 4.8$ has been reported at pH 12. [12] This 1:2 ($Cd(3\text{-}MPA)_2$) complex is highly soluble in aqueous solutions, making it a reliable precursor for QDs synthesis.

This complexation overview indicates that 3-MPA can bind strongly to cadmium atoms through its thiolate group. Although it is difficult to directly compare, $\log K_{f_1}$ and $\log K_{f_2}$ values obtained under different pH conditions,

the data suggest that thiolate species preferentially bind to cadmium to form 1:1 complexes. Once all cadmium atoms are coordinated in this 1:1 form, the excess thiolate species can further interact with these complexes to yield 1:2 $Cd(3\text{-MPA})_2$ species.

Based on these conclusions and in order to define the suitable pH range for feed preparation, several pH-metric titrations of pure 3-MPA and of 3-MPA in the presence of cadmium were carried out using sodium hydroxide. A representative titration curve is presented in Figure 3.6. Experimental details are provided in Section 6.2.4.6.

The main observation is the clear difference between the titration of pure 3-MPA and that performed in the presence of cadmium. In the first case, a regular pH increase is observed, whereas in the second, a significant buffering region appears, where the pH rise is hindered until both curves converge again above pH $\simeq$ 11. This hysteresis behaviour results from the consumption of thiolate species, formed upon NaOH addition, by cadmium ions, leading to the complexation cascade previously described.

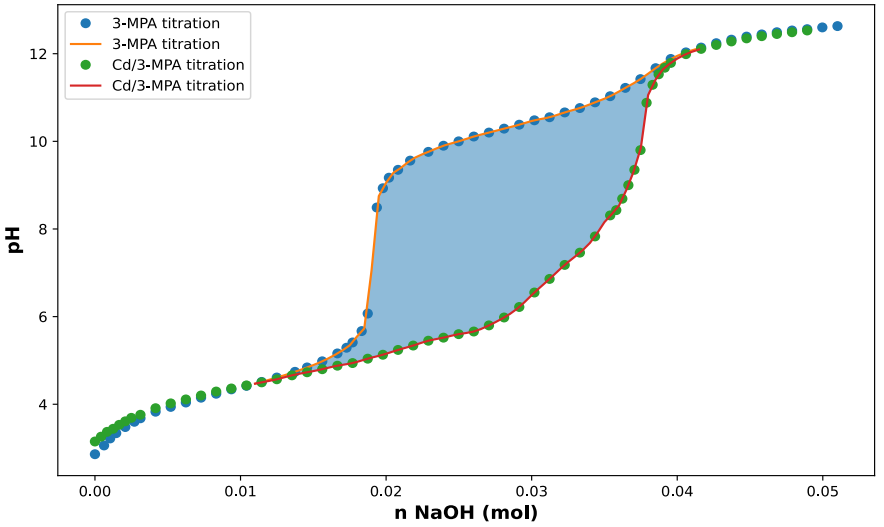

Figure 3.6. Representative pH-metric titration of pure and Cd-containing 3-MPA solutions.

Another interesting outcome of this titration is its semi-quantitative character. Indeed, the measured pH values can be converted into the number of moles of H^+. Integration of the hysteresis area can thus be related to the Cd:3-MPA ratio as a function of pH, allowing the construction of Figure 3.7.

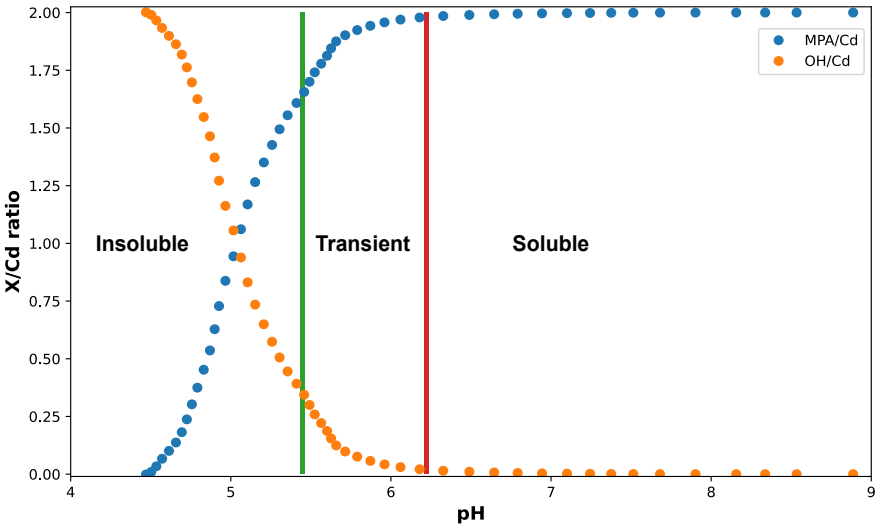

Figure 3.7. Calculated Cd:3-MPA ratio as a function of pH, with visual observations of solution state.

In Figure 3.7, the visual appearance of the solutions (insoluble, transient, or soluble) is reported together with the calculated Cd:3-MPA ratio. These results confirm that the final complex corresponds to a 1:2 Cd:3-MPA stoichiometry. This figure is highly valuable, as it defines the pH range suitable for CdX QDs synthesis while maintaining cadmium in a soluble form.

3.1.4 TCEP=X reactivity

The reactivity of the TCEP=X derivatives (X = O, S, Se) plays a central role in determining the behaviour of the overall system for CdX QDs synthesis. This reactivity depends mostly on the position of the chemical shift (δ) in ^{31}P-NMR, which is influenced by the electronic environment around the phosphorus atom.

These chemical shifts are summarized in Figure 2.3: 52.7 ppm, 41.4 ppm, and -6.8 ppm for TCEP=S, Se, Te, respectively. The shielding correlates with the electron density at the phosphorus center and reflects the strength and polarization of the P=X bond. This electronic effect directly influences the rate at which each TCEP=X transfers its chalcogen to cadmium. Therefore, in terms of reactivity: TCEP=Te > TCEP=Se > TCEP=S. This trend is further supported by the harshness of the experimental conditions required to produce QDs, as shown in Figure 2.14.

Finally, although the chemical shifts are relatively stable, pH variations may cause peak shifts, indicating changes in reactivity.

3.1.5 Cadmium to Chalcogen precursor ratio

A common approach to tune the emission properties of the generated QDs is to vary the cadmium-to-chalcogen (Cd/X) ratio. In organic solvents, the Cd/X ratio can be either smaller or larger than 1 (*e.g.*, $1 \leq Cd/X \leq 1$). In aqueous media, however, the precursors may react with water, leading to chalcogen oxidation and formation of its elemental form. For this reason, hydrothermal syntheses are typically performed with an excess of cadmium (*i.e.*, $Cd/X \geq 1$). [13]

In the case of the new chalcogenide transfer agent, besides its improved stability (demonstrated in Figure 6.1), experiments were performed by heating the three precursors (TCEP=X, where X = S, Se, or Te) up to 120 °C. In all cases, within a few seconds, elemental chalcogen was observed in the reaction medium. Therefore, as for other water soluble chalcogenide carriers, TCEP=X derivatives appear to undergo rapid oxidation at high temperature, according to Equation 3.7.

$$\mathrm{TCEP{=}X + H_2O \rightleftharpoons TCEP{=}O + 2\,H^+ + X_0} \tag{3.7}$$

This oxidation may cause several side effects, detailed below:

- **Unknown chalcogen excess:** The formation of QDs competes with the generation of elemental chalcogen. As a result, the effective chalcogen excess is unknown, which may lead to poor reproducibility.
- **Nucleation mechanism:** As discussed in Section 1.5.2, homogeneous nucleation is preferred, leading to soluble nuclei that sustain further crystal growth. However, the competitive oxidation reaction produces insoluble species, increasing the risk of heterogeneous nucleation of CdX QDs. According to the geometrical function ($f(\theta)$) (1.15 and 1.16), elemental X_0 may act as nucleation sites for CdX monomers, or lead to direct deposition on the inner surface of the reactor tubing (experimentally observed).
- **Crystal composition:** The concurrent formation of both CdX and X_0 monomers promotes heterogeneous crystal growth and decreases reproducibility.

Based on these observations and mechanistic considerations, the QDs synthesis was optimized using a Cd/X ratio ≥ 1.

3.1.6 Salt effect

This section investigates whether spectator ions influence nucleation and growth processes. According to the LaMer mechanism, these processes depend on the monomer concentration in the reaction medium. Spectator ions may affect both the solubility of monomeric units and the nucleation threshold.

In this context, a synthesis of CdSe QDs was attempted in the presence of NaCl. The first trials were conducted in a microfluidic setup, resulting in an unstable outlet flow: alternating segments of insoluble red powder and colorless solution. This observation indicates that nucleation occurs rapidly (likely due to heterogeneous nucleation, see $f(\theta)$ in 1.16, on the inner pipe surface), followed by significant crystal growth, producing segmented flow with macro CdSe crystals and colorless segments devoid of precursors.

The experiment was repeated in a batch reactor at a lower temperature (95 °C), yielding similar results: few nucleation events followed by substantial crystal growth, ultimately producing bulk CdSe powder rather than colloidal QDs. These results are likely due to two phenomena: first, the presence of NaCl reduces the solubility of CdX building blocks; second, the charged ions disturb the surface charge of the forming QDs, promoting aggregation.

3.1.7 Determination of experimental parameters

The review of commercially available cadmium salts identified two potential sources: $CdCl_2$ and $Cd(OAc)_2$. In both cases, the counter-anions exhibit interesting stabilizing properties for the formed QDs. Ultimately, $Cd(OAc)_2$ was selected due to its potential for further characterization by DOSY-NMR.

The selection of a stabilizing agent to encapsulate the cadmium cation and prevent the formation of $Cd(OH)_2$ led to several experimental investigations, as detailed in Section 3.1.3. Ultimately, 3-MPA was chosen as the stabilizing agent for enhanced stability and better control over reactivity. Its use however constraint to proceed under basic conditions, above 8, according to Figure 3.4.

The reactivity of the TCEP=X derivatives appears to be non-tunable and must be used as-is. The only available insight comes from the phosphorus chemical shift of each derivative, which suggests that during the optimization phase, the reaction temperature may follow the order of the chemical shifts: Te < Se < S.

The cadmium-to-chalcogen ratio commonly used in organic synthesis is limited in the aqueous phase. This is due to the instability of the chalcogen source under reaction temperatures, making the use of an excess chalcogen impossible, which could potentially lead to reactor coating. Based on this

observation, the cadmium-to-chalcogen ratio can vary, but always in favour of a cadmium excess.

Finally, the presence of spectator ions affects the solubility threshold, thereby influencing the dynamic nucleation and growth process. This parameter can be adjusted based on the phenomenon that needs to be favoured.

In summary, Section 3.1 helped to narrow down the system options: $Cd(OAc)_2$ salt will be used, with cadmium encapsulated by the 3-MPA stabilizing agent. The TCEP=X derivatives will be used as they are. The cadmium-chalcogen ratio can be adjusted, but always in favour of a cadmium excess. Lastly, the concentration of spectator ions will depend on the process to be favoured.

3.2 Microfluidic optimization

The QDs synthesis presented in Chapter 2 aimed solely to validate the new chalcogen agent (TCEP=X, with X = S, Se, or Te). In the current section, more focus is given to understanding the nanocrystal formation dynamics and, when possible, to optimizing the QDs properties. Taking advantage on the parameters narrowing performed in Section 3.1.

3.2.1 Metrics generalities

Prior to discuss the QDs synthesis, the main metrics used throughout this work are introduced in the current subsection, including several standard quantities, from the literature. For PLQY calculation, reference samples are required for calibration (*e.g.*, Fluoresceine, Rhodamine 6G, and Rhodamine 101).

1) General parameter

The first parameter introduced is the Effective residence time (ERT) $\theta(t, T)$. It is defined to reduce the dimensionality of the optimisation problem by grouping the residence time (t) and the temperature (T) into a single variable. Two empirical models are considered: the one-parameter expression (Equation 3.8) and the three-parameter expression (Equation 3.9), both inspired by Arrhenius-type behaviour.

$$\theta(t, T) = t \cdot \exp\left(-\frac{a}{T}\right) \tag{3.8}$$

Where:

- $\boldsymbol{\theta}$: Effective residence time [s],
- $\mathbf{t}$: Residence time [s],
- $\mathbf{T}$: Absolute temperature [K],
- $\mathbf{a}$: Thermal sensitivity constant [K].

$$\theta(t,T) = t^{\alpha} \cdot \exp\left(-\frac{\beta}{T}\right) \cdot T^{\gamma} \tag{3.9}$$

Where:

- $\boldsymbol{\theta}$: Effective residence time [s],
- $\mathbf{t}$: Residence time [s],
- $\mathbf{T}$: Absolute temperature [K],
- $\boldsymbol{\alpha}$: Time-correction constant [dimensionless],
- $\boldsymbol{\beta}$: Thermal sensitivity constant [K],
- $\boldsymbol{\gamma}$: Temperature-correction constant [dimensionless].

The most suitable model, either Equation 3.8 or 3.9, is selected according to statistical criteria (*i.e.*, by minimising both Akaike information criterion (AIC) and Bayesian information criterion (BIC)). In both formulations, the parameters a (one-parameter model) and β (three-parameter model) represent the reaction thermal sensitivity and can be related to an apparent activation energy using Equation 3.10:

$$a = \frac{E_a \cdot 10^3}{R} \qquad \text{or} \qquad \beta = \frac{E_a \cdot 10^3}{R}. \tag{3.10}$$

Where:

- $\mathbf{a} = \beta$: Thermal sensitivity constant [K],
- $\mathbf{E_a}$: Apparent activation barrier [kJ.mol^{-1}],
- $\mathbf{R}$: Gas constant [J.mol^{-1}.K^{-1}].

In practice, the absorption peak position is analysed as a function of the effective residence time (*i.e.,* $E_{\max}$ [nm] $= f(\theta(t,T))$). Model parameters are fitted by minimising an appropriate loss function.

Two empirical relationships can be considered: a linear dependence, $E_{\max} \sim \theta(t,T)$, and a logarithmic dependence, $E_{\max} \sim \ln(\theta(t,T))$.

A linear response of $E_{\max}$ is consistent with LaMer-type behaviour (Section 1.5.5), whereas a logarithmic response reflects a sigmoidal trend, characteristic of the FW mechanism.

2) UV/Vis based parameters

From the absorption spectra of the experimental samples, several quantities can be extracted:

- Position of the first excitonic peak, $\lambda_{\max}$ [nm], called E_{max} for convenience,
- Absorbance at $E_{\max}$, A_{peak} [dimensionless],
- Absorbance at the first valley, A_{valley} [dimensionless].

The value of A_{peak} can be directly used, as it reflects the QD concentration in the sample, and can be plotted against parameters such as time, temperature, or ERT.

The peak and valley absorbances can be combined to compute the peak to valley ratio (P/V ratio), defined as:

$$P/V = \frac{A_{\text{peak}}}{A_{\text{valley}}} \tag{3.11}$$

This metric, generally greater than 1, can be related to the FWHM, although it becomes less sensitive for larger QD diameters.

The evolution of the absorption peak energy E_{peak} as a function of the ERT can then be modelled by two equations, depending on the linearisation applied to $\theta(t, T)$ (*e.g.*, ERT determination).

a) $E_{\max} \sim \ln(\theta(t, T))$ (FW-type effective-time description):

Here, the logarithmic dependence refers to the effective-time scaling used to rationalize the sigmoidal evolution, rather than to a strictly logarithmic functional form.

The hypothesis that the reaction follows a FW mechanism mechanism is strongly supported by the experimental data. Consequently, Equation 3.12 is used to describe the evolution of the first excitonic peak position. This function exhibits a sigmoidal-like evolution with two horizontal asymptotes, in good agreement with the experimental behaviour.

Although Equation 3.12 has an empirical form, the sigmoidal evolution of E_{peak} does not arise from a statistical logistic function. Instead, it exhibits a non-symmetrical shape originating from a progressive decrease in the available surface during growth. This behaviour emerges from a physically motivated effective time formalism, in close analogy with the Finke-Watzky kinetic model.

$$E_{\text{peak}}(\theta(t,T)) = E_0 + \frac{E_\infty - E_0}{\exp\left(\frac{\alpha}{\theta_{\text{norm}}}\right)} \tag{3.12}$$

Where:

- $\mathbf{E_0}$: Initial peak position [nm],
- $\mathbf{E_\infty}$: Maximal peak position [nm],
- $\boldsymbol{\alpha}$: Growth-rate parameter [dimensionless],
- $\boldsymbol{\theta_{\text{norm}} = \frac{\theta(t,T)}{\theta(t,T)_{\max}}}$: Dimensionless extent of transformation [dimensionless].

Here, θ_{norm} is obtained from either Equation 3.8 or 3.9. Fitting this model yields the parameter α, while E_0 and E_∞ define the lower and upper bounds accessible under the given experimental conditions (*i.e.*, concentration and species ratio). The parameter α also enables interpolation of the peak position across the explored domain.

A dimensional form of α can be defined to give it a physical meaning (intrinsic growth rate), using:

$$\alpha_{\text{phys}} = \alpha_{\text{fit}} \cdot \theta(t,T)_{\max} \tag{3.13}$$

Where:

- $\boldsymbol{\alpha_{\text{phys}}}$: Intrinsic growth rate [s],
- $\boldsymbol{\alpha_{\text{fit}}}$: Fitted growth-rate parameter [dimensionless],
- $\boldsymbol{\theta(t,T)_{\max}}$: Maximum effective residence time [s].

b) $\boldsymbol{E_{\max} \sim \theta(t,T)}$:

In this restricted regime, the sigmoidal evolution can be locally approximated, and a simplified LaMer-type mechanism becomes relevant. This justifies the use of the straight-line approximation given in Equation 3.14.

$$E_{\text{peak}}(\theta(t,T)) = E_0 + k_{growth} \cdot \theta(t,T) \tag{3.14}$$

Where:

- $\mathbf{E_0}$: Initial peak position [nm],
- $\mathbf{k_{growth}}$: Growth-rate constant [nm.s^{-1}],
- $\boldsymbol{\theta(t,T)}$: Effective residence time (ERT) [s].

Therefore, the FW-type formulation provides a unified description of the full growth process, while the LaMer-type linear approximation remains valid over restricted effective-time intervals.

The comparison of these empirically determined constants between experiments must be conducted with great care, as the dynamic ranges explored (*i.e.*, temperature, time, peak position) and the material type (*i.e.*, bandgap) strongly influence the numerical values of the fitted parameters.

3) Emission based parameters

From the emission spectra recorded, the following parameters can be extracted:

- Position of the emission peak, E $\lambda_{\max}$ [nm],
- Emission intensity at $\lambda_{\max}$, E_{peak} [mA or dimensionless],
- FWHM [nm].

The value of $E\lambda_{\max}$ reflects the QDs size and can be analysed as a function of time, temperature, or ERT. Care must be taken to select the Stokes-shifted excitonic peak rather than the broad surface-state emission (see Figure 1.8).

The quantity E_{peak} corresponds to the emission intensity. Its absolute value depends on the excitation wavelength and on the detector characteristics, and may reflect the QDs efficiency in converting the excitation light.

The FWHM, determined at half of the peak maximum, provides a reliable spectroscopic estimate of the size distribution.

Additionally, for low-emission samples (*i.e.*, PLQY, metric presented below, of only a few percent), in which both surface and Stokes-shifted emissions are present, an additional improvement metric was introduced. It is based on the ratio between the integrated areas of the Stokes-shift emission and the surface emission, as shown in Equation 3.15.

$$\text{Stokes emission (\%)} = \frac{S_{\text{Stokes}}}{S_{\text{Stokes}} + S_{\text{Surface}}} \cdot 100 \tag{3.15}$$

Where:

- $\mathbf{S}_{\text{Stokes}}$: Integrated area of the deconvoluted Stokes-shift emission peak,
- $\mathbf{S}_{\text{Surface}}$: Integrated area of the deconvoluted surface emission peak.

Figure 3.8 illustrates this procedure: the green area (Stokes-shift emission) divided by the yellow area (surface emission) provides the metric.

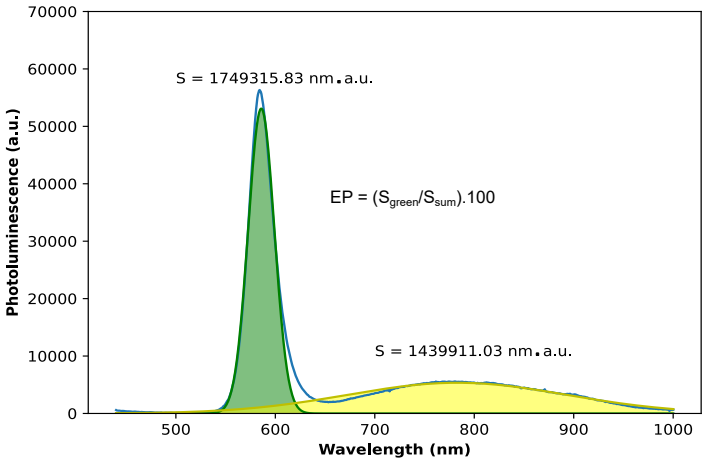

Figure 3.8. Emission metric for surface fluorescence. The peak deconvolution is obtained by fitting the spectrum with the sum of two Gaussian functions.

A higher ratio indicates improved material quality. To optimize the emission properties, this ratio should be as large as possible and ideally tends toward ∞.

4) Absorption- and emission-based parameters

Some metrics combine absorption and emission data and solvent properties. [14, 15] The absorbance of both the sample and the reference at the excitation wavelength (ideally matched), together with their emission spectra, are compared to standard references (*i.e.*, Fluorescein, Rhodamine 6G, and Rhodamine 101). The photoluminescence quantum yield (PLQY) is calculated using Equation 3.16.

$$PLQY(\%) = QY_{\text{ref}} \cdot \frac{S_{\text{sample}}}{S_{\text{ref}}} \cdot \frac{1 - 10^{-A_{\text{ref}}}}{1 - 10^{-A_{\text{sample}}}} \cdot \frac{\eta^2_{\text{sample}}}{\eta^2_{\text{ref}}} \cdot 100 \quad (3.16)$$

Where:

- $\mathbf{QY}_{\text{Fluorescein}}$: 89%,
- $\mathbf{QY}_{\text{Rhodamine 6G}}$: 91%,
- $\mathbf{QY}_{\text{Rhodamine 101}}$: 91.5%,
- **S**: Integrated emission peak,
- **A**: Absorbance at the excitation wavelength,
- $\boldsymbol{\eta}$: Refractive index (1.360 for QDs samples or NaOH 0.1 M, 1.335 for Rhodamine samples in ethanol).

3.2.2 CdS

The preliminary experiments conducted on CdS QD cores, summarised in Figure 2.14, led to an effective sulfur transfer toward the cadmium atom, as demonstrated by XRD (Figure 2.15). However, only poor-quality QDs were produced, without providing useful reaction insights.

A new set of experiments was conducted, taking into account the metrics introduced in Section 3.2.1. This series of experiments covered temperatures from 170 °C to 210 °C and residence times from 30 s to 120 s. For further experimental details, see Section 6.2.4.1.

For each experimental coordinates, samples were collected and analysed by UV/Vis absorbance and emission spectra. The first excitonic peak metrics were extracted (*i.e.*, peak position, absorbance at this position and absorbance at the first minimum). The data so produced were analysed through the models developed in Section 3.2.1 and, finally, the results are presented in Figures 3.9 to 3.11.

3.2.2.1 CdS peak position modelisation

Figure 3.9 presents the modelling of the CdS first excitonic peak as a function of the DET (θ_{norm}). The θ parametrisation was performed using the one parameter model (AIC = 65.17, BIC = 66.59). A more detailed comparison of the AIC/BIC values for the different θ values is provided in Section 6.2.5.2. These θ values lead to a thermal sensitivity constant of 8067 K, corresponding to an apparent activation energy $E_{a,\text{app}}$ of 67.07 kJ.mol^{-1}.

Based on this parameter, the CdS first excitonic peak modelling was carried out and is shown in Figure 3.9. In this model, the minimum observed peak position is 366 nm, which remains stable for a short time $\theta_{\text{norm}} \approx 0.0011$, which likely corresponds to the pre-nucleation (induction) regime, followed by a rapid increase associated with burst nucleation and early growth (*i.e.*, sigmoidal like shape) and tends toward 488 nm. This asymptotic value remains slightly blue shifted from the CdS bulk bandgap (*i.e.*, 512.4 nm) indicating that the particles do not reach the full bulk limit under the explored conditions.

Beyond defining the extrema of $\lambda_{\max}$, which set the accessible size range of the nanoparticles, the dominant steps of the FW mechanism can be highlighted through the derivatives of $E_{\text{peak}}(\theta)$ (see Section 6.2.5.1, Equation 6.1). Based on these metrics, a dimensionless effective time (θ_{norm}) can be associated with each dominant Finke-Watzky phase:

The analysis presented in Table 3.2 confirms the predominance of the FW mechanism: an induction phase from 0 to 0.0011 is followed by a rapid

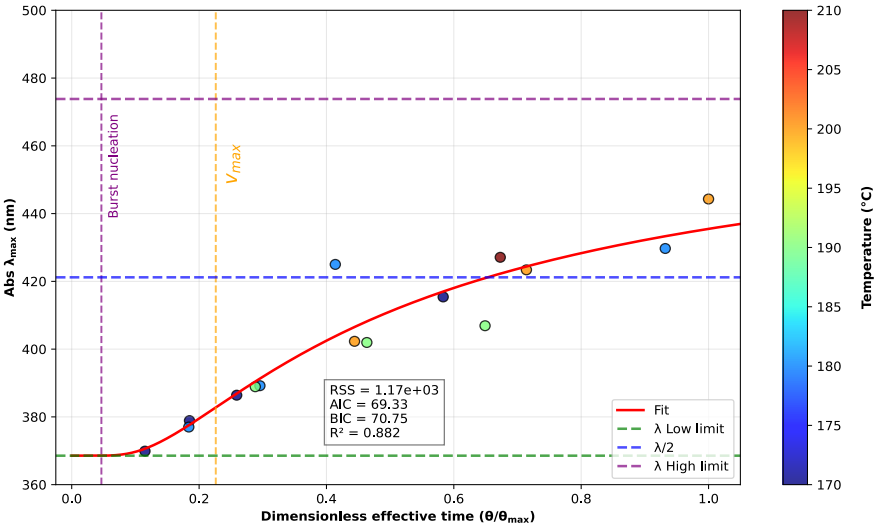

Figure 3.9. Modelling of the CdS QDs peak absorbance position as a function of the dimensionless effective time. $E_0 = 369$ nm, $E_\infty = 474$ nm, $\alpha = 0.453$.

Table 3.2. Association of dimensionless effective time θ_{norm} with the dominant FW mechanism phases.

Reaction Phase	θ_{norm} **range**
Induction phase	0 to 0.0011
Burst nucleation	0.0011
Growth acceleration	0.0011 to 0.226
v_{max}	0.226
Growth slow down	0.226 to 1 and beyond

acceleration due to burst nucleation, which generates a large surface area available for the autocatalytic reaction, resulting in growth acceleration up to $\theta_{\text{norm}} = 0.226$. Beyond this point, the reaction slows down as the available surface decreases.

3.2.2.2 CdS absorbance over growth

The second plot presents the characteristics of the first excitonic peak (*i.e.*, absorbance and peak position). Each experiment is associated with its Dimensionless effective time (DET), which reflects the harshness of the reaction conditions (*i.e.*, both time and temperature).

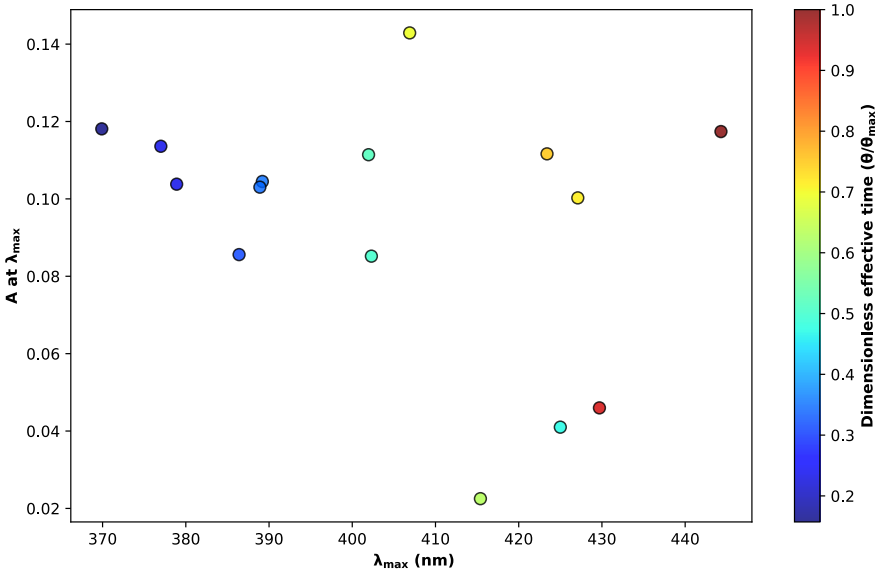

Figure 3.10. Absorbance values of CdS QDs as a function of the first excitonic peak position, each point being associated with its DET value.

The absorbance values are linked to the QDs concentration through the Beer-Lambert law and therefore provide an indicator of how the particle concentration evolves with size. These results are shown in Figure 3.10.

Under ideal conditions, the absorbance is expected to decrease as particle size increases, because the QD concentration usually declines once burst nucleation is reached, the particles are likely to growth. This behaviour is indeed observed between 370 nm and 390 nm. However, beyond this range the trend breaks down, and the absorbance values become more scattered, particularly under harsher reaction conditions.

This lack of a clear trend may arise from two main effects. First, although growth is expected to begin around 390 nm and should be completed near

410 nm, the observed behaviour deviates from this expected progression. Alternatively, heterogeneous nucleation (see Equation 1.16) may occur, leading to a less controlled nucleation process and consequently to poorly correlated QD concentrations.

3.2.2.3 CdS Peak-to-valley ratio over growth

The last part of the results analysis relies on the P/V ratio, calculated according to Equation 3.11. This ratio is generally a good indicator of the particle size distribution. It is particularly useful when the emission data are dominated by surface fluorescence, which otherwise makes discussing size distribution impossible. Ideally, the P/V ratio should be as large as possible, approaching one for large particle sizes, and may occasionally drop slightly below one.

Under real experimental conditions and following the LaMer steps, the P/V ratio is expected to decrease as particle size increases during the growth dominated phase, and then increase again during the Ostwald ripening regime, where size focusing occurs.

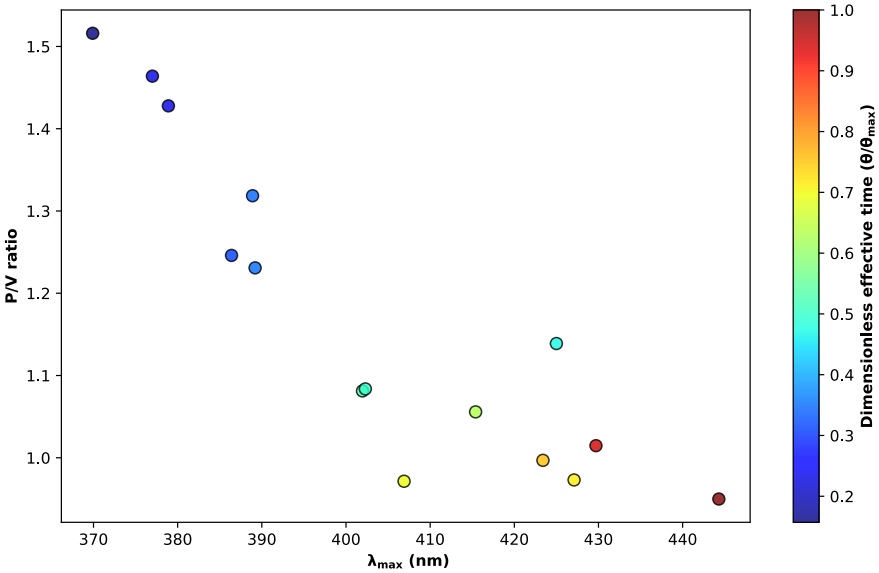

Figure 3.11. P/V ratio values of CdS QDs as a function of the first excitonic peak position, each point being associated with its DET value.

The experimental values are shown in Figure 3.11. As expected, the P/V ratio decreases for smaller particles and under softer experimental condition (*e.g.*, lower DET values). However, even upon reaching the identified Ostwald ripening regime, the P/V ratio continues to decrease.

This behaviour is related to the decrease of quantum confinement effects. As the particles approach the CdS bulk bandgap, the first excitonic peak becomes less well resolved, resulting in P/V ratio values close to or even slightly below one.

3.2.2.4 Discussion

The analysis of the CdS QDs UV/Vis spectra highlights several key parameters, including the first excitonic peak position, the absorbance at this wavelength, and the absorbance at the first valley. After appropriate data treatment, these metrics provide meaningful insights into the reaction dynamics.

In addition to the results presented above, the same data processing was applied to the control experiments performed using 3-MPA as the sole sulfur source (see Section 6.2.5.3). This enables a direct comparison between the two sulfur sources, TCEP=S and 3-MPA. In both cases, CdS QDs are formed, but the different precursor chemistries may modify the nucleation pathway through parallel reactions, resulting in different activation barriers.

The data analysis shows that both experiments follow a sigmoidal trend consistent with the model. The curve obtained with 3-MPA begins at a higher initial energy (*i.e.*, $E_0 = 404$ nm) compared to TCEP=S, but both converge toward a slightly blue-shifted CdS bulk bandgap (*i.e.*, $E_\infty = 477$ nm). The Finke-Watzky phases are also shifted to shorter DET values. These differences may arise from a higher initial free-cadmium concentration in the 3-MPA-based experiments.

The thermal sensitivity constants differ significantly as well, with a larger value for 3-MPA. This directly affects the apparent activation energy, which reaches 144.49 kJ $\cdot$ mol^{-1} compared to 67.07 kJ $\cdot$ mol^{-1} for TCEP=S. This difference indicates that TCEP=S is a more favourable sulfur source than 3-MPA, providing valuable insights into the reaction dynamics: between reactions 3.17 and 3.18, the latter is favoured.

$$\mathrm{Cd(3\text{-}MPA)_2} \xrightarrow[\mathrm{H_2O}]{\Delta} \mathrm{CdS} \tag{3.17}$$

$$\mathrm{Cd(3\text{-}MPA)_2 + TCEP{=}S} \xrightarrow[\mathrm{H_2O}]{\Delta} \mathrm{CdS + 3\text{-}MPA} \tag{3.18}$$

As a consequence of the higher apparent activation barrier, the concentration of CdS QDs increases only under harsher reaction conditions when 3-MPA is used, since more energy is required to form the nuclei. The P/V ratio evolves similarly for both reactions, confirming that the size distribution trends are mainly governed by growth mechanism rather than by the sulfur source.

Overall, the combined analysis of the peak position modelling, absorbance evolution, and P/V ratio metrics demonstrates that CdS QDs follow a classical LaMer type behaviour, with clearly identifiable nucleation, growth, and ripening stages. While the general trends align with the expected mechanisms, several deviations from ideal behaviour highlight the influence of experimental conditions, precursor chemistry, and quantum confinement on the reaction pathway. Taken together, these results provide a coherent and comprehensive picture of the CdS growth dynamics over the explored parameter space.

Additionally, the empirically determined kinetic constants offer valuable insight into the reaction mechanism: although cadmium is solubilised through its chelation by thiolate groups from 3-MPA, which can itself act as a sulfur donor, TCEP=S remains the more reactive sulfur source for CdS formation. This enhanced reactivity is consistent with the improved emission properties observed, likely resulting from surface passivation by the reaction side product (*i.e.*, TCEP=O).

3.2.3 CdSe

The preliminary experiments conducted to form CdSe QDs are summarised in Figure 2.14, successfully transferred selenium to cadmium, as proved by XRD analysis (Figure 2.15). However, QDs were produced, without providing useful reaction insights.

A set of experiments was performed, covering a broader range of temperatures from 160 °C to 235 °C and residence times from 4 s to 60 s and can take in account the metrics introduced in Section 3.2.1. Samples were collected for each experimental coordinates, at steady state and analyzed by UV/Vis and fluorescence spectroscopy. For further experimental details, see Section 6.2.4.2.

The predictive modelling of the UV/Vis properties showed consistent trends and allowed to cover a bandgap from 393 nm to 589 nm. However, the emission properties were very poor and dominated by defect-related (pinned) emission. Indeed, the Stokes-shift peak remained poor and improvement could only be achieved by favouring the core growth, reducing the defects contribution.

For this reason, a protocol for a ZnS shell growth was sought. In addition to reduce the toxicity of the QDs, relevant for further bio-applications, it resulted in an impressive improvement of the Stokes-shifted emission. The experimental details are provided in Section 6.2.4.3.

3.2.3.1 CdSe peak position modelisation

Figure 3.12 shows the evolution of the first excitonic peak of CdSe as a function of the dimensionless time parameter θ_{norm}. The data were fitted using a one-parameter model (AIC = 172.47, BIC = 177.30), yielding a thermal sensitivity constant of 8839 K and an apparent activation energy $E_{a,\text{app}} = 73.49\ \text{kJ} \cdot \text{mol}^{-1}$.

The lowest peak position is 393 nm, remaining nearly constant up to $\theta_{\text{norm}} \approx 0.0006$, corresponding to the pre-nucleation stage. This plateau is followed by a rapid increase during the nucleation and early growth (*i.e.*, sigmoidal behaviour), eventually approaching 589 nm. The asymptotic value is significantly blue-shifted relative to the bulk CdSe bandgap (712 nm), indicating that particle sizes do not reach the bulk limit under the experimental conditions.

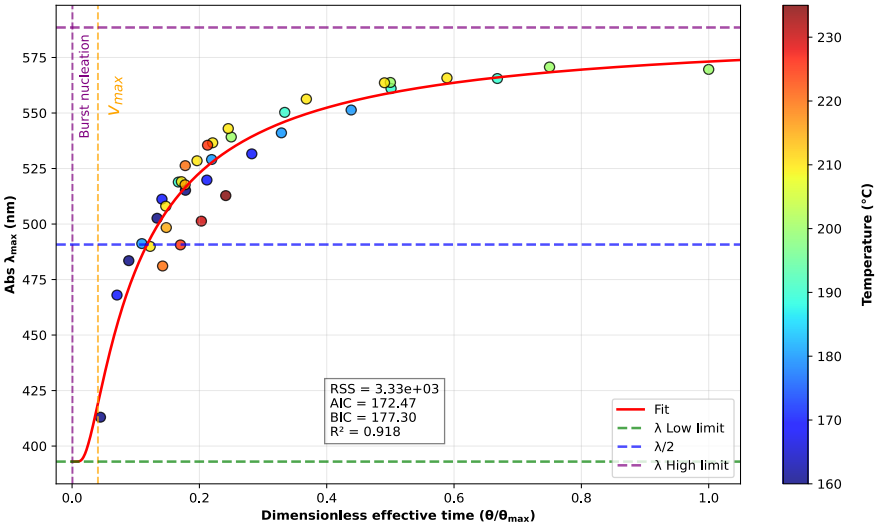

Figure 3.12. Modelling of the CdSe QDs peak absorbance position as a function of the dimensionless effective time. $E_0 = 393$ nm, $E_\infty = 589$ nm, $\alpha = 0.082$.

The analysis of derivatives of $E_{\text{peak}}(\theta)$ (Equations 6.1 and Section 6.2.5.1) allow associating θ_{norm} with the main Finke-Watzky stages. The results are summarized in Table 3.3.

These results suggest that all the Finke-Watzky phases remain limited to the early stages of the reaction, probably due to a faster reaction than CdS. This suggests that the reaction proceeds rapidly at the earliest stages, in the studied conditions, leading to an important consumption of reagents at the beginning of the reaction. This is in good agreement with the observation that the peak position accessible, that remain relatively far from the bulk CdSe bandgap.

Table 3.3. Association of dimensionless effective time θ_{norm} with the dominant FW mechanism phases.

Reaction Phase	θ_{norm} **range**
Induction phase	0 to 0.0006
Burst nucleation	0.0006
Growth acceleration	0.0006 to 0.041
v_{max}	0.041
Growth slow down	0.041 to 1 and beyond

3.2.3.2 CdSe absorbance over growth

Secondly, the first excitonic peak was investigated, its metrics (*i.e.*, absorbance and peak position) is associated with the DET. The absorbance values, that reflects the quantum dots concentration are presented in Figure 3.13.

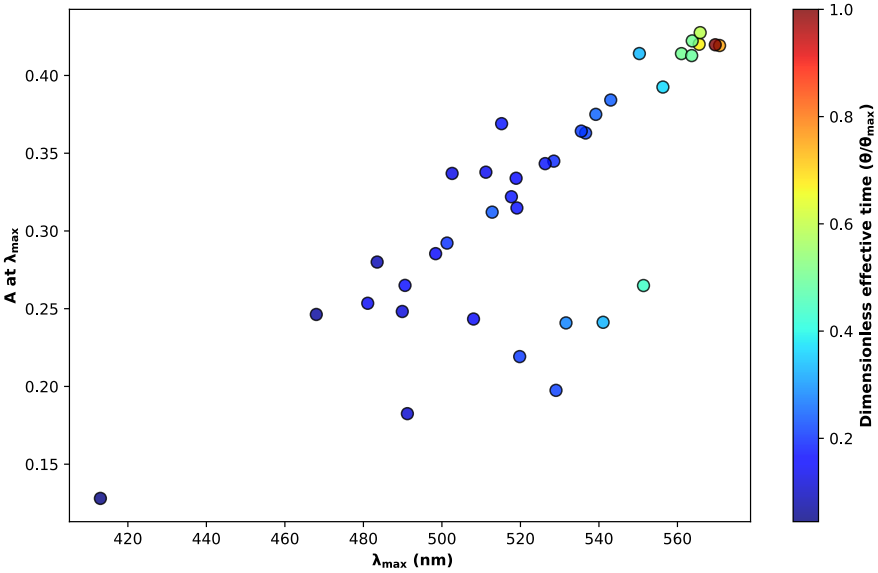

Figure 3.13. Absorbance values of CdSe QDs as a function of the first excitonic peak position, each point being associated with its DET value.

In the case of the CdSe synthesis, contrary to CdS, under more severe reaction conditions, the particles concentration increases constantly, almost in a linear way. This observation indicates that the upper nucleation threshold (*e.g.*, critical limiting super-saturation in Figure 1.14) is not reach during CdSe prepartion. Increasing the reaction conditions harshness still increases the QDs concentration.

3.2.3.3 CdSe Peak-to-valley ratio over growth

As an initial estimate of the size distribution, the P/V ratio was calculated for all CdSe samples using Equation 3.11. The resulting P/V ratio values are presented in Figure 3.14 as a function of the first excitonic peak position, each data point being associated with its corresponding DET value.

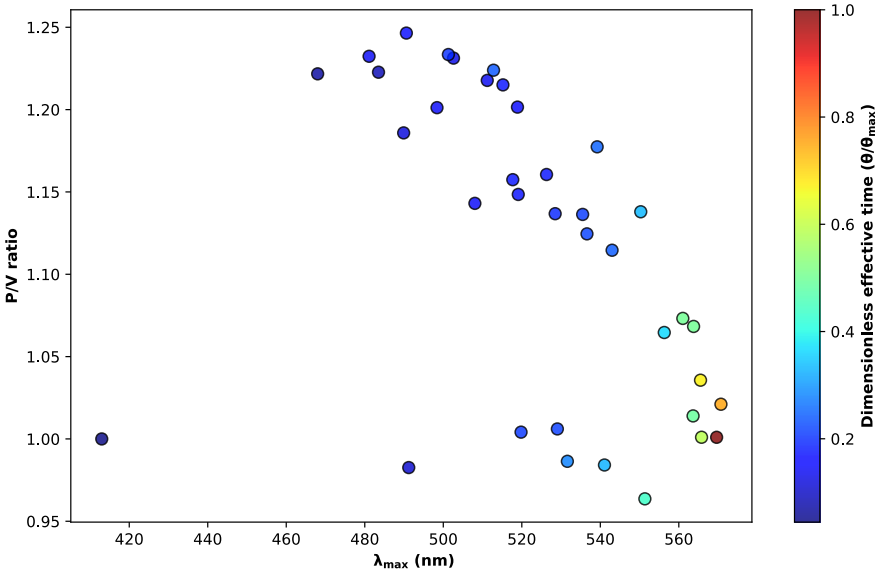

Figure 3.14. P/V ratio values of CdSe QDs as a function of the first excitonic peak position, each point being associated with its DET value.

Similarly to what was observed for CdS QDs, the P/V ratio steadily decreases as growth proceeds, reaching values close to unity. This behaviour suggests that the metric loses sensitivity once particles become larger, as the absorbance peak broadens and the valley becomes less defined. Consequently, the P/V ratio becomes less informative for evaluating size distribution at advanced growth stages.

3.2.3.4 CdSe emission intensity over growth

During the synthesis of CdSe QDs, and in contrast to CdS which only exhibited surface-related fluorescence, CdSe produced under more severe reaction conditions shows clear Stokes-shifted emission. This contribution becomes increasingly pronounced as the reaction conditions become harsher. To separate this component from trap-state emission, all emission spectra were fitted using a double Gaussian model, as illustrated in Figure 3.8. This approach enables independent analysis of the Stokes-shift emission and the trap-state contribution.

The first parameter examined was the peak emission intensity, presented in Figure 3.15.

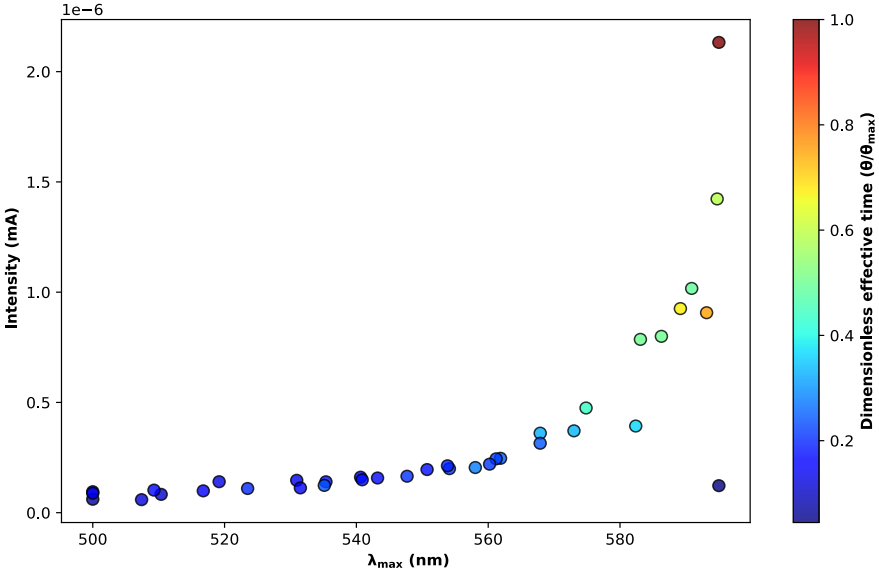

Figure 3.15. Emission intensity of CdSe QDs as a function of the first excitonic peak position, each point being associated with its DET value.

At early growth stages, corresponding to smaller particle sizes, the Stokes-shifted emission remains weak or barely detectable. As growth proceeds and the first excitonic peak red-shifts, the emission intensity increases strongly, following an approximately exponential trend. This behaviour is consistent with theoretical expectations: larger particles exhibit a lower surface to volume ratio, which reduces the relative contribution of surface-related (trap-state) emission. Consequently, the radiative recombination characteristic of the Stokes-shifted band becomes increasingly dominant, resulting in higher overall fluorescence intensity.

3.2.3.5 CdSe Stokes-shift emission contribution

This section examines the relative contributions of the two main emission types observed in CdSe QDs: the Stokes-shifted band and the surface trap-state emission. Their respective intensities were quantified using Equation 3.15. The resulting Stokes-shift emission proportion (in %) is plotted as a function of the emission peak position in Figure 3.16, with each data point associated with its corresponding DET value.

The observed trend mirrors the behaviour described in Figure 3.15. At early reaction stages, corresponding to smaller particle sizes, the Stokes-shifted contribution is nearly zero, indicating that the emission is dominated by

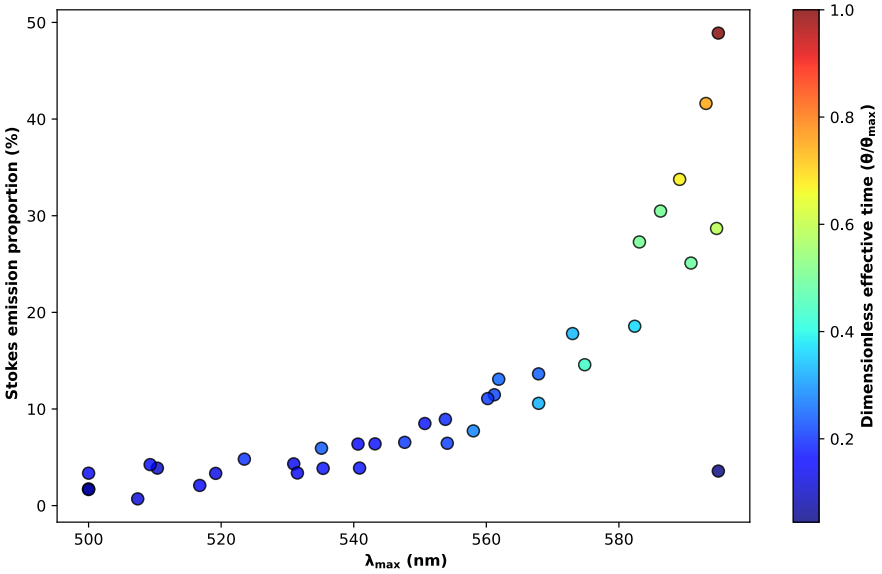

Figure 3.16. Stokes-shift emission proportion (%) of CdSe QDs as a function of the emission peak position, each point being associated with its DET value.

surface trap states. As the reaction progresses and the emission peak red-shifts, the Stokes-shift contribution increases sharply, approximately exponentially. This evolution is consistent with the reduction of surface defect influence as particle size increases, leading to a growing dominance of band-edge radiative recombination.

3.2.3.6 CdSe FWHM

In parallel with the P/V ratio analysis, the Gaussian fitting of the emission spectra also provides access to the Stokes-shift FWHM, which can be used as an additional indicator of size distribution. The FWHM values are presented in Figure 3.17 as a function of the Stokes-shift emission peak position, with each point associated with its corresponding DET value.

Although the data show some scatter, the overall trend appears opposite to that of the CdSe P/V ratio: the FWHM decreases steadily with increasing particle size, following an approximately linear trajectory from about 42 nm down to 35 nm. This behaviour reinforces the idea that the P/V ratio metric becomes less reliable for larger particles, whereas the FWHM provides a more consistent indication of spectral narrowing and improved size uniformity. More generally, this confirms that increasing particle size, similarly to the trend observed for the Stokes-shift contribution, has a beneficial effect on the optical properties of CdSe QDs.

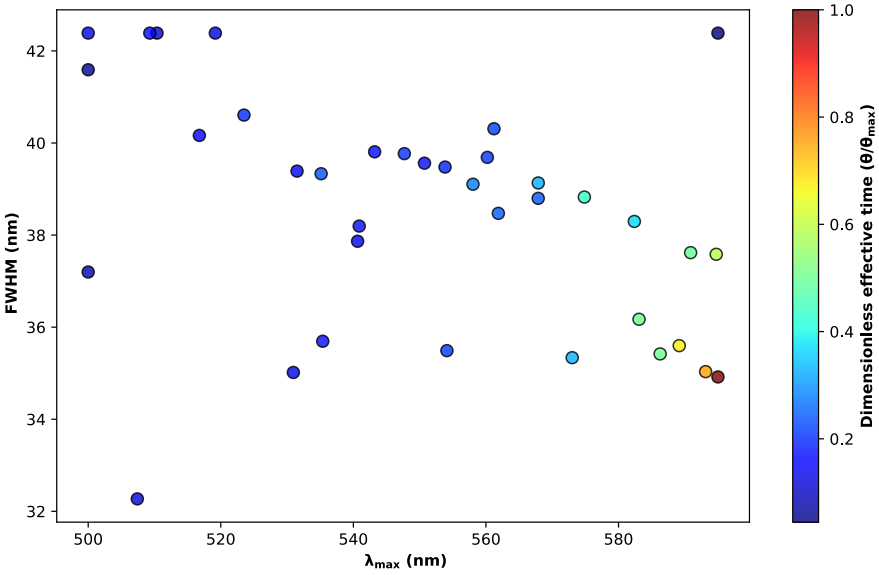

Figure 3.17. FWHM values of CdSe QDs as a function of the Stokes-shift emission peak position, each point being associated with its DET value.

3.2.3.7 Surface fluorescence issue

The conclusions are clear: increasing particle size improves the emission properties of CdSe QDs. However, trap-state emission is not completely suppressed, even for larger particles, and remains problematic when shorter-wavelength emission is required. A common strategy to mitigate this issue is the growth of a ZnS shell around the CdSe core, forming type-I CdSe/ZnS core–shell QDs, as described in Section 1.4.5. A schematic representation of this band-structure configuration is shown in Figure 3.18.

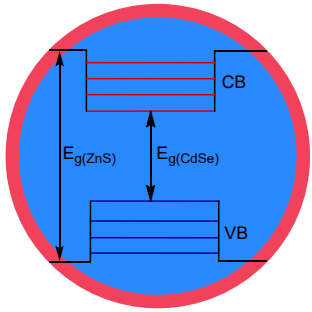

Figure 3.18. Bandgap scheme for type-I CdSe/ZnS core–shell QDs.

To address these limitations and fully exploit the optical potential of CdSe QDs, the synthesis of CdSe/ZnS core–shell structures was therefore undertaken.

3.2.3.8 CdSe/ZnS coreshell synthesis

To clearly illustrate the effect of shell growth, the CdSe core used in this study was synthesised at 190 °C with a residence time of 60 s. The ZnS shell formation was directly concatenated to the CdSe core synthesis, as depicted in Figure 3.19. Zinc chloride and thiourea (a more reactive sulfur source than TCEP=S) were used as precursors, and the temperature of the second reactor was kept deliberately low to avoid homogeneous nucleation of ZnS QDs. Further experimental details are provided in Section 6.2.4.3.

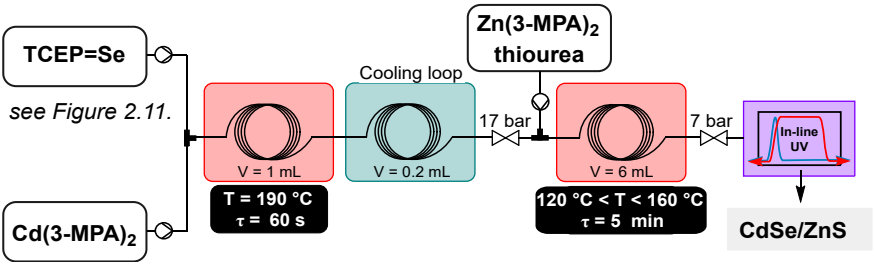

Figure 3.19. Concatenated process with the injection of Zn(3-MPA)2 and thiourea downstream the preparation of CdSe QDs.

Once the synthesis was completed, the samples were characterized *off-line* using UV/Vis absorption and emission spectroscopy. As for the CdSe QDs, the ratio of Stokes-shift to trap-state emission was calculated using Equation 3.15. The results are presented in Figure 3.20, where the Stokes-shift emission contribution is plotted as a function of the second reactor temperature (residence time: 5 min), with each point associated with the corresponding FWHM.

The curve exhibits a sigmoidal shape, with initial values close to 10 % Stokes-shift emission, which gradually increase and plateau above 50 %. The FWHM remains essentially constant, varying only slightly between 30 nm and 31 nm. This series of experiments demonstrates that the addition of a ZnS shell significantly enhances the emission properties of CdSe QDs without introducing notable drawbacks. Finally, it is important to note that the emission peak remains at a constant position (± 584 nm) during shell growth, supporting the hypothesis that core and shell growth processes are spatially separated.

3.2.3.9 HRTEM-EDX characterization

Following the parameters screening performed for the ZnS shell growth over the CdSe cores, the resulting nanoparticles were analysed by HRTEM and Energy-Dispersive X-ray (EDX) spectroscopy. The microscopy aimed to

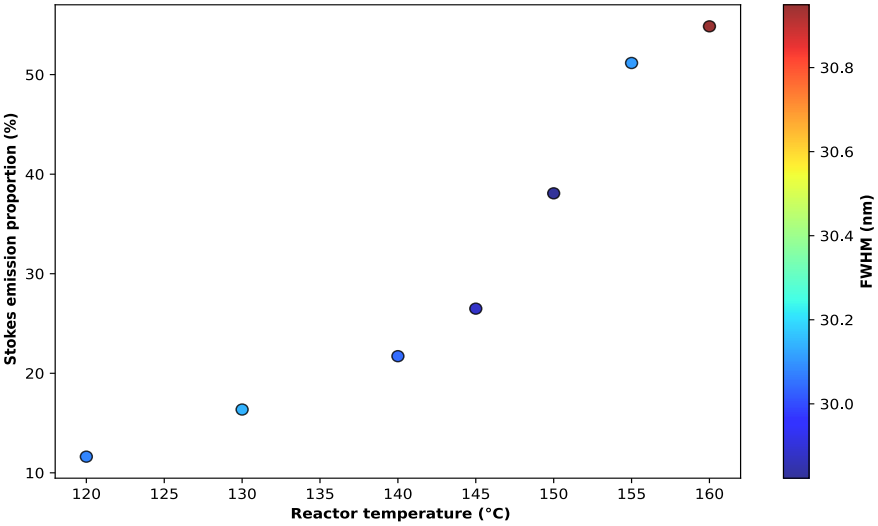

Figure 3.20. Effect of the temperature of the second reactor on the CdSe/ZnS QDs Stokes emission (%) and the peak FWHM. The peak position of the Stokes emission remained almost constant at 584 nm, corresponding to the CdSe core emission.

estimate the core and shell dimensions while EDX spectroscopy provided the elemental analysis of the atoms present in the nanoparticles.

To ensure reliable elemental analysis, the CdSe/ZnS QDs were purified by selective precipitation, followed by removal of the supernatant to eliminate unreacted precursors. The analytical results of the purified nanoparticles are presented in Figure 3.21.

The first observation made on the HRTEM is the egg-shell structure. Indeed, the CdSe cores being heavier they appear darker than the ZnS shell. In addition, some lighter particles are also visible, which suggest that a ZnS nucleation may occur in parallel of the shell growth.

The analysis of the HRTEM images from Figure 3.21 indicates that the CdSe average diameter of 2.8 ± 0.2 nm and a ZnS shell thickness of 1.2 ± 0.1 nm.

The EDX spectrum confirms the microscopy observations. All the expected elements are detected in the particles: Cd, Zn, Se, S. Traces of phosphorus are also observed, likely due to a ligation by the TCEP=O side-produced. Finally, the large amount of copper comes from the copper mesh grids used to support the sample.

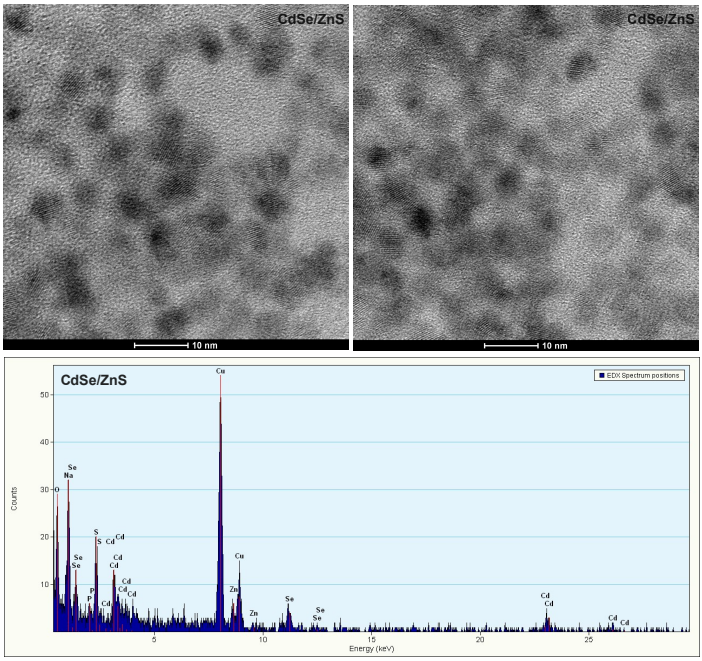

Figure 3.21. HRTEM images of CdSe/ZnS core–shell QDs (shell grown for 5 min at 160 °C) shown at the top, with the corresponding EDX spectrum displayed below.

3.2.3.10 Discussion

The empirical modelling performed on the UV/Vis absorption peak position for CdSe core formation shows an accessible range of bandgap accessible from 393 nm to 589 nm. This indicate that under the considered synthesis conditions the bulk bandgap (712 nm) cannot be reached. Furthermore, based on the Brus equation (1.4), the corresponding CdSe core size accessible range from 2.4 nm to 6.6 nm. Compared to the values reported in Table 1.11, ranging from 1.4 to 6 nm, the QDs obtained with TCEP=Se precursor are clearly in the upper size range.

The continuous increase in absorbance values (*e.g.*, QDs concentration) over the DET values confirms that the nucleation becomes burst-like. This trend approaches the ideal burst nucleation predicted by LaMer.

Regarding the emission properties of the CdSe core QDs, the peak intensity associated with the Stokes shift remains significantly limited for particles with a short DET, while its contribution increases exponentially as DET grows. This behaviour aligns well with the trap states described in Section 1.4.4.

Figure 3.16 highlights the dominant contribution of trap-state emission compared to the Stokes-shift emission. The trend of the Stokes contribution

aligns with the observed behaviour of the peak intensity. Therefore, the poor emission properties of the small CdSe core appear to be primarily limited by surface defects. The addition of a shell seems to be an appropriate solution to address this issue.

The analysis of the synthesized CdSe FWHM indicates that they typically range from 42 nm to 32 nm, with the majority falling between 40 nm and 34 nm. These values are slightly higher than those reported for the best CdSe cores in the literature, which typically range from 20 nm to 30 nm. [16]

For the emission properties improvement of the CdSe core, decision is made to concatenate the core formation with the growth of a ZnS shell. The experiments mostly aimed to tune the growth temperature to improve the Stokes emission of a given CdSe core. The results shown a significant improvement of the Stokes-shift emission. These positive results were coupled with consistentFWHM of around 30 nm, which aligns with the literature, while keeping the peak emission at the same position. This suggests that the growth shell is the only process taking place in the second reactor.

In addition to UV/Vis characterization of the CdSe/ZnS nanocrystals, HRTEM coupled with EDX spectroscopy was performed. This confirmed the egg-shell morphology of the QDs and allowed for the estimation of both core and shell dimensions. Finally, the elemental EDX analysis confirmed the presence of all the expected elements.

3.2.4 CdTe

The results obtained for CdTe QDs in the first part of this work, summarized in Figure 6.36 have shown that this type core has lower surface emission compared to CdS and CdSe, making it the most promising core formed.

Based on this observation, more experiments were carried out on this QD system than on the others. A set of experiments was performed, covering a broader range of temperatures from 130 °C to 200 °C and residence times from 15 s to 60 s, used to $\theta(t, T)$ calculation (introduced in Section 3.2.1), as well as the chalcogen excess, initial cadmium concentration and initial pH reaction. Samples were collected for each experimental coordinates, at steady state and analyzed by UV/Vis and fluorescence spectroscopy. In addition, the influence of chalcogen excess, initial cadmium concentration, and initial reaction pH was investigated. For further experimental details, see Section 6.2.4.4.

3.2.4.1 CdTe peak position modelisation

In this case, as for the other materials, temperature and residence time are reduced to a single effective parameter $\theta(t, T)$ using the one-parameter

model given in Equation 3.8. This dimensionality reduction is applied independently to each subset characterized by a unique combination of precursor concentration (C), chalcogen excess (Eq), and initial pH value (pH_0). The results are presented in Figure 3.22.

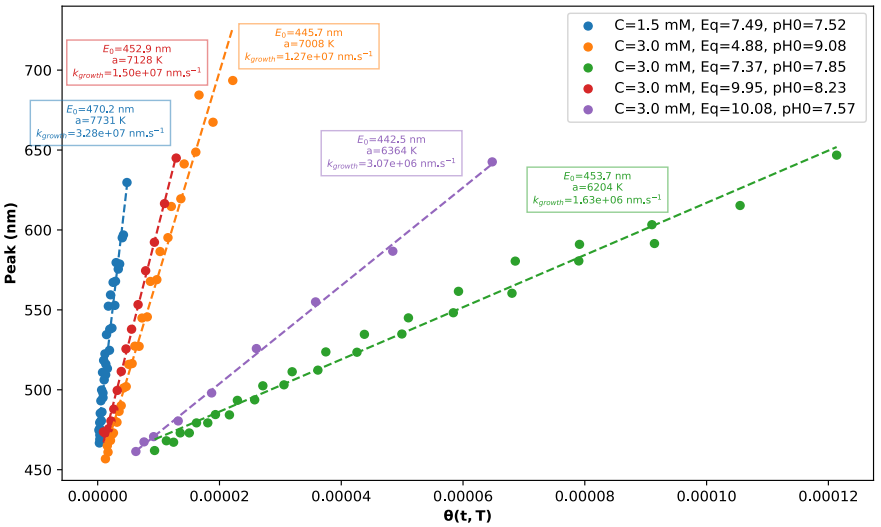

Figure 3.22. Modelling of the CdTe QDs peak absorbance position as a function of $\theta(t, T)$.

For CdTe QDs, a different data treatment was required. The correlation between E_{peak} and $\theta(t, T)$ is linear over the explored range, indicating that a simplified LaMer-type growth mechanism is more appropriate than a Finke–Watzky description. Consequently, the peak position evolution was modeled using the linear relation given in Equation 3.14, rather than the sigmoidal FW-type expression. The resulting fit parameters are summarized in Table 3.4.

Table 3.4. Model factors fit determined for CdTe QDs first excitonic peak, merits are presented in Table 6.15.

C (mM)	Eq	pH_0	a (K)	E_0 (nm)	k_{growth} ($nm.s^{-1}$)
1.5	7.5	7.52	7311.16	470.2	3.28e+07
3.0	5.0	9.08	7007.54	445.7	1.27e+07
3.0	7.5	7.85	6203.52	453.7	1.63e+06
3.0	10.0	8.23	7128.14	452.9	1.50e+07
3.0	10.0	7.57	6364.32	442.5	3.07e+06

Table 3.4 highlights several trends consistent with the experimental framework summarized in Figure 3.1. Lower cadmium concentration

(1.5 mM Cd(3-MPA)$_2$) leads to an initial peak position (E_0) red-shifted by approximately 20 nm compared to the 3.0 mM series, which can be attributed to delayed nucleation resulting from reduced monomer availability.

The initial pH value also strongly influences both the effective thermal constant and the crystal growth rate, with higher pH values (*e.g.*, 8.23 compared to 7.57) promoting faster growth kinetics. The influence of chalcogen excess appears to enhance reactivity as expected from kinetic considerations; however, this effect is partially convoluted with pH variations, making its isolated contribution more difficult to quantify.

3.2.4.2 CdTe absorbance over growth

The first excitonic peak was investigated, and its metrics (absorbance and peak position) were used to assess the DET. In particular, the absorbance values, which reflect the quantum dot concentration, are presented in Figure 3.23.

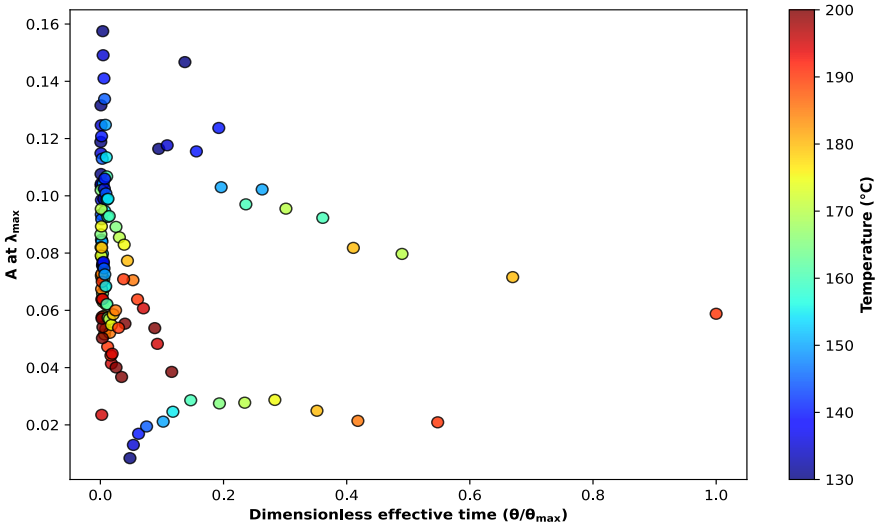

Figure 3.23. Absorbance values of CdTe QDs as a function of the first excitonic peak position, each point being associated with its DET value.

In most series, the particle concentration decreases fastly with increasing DET. The only exception is the series at C = 1.5 mM for the 45 s section, which shows a maximum before decreasing, illustrating the dynamic nucleation and growth processes. It is also clear that the reactions with the longest normalized θ values correspond to the lowest initial pH values ($\sim$7.5).

3.2.4.3 CdTe Peak-to-valley ratio over growth

Following the analysis of the absorbance values, the peak-to-valley ratio (P/V ratio) provides an initial estimate of the QDs size distribution and homogeneity. The P/V ratio was calculated for all CdTe samples using Equation 3.11. The resulting P/V ratio values are presented in Figure 3.14 as a function of the first excitonic peak position, each data point being associated with its corresponding DET value.

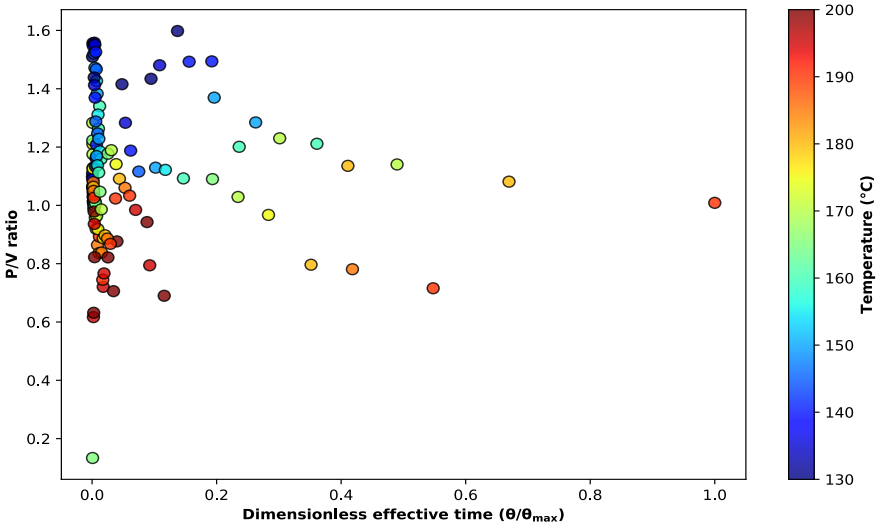

Figure 3.24. P/V ratio values of CdTe QDs as a function of the first excitonic peak position, each point being associated with its DET value.

Seamlessly compared to CdS and CdSe, CdTe despite its different growth mechanism exhibits a similar peak-to-valley behaviour, showing a continuous decrease. This trend appears to be mainly dictated by particle growth and is particularly relevant for smaller-sized quantum dots.

3.2.4.4 CdTe emission intensity over growth

The first parameter emission parameter that is examined is the peak emission intensity, presented in Figure 3.25. It is a first indication of the quantum efficiency of the particles formed. In contrast of CdS and CdSe, almost all the emission is Stokes-shift related. Only this emission is considered.

The evolution of the peak emission intensity shows trends similar to the absorbance values:

- A rapid increase with DET, particularly for the series with 3 mM of $Cd(3\text{-}MPA)_2$.

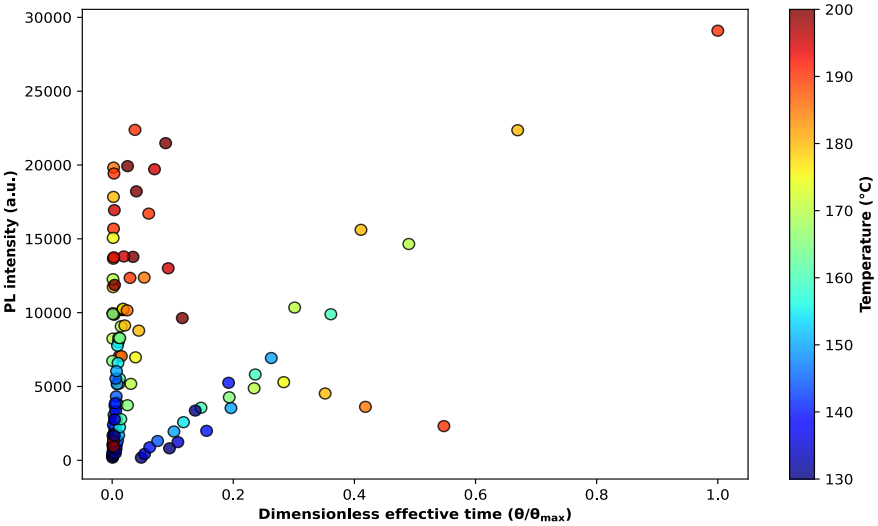

Figure 3.25. Emission intensity of CdTe QDs as a function of the first excitonic peak position, each point being associated with its DET value.

- Lower initial pH values tend to reduce the growth of the emission intensity.
- The series conducted at 1.5 mM of Cd(3-MPA)$_2$ exhibits signs of instability, likely leading to particle degradation and a corresponding loss of emission intensity.

Overall, the fluorescence intensity trends complement the absorbance measurements. Calculating the PLQY will provide a more complete picture of the emission efficiency and particle quality.

3.2.4.5 CdTe PLQY

The PLQY is a key metric that integrates information from both absorbance and emission spectra, calculated using Equation 3.16. For CdTe QDs, which exhibit significant emission, the PLQY provides a quantitative metric of the evolution of the emission efficiency during growth.

As expected, the emission intensity increases with the dimensionless effective time, indicating progressive particle growth and enhanced radiative emission. The only exceptions correspond to lower initial pH values and lower cadmium precursor concentrations, which limit the stability and emissive efficiency of the nanoparticles, as discussed in the previous section.

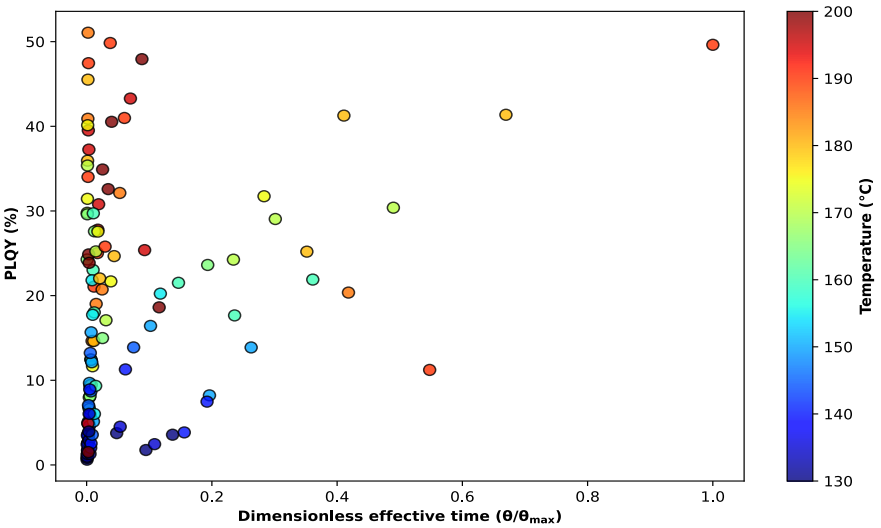

Figure 3.26. PLQY values of CdTe QDs as a function of the Stokes-shift emission peak position, each point being associated with its DET value.

3.2.4.6 CdTe FWHM

The FWHM is the last key parameter used to assess the quality of the synthesized QDs, as it reflects the size distribution of the particle population. Ideally, this metric should be minimized. The FWHM values are presented in Figure 3.27 as a function of the DET, with each point associated with its corresponding emission peak position.

In this case, a lower cadmium precursor concentration and a lower initial pH value lead to reduced FWHM values, indicating a narrower size distribution. This behaviour can be correlated with the lower particle concentrations observed in the absorbance measurements, which limit secondary growth and aggregation phenomena. The clear dependence of the FWHM on the emission peak position further confirms the strong relationship between particle size and size distribution, consistent with classical growth broadening mechanisms (see Figure 1.13).

3.2.4.7 Scale-up

Following the exploratory phase, a scale-up experiment was undertaken using updated experimental conditions, selected based on the trends identified in the previous sections.

The pilot scale-up setup is depicted in Figure 3.28 a. and b. (for more details, see Section 6.2.4.5). It consists of 2 concatenated reactors: an

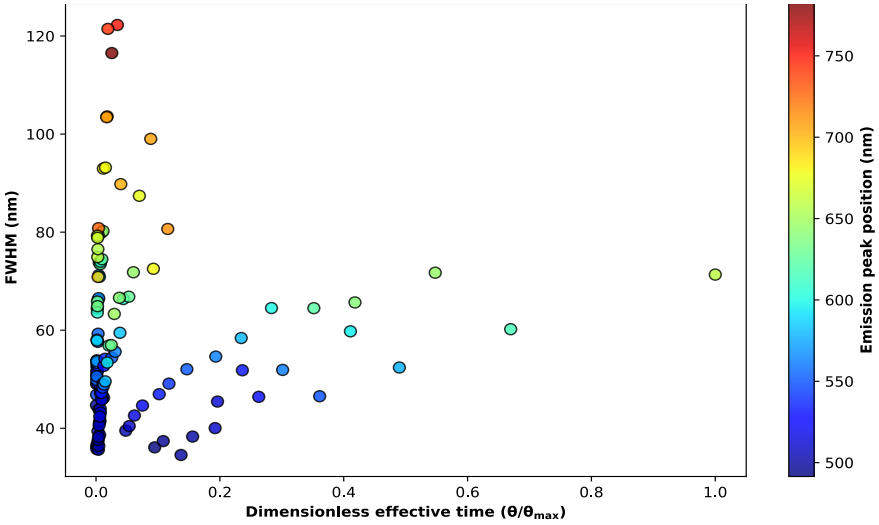

Figure 3.27. FWHM values of CdTe QDs as a function of the Stokes-shift emission peak position, each point being associated with its peak position value.

upstream generator of TCEP=Te, (see Figure 2.11), and a downstream mesofluidic reactor for the formation of the CdTe. The latter mesofluidic reactor is a commercial pilot scale unit (Corning® Advanced-Flow Reactor™G1 SiC, equipped with 6 Silicon Carbide fluidic modules connected in series and a 60 mL total internal volume). Post-reaction operations include a tube-in-tube heat exchanger, an *in-line* UV/Vis flow cell with a 5 mm optical pathway and a back pressure regulator prior to sample collection.

Samples were prepared at temperatures ranging from 130 °C to 190 °C, with residence times of 45 s or 60 s. The results indicated, similar to the lab-scale trials, that higher process temperatures and longer residence times resulted in larger particles (Figure 3.29). This was evidenced by a red shift in absorbance and emission peaks, along with an increased PLQY. However, this was counterbalanced by a broader size distribution, resulting in an increase in the FWHM.

The comparison between the results obtained with the microfluidic and mesofluidic setups highlights disparities. Metrics achieved by the mesofluidic reactor were lower than those observed in the microfluidic setup. Specifically, the emission range was narrower, spanning from 500 nm to 600 nm compared to 500 nm to 650 nm. The PLQY was also reduced, reaching approximately 18%, vs. 40% at an emission of 600 nm under microfluidic conditions. Additionally, size distribution metrics were less favourable in the mesofluidic setup, with a FWHM ranging from 40 nm to 70 nm compared to 35 nm to 60 nm. This disparity was attributed to the much higher turbulence within the mesofluidic reactor. High turbulence are likely to accelerate the recombination of nuclei, resulting in higher QD concentrations but with smaller particles

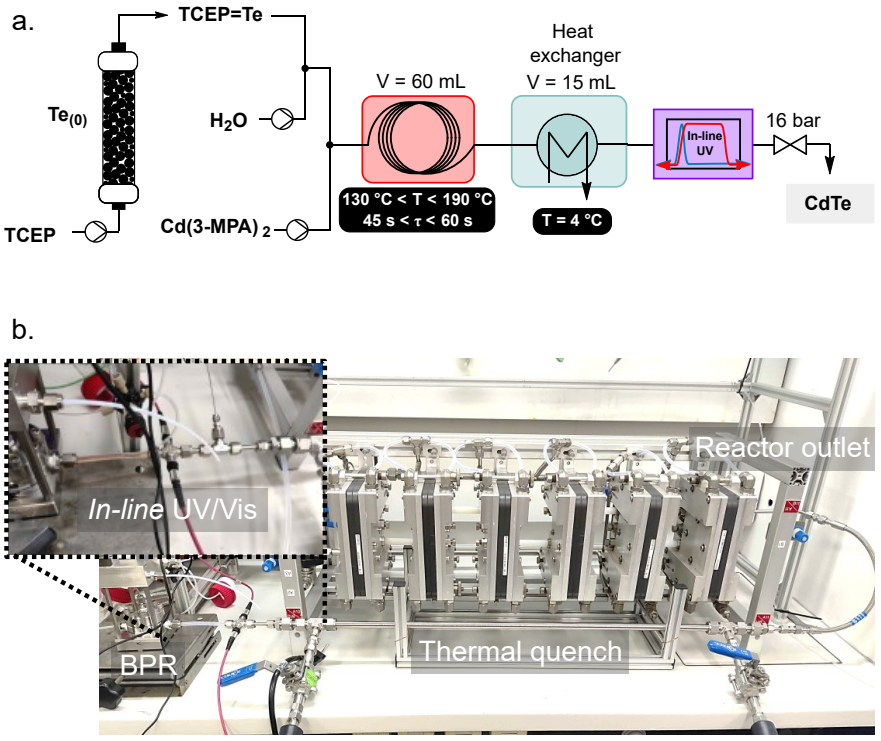

Figure 3.28. (a) Simplified flow chart of the mesofluidic setup used for the scalability trials toward CdTe (b) photograph of the experimental setup, featuring a Corning® Advanced-Flow Reactor™G1 SiC (60 mL of internal volume).

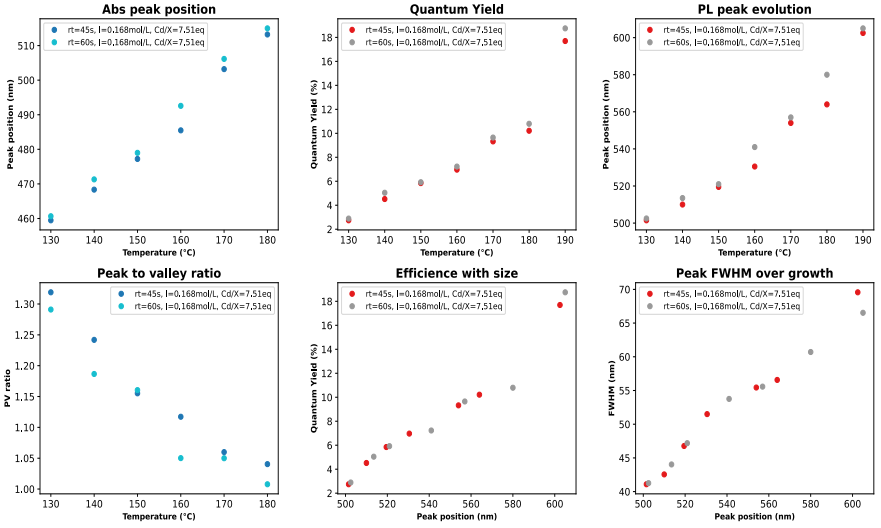

Figure 3.29. Comparison of the CdTe QDs main characteristics (prepared at temperatures ranging from 130 °C to 190 °C and residence times of 45 s or 60 s).

under similar reaction conditions. Nevertheless, this scale-up demonstrates the relevance of the concatenated approach, enabling the production of CdTe QDs at a rate of 80 mL.min^{-1}. As it is, the mesofluidic process allows the preparation of up to 40 g.day^{-1} of CdTe QDs with a relative PLQY of 18%.

3.2.4.8 Discussion

The modeling performed to predict the absorbance peak position differs from that of CdS and CdSe, as the position is a linear function of $\theta(t, T)$, indicating the formation of the CdTe core via an ideal LaMer mechanism. The peak position ranges from 442 nm to 700 nm, which can be translated, using the Brus equation, into particle sizes ranging from 1.6 nm to 6.7 nm. This versatility is unmatched by the literature overview presented in Table 1.11, which shows, at best, a size range from 3.1 nm to 6.4 nm.

The absorbance values tend to decrease with the increase of the DET. This is in good agreement with the LaMer mechanism: a burst nucleation process followed by a growth phase. Under harsher conditions, nucleation is quickly completed, leaving reagents available for further growth, while milder conditions lead to a higher concentration of particles and less particle growth.

In the emission field, the results are in good agreement with the UV/Vis observations. The fluorescence intensity increases with the harshness of the experimental conditions (*e.g.*, high temperature and high DET). This is due to the limited surface traps, which penalize the Stokes-shift emission, induced by significant growth.

The PLQY results emphasize the emission intensities, with values ranging from a few percent up to 50%. These values are typically in the upper average range for aqueous synthesis, plateauing at 53%. The results also show that longer DET limit the improvement of PLQY, which may be due to degradation.

The size distribution of the CdTe is, however, less favourable, with FWHM values rising up to 120 nm. These values are far too high for sensitive applications and should be closer to 30-40 nm. [16] These high values may be related to an uncontrolled growth process, as described in Figure **??**, leading to a broadening regime controlled by diffusion. One possible solution could be to improve the reactor design or attempt to spatially separate the nucleation and growth phases, allowing them to proceed at different temperatures.

The promising results obtained regarding size range flexibility and high PLQY make the transposition to a pilot-scale reactor interesting to demonstrate the scalability of the process. The experiments conducted were a transposition of one of the microfluidic cases. Overall, the reactor achieved impressive productivity, producing up to 40 g of CdTe QDs per day. A comparison of the metrics (*e.g.*, size range, PLQY, and FWHM) between

microfluidic and mesofluidic systems shows better metrics under microfluidic conditions. These lower results must be attributed to the scale change. Indeed, in the mesofluidic reactor, the flow regime is turbulent rather than laminar. The thermal homogeneity in a larger reactor is also more difficult to control. These factors may have contributed to the decline in QD quality metrics.

3.3 Mechanism insights

This section is dedicated to identifying the potential mechanistic pathway by which the new ternary phosphine acts as a chalcogen donor to the cadmium complex. The mechanism is here studied exclusively within the framework of organic synthesis. It is generally accepted that the reaction proceeds as follows: the chalcogen–ternary phosphine complex ($X{=}PR_3$) coordinates to the cadmium precursor (CdR_2). The resulting complex then undergoes thermal decomposition, yielding CdX, the oxidized phosphine ($O{=}PR_3$), and, depending on the nature of the stabilizing group (R_2), possible side products, as illustrated in Figure 3.30 [17–19].

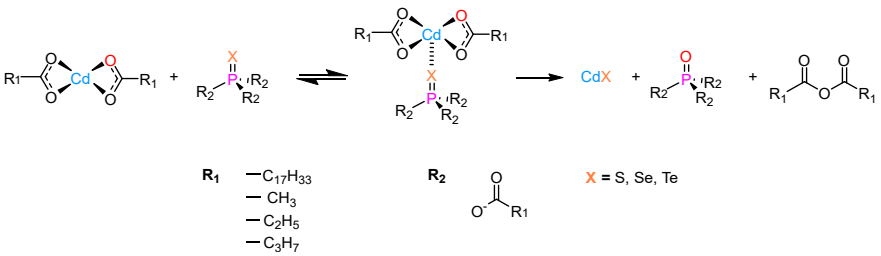

Figure 3.30. Mechanism formalized by Liu *et al.* in an organic solvent.

In this mechanism, the oxygen atoms originate from the carboxylate functions that stabilize the cadmium precursor. In aqueous systems, however, multiple potential oxygen sources exist, making the identification of the active species more challenging.

3.3.1 Isotopic labelling with $^{18}O-$water

To identify the inherent mechanistic features for the preparation of CdTe, the synthesis was performed in $^{18}O-$water. According to the literature focusing on organic phosphine-chalcogenide sources, [18, 20] it is generally accepted that cadmium and chalcogen sources form a complex in the initial stage of the reaction. Subsequently, this complex encounters an oxygen donor that polarizes the phosphorus–chalcogen bond leading to its rupture. This results in a cadmium–chalcogen bond and the corresponding phosphine oxide (here, $TCEP{=}O$).

The hypothesized mechanism is illustrated in Figure 3.31. In this scenario, the oxygen donor would be the solvent itself, water. It is supported by the pH variation observed along the reaction (*e.g.*, pH rises during the reaction).

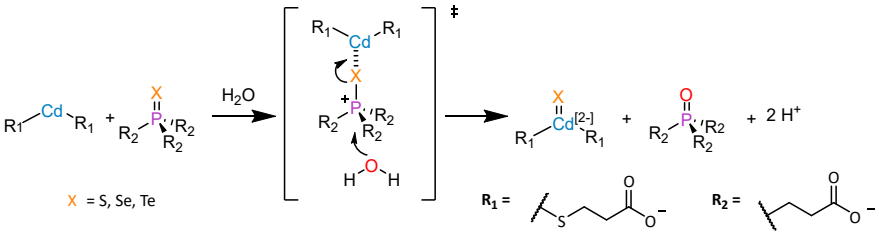

Figure 3.31. Hypothesized mechanism for CdX QDs formation in aqueous media.

To validate this hypothesis, a CdTe synthesis was carried out in ^{18}O-labelled water. After the reaction, the CdTe QDs were separated by sedimentation and the supernatant was analyzed by LC-MS (Figure 3.32 and described in Section 6.2.5.8). The mass spectra are compared with a reference peak of TCEP^{16}O.

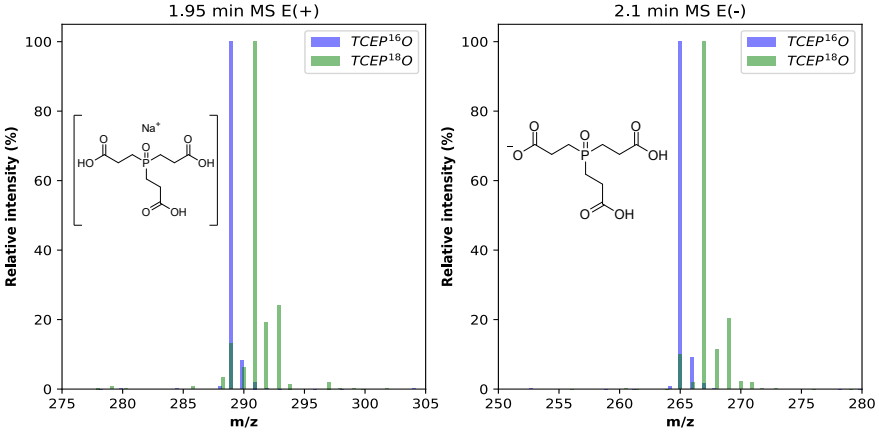

Figure 3.32. Mass spectra of TCEP^{18}O obtained from synthesis using labelled ^{18}O−water and a reference of TCEP^{16}O.

A +2 shift in the molecular ion was observed between the reference TCEP^{16}O and the TCEP^{18}O produced during the experiment. This observation confirms that in aqueous media, water serves as the oxygen donor, whereas in organic media, acetate is typically the donor. [18, 20] It also accounts for the pH decrease observed during our optimization under aqueous conditions. Accordingly, the next step is to investigate the pH sensitivity of the system and its influence on the reaction pathway.

3.3.2 Precursors pH-titration

A first attempt to assess the pH effect on the reaction system was conducted by acidic titration (using concentrated HCl) of various basic feeds: TCEP=X alone, TCEP=X with $Cd(3\text{-MPA})_2$, and $Cd(3\text{-MPA})_2$ alone. The titration was started at pH ∼12 to ensure that all pH-sensitive functions were fully deprotonated. HCl was added gradually, and the pH was measured after each addition. The results are presented in Figure 3.33.

A new parameter, the pH resistance (Δ), is introduced in this curve. It is defined as the variation in proton concentration, $[H^+]$, divided by the corresponding variation in pH:

$$\Delta = \frac{\Delta[H^+]}{\Delta pH}$$

This parameter quantifies how the proton concentration changes relative to pH variations, providing insight into the buffering capacity of the system. For further experimental details, see Section 6.2.4.6.

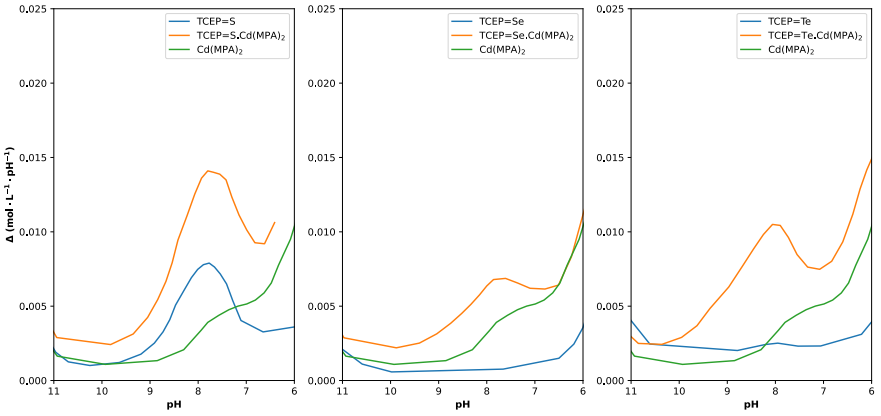

Figure 3.33. pH titration of each chalcogen transfer agent with (orange curve) and without cadmium precursor (blue curve), and of cadmium precursor alone (green curve) using concentrated HCl.

The orange curve (TCEP=X with $Cd(3\text{-MPA})_2$) is expected to correspond to the sum of the individual titration curves of TCEP=X and $Cd(3\text{-MPA})_2$, if no interaction occurs between the two species. Deviations from this additive behavior indicate the possible formation of new pH-active functions, which may provide insight into complexation.

The observations are split by chalcogen type:

- **Sulfur (TCEP=S):** The orange curve closely matches the sum of the individual curves of TCEP=S and Cd(3-MPA)$_2$. In the pH range 11 to 6, a peak is visible in both TCEP=S and the mixture, corresponding to sulfur protonation as shown in Equation 3.19. The similar behavior in both cases suggests that no significant complexation occurs between TCEP=S and Cd(3-MPA)$_2$.

$$\mathrm{TCEP{=}S} + \mathrm{H^+} \underset{\mathrm{H_2O}}{\overset{\mathrm{Ka_S}}{\rightleftharpoons}} \mathrm{TCEP^+{-}S{-}H} \tag{3.19}$$

- **Selenium (TCEP=Se):** The interpretation is less clear. The orange curve shows partial overlap with the sum of the individual components, but the origin of the observed peak remains ambiguous. Complementary Raman measurements are necessary to provide a more definitive assessment.

- **Tellurium (TCEP=Te):** The orange curve exhibits a new broad pH-active signal that is absent in the individual reagents. This behavior is consistent with the formation of a complex between TCEP=Te and Cd(3-MPA)$_2$, as suggested in Equation 3.20.

$$\mathrm{TCEP{=}Te} + \mathrm{Cd(3\text{-}MPA)_2} \underset{\mathrm{H_2O}}{\overset{\mathrm{Kf_{Te}}}{\rightleftharpoons}} \mathrm{TCEP{-}Te{-}Cd(3\text{-}MPA)_2} \tag{3.20}$$

The results obtained from the basic pH-metric titration are already informative. While the selenium derivative yields an ambiguous interpretation, the tellurium system exhibits a clear new pH-active signal indicative of complex formation. To resolve the uncertainties with selenium, complementary Raman measurements at each pH are necessary. These observations collectively highlight the chalcogen-dependent interactions with Cd(3-MPA)$_2$ and motivate further mechanistic investigation, particularly for tellurium, in the following section.

3.3.3 Precursors Raman monitoring

To extract as much information as possible, the titration was carried out in two stages. First, the TCEP=X precursor was placed in an argon-inerted flask, and the Cd(3-MPA)$_2$ precursor was added stepwise to monitor any potential chelation at basic pH ($\sim$ 12). Second, the pH titration was performed by gradual addition of concentrated HCl. After each addition, a Raman spectrum was recorded from 300 cm^{-1} to 1800 cm^{-1}. This procedure was repeated for each chalcogen system. For further experimental details, see Section 6.2.4.6.

The first results analyzed were the pH-metric curves. To assess the reproducibility of the process and to confirm the observations made in the

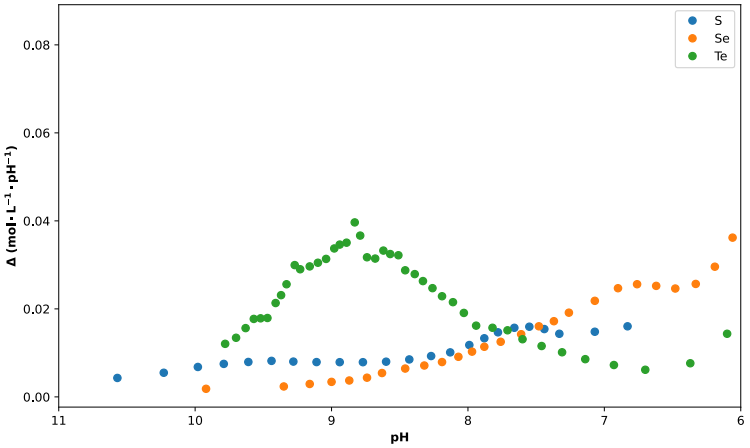

Figure 3.34. pH titration of each chalcogen transfer agent using concentrated HCl during the parallel Raman analysis.

previous section, the pH data are presented here as the pH resistance (Δ) as a function of pH, as shown in Figure 3.34.

The observations from this experiment are consistent with those in Figure 3.33: sulfur exhibits a small signal, likely corresponding to the protonation of TCEP=S; selenium shows a signal that remains ambiguous; and tellurium displays a pronounced peak, likely indicative of complexation between TCEP=Te and Cd(3-MPA)$_2$.

Prior to the HCl addition, Cd(3-MPA)$_2$ was incrementally added to reach the desired stoichiometry relative to the TCEP=X species. After each addition, a Raman spectrum was recorded, providing valuable information on whether complexes form between Cd(3-MPA)$_2$ and TCEP=X under basic conditions. All spectra are presented in Figure 3.35. It should be noted that changes in Raman intensity upon cadmium addition are mainly due to dilution effects. Therefore, the discussion will focus primarily on spectral shifts and the emergence of new vibrational bands rather than on intensity variations.

The discussion of the results will focus primarily on the analysis of the P=X bond, which was thoroughly described in Section 2.3.2.2. Any shifts in these vibrational frequencies may be attributed to the complexation involving the P=X bond.

These results confirm that sulfur and selenium do not exhibit shifts in their P=X bonds, reinforcing the idea that they do not interact with the added Cd(3-MPA)$_2$. However, in the case of tellurium, a new frequency band appears alongside one of the P=Te bands, providing a strong indication of an interaction between P=Te and cadmium, likely forming $R_3P-Te-Cd$.

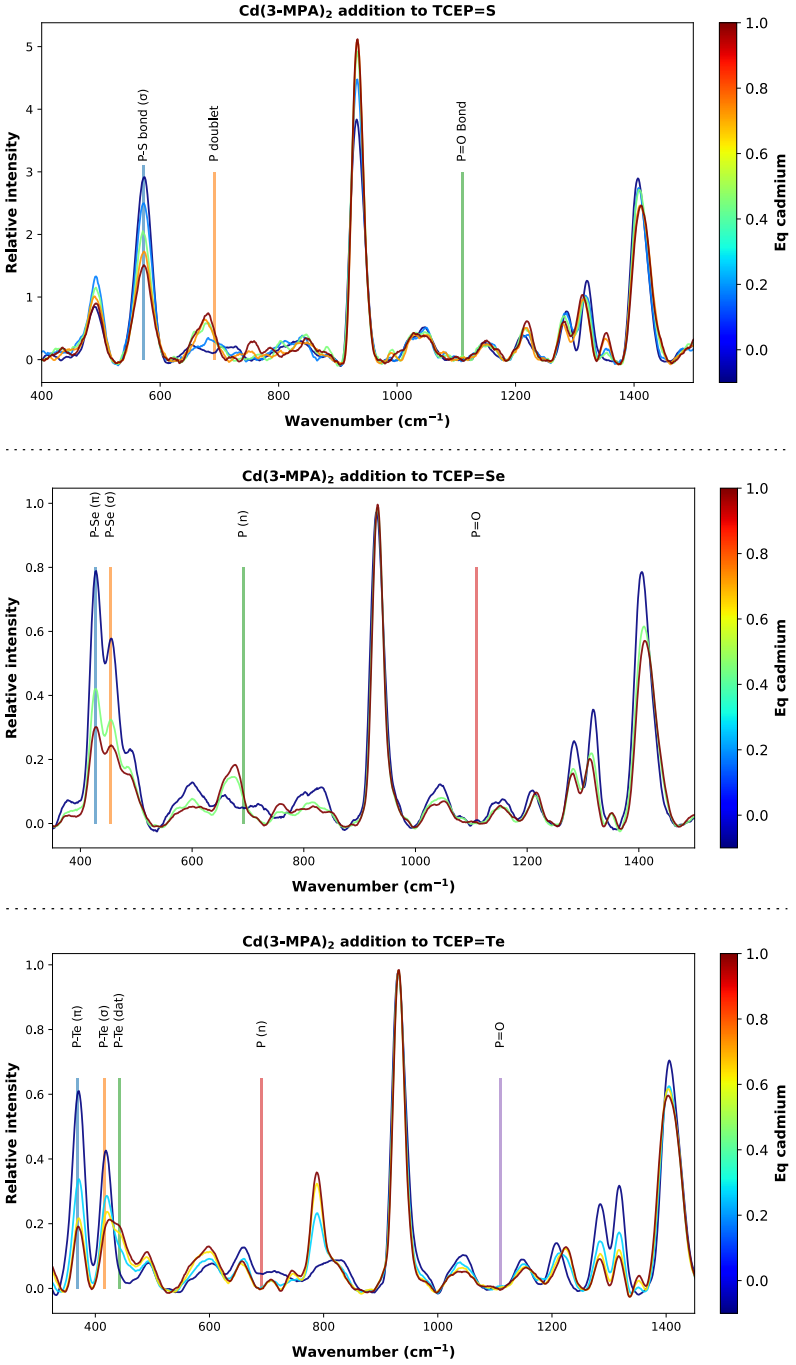

Figure 3.35. Raman visualization of the interaction between TCEP=X and Cd(3-MPA)$_2$ as a function of cadmium equivalents for sulfur (top), selenium (middle) and tellurium (bottom). Variations in absolute intensity are mainly attributed to dilution effects upon cadmium addition.

The spectra of the chalcogens also suggest that the nature of the bond evolves with the atom period. The P–S bond shows a single frequency at 572 cm^{-1}; given that the atoms are in the same period, which favors efficient orbital overlap, this bond is predominantly a σ bond. Additionally, TCEP−S was the only derivative exhibiting protonation upon HCl addition, as shown in Figure 3.33.

Selenium exhibits a double frequency band at 427 cm^{-1} and 454 cm^{-1}, which can be assigned to π and σ contributions, respectively. During $Cd(3\text{-}MPA)_2$ addition, these frequencies remain stable, and no additional side bands appear, indicating that selenium does not interact with cadmium and therefore no complexation occurs.

Finally, the tellurium spectra also show two frequencies at 369 cm^{-1} and 416 cm^{-1}, corresponding to π and σ bonds, respectively. Upon addition of $Cd(3\text{-}MPA)_2$, a new band grows at 442 cm^{-1}, which can be attributed to tellurium–cadmium complexation. This hypothesis is further supported by the decrease in the π contribution, likely due to electron redistribution resulting from complex formation.

After completing the addition of $Cd(3\text{-}MPA)_2$ to the TCEP=X solution, the mixture was acidified stepwise by HCl to reproduce the conditions shown in Figure 3.33, while monitoring via Raman spectroscopy. Following each HCl addition, a Raman spectrum was recorded. In these experiments, intensity variations are only mildly affected by dilution, as the added HCl volume is small relative to the total solution volume.

The observed changes over time are consistent with the previous discussion. Sulfur and selenium exhibit only minor spectral variations, particularly in the region of the P=X bond, confirming that these derivatives do not complex with $Cd(3\text{-}MPA)_2$. The P=X bond remains stable down to pH 6.

The tellurium spectra further confirm the previous results. The band at 442 cm^{-1} increases in intensity while the 369 cm^{-1} band decreases. Another subtle feature appears at 1110 cm^{-1}, corresponding to $R_3P{=}O$. [21] During HCl addition, the mixture turned yellowish, indicating that nucleation begins at room temperature solely due to pH change. This suggests that protons act as a catalyst for the reaction. These trends are even more apparent in Figure 3.37.

From these data, it is clear that the P=Te π contribution is converted into the P-Te-Cd complex (blue curve to green curve), while the TCEP=Te reagent is consumed and converted into TCEP=O via conversion of the P-Te σ into the P=O bond. This provides valuable mechanistic insight: at room temperature, a simple pH increase can initiate nucleation. This confirms that P=Te forms a complex with $Cd(3\text{-}MPA)_2$, generating a new pH-sensitive center. Likely, through its protonation equilibrium, it polarizes the P-Te bond,

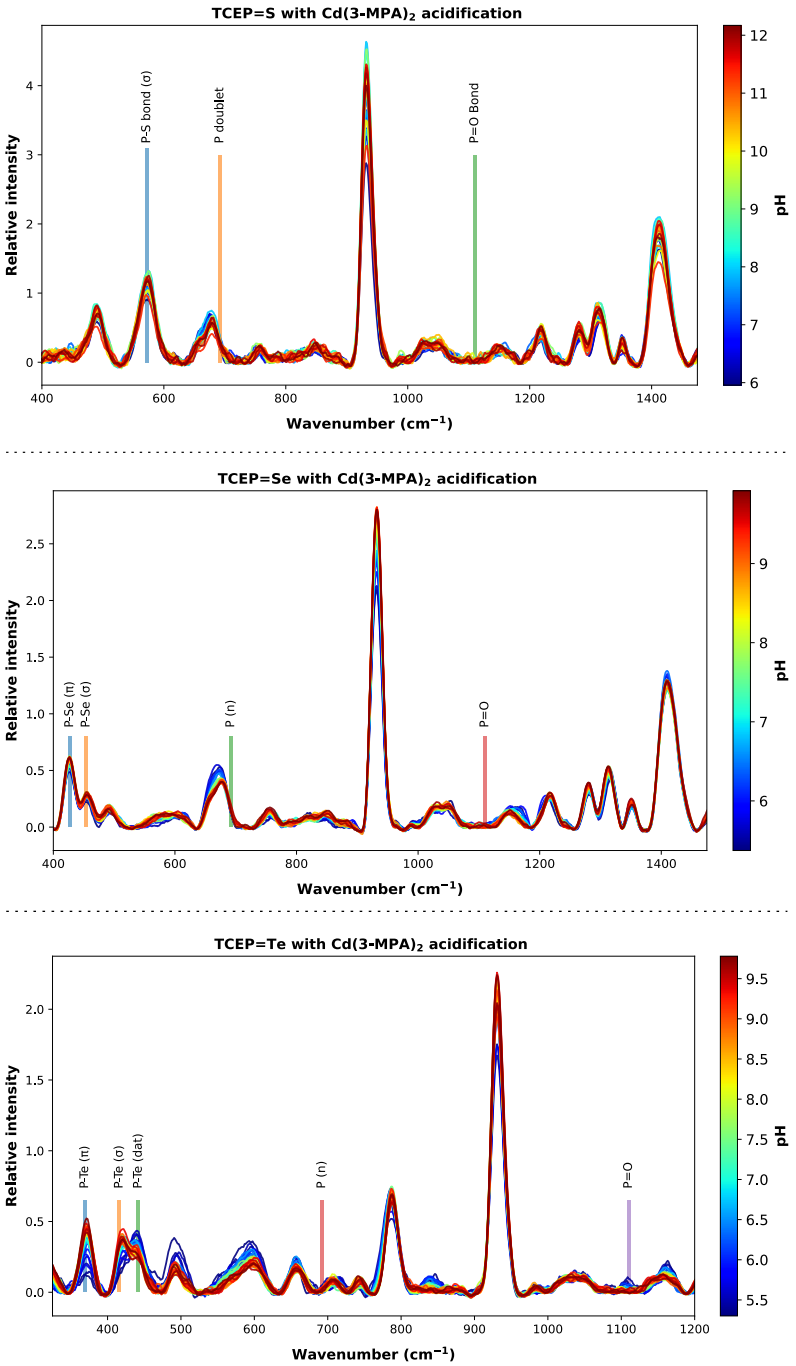

Figure 3.36. Raman monitoring of the interaction between TCEP=X and Cd(3-MPA)$_2$ as a function of medium acidification for sulfur (top), selenium (middle) and tellurium (bottom).

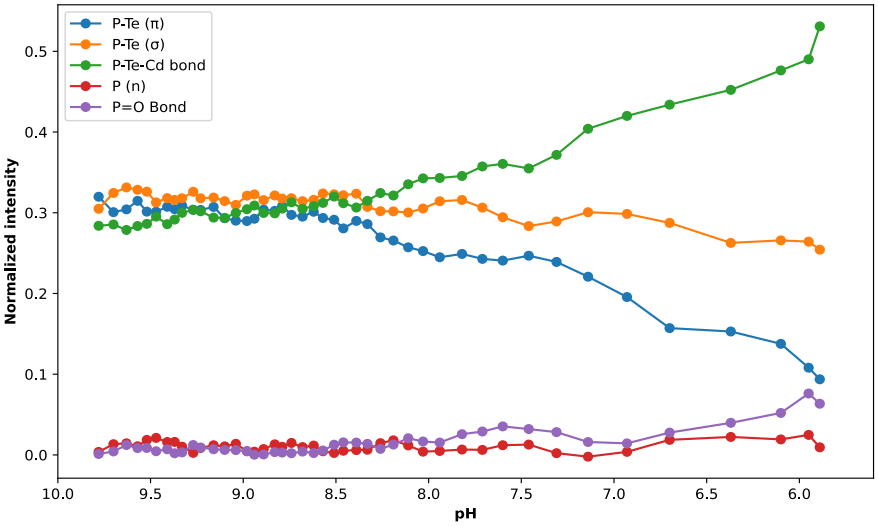

Figure 3.37. Raman intensity variations over HCl addition of various P=X related peaks.

weakening it and facilitating oxidation of TCEP by water, as described in Section 3.3.1.

3.3.4 XPS Surface Analysis

To further investigate the surface chemistry of the colloidal CdX (X = S, Se, Te) nanocrystals, X-ray photoelectrons spectroscopy (XPS) measurements were performed. Although no phosphorus 2p signals indicative of ligand–metal interactions were observed, likely due to desorption under high vacuum, XPS revealed unsaturated cadmium sites at the QD surface. Significant carboxylate signals were detected, arising from surface ligands such as 3-MPA, TCEP=O, and acetate counterions.

Quantitative analysis of the XPS spectra is summarized in Table 3.5, which reports binding energies (B.E.), full-width at half-maximum (FWHM), surface atomic concentrations, and Cd:X ratios.

Figure 3.38 highlights the characteristic XPS spectra for the different orbital families across the three QD compositions. Each column represents a distinct material, while each row corresponds to a specific orbital. The nanocrystal surfaces are generally non-stoichiometric, with Cd:X ratios below unity, indicative of a chalcogen-rich surface.

For CdTe, the additional Te[IV] peak (575.7 eV) signals partial surface oxidation, which may influence electronic and chemical properties. The C 1s and O 1s spectra reveal multiple organic functional groups, mainly

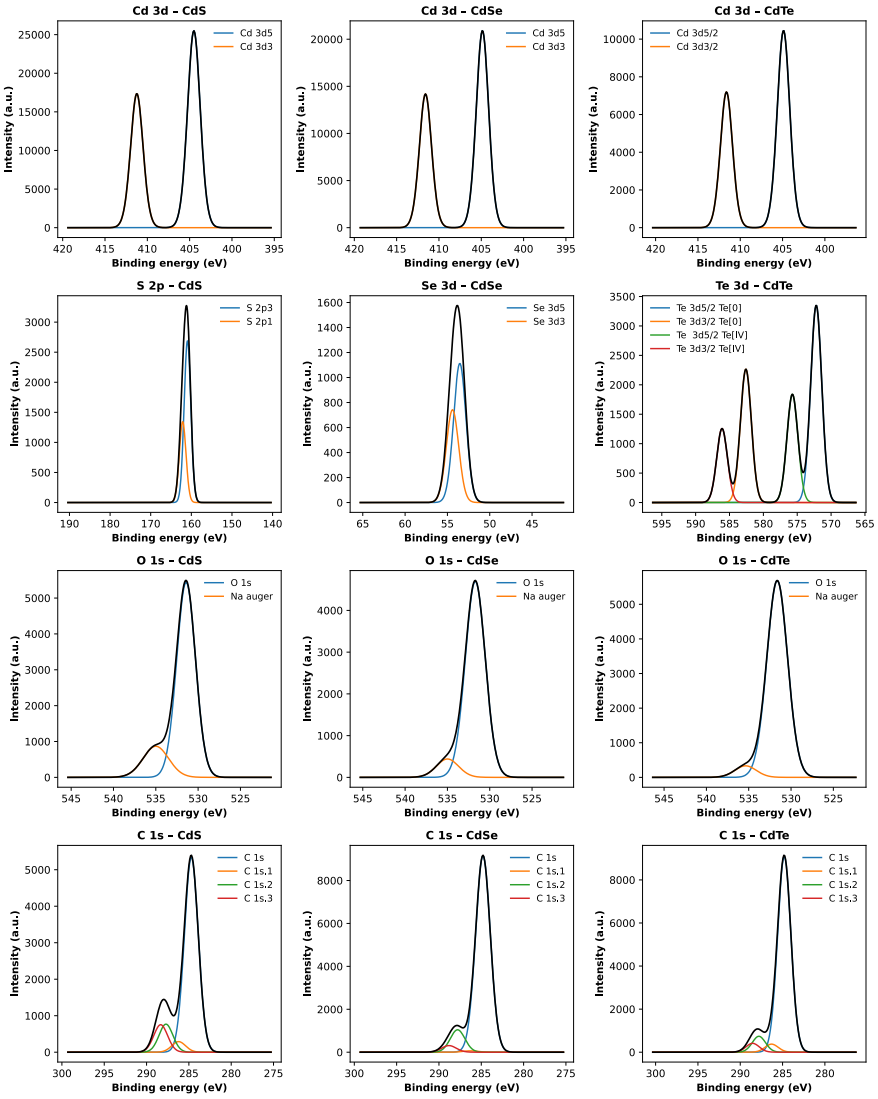

Figure 3.38. XPS analysis of CdX core (X = S, Se, Te). Each column corresponds to a distinct material (CdS, CdSe, CdTe), while each row represents the analyzed orbital families: *Cd 3d*, chalcogen (*S 2p*, *Se 3d*, *Te 3d*), oxygen (*O 1s*), and carbon (*C 1s*) signals.

Table 3.5. XPS analysis of CdX (X = S, Se, Te) QDs: Binding energy (B.E.), FWHM, surface atomic concentration (%), and surface atomic ratio. C 1s and O 1s contributions mainly originate from surface ligands such as 3-MPA and TCEP.

Material	Element/Group	B.E. (eV)	FWHM (eV)	Conc. surf. (%)	Ratio X/Cd
CdS	S $2p_{3/2}$	161.0	1.9	17.8	
	Cd $3d_{5/2}$	404.5	1.8	12.9	1.06
	O 1s / C 1s	531.4 / 284.8	2.1 / 1.7	13.7 / 42.8	
CdSe	Se $3d_{5/2}$	53.5	1.7	14.7	
	Cd $3d_{5/2}$	404.9	1.7	9.3	0.38
	O 1s / C 1s	531.7 / 284.8	2.0 / 1.9	6.8 / 52.0	
CdTe	Te $3d_{5/2}$ (Te^{IV})	575.7	1.9	0.7	
	Te $3d_{5/2}$ (Te^{0})	572.2	1.9	1.3	
	Cd $3d_{5/2}$	404.9	1.7	20.3	0.40
	O 1s (O=C-O, C-O)	531.6	2.9	2.1	
	C 1s (C-(C,H), C=O)	284.8	1.8	51.1	

carboxylates and carbonyls from ligands, emphasizing their role in colloidal stability and surface chemistry. This combined analysis underscores the chemical complexity of CdX QD surfaces and the importance of passivation for optoelectronic properties.

3.3.4.1 Mechanism Discussion

The series of experiments described above converge toward a comprehensive explanation of the overall reaction mechanism. A summary of the key findings is presented below:

- **Isotopic labelling:**

  Isotopic labelling using $^{18}O-$water revealed that the oxygen atom of water acts as the oxidizing agent toward TCEP=X, forming TCEP=O. As a corollary, the reaction medium becomes progressively more acidic over time due to this oxidation.

- **Precursors pH titration:**

  pH titrations with HCl revealed distinct behaviors for the different chalcogen precursors. For sulfur, TCEP=S is protonated in its free form, but it likely does not complex with $Cd(3\text{-MPA})_2$. The selenium derivative shows similar behavior: no protonation of the free form

TCEP=Se and no detectable complexation with Cd(3-MPA)$_2$. These selenium results are tentative and require further experiments for confirmation.

In contrast, for tellurium, the free form TCEP=Te appears not to be protonated by HCl. However, in the presence of Cd(3-MPA)$_2$, a new pH-active site emerges, likely associated with complex formation. To confirm this hypothesis, pH titration experiments are repeated while monitoring the system via Raman spectroscopy.

- **Precursors Raman monitoring:**

  This experiment complements the pH titration: after each addition, a Raman spectrum is recorded. The reaction proceeds in two stages: first, stepwise addition of Cd(3-MPA)$_2$, followed by HCl titration.

  These experiments show that the sulfur reagent is protonated in its free form but not complexed with Cd(3-MPA)$_2$. Selenium is neither protonated nor complexed by cadmium. Tellurium, however, appears both complexed by Cd(3-MPA)$_2$ and capable of generating a new pH-active site, which catalyzes the formation of CdTe QDs.

- **XPS surface analysis:**

  XPS analysis of the as-synthesized QD cores (CdS, CdSe, CdTe) indicates that particle stabilization primarily occurs via carboxylate ligands. Except for CdS, all cores exhibit a surface deficiency in cadmium atoms, likely due to autocatalytic surface reactions and sample washing prior to analysis, which may remove surface-adsorbed cadmium.

  For CdTe, an additional Te^{IV} peak is observed, indicating partial surface oxidation. This suggests that tellurium-containing cores are sensitive to atmospheric oxygen and can undergo oxidation under ambient conditions.

3.4 Discussion

The various observations made in the current chapter provide good insight into the reaction pathways, depending on the chalcogen involved in the reaction. This discussion aims to summarize all this information to provide an overview as complete as possible for each core.

3.4.1 CdS

The formation of CdS QDs likely proceeds through a chemical reaction between TCEP–S and Cd(3-MPA)$_2$, corresponding to a second-order reaction. Since TCEP–S is pH-sensitive, it can be protonated in its free form. Under its protonated form (TCEP–S–H), the reactivity toward Cd(3-MPA)$_2$ is

expected to be lower than that of the neutral TCEP=S. Consequently, the pH of the medium should remain relatively high, especially considering the release of protons during the reaction.

In the case of CdS QDs, TCEP=S is the less reactive TCEP=X derivative, requiring higher temperatures to transfer the sulfur atom to the cadmium, resulting in a longer induction period. These harsher conditions lead to competition between 3-MPA and TCEP=S as sulfur sources. Nonetheless, the real sulfur donor for generating CdS QDs, the reliability of TCEP=S has been proven by its contribution to the improvement of optical properties, suggesting its adsorption on the QDs surface, although XPS did not show its presence.

Kinetic fitting performed during reaction optimization in the microfluidic reactor indicates that crystal growth follows a Finke–Watzky mechanism (FW mechanism). This implies that the initial formation of CdS nuclei via the second-order reaction is slow. Once nucleation occurs, after the induction period, growth accelerates due to surface autocatalysis. It is hypothesized that after nuclei formation, $Cd(3\text{-MPA})_2$ adsorbs onto the particle surface, lowering the activation barrier and allowing TCEP–S to react more efficiently at the surface, thereby contributing to crystal growth.

Besides the accumulation of information about the formation of CdS nanocrystals, their optical properties remained poor. The fundamental reason behind this remains unknown. Unlike CdSe, the literature does not mention the creation of intermediate energy levels due to the use of 3-MPA as a stabilizing agent. However, regardless of the mechanism behind these poor emission properties, it is likely that revealing the Stokes-shift emission requires the use of core-shell structures.

3.4.2 CdSe

The formation of CdSe QDs also involves a reaction between TCEP=Se and $Cd(3\text{-MPA})_2$. Unlike sulfur, TCEP=Se appears neither protonated under its free form nor strongly complexed with cadmium prior to react together to generate the CdSe monomeric blocs.

The reactivity of TCEP=Se towards $Cd(3\text{-MPA})_2$ remains moderate, and high temperatures (up to 235 °C) are required to form the CdSe QDs. This high temperature may also increase the risk of CdS formation with 3-MPA as a sulfur donor. However, the XRD spectrum shows that the crystals are mostly composed of CdSe molecules. If CdS molecules are formed, their number remains marginal regarding to the CdSe ones.

Kinetic analysis indicates that CdSe growth also follows a Finke–Watzky mechanism (FW mechanism). After the induction period, surface autocataly-

sis accelerates growth as Cd(3-MPA)$_2$ adsorbs onto the particle surface, facilitating further reaction of TCEP=Se at the surface. XPS analysis shows a slight cadmium deficiency at the surface, consistent with a Se-rich layer, which may influence optical and electronic properties.

Regarding the optoelectronic properties, the CdSe cores themselves exhibit surface defects, leading to the formation of trap states. This phenomenon is attenuated by particle growth, improving the Stokes-shift emission. A second method highlighted to minimize the pinned emission involves the addition of a ZnS shell on the surface of the CdSe core, forming a type I core-shell structure.

The concatenated procedure for core-shell formation was successfully implemented and showed the growth of CdSe and ZnS to be spatially separated, allowing for a distinctive growth nature of the molecules. In addition to the emission improvement, HRTEM coupled with EDX characterization confirmed the egg-shell morphology, as well as the elemental analysis, which confirmed the addition of the ZnS shell.

3.4.3 CdTe

In the case of CdTe, the reaction between TCEP=Te and Cd(3-MPA)$_2$ is more complex. The sole TCEP=Te is not protonated by HCl, but in the presence of cadmium, a new pH-active site emerges, suggesting complex formation. This complex likely catalyzes the formation of the monomeric CdTe building blocs especially under acidic conditions, as shown by *in-situ* Raman monitoring.

The fast formation of CdTe molecules induces, as described by LaMer, a burst nucleation. Depending on the intensity of the nucleation, particle growth proceeds and consumes most of the remaining reagents. There is a direct correlation between the particle size and their properties. Indeed, larger particles exhibit better optoelectronic properties but poorer size distribution.

Since the reaction kinetics are very fast, due to the highly complex reactivity, the reaction proceeds at a lower temperature than CdS and CdSe. Seamlessly, due to the high reactivity of the tellurium derivatives, the mechanism proceeds homogeneously, without requiring surface autocatalysis for the growth step.

XPS analysis reveals a cadmium-deficient surface and the presence of Te[IV] species, indicating partial surface oxidation. These observations highlight the higher reactivity of the tellurium precursor and the susceptibility of CdTe QDs to oxidation, which may affect surface chemistry and stability.

Together, these analyses provide a coherent picture of the nucleation and growth mechanisms of CdX QDs, highlighting the influence of chalcogen identity on reaction kinetics, surface composition, and stability.

3.5 Conclusions

This optimisation chapter has unveiled several key experimental insights. Preliminary experiments identified tunable parameters and clarified the underlying reactivity (Figure 3.1).

The choice of cadmium precursor was critical: both $CdCl_2$ and $Cd(OAc)_2$ provide a suitable compromise for aqueous synthesis. For further characterization using DOSY-NMR method, $Cd(OAc)_2$ was favoured over $CdCl_2$.

Under basic pH, cadmium requires strong surface stabilization to prevent $Cd(OH)_2$ formation. Several stabilizing agent were considered. However, the well known 3-MPA was confirmed as an effective stabilizer, with a minimal stoichiometry of 1:2 relative to cadmium, as confirmed by pH-metry titration.

The Cd:X ratio must be carefully controlled. In the case of aqueous synthesis, the Cd:X ratio should be equal or higher than 1. Indeed, under high temperature, the TCEP=X precursors are unstable and form back elemental chalcogen. These elemental chalcogen being unsoluble, they are likely to deposit on reactor wall or promote heterogeneous nucleation.

Regarding the core synthesis, CdS and CdSe follow a Finke–Watzky mechanism, proceeding in two stages: slow nucleation characterized by an induction phase, followed by accelerated growth due to surface autocatalysis on the QDs. In contrast, CdTe follows a LaMer-type mechanism, enabled by precursor complexation and acidic catalysis, leading to rapid initial nucleation and reduced autocatalytic contribution.

Finally, regarding the optical properties of the synthesized QDs, CdS still exhibits an exclusive surface emission contribution, although the presence of TCEP=X derivatives seems to enhance the surface emission intensity. CdSe, on the other hand, shows the first traces of Stokes-shift emission. To further boost the surface Stokes emission, type I core-shell synthesis was attempted by adding a ZnS layer, which led to improved Stokes emission. CdTe proved to be the most promising core, already shows good emission properties in initial trials. An intensified optimization process resulted in particles with a PLQY of up to 50%. This synthesis was successfully transposed to a flow process, although a slight decrease in emission properties was observed. Nonetheless, this scale-up successfully enabled the production of QDs with good emission properties at a large scale.

The mechanistic investigations conducted to unveil the fundamental steps behind particle formation revealed some interesting details. First, the oxygen source for the TCEP oxidation was identified as the solvent, thanks to isotopic labeling. The pH-titration, monitored by Raman *in-situ*, showed that TCEP=S alone is pH-sensitive and that TCEP=Te complexes with

$Cd(3\text{-}MPA)_2$, leading to a new pH-active center. This pH center is crucial for controlling the formation rate of CdTe QDs.

References

[1] Gauthier Emonds-alt et al. “Exploring the Fundamentals of Microreactor Technology with Multidisciplinary Lab Experiments Combining the Synthesis and Characterization of Inorganic Nanoparticles”. In: *Journal of chemical education* 94 (2017), pp. 775–780. DOI: 10.1021/acs.jchemed.6b00899.

[2] Jacques Tonneau. *Tables de chimie: un mémento pour le laboratoire*. 2e édition. Bruxelles: De Boeck Supérieur, 2000, pp. 64–76. ISBN: 978-2-8041-3301-6.

[3] Stepan S. Batsanov. “Energy Electronegativity and Chemical Bonding”. In: *Molecules* 27 (23 Nov. 2022), pp. 8215–8233. ISSN: 14203049. DOI: 10.3390/molecules27238215.

[4] Ralph. G. Pearson. “Absolute electronegativity and absolute hardness of Lewis acids and bases”. In: *Journal of the American Chemical Society* 107 (24 Nov. 1985), pp. 6801–6806. ISSN: 00027863. DOI: 10.1021/ja00310a009.

[5] Zusakhe Nguqu, Olamide Abiodun Daramola, and Francis Birhanu Dejene. “Effect of different cadmium sources on the optical and structural properties of CdTe quantum dots (QDs) co-stabilized with GSH-TGA”. In: *Results in Chemistry* 15 (May 2025), pp. 102214–102225. ISSN: 2211-7156. DOI: 10.1016/j.rechem.2025.102214.

[6] Rama Mohana Rao Dumpala et al. “Protonation of Phosphonocarboxylates in Aqueous Medium: An Experimental and Theoretical Investigation”. In: *Journal of Chemical and Engineering Data* 67 (9 Sept. 2022), pp. 2174–2181. ISSN: 15205134. DOI: 10.1021/acs.jced.2c00156.

[7] Pierre-Henri C Heubel and Alexander I Popov. “Acid Properties of Some Phosphonocarboxylic Acids”. In: *Journal of Solution Chemistry* 8 (Sept. 1979), pp. 615–625. ISSN: 15728927. DOI: 10.1007/BF01033692.

[8] Richard M Farmer, P.-H C Heubel, and Alexander I Popov. “Complexation Properties of Phosphonocarboxylic Acids in Aqueous Solutions”. In: *Journal of Solution Chemistry* 10 (8 1981), pp. 523–532. ISSN: 15728927. DOI: 10.1007/BF00646933.

[9] Wushuang Wan et al. “Room-temperature formation of CdS magic-size clusters in aqueous solutions assisted by primary amines”. In: *Nature Communications* 11 (1 Aug. 2020), pp. 4–11. ISSN: 20411723. DOI: 10.1038/s41467-020-18014-6.

[10] Patrick K. Tamukong, Wadumesthrige D.N. Peiris, and Svetlana Kilina. “Computational insights into CdSe quantum dots’ interactions with acetate ligands”. In: *Physical Chemistry Chemical Physics* 18 (30 June 2016), pp. 20499–20510. ISSN: 14639076. DOI: 10.1039/c6cp01665k.

[11] Levi Lystrom et al. “Surface-Induced Deprotonation of Thiol Ligands Impacts the Optical Response of CdS Quantum Dots”. In: *Chemistry of Materials* 33 (3 Feb. 2021), pp. 892–901. ISSN: 15205002. DOI: 10.1021/acs.chemmater.0c03610.

[12] Murthy A Vairavamurthy et al. “The interaction of hydrophilic thiols with cadmium: investigation with a simple model, 3-mercaptopropionic acid”. In: *Marine Chemistry* 70 (2000), pp. 181–189. ISSN: 0304-4203. DOI: 10.1016/S0304-4203(00)00023-2.

[13] “Variation of cadmium sulfide nanoparticle size and photoluminescence intensity with altered aqueous synthesis conditions”. In: *Colloids and Surfaces A: Physicochemical and Engineering Aspects* 254 (1-3 Mar. 2005), pp. 147–157. ISSN: 09277757. DOI: 10.1016/j.colsurfa.2004.11.024.

[14] “Determination of the fluorescence quantum yield of quantum dots: Suitable procedures and achievable uncertainties”. In: *Analytical Chemistry* 81 (15 2009), pp. 6285–6294. ISSN: 00032700. DOI: 10.1021/ac900308v.

[15] Christian Würth et al. “Relative and absolute determination of fluorescence quantum yields of transparent samples”. In: *Nature Protocols* 8 (8 2013), pp. 1535–1550. ISSN: 17502799. DOI: 10.1038/nprot.2013.087.

[16] Debasis Bera et al. “Quantum dots and their multimodal applications: A review”. In: *Materials* 3.4 (2010), pp. 2260–2345. ISSN: 19961944. DOI: 10.3390/ma3042260.

[17] Mengying Li et al. “Hydrothermal synthesis of highly luminescent CdTe quantum dots by adjusting precursors’ concentration and their conjunction with BSA as biological fluorescent probes”. In: *Talanta* 72 (1 Apr. 2007), pp. 89–94. ISSN: 00399140. DOI: 10.1016/j.talanta.2006.09.028.

[18] Raúl García-Rodríguez and Haitao Liu. “Mechanistic study of the synthesis of CdSe nanocrystals: Release of selenium”. In: *Journal of the American Chemical Society* 134 (3 Jan. 2012), pp. 1400–1403. ISSN: 00027863. DOI: 10.1021/ja209246z.

[19] Leah C. Frenette and Todd D. Krauss. “Uncovering active precursors in colloidal quantum dot synthesis”. In: *Nature Communications* 8 (1 Dec. 2017). ISSN: 20411723. DOI: 10.1038/s41467-017-01936-z.

[20] Haitao Liu, Jonathan S. Owen, and A. Paul Alivisatos. “Mechanistic study of precursor evolution in colloidal group II-VI semiconductor nanocrystal synthesis”. In: *Journal of the American Chemical Society* 129 (2 Jan. 2007), pp. 305–312. ISSN: 00027863. DOI: 10.1021/ja0656696.

[21] Fumio Watari. “Vibrational Spectra of Trimethylphosphine Telluride and P-Te Stretching Force Constant”. In: *Inorganic Chemistry* 20 (6 1981), pp. 1776–1779.

Chapter 4

Conclusions

The present research project aimed to bridge part of the gap in emission properties between quantum dots synthesized in organic solvents and those obtained through aqueous or hydrothermal routes. In this context, a new family of water-soluble chalcogen precursors (X = S, Se, Te) was investigated. Analogous to trioctylphosphine (TOP) in organic-phase syntheses, tris(2-carboxyethyl)phosphine (TCEP) was demonstrated to act as a versatile reduced chalcogen carrier, capable of transferring sulfur, selenium, or tellurium atoms under aqueous conditions.

The beginning of the manuscript is dedicated to an extensive and didactic introduction aimed at providing a comprehensive overview of the nature of quantum dots, their applications, and properties. Their nanometric preparation is reviewed to give an overview of the synthesis methodology and strategies to achieve high-quality nanoparticles. After a discussion of reactor technologies with a focus on microfluidics, the introduction thoroughly reviews the chemistry behind QD preparation. This is concluded by the problem that the current thesis aims to address.

In a first experimental chapter, the formation of TCEP=X species was optimized in batch using a DoE approach. Kinetic investigations were then carried out to identify the key parameters governing reaction rate and selectivity. These studies demonstrated that chalcogen transfer occurs at the interface between elemental chalcogen and water, highlighting the interfacial nature of the reaction mechanism. Importantly, this chemistry was successfully transposed to continuous-flow conditions, leading to remarkably high space–time yields and demonstrating compatibility with large scale reactors. As a proof of concept, the resulting TCEP=X precursors were subsequently employed to feed a CdX quantum dot synthesis reactor.

A systematic investigation of precursor reactivity revealed that the nature of the chalcogen plays a decisive role in the overall reaction pathway.

Isotopic labelling experiments confirmed that water acts as the oxidant in the transformation of TCEP=X into TCEP=O, leading to progressive acidification of the reaction medium. This process, combined with pH-dependent precursor speciation, governs the availability of reactive chalcogen species and thus controls nucleation and growth kinetics.

For CdS and CdSe, nanocrystal formation follows a Finke–Watzky-type mechanism, characterized by slow homogeneous nucleation followed by accelerated growth driven by surface autocatalysis. In contrast, CdTe formation proceeds through a LaMer-type mechanism, enabled by the complexation between cadmium and tellurium species, which introduces a new pH-active site and promotes rapid, acid-catalyzed nucleation. This fundamental mechanistic difference accounts for both the faster kinetics and the enhanced optical properties observed for CdTe quantum dots.

Surface-sensitive analyses further demonstrated that all CdX nanocrystals synthesized in aqueous media exhibit non-ideal surface stoichiometry. XPS measurements revealed cadmium-deficient, chalcogen-rich surfaces predominantly stabilized by carboxylate ligands, with partial oxidation observed for tellurium-containing samples. These findings highlight the intrinsic reactivity of aqueous-grown quantum dot surfaces and their susceptibility to ligand exchange and oxidative processes.

From an optical standpoint, CdS nanocrystals remained dominated by surface-related emission, despite improvements induced by the presence of TCEP=X derivatives. CdSe showed the first evidence of Stokes-shifted emission, which could be further enhanced by the growth of a ZnS passivation shell. CdTe emerged as the most promising system, reaching photoluminescence quantum yields of up to 50 % after extensive optimization. Importantly, this synthesis was successfully translated to continuous-flow conditions, enabling scalable production, albeit with a moderate decrease in emission efficiency.

Overall, this work establishes TCEP-based chalcogen transfer as a unified, scalable, and mechanistically distinct strategy for the aqueous synthesis of CdX quantum dots. Beyond providing a rational framework to understand precursor reactivity and growth mechanisms, these results lay the foundations for the controlled and environmentally benign production of luminescent nanocrystals in water.

Chapter 5

Prospectives

Beyond its direct achievements, the present project has opened several research directions that could not be fully explored within the timeframe of this work. In this chapter, some of these unfinished ideas are discussed, and preliminary results are presented where available.

5.1 Self-mapping CdX QDs

This section focuses on the advances achieved in the PAT. Most of the concepts discussed herein build upon the developments presented in Section 1.6, with a particular emphasis on automation. Over the past decade, the microfluidics community has shown a growing interest in fast screening platforms. Quantum dots constitute particularly suitable model systems for such approaches, as downstream characterization can be readily achieved through UV/Vis absorption and fluorescence spectroscopy, providing rich and complementary information on the synthesized nanomaterials.

Building on this context, the present project benefited from an internship dedicated to process automation, *in-line* data science, and ML at North Carolina State University, under the supervision of Prof. Milad Abolhasani. In this environment, automation strategies based on LabVIEW® software were combined with data analysis and machine learning routines implemented in Python. Elements of these approaches were already leveraged in Chapter 2 for the transposition to flow of the preparation of TCEP=X precursors (see Figure 2.11).

The results presented in Chapter 2 highlighted the flexibility offered by the use of TCEP as a chalcogen carrier and constitute the first building block of the setup proposed here. This strategy significantly enhances the potential for

fully integrated and automated microfluidic platforms incorporating feedback control loops. Furthermore, as a proof of concept, a DoE was successfully implemented using an automated setup (results not shown in the present work), demonstrating the practical feasibility of such an approach.

The combination of these two developments provides a framework capable of autonomously mapping the formation space of CdX/ZnS quantum dots. In addition to automated reagent delivery, real-time data acquisition and analysis enable continuous learning strategies, such as the training of neural networks. Once trained, these models can propose new experimental conditions, which are subsequently fed back into the system to iteratively optimize the properties of the synthesized nanoparticles.

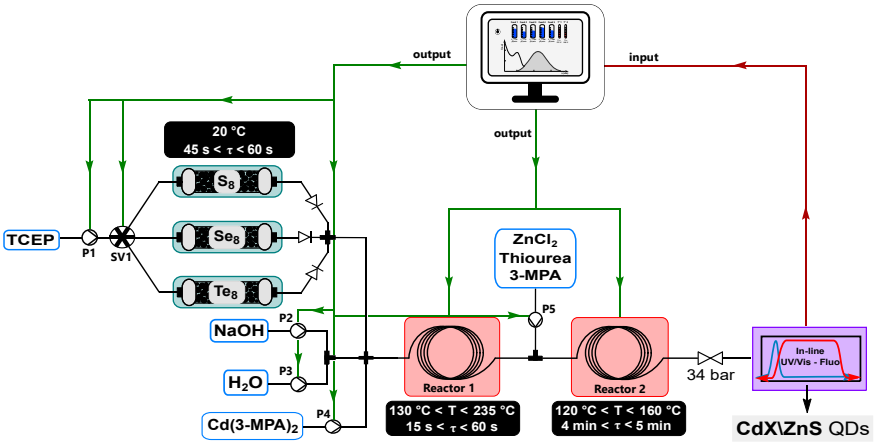

Figure 5.1. Self-mapping CdX/ZnS QDs in a compact and automated setup.

Within this framework, a conceptual setup is proposed in Figure 5.1. Taking advantage of the *in-line* synthesis of TCEP=X precursors, the system is designed to pump the TCEP precursor (pump 1) through a column containing one of the three elemental chalcogens. Depending on the desired core composition, the flow is directed, via the controlled rotation of a switching valve, through the appropriate column, thereby feeding the reactor with freshly generated precursor.

Pumps 2, 3, and 4 simultaneously supply reactor 1 with NaOH solution, water, and $Cd(3\text{-MPA})_2$ solution, respectively. Appropriate calculations allow adjustment of key parameters highlighted in Figure 3.1, such as precursor concentration, chalcogen excess, and initial pH. As demonstrated in Chapter 3, these parameters are critical for tuning the reactivity toward the formation of CdX quantum dots.

Downstream of reactor 1, an additional feed is introduced via pump 5 ($Zn(3\text{-MPA})_2$ with TU). The combined streams are then directed to reactor 2, where the growth of a ZnS shell over the CdX core occurs, leading to an

improvement in the PLQY. It is worth noting that, in the presence of a residual chalcogen excess downstream of reactor 1, this excess may react with the zinc precursor to form a ZnX interfacial layer. Such a layer is expected to exhibit a reduced lattice mismatch with the CdX core compared to ZnS, potentially promoting improved interfacial coherence (see Table 1.1).

Finally, the downstream section of the setup is monitored by UV/Vis absorption and fluorescence spectroscopy, enabling full characterization based on the metrics summarized in Section 3.2.1. These data (red arrows) are subsequently used to train a machine learning model, which proposes new experimental conditions that are fed back into the system (green arrows). [1]

Ultimately, this setup could be operated using DFE, which represent a particularly powerful strategy to accelerate reaction screening in continuous-flow systems. The concept of real flow-reactor dynamics was briefly introduced in Section **6)** through the discussion of breakthrough curves $F(t)$. By continuously varying the input conditions rather than performing discrete experiments, and by explicitly accounting for the reactor response described by $F(t)$, DFE enables the rapid exploration of large parameter spaces while drastically reducing reagent consumption and experimental time.

Beyond simple acceleration, DFE is especially well suited for integration with automated and data-driven workflows. In the context of quantum dot synthesis, where optical properties are highly sensitive to small variations in experimental conditions, dynamic modulation of flow rates and compositions allows the extraction of dense, information-rich datasets from a single experiment. Such data intensification strategies have recently been shown to be highly effective for quantum dot synthesis, enabling reductions in screening time by one to two orders of magnitude. [2]

More broadly, the combination of DFE with real-time spectroscopic monitoring and machine learning-assisted decision-making opens the door to truly autonomous experimentation. In this paradigm, the reactor is no longer operated as a static synthesis platform, but rather as an adaptive system capable of continuously refining its operating conditions in response to incoming data. This approach constitutes a natural evolution toward self-driving laboratories for nanomaterial synthesis.

5.2 Kinetic model development

To begin this prospective section, it is important to clearly differentiate the levels of modeling that can be employed to describe the formation of quantum dots. At a basic level, models often reduce the particle to their average properties (*e.g.*, peak position) rather than considering the full population through a size distribution. Such models, including LaMer or Finke–Watzky approaches, are relatively simple to represent but do not capture the complete

dynamics of the system. In contrast, a population-based approach, such as a Fokker–Planck formulation, can account for the full size distribution. [3, 4] However, this latter approach requires substantially more information about the system and is mathematically more challenging to solve.

5.2.1 Limitations of the existing model

This section focuses on simpler models, such as LaMer or the FW mechanism. Both approaches have been subject to criticism regarding their range of validity. The LaMer model is criticized mainly for two reasons: Firstly, the burst nucleation it describes does not apply to all systems, as some exhibit a significant induction period. Secondly, it does not account for the autocatalytic contribution to particle growth. [5, 6] The Finke–Watzky model has also been critiqued, particularly because the autocatalytic surface area is assumed to remain constant throughout the reaction. [7]

In this context, Perala *et al.* attempted to extend the FW mechanism by including a Population Balance Models Learning (PBM) contribution, which accounts for the variation of surface area over the course of the reaction. However, the complexity of the PBM formulation, involving partial differential equations similar to the Fokker–Planck approach, substantially increases the model's mathematical difficulty. Therefore, there is a clear motivation to develop a new, simpler model for particle formation that can capture essential dynamics without the full complexity of population-based methods.

5.2.2 New modeling approach

In the present work, limitations of the Finke–Watzky model were observed when attempting to describe the evolution of the peak position during the reaction (ERT) for CdS and CdSe QDs (see Sections 3.2.2 and 3.2.3). Specifically, the FW mechanism predicts a symmetry between the post-nucleation acceleration and deceleration phases, which was not observed experimentally. Empirically, the data were better fitted using a non-symmetrical sigmoid function (see Equation 3.12).

The Finke–Watzky formalism, however, introduces a very interesting concept: the surface acting as a catalyst for particle growth. However, its limitations arise from this very assumption: the surface variation. Indeed, it is considered as constant, which, in the case of quantum dots synthesis, requires some adjustment. The model will be therefore rethought.

From the basic chemical equations, scheme provided in Figure 5.2, the general behaviour of diatomic nanoparticles formation can be described as follows:

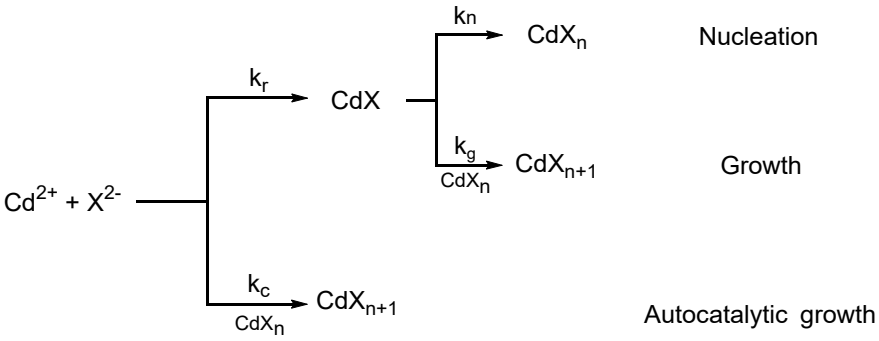

Figure 5.2. Diatomic nanoparticles formation new mechanism proposal.

- The two atoms of interest (*e.g.*, Cd^{2+} and X^{2-}) react to form the monomeric building block (CdX).
- The so-obtained CdX block can either undergo nucleation, if the CdX concentration is sufficiently high, or migrate to an available surface to participate in the growth process.
- Alternatively, in the presence of catalytic surface (*e.g.*, nanoparticle in formation), Cd^{2+} adsorbs through a Langmuir isotherm, on the surface of the particle to generate an activated form. Once formed, the X^{2-} can react on the active site through a Eley-Rideal mechanism. [8] It is then hypothesized that the newly formed CdX unit is assumed to remain on the surface and contributes to the particle growth.

Based on the Figure 5.2, the following kinetic equations can be posed, assuming $[Cd]_0 = [X]_0$:

$$\begin{cases} \dfrac{d[Cd]}{dt} = \dfrac{d[X]}{dt} = -k_r[X]^2 - k_c[QDs].[X]^2 \\ \dfrac{d[CdX]}{dt} = k_r[X]^2 - k_g[QDs].[CdX] - k_n.[CdX]^n \\ \dfrac{d(D)}{dt} = k_c[QDs].[X]^2 + k_g[QDs][CdX] \\ \dfrac{dn}{dt} = k_n[CdX]^n \end{cases} \tag{5.1}$$

These equations can be rewritten by explicitly accounting for surface chemistry, leading to effective rate laws derived from adsorption equilibria and surface reactions.

First, the adsorption (Langmuir isotherm) of the CdX building block on the surface of CdX particles for growth process can be modified as follow.

$$k_g[QDs].[CdX] = k_g \frac{k_{a1}[CdX]}{1 + k_{a1}.[CdX]}.4\pi.D^2.n(t) \tag{5.2}$$

Then, the autocatalytic reaction on the surface, issued from the FW mechanism, reacting through Eley-Rideal mechanism is formulated as follow.

$$k_c[QDs].[X]^2 = k_c. \frac{k_{a,Cd}.[Cd]}{1 + k_{a,Cd}.[Cd]}.[X].4\pi.D^2.n(t) \tag{5.3}$$

In practice, this new formalism can be solved using much simpler methods than those required for Fokker–Planck or PBM approaches. Specifically, the QD diameter can be estimated using the Brus equation (Equation 1.4), while the particle number can be inferred from the particle concentration obtained via an empirical model for the ϵ term in the Beer–Lambert law. [9] In practice, these differential equations cannot be solved analytically, but they can be numerically integrated to determine the kinetic constants.

In the general case, the growth of diatomic quantum dots can be described by a system accounting for both homogeneous monomer reactions, surface-catalyzed growth, and nucleation. Defining the total surface available as:

$$S(t) = 4\pi D(t)^2\, n(t),$$

The kinetic equations then become, assuming $[Cd]_0 = [X]_0$:

$$\begin{cases} \dfrac{d[Cd]}{dt} = \dfrac{d[X]}{dt} = -k_r[X]^2 - k_c \dfrac{k_{a,Cd}[Cd]}{1 + k_{a,Cd}[Cd]}[X]\, S(t) \\ \dfrac{d[CdX]}{dt} = k_r[X]^2 - k_g \dfrac{k_{a1}[CdX]}{1 + k_{a1}[CdX]}\, S(t) - k_n[CdX]^n \\ \dfrac{dD}{dt} = k_c \dfrac{k_{a,Cd}[Cd]}{1 + k_{a,Cd}[Cd]}[X]\, S(t) + k_g \dfrac{k_{a1}[CdX]}{1 + k_{a1}[CdX]}\, S(t) \\ \dfrac{dn}{dt} = k_n[CdX]^n \end{cases} \tag{5.4}$$

- $S(t) = 4\pi D(t)^2\, n(t)$ is the total available surface for adsorption,
- $\dfrac{k[A]}{1 + k[A]}$ describes Langmuir-type adsorption effects.

This equation system 5.4 has the advantage of addressing the criticisms previously raised for both the LaMer and Finke–Watzky models, while remaining sufficiently general to reduce to either model as a limiting case.

Indeed, taking into account the limiting cases, the equation system simplified to previously known models:

- At low surface coverage and constant surface, the autocatalytic term from the Finke–Watzky model simplifies:

$$k_c \frac{k_{a,Cd}[Cd]}{1 + k_{a,Cd}[Cd]}[X].S(t) \sim k'_c.[QDs][Cd][X] \tag{5.5}$$

- In the limit of high monomer concentration, such that $k_{a1}[CdX] \gg 1$, the surface becomes saturated with CdX units and adsorption is no longer rate-limiting. Under these conditions, growth is controlled by the flux of monomer from the solution to the particle surface, corresponding to the growth regime described in the LaMer model. In this framework, the simplification made in Equation 5.2 is no longer valid, the system effectively reduces to the classical LaMer mechanism.

In conclusion, this approach provides a physically grounded and experimentally accessible framework that reconciles classical nucleation and growth models within a unified formalism. By explicitly accounting for surface evolution and adsorption-controlled growth, it naturally bridges the LaMer and Finke–Watzky models as limiting cases. This framework offers a tractable route for extracting kinetic parameters from experimental data and can be further extended to include more complex surface chemistries or additional observables.

5.2.3 Full Mechanistic Proposal

Aside from the new formalism proposed to describe the evolution of mean metrics during QD formation, the mechanistic insights discussed in Section 3.3 provide an overview of the system, although the picture remains incomplete. In addition to crystallization-related information, purely kinetic aspects were not explicitly considered at that stage, as a full mechanistic description could not be established. Nevertheless, it is possible to advance further considerations, particularly regarding monomer generation.

Based on mechanistic evidence, the following reaction schemes can be proposed:

- **CdS and CdSe kinetics**

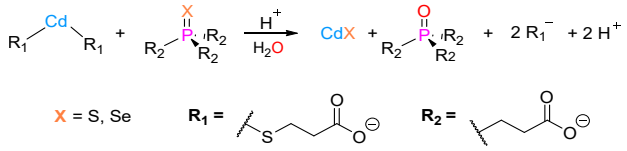

(5.6)

In this proposed mechanism, valid for CdS and CdSe, the reaction is considered second-order with respect to TCEP=X and $Cd(3\text{-MPA})_2$. The reaction proceeds in water, which also acts as an oxygen source for TCEP=X. The presence of H^+ is included in the mechanism because the sulfur derivative can be protonated, influencing its reactivity toward $Cd(3\text{-MPA})_2$. The fate of 3-MPA is not explicitly known; it is hypothesized to be released into the medium in deprotonated form and may act as a stabilizing agent.

Based upon these information the kinetic formation of CdS and CdSe building block can be posed as follow:

$$\frac{d[\mathrm{CdX}]}{dt} = k_{\mathrm{eff}}\,[\mathrm{TCEP{=}X}]\,[\mathrm{Cd(3\text{-}MPA)_2}] \tag{5.7}$$

- **CdTe kinetics**

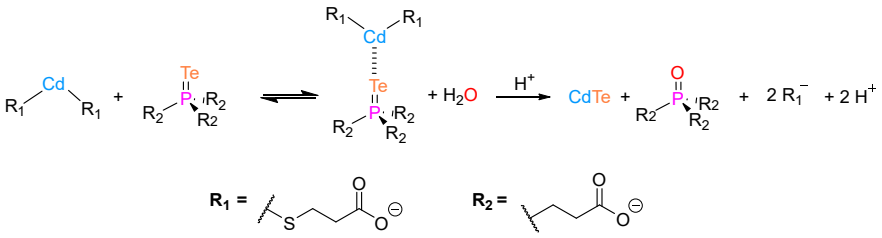

(5.8)

For CdTe, the reaction is considered second-order with respect to TCEP=Te and $Cd(3\text{-MPA})_2$, or first-order regarding the complexation of these two species. Water acts as an oxygen source, and H^+ influences the protonation of the pH-sensitive site created upon complexation,

affecting the complex's reactivity. The fate of 3-MPA is again hypothesized as deprotonated in solution and acting as a stabilizing agent.

Based upon these information the kinetic formation of CdTe can be posed as follow:

$$\frac{d[\text{CdTe}]}{dt} = k_d \left[\text{TCEP=Te} \cdot \text{Cd(3-MPA)}_2\right] \tag{5.9}$$

Using the complexation equilibrium:

$$\left[\text{TCEP=Te} \cdot \text{Cd(3-MPA)}_2\right] = K_f \left[\text{TCEP=Te}\right] \left[\text{Cd(3-MPA)}_2\right] \tag{5.10}$$

we obtain the final kinetic expression:

$$\frac{d[\text{CdTe}]}{dt} = k_d K_f \left[\text{TCEP=Te}\right] \left[\text{Cd(3-MPA)}_2\right] \tag{5.11}$$

- **Experimental attempt for model solving**

  Based on the proposed models, experimental attempts were carried out to numerically solve the differential equations. In agreement with the equimolar condition ($[\text{TCEP=X}] = [\text{Cd(3-MPA)}_2]$), the reactions were performed in batch and monitored by ^{1}H-, ^{31}P-, and ^{113}Cd-NMR.

  The main objective was to follow, via ^{31}P-NMR, the consumption of TCEP=X species. Quantitative signal integration combined with mass balance allowed monitoring of reagent consumption over time. Additional measurements in ^{1}H- and ^{113}Cd-NMR were performed to obtain complementary information on the reaction progress. The preliminary results are presented in Figures 5.3 and 5.4.

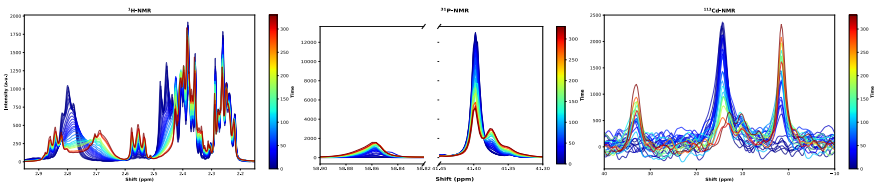

Figure 5.3. ^{1}H-, ^{31}P-, and ^{113}Cd-NMR monitoring of CdSe formation over time.

The results obtained for CdSe monitoring did not strictly follow the trends observed in the mechanistic study presented in Section 3.3.

Over time, the TCEP=Se signal ($\delta = 41.4$ ppm) that should convert into TCEP=O ($\delta = 58.86$ ppm) exhibited slight shoulders at lower chemical shifts. These additional signals are currently unknown and may be related to thermally activated complexation. This hypothesis is supported by ^{113}Cd-NMR, where the Cd(3-MPA)$_2$ signal ($\delta = 15$ ppm) is consumed to form two new signals ($\delta = 33$ ppm and $\delta = 2$ ppm), whose nature remains unclear. Finally, the methylene signals of 3-MPA (ranging from 2.9 ppm to 2.42 ppm) also shift during the same time frame.

These observations suggest that even the selenium derivative undergoes energy-dependent complexation, forming at temperatures higher than room temperature. The exact nature of these complexes is unknown, but at least two distinct species appear to be formed.

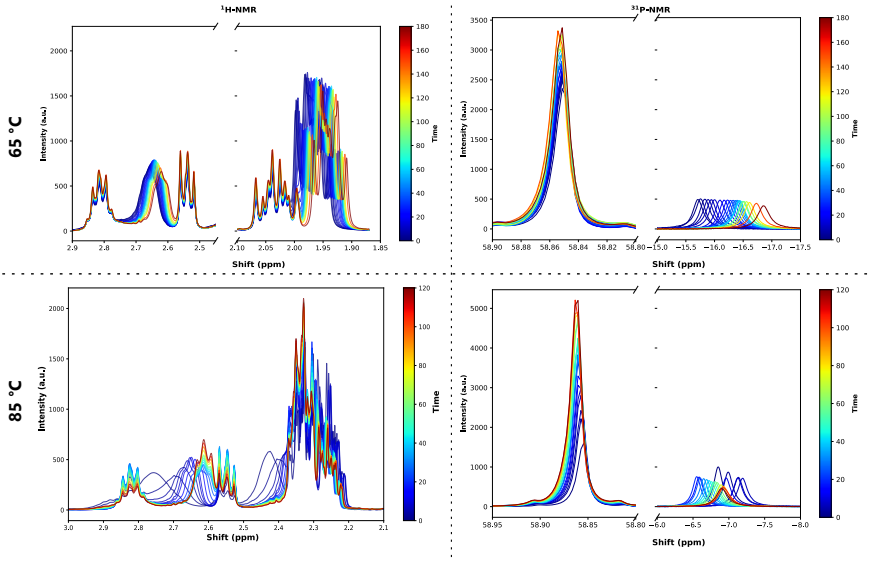

Figure 5.4. ^{1}H- and ^{31}P-NMR monitoring of CdTe formation over time under 65 °C (top row) and 85 °C (bottom row).

In the case of CdTe formation monitoring, the collected information also indicates a more complex system than initially expected. Two experiments were performed at 65 °C and 85 °C.

At 65 °C, the observations are largely consistent with the hypothesized mechanism: the TCEP=Te signal is broad at $\delta = -15.75$ ppm and gradually shifts to lower chemical shift over time, suggesting an increased reaction rate due to medium acidification, which may indicate a catalytic effect. The TCEP=Te signal eventually disappears as TCEP=O forms. The methylene signals (from 2.9 ppm to 2.4 ppm) follow a similar homogeneous trend, showing slight shifts consistent with the acidification.

At 85 °C, however, the ^{1}H-NMR exhibits a different pattern: the methylene signals behave similarly to what was observed during CdSe synthesis. In ^{31}P-NMR, the chemical shift initially moves from -6.8 ppm to -7.2 ppm, as seen at 65 °C, but then shifts back to -6.5 ppm before returning toward shielding. These differences may indicate the formation of thermally induced complexes that were not observed in Raman spectroscopy.

- **Conclusion**

  The modelization developed appears convincing based on the results presented in Section 3.3. However, the transition to thermally activated systems reveals that the true mechanism is more complex than initially anticipated. Literature reports indicate that tellurium can undergo metal complexation, [10] while selenium is hypothesized to require thermal activation through various steps. [11]

  These pathways have been demonstrated primarily in organic solvents. Yet, the possibilities of complexation and activation in aqueous media remain largely unexplored. To fully elucidate these mechanisms, a more systematic campaign of NMR-monitored experiments should be undertaken, including advanced 2D-NMR techniques. [12–14]

5.3 Biofunctionalization

One of the main motivations for synthesizing quantum dots in water is the biocompatibility acquired during the process. Indeed, for bioapplications, it is crucial to have water-soluble QDs. To avoid the ligand exchange typically required to achieve this property, an exchange that leads to a loss of optoelectronic properties, it is preferable to synthesize them directly in water.

Once the QDs are soluble, they can be functionalized with various types of biomolecules, imparting unique properties that are influenced by the nature of the molecule. There are various approaches to functionalizing QDs, either through non-specific bonding (adsorption) or via chemical bond formation. Among the chemical bonding methods, amide coupling involves the reaction between a carboxylic acid group on the QD surface and an amine group on the biomolecule. Thiol binding refers to the addition of thiol-functionalized biomolecules to the QD solution for direct surface attachment. Lastly, click chemistry, which typically involves azide-functionalized biomolecules reacting with carboxylic acids, is another widely used method for QD functionalization [15].

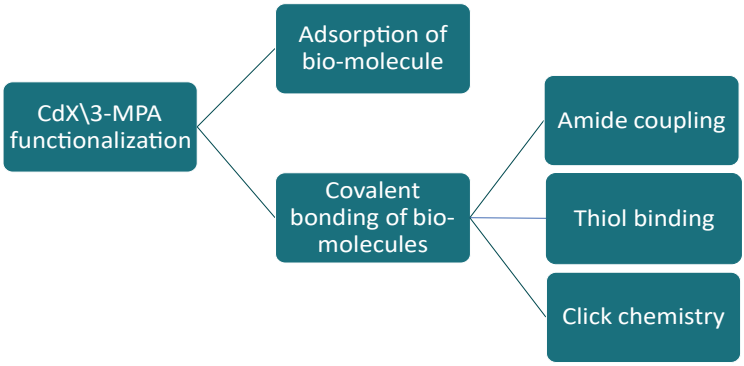

Figure 5.5. Overview of the chemical possibilities to functionalize the QDs with biomolecules.

5.3.1 Protocol for Stable CdTe QDs at Neutral pH

The standard method to perform this coupling is in Phosphate Buffer Saline (PBS) solution.

Initially, the crude solution was purified by precipitation, following the protocol described in Section 6.2.5.6. The purified samples were then solubilized back to their initial volume using three different PBS solutions, see Section 6.3.1 for PBS solution detail.

In all three cases, the procedure led to the coalescence of the samples. To address this issue, the hypothesis is to perform a post-treatment of the QDs to saturate the surface with 3-MPA, which prevents coalescence due to the moderate pH in the saline solution.

The saturate the QDs surface, the sample is purified then mixed with a 3-MPA solution, purified and finally dispersed in the three phosphate buffers, described in the tables from 6.18 to 6.20, and kept for stability validation, see Section 6.3.1 for additional details. The result is shown in Figure 5.6.

The results show that for phosphate buffers 1 and 3, the particle sediment but do not lose their luminescence. However, with PBS 2, the solution remains perfectly soluble.

In conclusion, to achieve the biofunctionalization of the homemade QDs, a post-treatment is necessary to keep the particle soluble in a 3-MPA solution. The particles are then stable in the functionalization reaction medium.

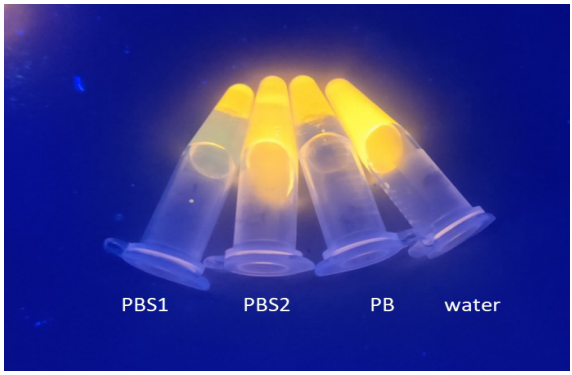

Figure 5.6. Picture of the redispersed QDs, under 365 nm irradiation, in the 3 phosphate buffers and water for control.

5.3.2 Biofunctionalization with Biotin

Following the stabilization of the quantum dots in synthesis medium, an important future direction lies in the development of strategies for biofunctionalization using biotin. Due to its high reactivity with a broad range of biomolecules, biotin-functionalized quantum dots represent a promising model system for further studies in targeted biological applications.

Future work would explore the modification of biotin to introduce reactive groups, such as thiols, that enable efficient attachment to the quantum dot surface. [16, 17] Optimizing the functionalization strategy may improve stability, solubility, and controlled orientation of the biomolecule on the nanoparticle, which are critical factors for subsequent biological interactions.

One strategy considered consists of modifying biotin with 2-aminoethane-1-thiol (cysteamine), which contains an amine group that can be linked to biotin via an amide bond and a thiol group that can be used to functionalize the quantum dots. After the amide bond formation, the protective group is removed. Experimental details are provided in Section 6.3.2.

Additionally, the verification of biotin attachment remains a key step. Techniques such as DOSY NMR or FRET with streptavidin-functionalized dyes could provide more definitive evidence of successful functionalization and quantify binding efficiency. Exploring these approaches would not only confirm the functionalization but also provide insight into the dynamics and accessibility of biotin on the quantum dot surface.

Overall, this perspective highlights potential avenues for enhancing quantum dot biofunctionalization, focusing on methodological optimization, stability improvements, and rigorous verification of biomolecular attachment.

5.3.3 Biofunctionalization of QDs through Staudinger Ligation

While the protocol described in Section 5.3.2 provides reasonable yields and purity, it remains tedious and does not apply to a broad range of biomolecules. Therefore, a more versatile protocol was sought to tag biomolecules with quantum dots. One potential solution lies in Staudinger ligation, a reaction from the click chemistry family that promotes selective bonding under mild conditions, minimizing side reactions. The Staudinger ligation involves the reaction between a phosphine ($P(R_1)_3$) and an azide (N_3R_2), leading to the formation of an amide bond, as illustrated in Figure 5.7. [18]

1) General methodology

The strength of this strategy lies in the versatility offered by the nature of R_1 and R_3. In this context, R_1 can be a modified ligand on the quantum dot (QD) surface, while R_3 represents an azidized biomolecule. This versatility is key, as the azidation process can be applied to a wide range of biomolecules, making this approach suitable for various bioapplications.

The selective and mild conditions of click chemistry make it particularly attractive for biofunctionalization, avoiding the harsh conditions typical of chemical conjugation methods. Moreover, by using click chemistry, unwanted side reactions are minimized, preserving the integrity of both the biomolecule and the quantum dot.

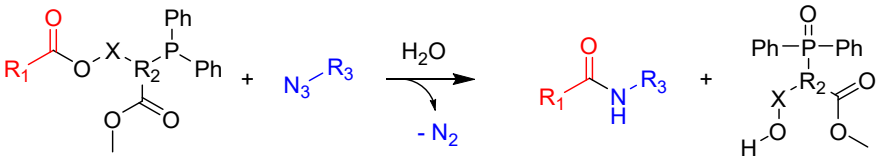

Figure 5.7. General Mechanism for the Staudinger ligation (Bertozzi method), leading to the formation of an amide bond between an azide-functionalized molecule and a phosphine-functionalized one. In this case, X represents an undetermined carbon chain.

2) Biomolecule Azide Modification

This methodology opens up the possibility of attaching various biomolecules to quantum dots, including, but not limited to, proteins, peptides, DNA, biotin, and more. The main advantage of this method lies in the customizability of the reaction, allowing for the selective tagging of a wide variety of biomolecules with quantum dots.

The biomolecule can be azidized through a single-step reaction using aqueous diazo transfer via imidazole-1-sulfonyl azide hydrochloride [19].

This reagent introduces azide groups non-specifically on lysine side chains or on the N-terminal enzymes of the biomolecule.

The relatively mild synthesis conditions make this protocol compatible with a broad range of biomolecules, with the reaction occurring at room temperature in water under basic conditions, as illustrated in Figure 5.8. In this protocol, 1 eq of imidazole-1-sulfonyl azide hydrochloride is used for every 1.75 eq of amine in the target molecule.

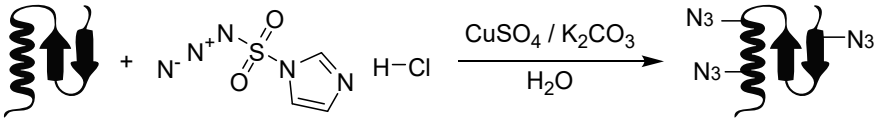

Figure 5.8. Azide functionalization of biomolecules by imidazole-1-sulfonyl azide hydrochloride under mild conditions.

3) QDs Surface Modification

Finally, the QDs stabilized by 3-MPA can undergo surface modification of their carboxylic terminal group. This modification can proceed through EDC/NHS activation of the carboxylic acid, followed by reaction with an amine terminal group to form an amide bond [20]. An example of this potential reaction path is illustrated in Figure 5.9.

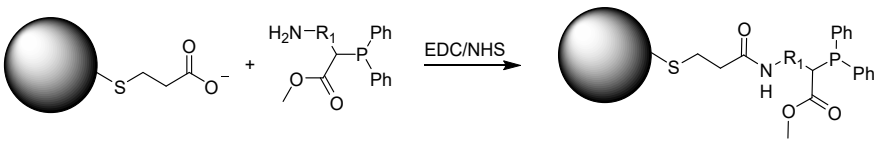

Figure 5.9. Surface functionalization of QDs−COOH with a phosphine, through EDC/NHS activation, in preparation for a Staudinger ligation.

4) Conclusion

In this section, we have proposed a hypothetical yet versatile protocol for QDs−COOH biofunctionalization through Staudinger ligation. This protocol is designed to adhere to the principles of click chemistry. However it remains purely theoretical and experimental synthesis must be conduced to enforce the proposed chemical pathway.

References

[1] Kameel Abdel-Latif et al. "Self-Driven Multistep Quantum Dot Synthesis Enabled by Autonomous Robotic Experimentation in Flow". In: *Advanced Intelligent Systems* 3 (2 Feb. 2021). ISSN: 2640-4567. DOI: 10.1002/aisy.202000245.

[2] Fernando Delgado-Licona et al. "Flow-driven data intensification to accelerate autonomous inorganic materials discovery". In: *Nature Chemical Engineering* (July 2025). ISSN: 2948-1198. DOI: 10.1038/s44286-025-00249-z.

[3] Jane Y. Rempel, Moungi G. Bawendi, and Klavs F. Jensen. "Insights into the kinetics of semiconductor nanocrystal nucleation and growth". In: *Journal of the American Chemical Society* 131 (12 Apr. 2009), pp. 4479–4489. ISSN: 00027863. DOI: 10.1021/ja809156t.

[4] Richard M. Maceiczyk, Leonard Bezinge, and Andrew J. Demello. "Kinetics of nanocrystal synthesis in a microfluidic reactor: Theory and experiment". In: *Reaction Chemistry and Engineering* 1 (3 June 2016), pp. 261–271. ISSN: 20589883. DOI: 10.1039/c6re00073h.

[5] Murielle A Watzky and Richard G Finke. "Transition Metal Nanocluster Formation Kinetic and Mechanistic Studies. A New Mechanism When Hydrogen Is the Reductant: Slow, Continuous Nucleation and Fast Autocatalytic Surface Growth". In: *Journal of the American Chemical Society* 119 (43 Oct. 1997), pp. 10382–10400. DOI: 10.1021/ja9705102.

[6] Lucian Bentea, Murielle A. Watzky, and Richard G. Finke. "Sigmoidal Nucleation and Growth Curves Across Nature Fit by the Finke-Watzky Model of Slow Continuous Nucleation and Autocatalytic Growth: Explicit Formulas for the Lag and Growth Times Plus Other Key Insights". In: *Journal of Physical Chemistry C* 121 (9 Mar. 2017), pp. 5302–5312. ISSN: 19327455. DOI: 10.1021/acs.jpcc.6b12021.

[7] Siva Rama Krishna Perala and Sanjeev Kumar. "On the two-step mechanism for synthesis of transition-metal nanoparticles". In: *Langmuir* 30 (42 Oct. 2014), pp. 12703–12711. ISSN: 15205827. DOI: 10.1021/la503199m.

[8] R. Prins. "Eley–Rideal, the Other Mechanism". In: *Topics in Catalysis* 61 (9-11 June 2018), pp. 714–721. ISSN: 10225528. DOI: 10.1007/s11244-018-0948-8.

[9] W. William Yu, Y. Andrew Wang, and Xiaogang Peng. "Formation and Stability of Size-, Shape-, and Structure-Controlled CdTe Nanocrystals: Ligand Effects on Monomers and Nanocrystals". In: *Chemistry of Materials* 15 (22 Nov. 2003), pp. 4300–4308. ISSN: 08974756. DOI: 10.1021/cm034729t.

[10] Juan Carlos Pérez-Sánchez et al. “Unravelling the role of triisopropylphosphane telluride in Ag(i) complexes”. In: *Inorganic Chemistry Frontiers* 10 (22 Aug. 2023), pp. 6519–6525. ISSN: 20521553. DOI: 10.1039/d3qi01485a.

[11] Leah C. Frenette and Todd D. Krauss. “Uncovering active precursors in colloidal quantum dot synthesis”. In: *Nature Communications* 8 (1 Dec. 2017). ISSN: 20411723. DOI: 10.1038/s41467-017-01936-z.

[12] Mingyang Liu et al. “Probing intermediates of the induction period prior to nucleation and growth of semiconductor quantum dots”. In: *Nature Communications* 8 (June 2017). ISSN: 20411723. DOI: 10.1038/ncomms15467.

[13] Laura Piveteau et al. “Resolving the Core and the Surface of CdSe Quantum Dots and Nanoplatelets Using Dynamic Nuclear Polarization Enhanced PASS-PIETA NMR Spectroscopy”. In: *ACS Central Science* 4 (9 Sept. 2018), pp. 1113–1125. ISSN: 23747951. DOI: 10.1021/acscentsci.8b00196.

[14] Yunhua Chen et al. “Revealing the Surface Structure of CdSe Nanocrystals by Dynamic Nuclear Polarization-Enhanced 77Se and 113Cd Solid-State NMR Spectroscopy”. In: *Journal of the American Chemical Society* 143 (23 June 2021), pp. 8747–8760. ISSN: 15205126. DOI: 10.1021/jacs.1c03162.

[15] Ajay Singh Karakoti et al. “Surface functionalization of quantum dots for biological applications”. In: *Advances in Colloid and Interface Science* 215 (Nov. 2015), pp. 28–45. ISSN: 00018686. DOI: 10.1016/j.cis.2014.11.004.

[16] Marketa Ryvolova et al. “Biotin-modified glutathione as a functionalized coating for bioconjugation of CdTe-based quantum dots”. In: *Electrophoresis* 32 (13 2011), pp. 1619–1622. ISSN: 01730835. DOI: 10.1002/elps.201000634.

[17] Vijaya Bharathi M. et al. “Green synthesis of highly luminescent biotin-conjugated CdSe quantum dots for bioimaging applications”. In: *New Journal of Chemistry* 44 (39 2020), pp. 16891–16899. ISSN: 13699261. DOI: 10.1039/d0nj03075a.

[18] Christin Bednarek et al. “The Staudinger Ligation”. In: *Chemical Reviews* 120 (10 2020), pp. 4301–4354. ISSN: 15206890. DOI: 10.1021/acs.chemrev.9b00665.

[19] Stijn F.M. Van Dongen et al. “Single-step azide introduction in proteins via an aqueous diazo transfer”. In: *Bioconjugate Chemistry* 20 (1 2009), pp. 20–23. ISSN: 10431802. DOI: 10.1021/bc8004304.

[20] Tuomas Näreoja et al. “Super-sensitive time-resolved fluoroimmunoassay for thyroid-stimulating hormone utilizing europium(III) nanoparticle labels achieved by protein corona stabilization, short binding time, and serum preprocessing”. In: *Analytical and Bioanalytical Chemistry* 409 (13 May 2017), pp. 3407–3416. ISSN: 16182650. DOI: 10.1007/s00216-017-0284-z.

Chapter 6

Appendices and Supplementary Information

6.1 Chapter 2: Supplemental Materials and Analysis

6.1.1 General information

High-field NMR experiments (structural identification of intermediates and determination of NMR conversions for the batch experiments) were carried out with a Bruker Avance III 400 MHz spectrometer in D_2O. The chemical shifts (δ) are reported relative to the solvent residual peak or to H_3PO_4 (^{31}P-NMR). *In-line* monitoring with low-field ^{31}P-NMR experiments was carried out with a Magritek Spinsolve Ultra Phosphorus 43 MHz equipped with a flow-through glass cell (Spinsolve RM2 kit).

Transmission electron microscopy (TEM) was performed with a LaB6-Tecnai G2 under 180 kV acceleration voltage, in bright field mode, on 200 mesh carbon-coated cupper grids.

X-ray powder diffraction (XRD) was used to characterize the crystal structure (Bruker AXS D8 Discover) using Cu K radiation. The samples were analyzed on a zero background substrate.

Absorbance measurements were recorded on an AvaSpec-ULS2048XL EV spectrometer (Ultra-low Stray light Fiber optic Spectrometer, 75 mm AvaBench, 2048 large 500 µm pixel back-thinned CCD detector), equipped with an AvaLight-DH-S light source (Deuterium-Halogen light source, 190-2500 nm, incl. TTL shutter). *In-line* absorbance measurements were carried out

with an Avantes CUV-ALL/UV/VIS cuvette sample holder (10x10 mm), equipped with a flow-through cell (3 in 1, Hellma 176-760-15-40). *Off line* analyses were performed in PMMA cells with the Avantes. The source, the holder and the analyzer were connected with Avantes FCB-UVIR400 fiber optic cables (bifurcated cable 2x400 µm, 2 or 1 m length, SMA terminations).

Photoluminescence experiments were recorded offline with a Shimadzu RF-6000 Spectrofluorimeter in Fluorescence quartz-made macro cells (Hellma 101-10-40).

Caution: This work involves the use of heavy metals (cadmium) and chalcogens (sulfur, selenium, tellurium). These compounds should be handled under a fume hood and with appropriate personal protective equipment (PPE). All the effluents generated must be disposed in appropriate containers with special labels following the instruction of EH&S authorities. All glassware must be cleaned with commercial bleach (aqueous sodium hypochlorite for chalcogen decontamination).

6.1.2 Reagent and solvent

The reagents and solvents were purchased from commercial sources; these compounds are used without purification (Table 6.1).

Cadmium acetate and sodium borohydride must be stored under anhydrous conditions and tris-(carboxyethyl)phosphine (TCEP).hydrochloride must be stored at 4 °C.

6.1.3 Continuous flow setups

6.1.3.1 Microfluidic setups and parts

All microfluidic setups were assembled with commercially available parts.

1. Pumps

   Knauer AZURA P 4.1S HPLC pumps were used to handle all the liquid streams for microfluidic experiments.

2. PFA tubing

   PFA coil reactors and collection lines were constructed from PFA tubing (high purity PFA; 1.58 mm outer diameter, 500 µm internal diameter).

3. SS tubing

   The stainless tubing reactors were built with 316 stainless steel tubing (1.58 mm outer diameter, 500 or 750 µm internal diameter).

Table 6.1. Solvents, chemicals and suppliers

Solvent	Purity (%)	CAS number	Supplier
Deuterium Oxide	99.90	7789-20-0	Eur-isotop
Ethanol (absolute)	99	64-17-5	VWR
Water HiPerSolv CHROMANORM®	/	7732-18-5	VWR
Chemicals	**Purity (%)**	**CAS number**	**Supplier**
3-Mercaptopropionic acid	99	107-96-0	Alfa Aesar
Cadmium acetate dihydrate	98	5743-04-4	Sigma Aldrich
Oxalic acid anhydrous	$\geq$ 97	144-62-7	Fluka Analytical
Selenium powder *200 mesh*	99.999	7782-49-2	Alfa Aesar
Sodium borohydride	$\geq$ 98	16940-66-2	TCI
Sodium hydroxide	$\geq$ 97	1310-73-2	VWR
Sulfur	99.98	7704-34-9	Aldrich
Tellurium *200 mesh*	99.8	13494-80-9	Aldrich Chemistry
Tellurium *-18+60 mesh*	99.999	13494-90-9	Alfa Aesar
Tris-(2-carboxyethyhl)phosphine .hydrochloride	99.5	51805-45-9	Chem-Impex

4. Connectors, ferrules and mixers

   Sections of the reactor that were not subjected to high temperatures and pressures were equipped with coned PEEK fittings and micromixers. Sections of the reactor that were subjected to high temperatures and pressures were equipped with Valco SS fittings, ferrules and unions. Connectors, ferrules and unions were purchased from IDEX/Upchurch or from VICI.

5. Check valves

   Check valves were inserted before the cross junction to prevent cross-contamination of the chalcogen columns and were purchased from IDEX/Upchurch Scientific.

6. Back pressure regulators

   To control the pressure inside the reactor, back pressure regulators of 100, 250 and 500 psi were used (IDEX/Upchurch Scientific).

7. Thermoregulatory devices

   Thermoregulation of PFA coil reactors was performed with a Heidolph™MR Hei-Tec® equipped with a Pt-1000 temperature sensor. The stainless steel coil reactors were embedded in a GC oven (Thermo Finnigan Interscience GC trace).

8. Setup flow parts and vendors

   Continuous flow parts and vendors are gathered in Table 6.2.

6.1.3.2 Mesofluidic setups and parts

1. Pumps

   During the scalability trials at pilot scale, a Knauer AZURA P 4.1S HPLC pump, an Isco Teledyne 5000D dual syringe pump and a Corning® AFR™G1 dosing line (equipped with a Hastelloy HNP microgear pump) were used to handle liquids.

2. PFA tubing

   PFA coil reactors and collection lines were constructed from PFA tubing (high purity PFA 1/8"; 3.175 mm outer diameter, 1.65 mm internal diameter or high purity PFA 1/4"; 6.35 mm outer diameter, 3.2 mm internal diameter), and purchased from Swagelok.

3. SS tubing

   The stainless tubing reactors are built with 316 stainless steel tubing (3.175 mm outer diameter, 1.14 mm internal diameter), and purchased from Swagelok.

Table 6.2. Connectors, ferules and unions

Part	Details	Vendor	Reference
Connectors	One-Piece Fingertight, PEEK, 10-32 Coned, for 1/16" o.d.	IDEX/Upchurch Scientific	F-120X
	Super Flangeless Nuts, natural PEEK 1/4-28 thread for 1/16" o.d. tubing	IDEX/Upchurch Scientific	P-255X
	Super Flangeless Ferrule Tefzel (ETFE) and SS ring 1/4-28 thread for 1/16" o.d. tubing	IDEX/Upchurch Scientific	P-259X
	303SS 10-32 NUTS for 1/16" o.d.	VICI (Valco Ins. Co. Inc.)	Zn1-10
	303SS union for 1/16" o.d. tubing with 0.5 mm BORE	VICI (Valco Ins. Co. Inc.)	ZU1M
	316 SS column end fitting 1/4" 1/16" 4 mm 4.6 mm cone, removable 2 µm frit	VICI (Valco Ins. Co. Inc.)	CEF 414.6F
Mixers	T-mixer, natural PEEK 1/4-28 thread for 1/16" o.d. tubing, 0.02" through hole	IDEX/Upchurch Scientific	P-712
	Cross assembly, natural PEEK 1/4-28 thread for 1/16" o.d. tubing, 0.02" through hole	IDEX/Upchurch Scientific	P-722
Tubing	High-purity PFA tubing, 1.58 mm outer diameter, 500 µm internal diameter	VICI (Valco Ins. Co. Inc.)	JR-T-4002-M25
	316 Stainless steel tubing 1/16" o.d. tubing, 0.03" through hole	VICI (Valco Ins. Co. Inc.)	TSS-130
	High-purity 1/8" and 1/4" PFA tubing, including appropriate PFA connections	Swagelok	PFA-T2-030-100 PFA-T4-047-100
	316/316L Stainless Steel Seamless Tubing, 1/4 in. od x 0.035 in.	Swagelok	SS-T4-S-035
Check-valve	Check-valve *in-line* 3 psi	IDEX/Upchurch Scientific	CV-3315
Back pressure regulators	BPR Assembly 100, 250, 500 psi	IDEX/Upchurch Scientific	P-787, P-788, P-789, U- 610

4. Connectors, ferrules and mixers

   Sections of the reactor that were not subjected to high temperatures were equipped with PFA Swagelok connectors. Sections of the reactor that were subjected to high temperatures were equipped with Swagelok SS fittings, ferrules and unions. Connectors, ferrules and unions were purchased from IDEX/Upchurch and from Swagelok PFA fittings

5. Back pressure regulator

   A dome-type BPR (BPR-1000 from Zaiput Flow Technologies) was inserted downstream the pilot scale mesofluidic setup. Cracking pressure setpoints were regulated with compressed nitrogen gas (AirLiquide).

6. Thermoregulatory devices

   The chalcogen column was thermostated with a Huber Ministat (Lauda Therm 180 thermal fluid). The Corning® AFR™G1 SiC reactor was thermostated by a Lauda XT 280 thermostat (Lauda Therm 180 thermal fluid).

7. Setup flow parts and vendors

   Continuous flow parts and vendors are gathered in Table 6.3.

6.1.4 Setups and protocols

6.1.4.1 Batch optimization of TCEP=S

An aqueous solution 0.2 M of TCEP was prepared by dissolving TCEP.HCl (0.573 g, 2 mmol, 1 equiv.) with milliQ water. The pH was adjusted to the desired value (5, 8, 11) with 2 M aqueous NaOH then the solution was filled up to 10 mL with milliQ water in a volumetric flask. The solution was then quickly transferred into a 25 mL round-bottom flask and degassed with a flow of Argon) for 15 min. Then, the needed amount of chalcogen (S: 0.096 g, 3 mmol, 1.5 equiv.; 0.144 g, 4.5 mmol, 2.25 equiv.; 0.192 g, 6 mmol, 3 equiv.) was added under inert atmosphere and the solution was stirred (750, 825 and 900 rpm) at room temperature. The reaction was carried out until reaching the desired reaction time (20 min, 40 min, 60 min). Then, 300 µL of the mixture was pipetted out and transferred in a NMR tube (syringe equipped with a polysulfone filter 0.5 µm to remove the chalcogen particles), then 300 µL of degassed D_2O were added. During the operation, the tube was kept under an argon atmosphere to prevent TCEP=X oxidation (to TCEP=O). An insert containing H_3PO_4 as internal standard was added in the NMR tubes which were analyzed by high field ^{31}P-NMR (162 MHz).

Table 6.3. Connectors, ferules and unions

Part	Details	Vendor	Reference
Connectors	One-Piece Fingertight, PEEK, 10-32 Coned, for 1/16" o.d.	IDEX/Upchurch Scientific	F-120X
	Super Flangeless Nuts, natural PEEK 1/4-28 thread for 1/16" o.d. tubing	IDEX/Upchurch Scientific	P-255X
	316 Stainless Steel Nut for 1/8 in. Tube Fitting	Swagelok	SS-202-1
	316 Stainless Steel Nut for 1/4 in. Tube Fitting	Swagelok	SS-402-1
	Tube Fitting, Bulkhead Union, 1/8 in. x 1/4 in. Tube o.d.	Swagelok	SS-200-61-4
	PFA Tube Fitting, 1/4 in. Nut	Swagelok	PFA-422-1
Mixers	T-mixer, natural PEEK 1/4-28 thread for 1/16" o.d. tubing, 0.04" through hole	IDEX/Upchurch Scientific	P-712
Tubing	High-purity PFA tubing, 1.58 mm outer diameter, 500 µm internal diameter	VICI (Valco Ins. Co. Inc.)	JR-T-4002-M25
	High-purity 1/8" and 1/4" PFA tubing, including appropriate PFA connections	Swagelok	PFA-T2-030-100 PFA-T4-047-100
	316/316L Stainless Steel Seamless Tubing, 1/8 in. od x 0.040 in. Wall	VICI (Valco Ins. Co. Inc.)	TSS240
Back pressure regulators	Dome type BPR	Zaiput Flow Technologies	BPR 1000

6.1.4.2 Batch optimization of TCEP=Se

An aqueous solution 0.2 M of TCEP was prepared by dissolving TCEP.HCl (0.573 g, 2 mmol, 1 equiv.) with milliQ water. The pH was adjusted to the desired value (7, 8.75, 10.5) with 2 M aqueous NaOH then the solution was filled up to 10 mL with milliQ water in a volumetric flask. The solution was then quickly transferred into a 25 mL round-bottom flask and degassed with a flow of Argon) for 15 min. Then, the needed amount of chalcogen (0.160 g, 2 mmol, 1 equiv.; 0.240 g, 3 mmol, 1.5 equiv.; 0.320 g, 4 mmol, 2 equiv.) was added under inert atmosphere and the solution was stirred at 750 rpm) at room temperature. The reaction was carried out until reaching the desired reaction time (10 min, 15 min, 20 min). Then, 300 µL of the mixture was pipetted out and transferred in a NMR tube (syringe equipped with a polysulfone filter 0.5 µm to remove the chalcogen particles) then 300 µL of degassed D_2O were added. During the operation, the tube is kept under an argon atmosphere to prevent TCEP=X oxidation (to TCEP=O). An insert containing H_3PO_4 as internal standard was added in the NMR tubes which were analyzed by high field ^{31}P-NMR (162 MHz).

6.1.4.3 Batch optimization of TCEP=Te

An aqueous solution 0.2 M of TCEP was prepared by dissolving TCEP.HCl (1.433 g, 5 mmol, 1 equiv.) with milliQ water. The pH was adjusted to 10.7 with 2 M aqueous NaOH then the solution was filled up to 25 mL with milliQ water in a volumetric flask. The solution was then transferred into a modified three-necked round-bottom flask, see Figure 2.8, and degassed with a flow of Argon over 15 min. Then, the needed amount of tellurium of various granulometry (18-60 mesh, 200 mesh) (0.9570 g, 7.5 mmol, 1.5 equiv.; 1.4355 g, 11.25 mmol, 2.25 equiv.; 1.9140 g, 15. mmol, 3 equiv.) was added under inert atmosphere and the solution was stirred (500 or 750 rpm) at room temperature. The Raman probe was inserted into the solution and the mixing was started. The reaction was monitored after the addition of tellurium (corresponding to the initial time, t0). Spectra were recorded every 30 s ranging from 326 cm^{-1} to 1805 cm^{-1}. The signal of interest is the vibration P-Te at 370 cm^{-1}. For experimental details, see section 2 and figure 2.8.

6.1.4.4 Stability study for TCEP=Te

1. Stability of TCEP=Se vs NaHSe in water (open flask)

   The stability of TCEP=Se was assessed by comparing it to NaHSe. While NaHSe quickly turns red due to oxidation (Figure S1), TCEP=Se remains transparent, indicating its higher resilience to oxidation. Deselenization of TCEP=Se allows the oxidation of selenide (-II) into

selenium (0), forming TCEP (P = +III) in solution. TCEP is then further oxidized into TCEP=O (P = +V) by the oxygen in the air. After 16 hours, less than 1% of TCEP=O was observed in a 0.02 M solution. In a 0.5 M solution at room temperature, after 4 weeks, 98% of TCEP=Se and 2% of TCEP=O were detected (by ^{31}P-NMR), demonstrating the much higher stability of TCEP=Se compared to NaHSe. This stability is advantageous for the subsequent formation of quantum dots.

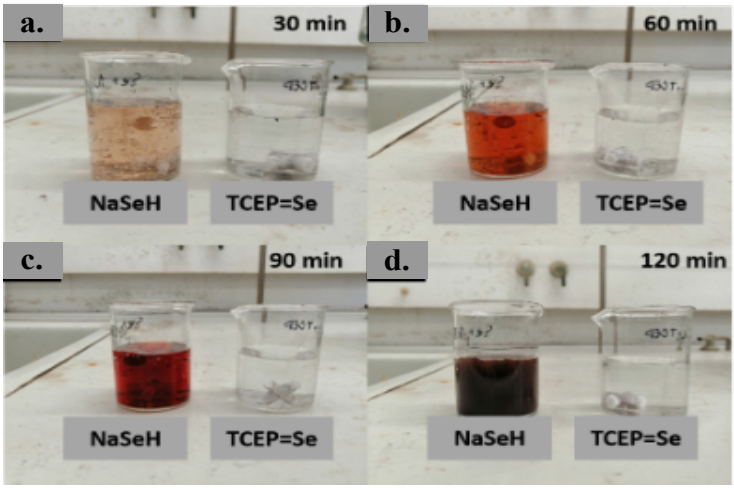

Figure 6.1. Stability of TCEP=Se (right) vs NaHSe (left) in aqueous solutions left open to air after **a.** 30 min, **b.** 60 min, **c.** 90 min, **d.** 120 min.

2. Model Stability study for TCEP=Te

An aqueous solution 0.08 M of TCEP was prepared by dissolving TCEP · HCl (1.1464 g, 4 mmol, 1 equiv.) with milliQ water. The pH was adjusted to 10 with 1 M aqueous NaOH then the solution was filled up to 50 mL with milliQ water in a volumetric flask. The solution was then quickly transferred into a 100 mL round-bottom flask and degassed with a flow of Argon for 15 min. Then, the needed amount of tellurium (1.5312 g, 12 mmol, 3 equiv.) was added under inert atmosphere and the solution was stirred at 50 °C under 800 rpm mixing. After 10 min of reaction, the conversion of TCEP into TCEP=Te was confirmed by ^{31}P-NMR (162 MHz). Finally, the stopper was removed, and a sample was collected every 10 min for 110 min. 300 μL of the mixture was pipetted out and transferred in a NMR tube (syringe equipped with a polysulfone filter 0.5 μm to remove the chalcogen particles), then 300 μL of degassed D_2O were added.

6.1.4.5 Raman monitoring of TCEP=X formation

1. Preliminary pH optimization

   Preliminary tests have shown that the pH had a major influence on the conversion rate towards TCEP=X species. The optima found with the model generated with the DoE were for sulfur 7.5-9 and for selenium 8-9.5. However, the use of these ranges led to a lower conversion rate than predicted. Prior to the kinetic experiments, pH was optimized to set optimal values for the 3 precursors (TCEP=S, TCEP=Se, TCEP=Te).

   (a) Sulfur

   To determine the optimum pH, experiments were realized by varying the pH while keeping the other parameters constant (residence time = 15 min, 0.2 M of TCEP (prepared by dissolving TCEP · HCl (0.5732 g, 2 mmol, 1 equiv.) with milliQ water), chalcogen excess = 1.5 equiv. (0.0962 g, 3 mmol), mixing = 850 rpm). The pH of the TCEP solution was adjusted by adding 2 M NaOH to pH values of 9.84, 10.34, 10.72, 10.88, and 11.35. The corresponding solutions were degassed for 15 min with argon, prior to the addition of sulfur. After 15 min of reaction, the mixing was stopped and then, 300 μL of the mixture was pipetted out and transferred into a NMR tube (syringe equipped with a polysulfone filter 0.5 μm to remove the chalcogen particles) and 300 μL of degassed D_2O were added. During the operation, the NMR tube was kept under an argon atmosphere to prevent oxidation. An H_3PO_4 insert was added as an internal standard, and the sample was analyzed by high field ^{31}P-NMR (162 MHz). The results are provided in Figure 6.2.

   (b) Selenium

   To determine the optimum pH, experiments were realized by varying the pH while keeping the other parameters constant (residence time = 15 min, 0.2 M of TCEP (prepared by dissolving TCEP · HCl (0.5732 g, 2 mmol, 1 equiv.) with milliQ), chalcogen excess = 1.5 equiv. (0.2369 g, 3 mmol), mixing = 850 rpm). The pH of the TCEP solution was adjusted by adding 2 M NaOH to pH values of 10.11, 10.46, 11.07, or 11.53. Each solution was degassed for 15 min with argon, prior to the addition of selenium. After 15 min of reaction, 300 μL of the mixture were pipetted out and transferred in a NMR tube (syringe equipped with a polysulfone filter 0.5 μm to remove the chalcogen particles). 300 μL of degassed D_2O were added under an argon atmosphere to prevent oxidation. An H_3PO_4 insert was added as an internal

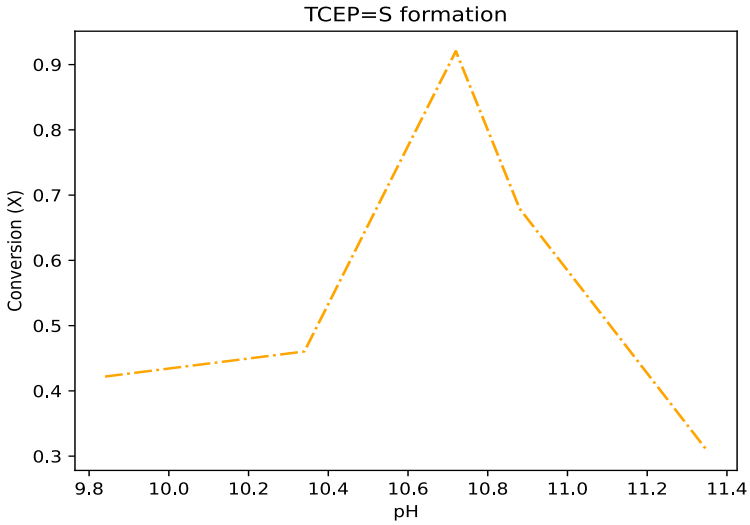

Figure 6.2. pH optimization for TCEP=S formation

standard, and the sample was analyzed by high field ^{31}P-NMR (162 MHz). The results are provided in Figure 6.3.

2. Experimental setup for *in-situ* Raman monitoring

   In situ reaction and kinetic monitoring for the formation of TCEP=X (X = S, Se, Te) were carried out in a modified 3-neck round bottom flask for the hosting of a 5/8" Raman probe (Avaraman-PRB-FIP-532 from Avantes) (Figure 2.8). The spectra were recorded with a Raman spectrometer (Horiba Labram-300) excited with a DPSS laser emitting at 532 nm (CNI optoelectronics MLL-U-532, 300 mW).

3. Monitoring of TCEP=S formation

   A 0.2 M aqueous solution of TCEP was prepared by dissolving TCEP · HCl (1.433 g, 5 mmol, 1 equiv.) with milliQ water. The pH was adjusted to 10.7 with 2 M aqueous NaOH, then the solution was filled up to 25 mL with milliQ water in a volumetric flask. The solution was then transferred into a modified 3-neck round-bottom flask (Figure 6.2), degassed with a flow of argon over 15 min and immerged into a thermostated water bath (at 30 °C, 40 °C, or 50 °C) for 10 min. Then, sulfur (0.4812 g, 15 mmol, 3 equiv.) was added in one portion. The Raman probe was then inserted into the solution and the mixing restarted. The reaction was monitored, after the addition of sulfur (corresponding to the initial time, t_0). Spectra were recorded every 30 s for 2 h, in the wavenumber range from 513 cm^{-1} to 1961 cm^{-1}. The signal of interest is the vibration P-S at 570 cm^{-1}.

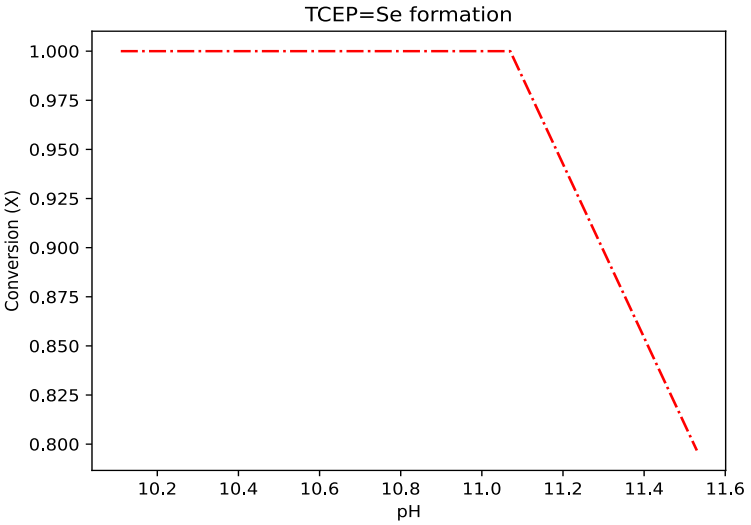

Figure 6.3. pH optimization for TCEP=Se formation

4. Monitoring of TCEP=Se formation

   An aqueous solution 0.2 M of TCEP was prepared by dissolving TCEP · HCl (1.433 g, 5 mmol, 1 equiv.) with milliQ water. The pH was adjusted to 10.7 with 2 M aqueous NaOH then the solution was filled up to 25 mL with milliQ water in a volumetric flask. The solution was then transferred into a modified 3-neck round-bottom flask (Figure 2.8), and degassed with a flow of argon over 15 min. The reactor was thermostated at various temperatures (at 30 °C, 40 °C, 50 °C, and 60 °C) for 10 min. Then, selenium (0.5922 g, 7.5 mmol, 1.5 equiv.) was added. The reaction was monitored, after the addition of selenium (corresponding to the initial time, t_0). Spectra were recorded every 15 s for 2 h, in the wavenumber range from 316 cm^{-1} to 1805 cm^{-1}. The signal of interest is the vibration P-Se at 428 cm^{-1}.

5. Monitoring of TCEP=Te formation

   An aqueous solution 0.2 M of TCEP was prepared by dissolving TCEP · HCl (1.433 g, 5 mmol, 1 equiv.) with milliQ water. The pH was adjusted to 10.7 with 2 M aqueous NaOH then the solution was filled up to 25 mL with milliQ water in a volumetric flask. The solution was then transferred into a modified 3-neck round-bottom flask (Figure 2.8), and degassed with a flow of argon for 15 min and thermostated at various temperatures (at 30 °C, 40 °C, 50 °C, and 60 °C) for 10 min. Then, tellurium (0.9570 g, 7.5 mmol, 1.5 equiv.) was added. The reaction was monitored after the addition of tellurium (corresponding to the initial time, t_0). Spectra were recorded every 15 s for 2 h, in the wavenumber range from 326 cm^{-1} to 1805 cm^{-1}. The signal of interest is the vibration P-Te at 376 cm^{-1}.

6.1.4.6 Transposition in flow of TCEP=X synthesis (lab scale)

1. Design of the chalcogenide bed-packed column

   The reactors used for the flow synthesis of TCEP=X species were constructed from SS tubing (15 cm length, SS-T4-S-065 from Swagelok) with a 2.46 mL internal volume. Both ends of the packed-bed columns were equipped with a column end fitting encompassing a 2 µm frit at the outlet (CEF 414.6F) for preventing chalcogenide leaching. The 3 columns were filled with sulfur (1.91 g), selenium (3.74 g) and tellurium (7.29 g), respectively. For each column, the dead volume was measured and based on that, the porosity (ϵ) of each column was estimated to ϵ = 0.287, 0.098, 0.434, respectively. The reduction of elemental chalcogen (S, Se, Te) was carried out by infusing a TCEP aqueous solution (pH = 10.7) with a Knauer Azura P4.1S HPLC pump (10 mL stainless steel head). The TCEP feed solution was redirected through a selector valve (Vici C25-3186), enabling the switch between the 3 packed-bed columns filled with sulfur, selenium or tellurium, respectively. The outlet of each column was also equipped with a check valve (IDEX/Upchurch Scientific CV-3315) to prevent back flow and cross-contamination. The reaction effluents converged to a cross-junction mixer and were monitored by *in-line* ^{31}P-NMR (Benchtop 43 MHz Spinsolve™spectrometer from Magritek® equipped with a flow-through cell). The system is illustrated in Figure 6.4. A detailed experimental setup is provided in Figure 6.5.

2. TCEP feed preparation

   An aqueous solution 0.2 M of TCEP was prepared by dissolving TCEP · HCl (14.33 g, 50 mmol, 1 equiv.) with milliQ water. The pH was adjusted to 10.7 with 2 M aqueous NaOH, then the solution was filled up to 250 mL with milliQ water in a volumetric flask. The solution was then transferred into a 250 mL round-bottom flask and degassed with argon for 20 min.

6.1.4.7 Concatenated microfluidic preparation of QDs synthesis

The setup for the concatenated synthesis of the CdX QDs (X=S, Se, Te) consisted in two main modules: (a) the first module relied mostly on the packed-bed system illustrated in Figure 6.4 and Figure 6.5 for the reduction of chalcogens; (b) the second module concerned the transfer of chalcogens to a cadmium source for the synthesis of the QDs. A cooling loop was inserted downstream the second module for thermal quenching prior to *in-line* analysis by UV/Vis spectroscopy (Figure 6.6).

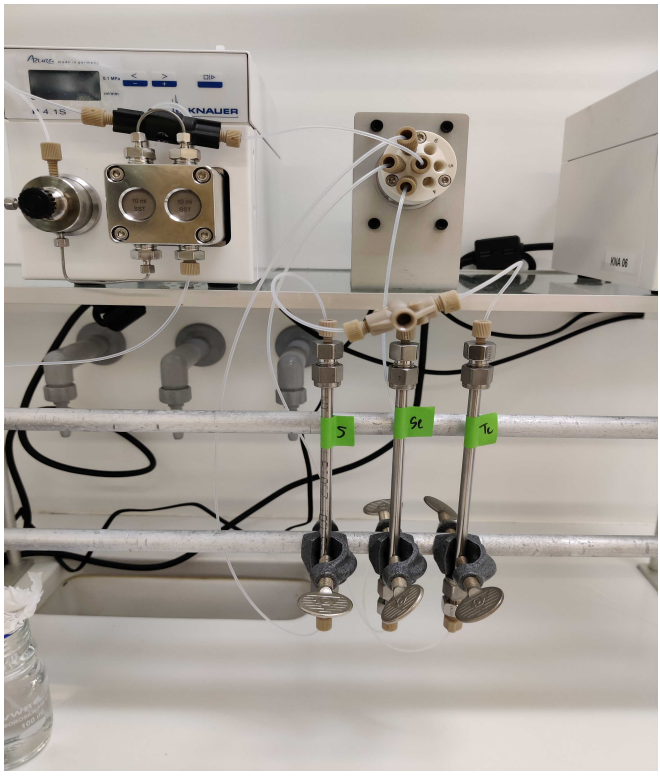

Figure 6.4. Column design in the setup

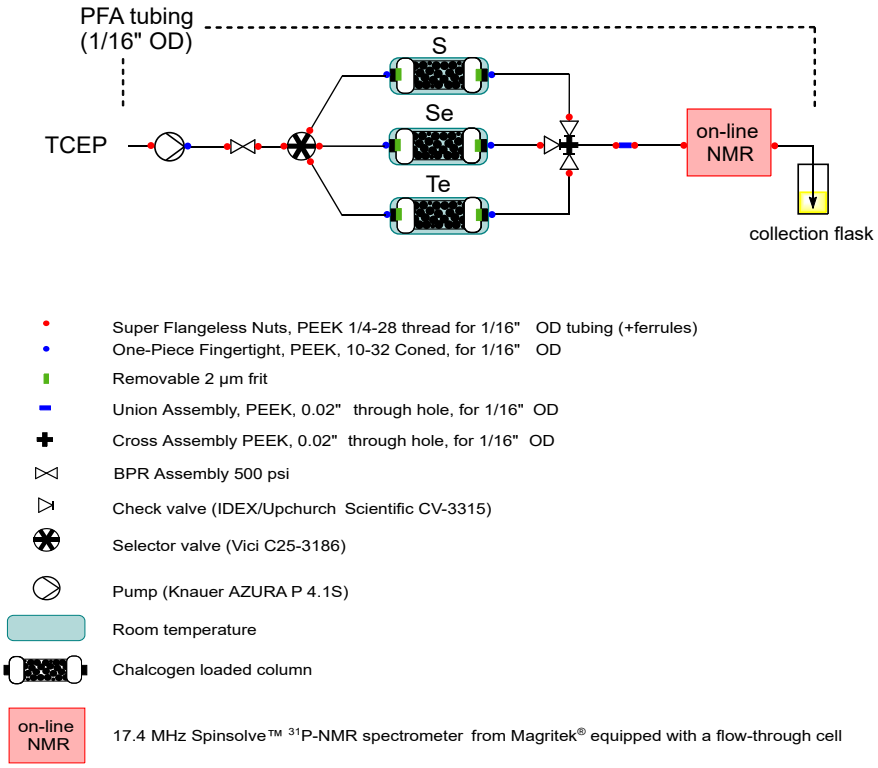

Figure 6.5. Scheme of the overall setup for the transposition in flow of TCEP=X (X = S, Se, Te) synthesis

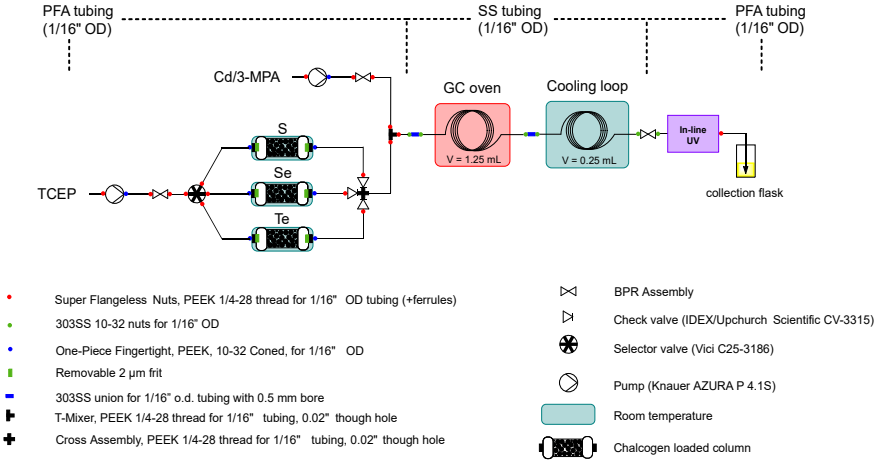

Figure 6.6. Scheme of the overall setup for the transposition in flow of TCEP=X (X = S, Se, Te) synthesis

1. Setup

   The elemental chalcogen reduction was carried out by infusing a TCEP aqueous solution (pH = 10.7) with a Knauer Azura P4.1S pump (10 mL stainless steel head). The TCEP feed solution was redirected through a selector valve (Vici C25-3186) allowing to switch among 3 bed-packed columns filled with sulfur, selenium or tellurium, respectively. To prevent leaching of the elemental chalcogen, a 2 μm frit was added at the outlet of the columns. The outlet of each column was also equipped with a check valve (IDEX/Upchurch Scientific CV-3315) to prevent back flow and cross-contamination. The freshly prepared solution of TCEP=X is mixed in a T mixer with the feed aqueous solution of $Cd(3\text{-}MPA)_2$ (handled through a Knauer Azura P4.1S pump, 10 mL stainless steel head). Note that to ensure a more stable flow rate, both the Knauer pumps were equipped with a 250 psi BPR. The microfluidic SS coil reactor was thermoregulated with a Thermo Finnigan Interscience GC oven, which allowed to reach the desired temperatures under a back pressure of 500 psi (IDEX/Upchurch Scientific P-788). The reactor effluent was thermally quenched and analyzed by *in-line* UV/Vis spectroscopy (AvaSpec-ULS2048XL EV spectrometer equipped with a Charge-Coupled Device detector and a deuterium-halogen light source), as depicted in Figure 6.6.

2. *In-line* monitoring

   The *in-line* monitoring was performed inside a flow-through cells (3 in 1) from Hellma Analytics (176-760-15-40) allowing to perform UV/Vis and/or photoluminescence (5 and 10 mm pathlength) independently or at once. This flow cell was placed inside a cuvette holder (Avantes CUV-ALL-UV/VIS) connected to both sources (UV/Vis: Avalight DH-S-BAL and PL: Avalight HPLED-385) with a 600 μm core optical fibers (FC-UVIR600-1). A second type of *in-line* was performed by measuring directly through a PFA tubing (500 μm ID), sandwiched by 2, 3D printed, bloc of PLA including two SMA screws to fit the optical fibers. The signal was monitored by a spectrophotometer (Avaspec-ULS2048XL-EVO-RS-UA) and treated with Avasoft software. Illustrations of the various configurations are provided in Figure 6.7.

3. Concatenated preparation of CdS

   (a) Preparation of the feed solutions

   A 0.02 M aqueous solution of TCEP was prepared by dissolving TCEP · HCl (0.5732 g, 2 mmol, 1 equiv.) with milliQ water. The pH was adjusted to 10.7 with 2 M aqueous NaOH, then the solution was filled up to 100 mL with milliQ water in a volumetric flask. The solution was transferred into a round-bottom flask and degassed with a flow of argon over 15 min.

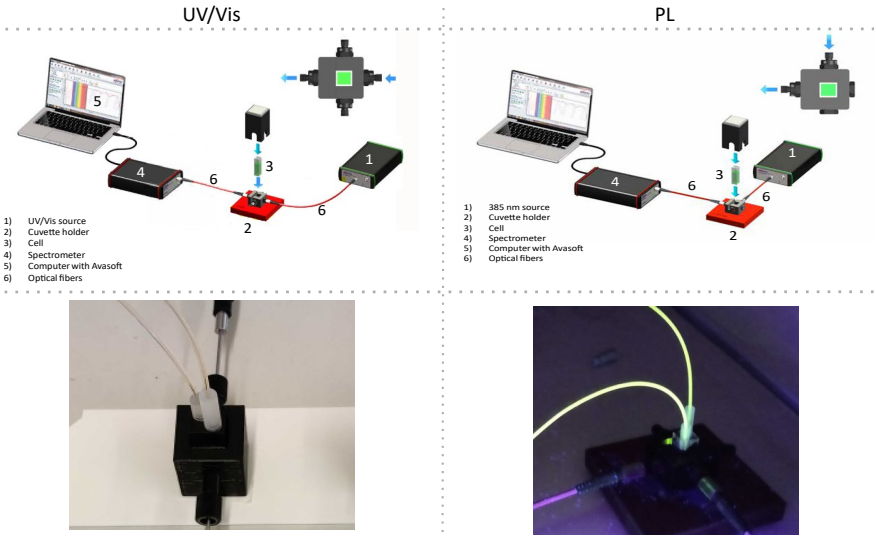

Figure 6.7. Schemes and pictures of experimental configuration for UV/Vis and PL measurements (scheme adapted from [1])

The cadmium precursor feed solution was prepared by dissolving $Cd(OAc)_2$ (0.3332 g, 1.25 mmol, 1 equiv.) and 3-MPA (0.3317 g, 3.125 mmol, 2.5 equiv.) in milliQ water. The pH of the solution was adjusted to 11 by addition of 1 M aqueous NaOH. The solution was next filled up to 250 mL with milliQ water in a volumetric flask.

(b) Modus operandi

The TCEP feed solution was infused (flow rates of 0.25 $mL.min^{-1}$ and 0.33 $mL.min^{-1}$) through a column filled with elemental sulfur (1.991 g, 62.2 mmol). The resulting stream of TCEP=S was mixed through a T-mixer with the cadmium precursor feed solution, which was infused at flow rates of 1 $mL.min^{-1}$ and 1.33 $mL.min^{-1}$, respectively. The SS reactor coil (1.25 mL, 1/16" SS tubing) was heated up to 170 °C, 180 °C, 190 °C, 200 °C with residence times of 45 s and 60 s, respectively under a downstream pressure of 500 psi. The reactor effluent was thermally quenched and analyzed by *in-line* UV/Vis spectroscopy (10 mm light path).

4. Concatenated preparation of CdSe

(a) Preparation of the feed solutions A 0.02 M aqueous solution of

TCEP was prepared by dissolving TCEP · HCl (0.5732 g, 2 mmol, 1 equiv.) with milliQ water. The pH was adjusted to 10.7 with 2 M aqueous NaOH, then the solution was filled up to 100 mL

with milliQ water in a volumetric flask. The solution was then transferred into a round-bottom flask and degassed with a flow of argon over 15 min.

The cadmium precursor feed solution was prepared by dissolving $Cd(OAc)_2$ (0.6663 g, 2.5 mmol, 1 equiv.) and 3-MPA (0.6634 g, 6.25 mmol, 2.5 equiv) with milliQ water. The pH was adjusted to 11 by addition of 1 M aqueous NaOH, then the solution was filled up to 500 mL with milliQ water in a volumetric flask.

(b) Modus operandi

The TCEP feed solution was infused (flow rates of 0.25 $mL.min^{-1}$ and 0.33 $mL.min^{-1}$) through a column filled with elemental selenium (3.743 g, 47.4 mmol). The resulting stream of TCEP=Se was mixed through a T-mixer with the cadmium precursor feed solution, which was infused at flow rates of 1 $mL.min^{-1}$ and 1.33 $mL.min^{-1}$, respectively. The SS reactor coil (1.25 mL, 1/16" SS tubing) was heated up to 160 °C, 170 °C, 180 °C with residence time of 45 s and 60 s, respectively under a downstream pressure of 500 psi. The reactor effluent was thermally quenched and analyzed by *in-line* UV/Vis spectroscopy (10 mm light path).

5. Concatenated preparation of CdTe

(a) Preparation of the feed solutions A 0.003 M aqueous solution of

TCEP was prepared by dissolving TCEP · HCl (0.2150 g, 0.75 mmol, 1 equiv.) with milliQ water. The pH was adjusted to 10.7 with 2 M aqueous NaOH then the solution was filled up to 250 mL with milliQ water in a volumetric flask. The solution was then transferred into a round-bottom flask and degassed with a flow of argon over 15 min.

The cadmium precursor feed solution was prepared by dissolving $Cd(OAc)_2$ (0.9995 g, 3.75 mmol, 5 eq) and 3-MPA (0.9951 g, 9.375 mmol, 12.5 equiv.) with milliQ water. The pH was adjusted to 10.7 by addition of 1 M aqueous NaOH, then the solution was filled up to 250 mL with milliQ water in a volumetric flask.

(b) Modus operandi

The TCEP feed solution was infused (flow rates of 0.625 $mL.min^{-1}$ and 0.833 $mL.min^{-1}$) through a column filled with elemental tellurium (7.290 g, 57.4 mmol). The resulting stream of TCEP=Te was mixed through a T-mixer with the cadmium precursor feed, which was infused at flow rates of 0.625 $mL.min^{-1}$ and 0.833 $mL.min^{-1}$, respectively. The SS reactor coil (1.25 mL, 1/16" SS tubing) was heated up to 140 °C, 145 °C, 150°C with a residence time of 45 s, respectively and a downstream pressure of 500 psi. The reactor effluent was thermally quenched and analyzed by *in-line* UV/Vis spectroscopy (10 mm light path).

6.1.4.8 Pilot scale flow synthesis of CdTe

The scalability of our protocol was validated to produce of CdTe QDs. The pilot scale setup featured the upstream preparation of TCEP=Te, its dilution with a 0.05 M aqueous NaOH stream and tellurium transfer with a $Cd(3\text{-}MPA)_2$ aqueous feed. The transfer of tellurium to cadmium occurred at temperatures ranging from 135 °C to 145 °C in a commercial mesofluidic Corning® AFR™G1 SiC reactor operated under 7 bar of counterpressure. The reactor effluent was thermally quenched through a cooling loop prior to *in-line* UV/Vis spectroscopy. A detailed flow chart is depicted in Figure

1. Detailed setup for the pilot scale production of CdTe

   The aqueous feed solution of TCEP was pumped with a Knauer Azura P4.1S HPLC pump (10 mL stainless steel head) through a thermostated packed-bed column filled with tellurium (Section 4.8.2 and Figure S11 for the detailed description of the thermostated packed-bed column). The aqueous effluent containing TCEP=Te was then diluted with a stream of aqueous NaOH through a PEEK T-mixer (0.04" internal bore). The NaOH feed was dosed with an Isco Teledyne 5000D dual syringe pump. After dilution and pH adjustment, the stream of TCEP=Te was then mixed with the aqueous cadmium feed, which was pumped with a Corning® AFR™G1 dosing line (equipped with HNP microgear pump). Both solutions then reacted in a mesolfuidic Corning® AFR™G1 SiC reactor equipped with 6 Silicon Carbide fluidic modules (10 mL internal volume each) connected in series. The temperature of the reactor was controlled by a Lauda XT 280 thermostat (using a Lauda Therm 180 thermal fluid) at temperatures ranging from 135 to 145 °C. The entire pilot scale setup was operated under 7 bars of counterpressure (Zaiput BPR-1000). The reactor effluent was thermally quenched through a 1/8" SS cooling loop (15 mL internal volume, operated at 0 °C) prior to *in-line* UV/Vis analysis (Avantes Flow cell-1/4", 5 mm pathlength).

2. Thermostated column

   The packed-bed column was thermostated for long runs at pilot scale to ensure reproducibility. The design (Figure S11) featured a tube-in-tube column setup. The outer tube consisted of PFA tubing (3/4 in., o.d x 0.062 in. wall, 10 cm length). The outer tube was connected to a Huber Ministat (Lauda Therm 180 thermal fluid) for thermostatization. The inner tube consisted of PFA tubing (1/4 in. o.d x 0.047 in. wall, 26 cm length) and was packed with tellurium.

3. Feed preparation

   A 1 M aqueous stock solution (500 mL) of NaOH 1 M was prepared by dissolving 20.00 g (0.5 mol) of NaOH in milliQ water in a volumetric flask.

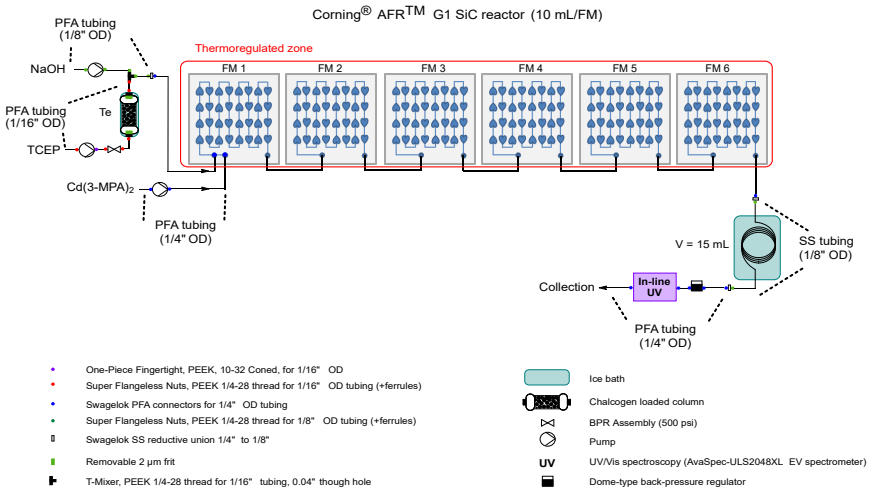

Figure 6.8. Detailed setup for the scalability trials toward CdTe

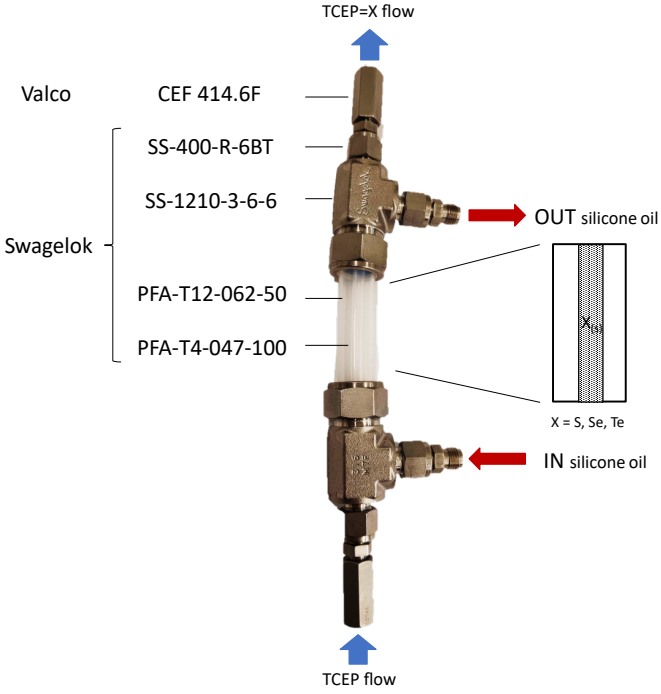

Figure 6.9. Homemade tube in tube reactor for chalcogen reduction

The aqueous 0.2 M solution of TCEP was prepared by dissolving TCEP · HCl (5.732 g, 20 mmol, 1 equiv.) with milliQ water. The solution was filled up to 100 mL with NaOH 1 M water in a volumetric flask. The solution was then transferred into a round-bottom flask and degassed with a flow of argon over 15 min.

The cadmium precursor feed solution was prepared by dissolving $Cd(OAc)_2$ (3.1984 g, 12 mmol, 1 equiv.) and 3-MPA (3.1842 g, 30 mmol, 2.5 equiv.) in milliQ water. The pH was then adjusted by the addition of 75 mL 1 M aqueous NaOH, then the solution was filled up to 2000 mL with milliQ water in a volumetric flask.

4. Modus operandi

The 0.2 M TCEP feed solution was infused at a flow rate of 1.2 $mL.min^{-1}$ through a column filled with elemental tellurium (7.34 g, 57.8 mmol). The resulting stream of TCEP=Te was diluted and pH-adjusted with a stream of aqueous NaOH (0.05 M) through a PEEK T-mixer (flow rate of 28.8 $mL.min^{-1}$ to 45 $mL.min^{-1}$). After dilution and pH adjustment, the stream of TCEP=Te was then mixed with the aqueous cadmium feed, which was injected at a flow rate of 40 $mL.min^{-1}$. CdTe QDs were obtained at process temperatures ranging from 135 °C to 145 °C (7 bar of counterpressure) with a residence time of 41.7 s to 51.4 s.

6.1.5 Additional experimental details

6.1.5.1 Transposition of the TCEP=X synthesis in flow

To estimate the interest of the transposition in flow, the metric used for comparisons is the Space-Time Yield (STY). This metric is a practical way to compare the productivity of reactors using various designs. The space-time yield is calculated as follows:

$$\mathrm{STY} = \frac{m'}{V_{\mathrm{rea}}} = \frac{C \cdot MM \cdot V'_{\mathrm{max}}}{V_{\mathrm{rea}}} \tag{2.14}$$

Where:

- **STY:** Space-time yield [$g.L^{-1}.min^{-1}$],
- **m':** Mass rate [$g.min^{-1}$],
- $\mathbf{V_{rea}}$**:** Reactor volume [L],
- **C:** Product concentration [$mol.L^{-1}$],

- **MM:** Molar mass of the product [g.mol^{-1}],
- **V'$_{max}$:** Maximum flow at which total conversion was observed [L.min^{-1}].

6.1.5.2 Productivity of TCEP=Te over time

The purpose of this experiment was to monitor the production of TCEP=Te over time and assess whether this packed-bed approach is amenable for long runs. Reaction monitoring was carried out by *in-line* ^{31}P-NMR (Figure 6.10). The results show that up to 200 min, the conversion of TCEP towards TCEP=Te reached completion without the formation of the degradation product (TCEP=O). The packed-bed column setup was therefore validated to sustain a constant production of TCEP=Te for long runs.

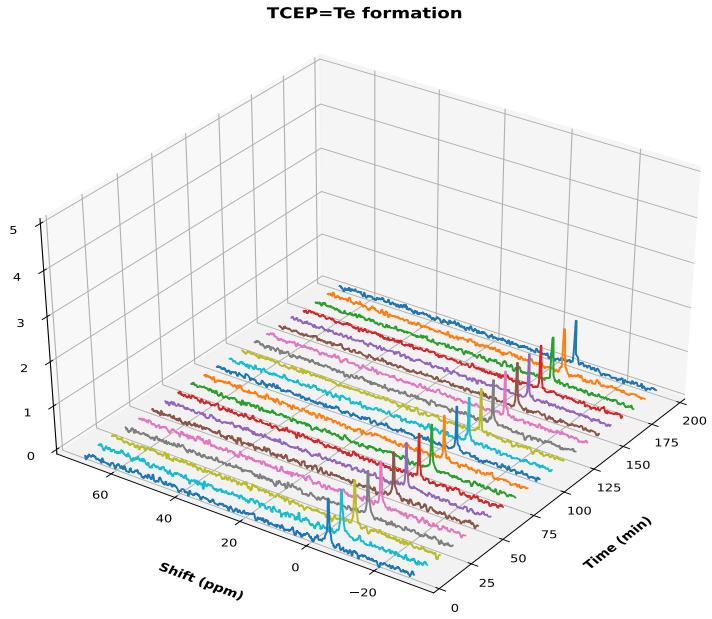

Figure 6.10. Monitoring of the productivity toward TCEP=Te

6.1.5.3 Control experiment for the preparation of CdS

To rule out the potential contribution of 3-MPA (3-mercaptoproponic acid) as a potential source of sulfur in the production of CdS QDs, a control experiment was performed in the absence of TCEP=S. Indeed, 3-MPA is used as a capping agent and chelates the cadmium source, and could therefore potentially transfer sulfur to cadmium under high temperatures.

The control experiment was conducted as follows: an aqueous feed of Cd(3-MPA)$_2$ was prepared by dissolving Cd(OAc)$_2$ (0.3332 g, 1.25 mmol, 1

equiv.) and 3-mercaptopropionic acid (0.4644 g, 4.375 mmol, 3.5 equiv.) in an aqueous NaOH solution (pH = 11) in a 250 mL volumetric flask. The resulting feed solution was injected in the same reactor setup (Figure 6.11) as for the CdS QDs synthesis (section 6.1.4.7).

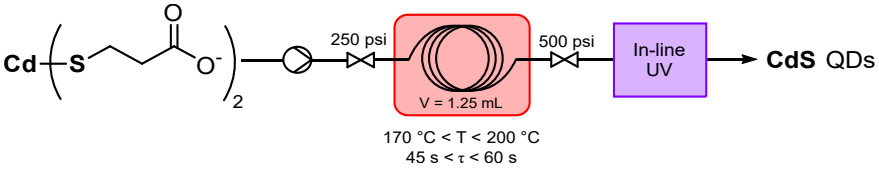

Figure 6.11. Control experiment for the preparation of CdS QDs in the absence of TCEP=S

A comparison with the control results of these experiments and the CdS synthesis with TCEP=S is depicted in Figure 6.12. Each plot contains the UV/Vis (left) and the photoluminescence results (right). The comparison of these two plots leads to the following observations:

- The use of 3-MPA allows the formation of CdS QDs. They exhibit a larger size and narrower size distribution than those synthesized with TCEP=S, under the same conditions. However, the use of TCEP=S allows to generate more nanoparticles (see UV/Vis spectra).

- The CdS QDs synthesized with TCEP=S as the chalcogen transfer agent are endowed with stronger photoluminescence than QDs obtained with 3-MPA. Both have broad emissions.

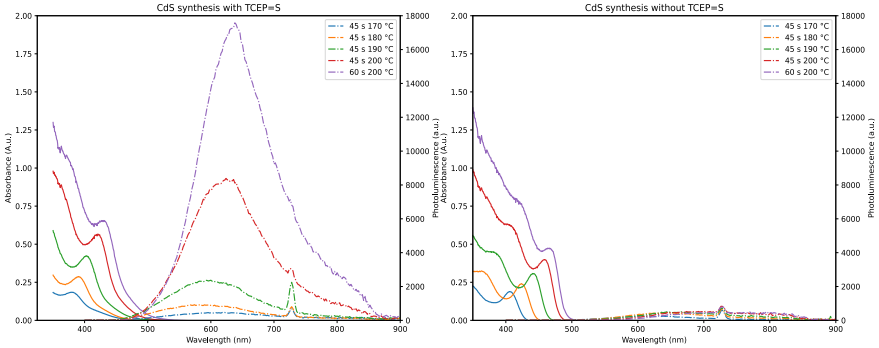

Figure 6.12. UV/Vis and fluorescence plots for: right CdS synthesis with TCEP=S, left: CdS synthesis with 3-MPA, (A.u. = Absorbance units). Note that the UV/Vis data from the left plot were obtained from tube through flow cell (500 µm light path).

In conclusion, 3-MPA can potentially play the role of sulfur agent under basic conditions at high temperatures. [2] It allows an efficient transfer of

sulfur to cadmium (narrower size distribution and larger QDs), however, they exhibit lower emission properties and generate less particles than TCEP=S. It seems therefore that the use of TCEP=S improves the emission properties of the CdS QDs and increases the particle concentration.

6.1.5.4 Additional experimental details for the scalability trials on CdTe QDs

During the scalability experiments, the influence of various parameters such as temperature, residence time and ionic strength (via the sodium hydroxide flow rate) were quickly scouted with *in-line* UV. Representative results of these experiments are presented in Figure 6.13.

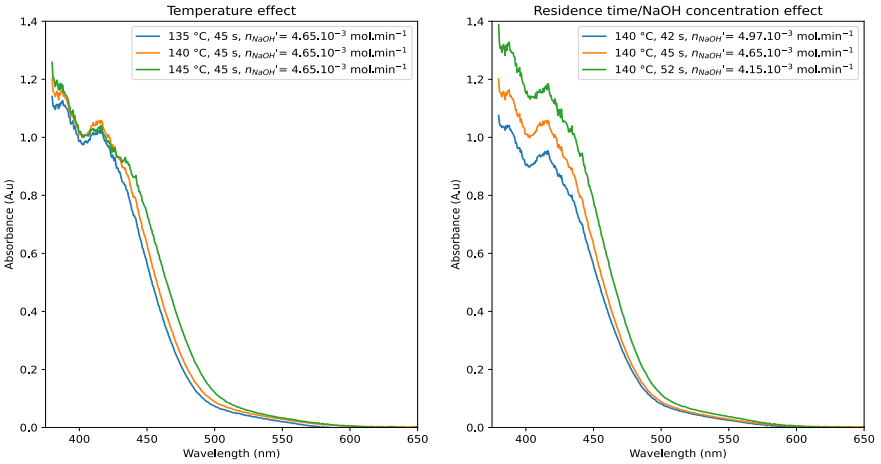

Figure 6.13. *In-line* reaction monitoring through UV/Vis spectroscopy for the pilot scale trials toward CdTe. The *in-line* module enabled to rapidly assess the effect of the operating conditions (temperature and residence time) and to monitor process stability once optimal conditions are identified

Several trends emerge from these curves. First, temperature appears to have a limited effect on the signal intensity. However, an increase in temperature broadens the signals and is likely to induce, in addition to the primary exitonic peak at 415 nm, a secondary shoulder at 435 nm. This suggests that temperature influences the size distribution of the QDs, leading to a broader range of sizes. On the other hand, residence time exerts a notable impact on the absorbance of the solution. A longer residence time within the reactor results in the production of particles of similar size, thus increasing the overall particle concentration. These promising trends need to be considered in conjunction with the high productivity achieved by the reactor.

6.1.5.5 Compounds characterization

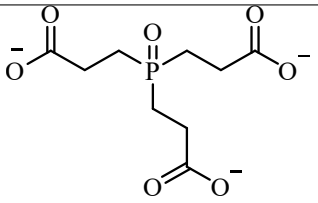 $C_9H_{12}O_7P^{3-}$ MW = 263,163	**3,3',3"-(oxo- λ^5-phosphanetriyl) tripropionate (TCEP=O) ^{1}H-NMR (400 MHz, D_2O)**: δ 2.48 – 2.27 (m, 2H), 2.20 – 1.98 (m, 2H). **^{13}C-NMR (101 MHz, D_2O)**: δ 180.33 (d, J = 15.1 Hz), 28.73 (d, J = 3.5 Hz), 23.22 (d, J = 65.5 Hz). **^{31}P-NMR (162 MHz, D_2O)**: δ 58.78.
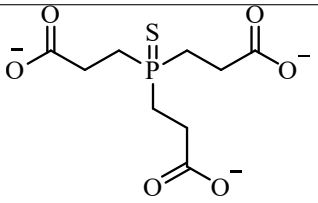 $C_9H_{12}O_6PS^{3-}$ MW = 279,224	**3,3',3"-(thioxo- λ^5-phosphanetriyl) tripropionate (TCEP=S) ^{1}H-NMR (400 MHz, D_2O)**: δ 2.52 – 2.40 (m, 2H), 2.29 – 2.16 (m, 2H). **^{13}C-NMR (101 MHz, D_2O)**: δ 180.37 (d, J = 15.9 Hz), 29.79 (d, J = 3.4 Hz), 26.09 (d, J = 50.8 Hz). **^{31}P-NMR (162 MHz, D_2O)**: δ 52.65.
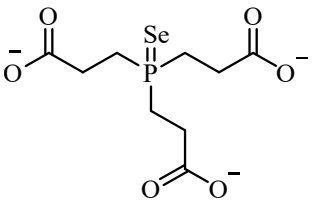 $C_9H_{12}O_6PSe^{3-}$ MW = 326,14	**3,3',3"-(selenoxo- λ^5-phosphanetriyl) tripropionate (TCEP=Se) ^{1}H-NMR (400 MHz, D_2O)**: δ 2.52 – 2.40 (m, 2H), 2.38 – 2.27 (m, 2H). **^{13}C-NMR (101 MHz, D_2O)**: δ 180.17 (d, J = 16.3 Hz), 30.56 (d, J = 3.2 Hz), 25.85 (d, J = 44.4 Hz). **^{31}P-NMR (162 MHz, D_2O)**: δ 43.42, 41.47, 39.52. **^{77}Se-NMR (76 MHz, D_2O)**: δ (d, J = 630.1 Hz). The NMR data matched those reported in the literature [3]
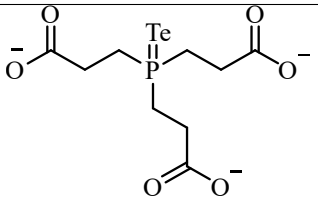 $C_9H_{12}O_6PTe^{3-}$ MW = 374,76	**3,3',3"-(telluroxo- λ^5-phosphanetriyl) tripropionate (TCEP=Te) ^{1}H-NMR (400 MHz, D_2O)**: δ 2.42 – 2.23 (m, 2H), 2.23 – 2.09 (m, 2H). **^{13}C-NMR (101 MHz, D_2O)**: δ 180.57 (d, J = 15.4 Hz), 32.53 **(d, J = 3.4 Hz)**, 24.88 (d, J = 26.5 Hz). **^{31}P-NMR (162 MHz, D_2O)**: δ -9.65.

6.1.5.6 Copy of the spectra (NMR, Raman or UV/Vis, photoluminescence)

1) TCEP

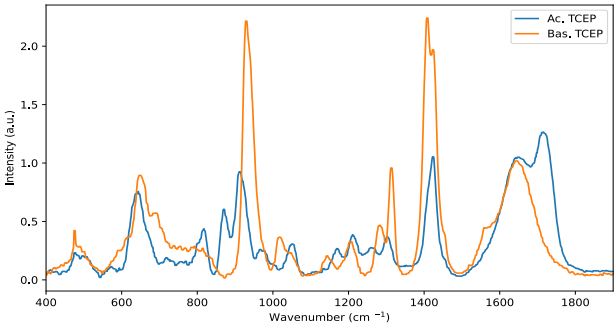

Figure 6.14. Reference Raman spectra for acidic and basic TCEP, (a.u. = arbitrary units)

2) TCEP=O

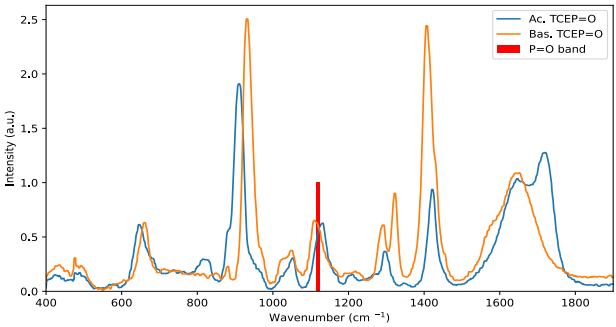

Figure 6.15. Reference Raman spectra for acidic and basic TCEP=O, (a.u. = arbitrary units)

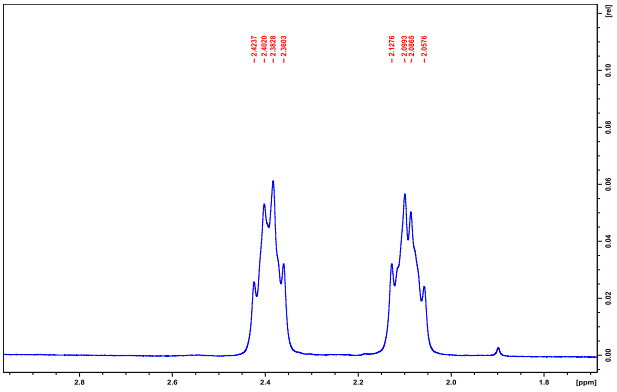

Figure 6.16. ^{1}H-NMR (400 MHz, D_2O), of TCEP=O

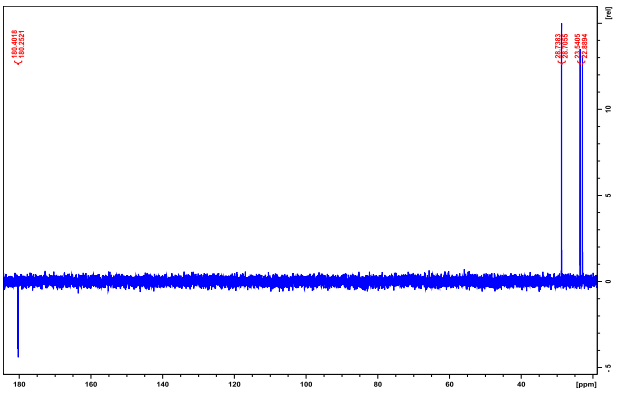

Figure 6.17. ^{13}C-NMR (101 MHz, D_2O), of TCEP=O

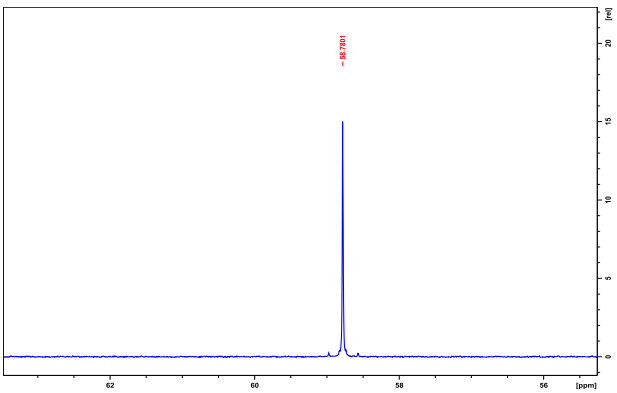

Figure 6.18. ^{31}P-NMR (162 MHz, D_2O), of TCEP=O

3) TCEP=S

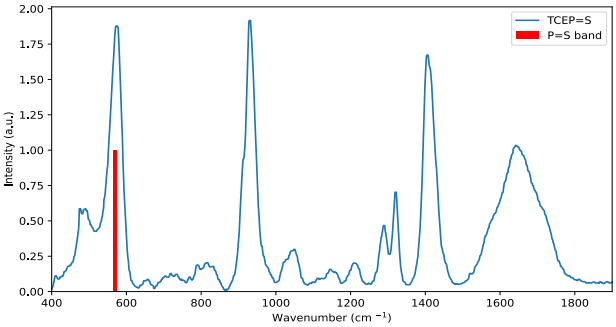

Figure 6.19. Reference Raman spectra for TCEP=S, (a.u. = arbitrary units)

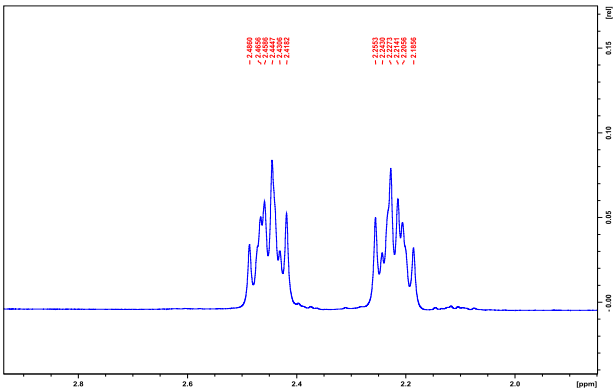

Figure 6.20. ^{1}H-NMR (400 MHz, D_2O), of TCEP=S

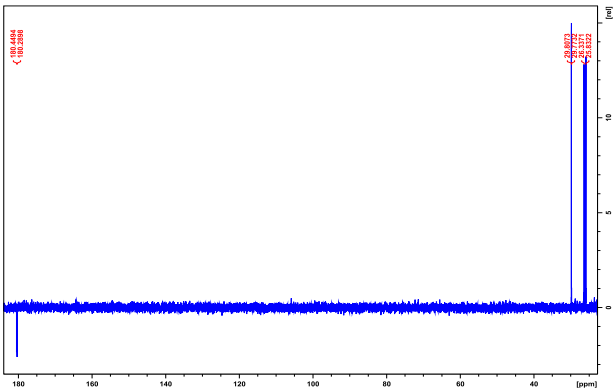

Figure 6.21. ^{13}C-NMR (101 MHz, D_2O), of TCEP=S

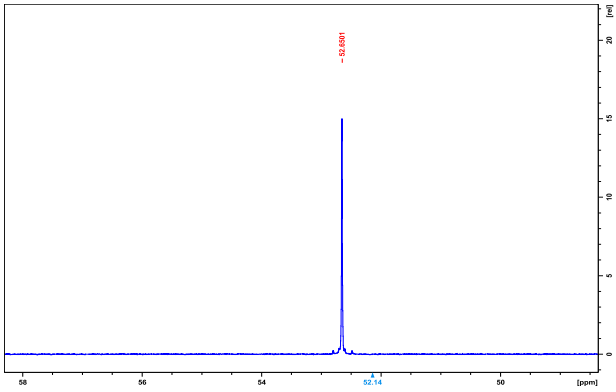

Figure 6.22. ^{31}P-NMR (162 MHz, D_2O), of TCEP=S

4) TCEP=Se

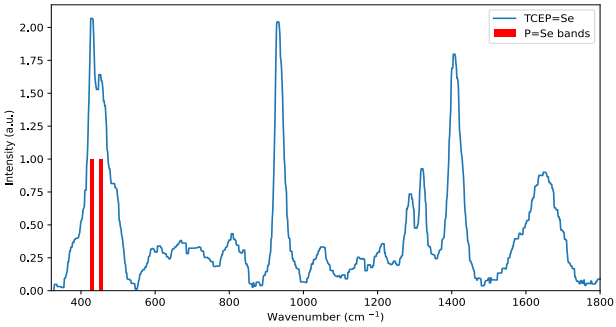

Figure 6.23. Reference Raman spectra for TCEP=Se, (a.u. = arbitrary units)

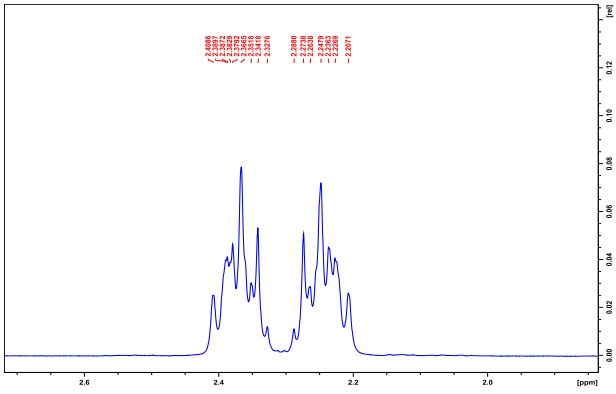

Figure 6.24. ^{1}H-NMR (400 MHz, D_2O), of TCEP=Se

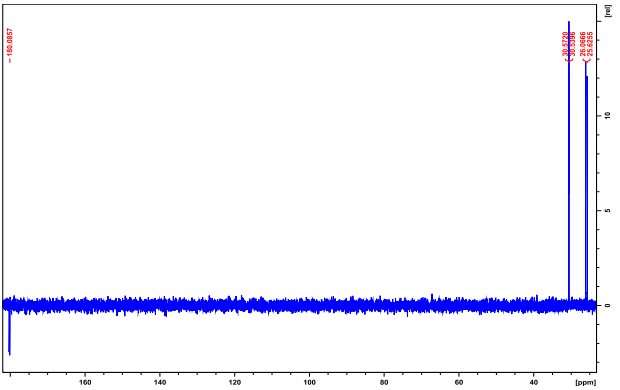

Figure 6.25. ^{13}C-NMR (101 MHz, D_2O), of TCEP=Se

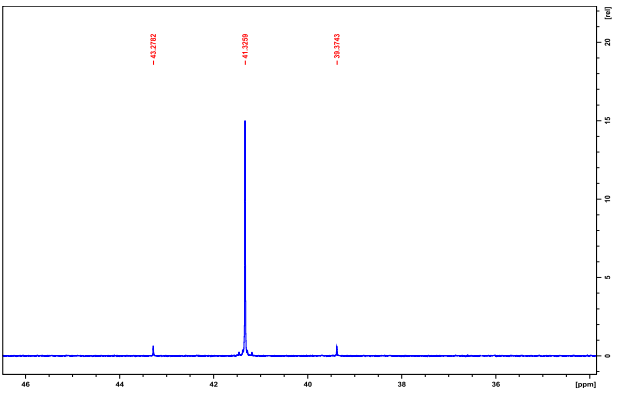

Figure 6.26. ^{31}P-NMR (162 MHz, D_2O), of TCEP=Se

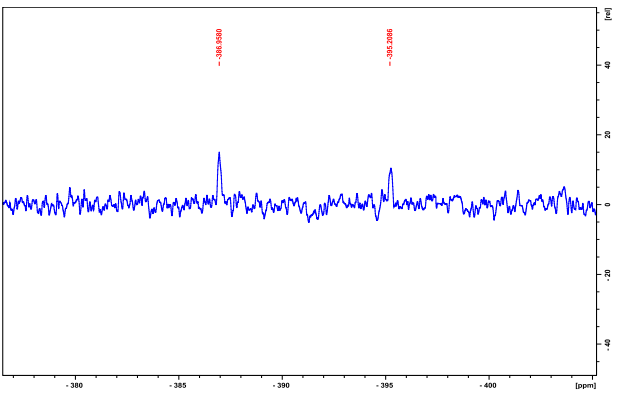

Figure 6.27. ^{77}Se-NMR (76 MHz, D_2O), of TCEP=Se

5) TCEP=Te

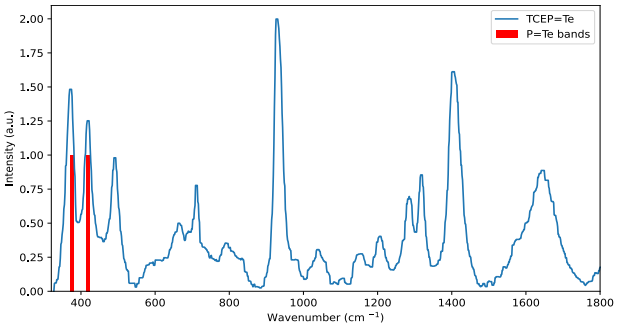

Figure 6.28. Reference Raman spectra for TCEP=Te, (a.u. = arbitrary units)

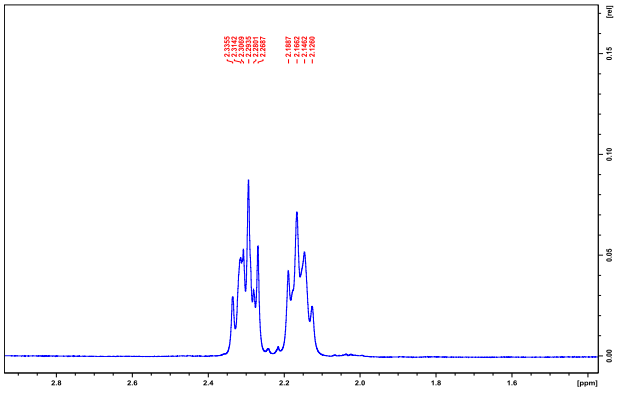

Figure 6.29. ^{1}H-NMR (400 MHz, D_2O), of TCEP=Te

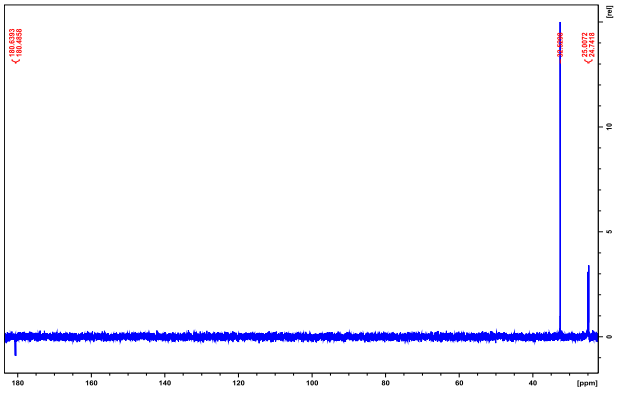

Figure 6.30. ^{13}C-NMR (101 MHz, D_2O), of TCEP=Te

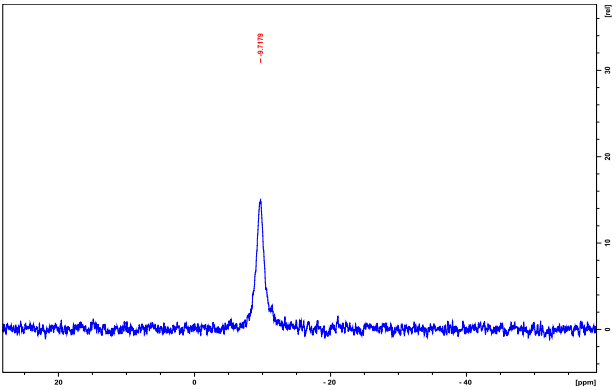

Figure 6.31. ^{31}P-NMR (162 MHz, D_2O), of TCEP=Te

6) CdS

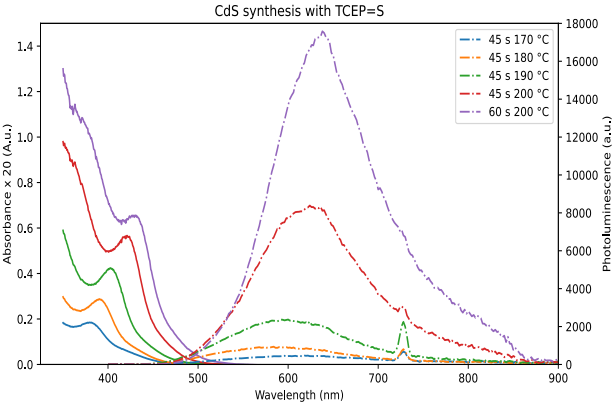

Figure 6.32. UV/Vis and photoluminescence spectra for the synthesized CdS QDs, (A.u. = Absorbance units, a.u. = arbritrary units)

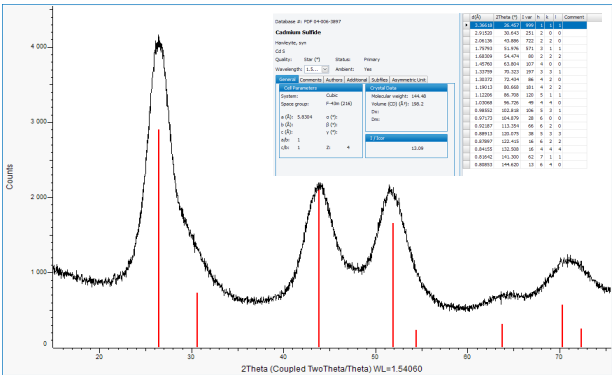

Figure 6.33. Powder XRD analysis of CdS, tune cell and its peak references

7) CdSe

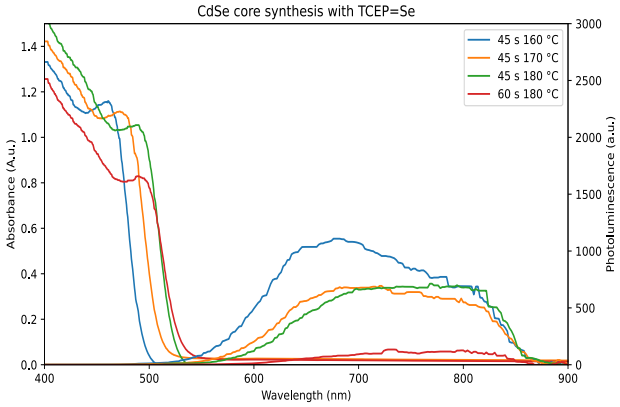

Figure 6.34. UV/Vis and photoluminescence spectra for the synthesized CdSe QDs, (A.u. = Absorbance units, a.u. = arbritrary units)

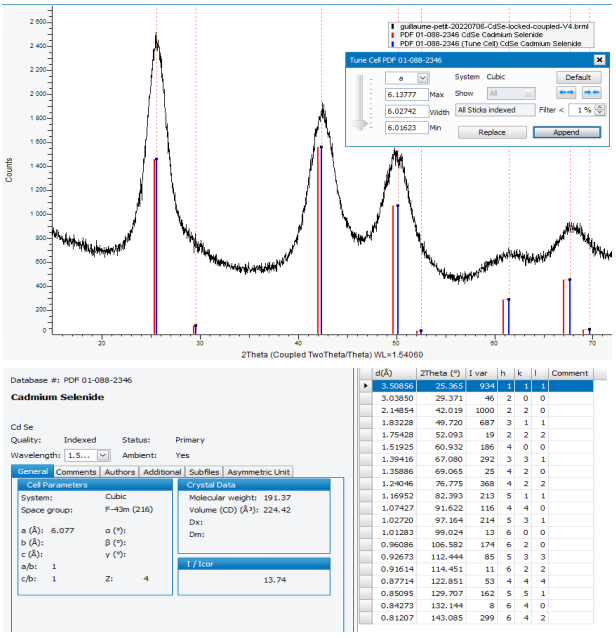

Figure 6.35. : Powder XRD analysis of CdSe, tune cell and its peak references

8) CdTe

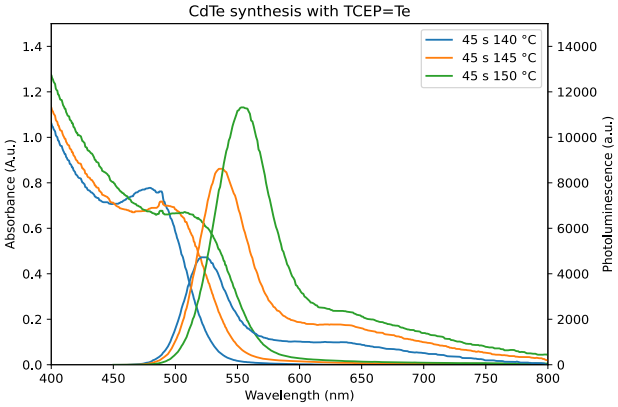

Figure 6.36. UV/Vis and photoluminescence spectra for the synthesized CdTe QDs, (A.u. = Absorbance units, a.u. = arbritrary units)

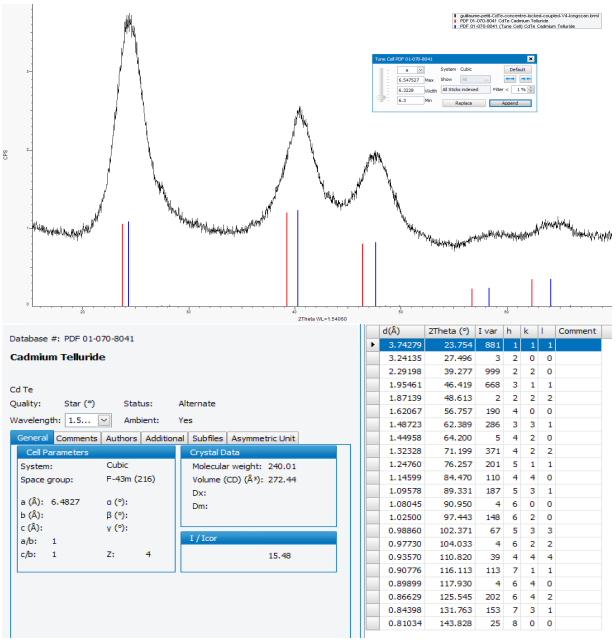

Figure 6.37. : Powder XRD analysis of CdTe, tune cell and its peak references

6.1.5.7 DFT calculations

To validate the frequencies impacted by the formation of TCEP=X from TCEP and their corresponding bond, DFT calculations were performed to simulate Raman spectra. Calculations were performed using the Gaussian 16 [4] package and implicit solvation (SMD, solvent = water). Optimization and characterization with vibrational analysis of the stationary points were carried out at the B3LYP/6-311++ G(d/p) level of theory for C, H, O, P, S and LANL2DZ for Se and Te. The Cartesian coordinates of the optimized molecules are provided in table 6.4.

Table 6.4. Cartesian coordinates of the optimized forms of TCEP=X (X=O, S, Se, Te)

Molecule	Cartesian coordinates
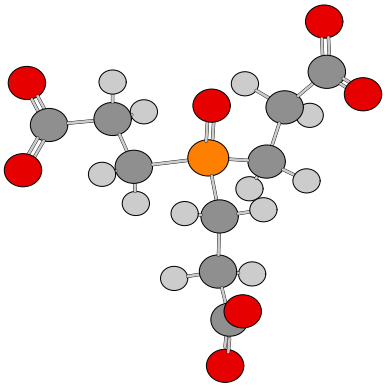 TCEP=O	C 1.85205100 0.07773900 0.74497500
	H 2.20619600 1.09041200 0.95839800
	H 1.97532800 -0.50556000 1.66237000
	C 2.64554600 -0.54340000 -0.40682700
	H 2.49919000 0.02463800 -1.33087200
	H 2.29941300 -1.55919100 -0.61641900
	C 4.16509700 -0.62512500 -0.18025200
	C -0.18976900 1.22028200 -1.03967600
	H 0.65357400 1.91141800 -1.11284100
	H -0.10805600 0.52461200 -1.87936400
	C -1.51084300 1.99759800 -1.11656400
	H -1.65851600 2.31340500 -2.15639600
	H -2.36543400 1.36775700 -0.86594500
	C -0.58248700 -1.45571000 0.19938300
	H -0.10925500 -1.82578700 -0.71343600
	H -0.20524000 -2.06268600 1.02858600
	C -2.10614600 -1.56046000 0.11007200
	H -2.48496500 -0.96852600 -0.72966300
	H -2.57505000 -1.14915900 1.00774700
	C -2.65075200 -2.98523100 -0.08383900

Continued on next page

Table 6.4 – Continued from previous page

Molecule	Cartesian coordinates
	C -1.58467000 3.28576300 -0.28208400
	O -0.51697700 3.92180200 -0.05158100
	O -3.90589200 -3.12257300 0.03935400
	O 4.82916800 -1.20303300 -1.09350200
	O -1.85087600 -3.92127500 -0.36561900
	O -2.73982100 3.66249400 0.08059400
	O 4.66410700 -0.12466600 0.86582400
	P 0.04619000 0.23863900 0.49859200
	O -0.61073400 0.88604600 1.72466000
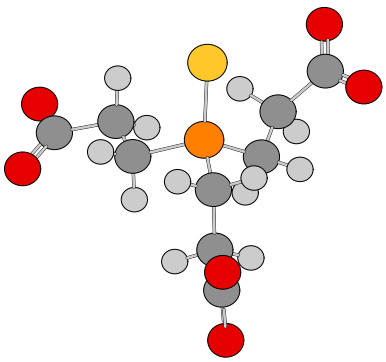 TCEP=S	C -1.91852200 -0.20499500 0.67962100
	H -2.17296200 -1.23504000 0.94163300
	H -2.12662900 0.41061400 1.55809700
	C -2.73539100 0.26560400 -0.52602500
	H -2.53318800 -0.35631300 -1.40223900
	H -2.46711700 1.28791700 -0.80819800
	C -4.25980800 0.25798600 -0.31393100
	C 0.24755600 -1.12643700 -1.07114200
	H -0.47962800 -1.94079600 -1.10561700
	H 0.00366000 -0.43854100 -1.88572300
	C 1.66572700 -1.68259100 -1.24756400
	H 1.84606900 -1.80805500 -2.32217400
	H 2.42497300 -0.98553600 -0.89293600
	C 0.34809900 1.57357300 0.16881800
	H -0.25438200 1.89792200 -0.68387000
	H -0.00311600 2.12249600 1.04665600
	C 1.83021400 1.84472000 -0.08318300
	H 2.16887500 1.33536700 -0.98988300
	H 2.43789700 1.44713400 0.73480800
	C 2.20251700 3.32749300 -0.24354700

Continued on next page

Table 6.4 – Continued from previous page

Molecule	Cartesian coordinates
	C 1.94042600 -3.06341400 -0.63211800
	O 0.98669600 -3.88716100 -0.53114700
	O 3.43064400 3.56907000 -0.44880900
	O -4.95863500 0.58514900 -1.32027300
	O 1.29896400 4.20673900 -0.16803300
	O 3.14513100 -3.31655400 -0.32763600
	O -4.72729500 -0.05771400 0.81564500
	P -0.08690100 -0.18841800 0.48481600
	S 0.82063200 -0.92867200 2.12460400
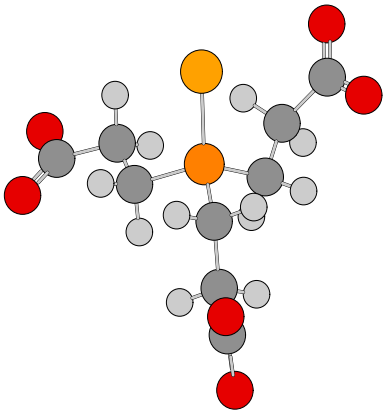 TCEP=Se	C -1.98111700 -0.26493700 0.50555600
	H -2.14315800 -1.32842200 0.69677100
	H -2.17713000 0.26476800 1.44061000
	C -2.89657200 0.23504400 -0.61517500
	H -2.69104700 -0.28821100 -1.55284100
	H -2.72869700 1.29751900 -0.81350400
	C -4.40171800 0.07627600 -0.33272200
	C 0.15715200 -0.90157800 -1.42116200
	H -0.52704800 -1.74991700 -1.48790800
	H -0.15740600 -0.16937200 -2.17007100
	C 1.59340900 -1.36312600 -1.69393800
	H 1.73233000 -1.39897300 -2.78127900
	H 2.33015100 -0.65234300 -1.31887300
	C 0.13163600 1.71412400 0.00716200
	H -0.52218800 2.04641700 -0.80422800
	H -0.22826600 2.17512500 0.92997100
	C 1.58034700 2.11075400 -0.27381900
	H 1.92794600 1.67809900 -1.21464700
	H 2.24218800 1.72126100 0.50678500
	C 1.82473400 3.62754200 -0.34246400

Continued on next page

Table 6.4 – Continued from previous page

Molecule	Cartesian coordinates
	C 1.96489700 -2.77045400 -1.19668800
	O 1.05185900 -3.63517800 -1.07500700
	O 2.96469800 3.98802600 -0.76374900
	O -5.17669500 0.41605800 -1.27676300
	O 0.91185800 4.41687000 0.03023800
	O 3.19841700 -2.99132200 -1.00412300
	O -4.77917900 -0.36167400 0.78898600
	P -0.17351100 -0.09024300 0.20412300
	Se 0.95119800 -0.93195300 1.88500600
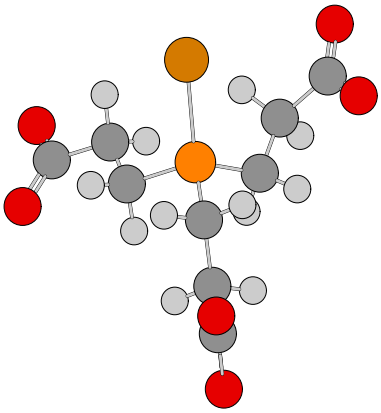 TCEP=Te	C 2.01090300 -0.49031400 -0.43119200
	H 1.99449300 -1.57645200 -0.54582500
	H 2.19975900 -0.06548100 -1.41992200
	C 3.08741900 -0.06306600 0.57002700
	H 2.90199000 -0.50623200 1.55253000
	H 3.08275100 1.02057200 0.71598100
	C 4.52338500 -0.44955700 0.17180300
	C -0.00514600 -0.60741300 1.72159900
	H 0.58765900 -1.51724800 1.83168000
	H 0.44510300 0.15619500 2.36240300
	C -1.45286600 -0.87671600 2.14270900
	H -1.52563900 -0.72571800 3.22619900
	H -2.15141900 -0.16819200 1.69529200
	C 0.28326500 1.83418900 0.05231500
	H 1.04006800 2.11735900 0.78892600
	H 0.63701900 2.16050500 -0.92872300
	C -1.06089200 2.47474600 0.38859100
	H -1.41060400 2.15411800 1.37430200
	H -1.82667300 2.15736000 -0.32538600
	C -1.05382100 4.01229000 0.39051300

Continued on next page

Table 6.4 – Continued from previous page

Molecule	Cartesian coordinates
	C -1.97784900 -2.30137600 1.89599200
	O -1.15174200 -3.23552700 1.69905500
	O -2.16059400 4.57091000 0.65642200
	O 5.43415700 -0.08618200 0.97551500
	O 0.01911000 4.62688800 0.13292800
	O -3.23502100 -2.45140600 1.96907500
	O 4.71972300 -1.08792500 -0.89913100
	P 0.28533900 -0.00667100 -0.00286100
	Te -1.25742400 -0.86533600 -1.69172300

6.2 Chapter 3: Supplemental Materials and Analysis

6.2.1 General information

High-field NMR experiments (structural identification of intermediates and determination of NMR conversions for the batch experiments) were carried out with a Bruker Avance III 400 MHz spectrometer in D_2O. The chemical shifts (δ) are reported relative to the solvent residual peak or to H_3PO_4 (^{31}P-NMR).

High resolution transmission electron microscopy (HRTEM) was performed with a LaB6-Tecnai G2 under 200 kV acceleration voltage, in bright field mode, on 200 mesh carbon-coated cupper grids. The sample was deposed on a beryllium support due to the EDX measurements.

Absorbance measurements were recorded on an AvaSpec-ULS2048XL EV spectrometer (Ultra-low Stray light Fiber optic Spectrometer, 75 mm AvaBench, 2048 large 500 µm pixel back-thinned CCD detector), equipped with an AvaLight-DH-S light source (Deuterium-Halogen light source, 190-2500 nm, incl. TTL shutter). *In-line* absorbance measurements were carried out with an Avantes CUV-ALL/UV/VIS cuvette sample holder (10x10 mm), equipped with a flow-through cell (3 in 1, Hellma 176-760-15-40). *Offline* analyses were performed in PMMA cells with the Avantes. The source, the holder and the analyzer were connected with Avantes FCB-UVIR400 fiber optic cables (bifurcated cable 2x400 µm, 2 or 1 m length, SMA terminations). For CdSe core QDs, the measures were acquired using a QE65000 Spectrometer from Ocean Optics. The sample was excited by a Balanced Deuterium Tungsten Source DH-2000-BAL (210 nm to 2500 nm), also from Ocean Optics.

Photoluminescence experiments were recorded *off-line* with a Shimadzu RF-6000 Spectrofluorimeter in Fluorescence quartz-made macro cells (Hellma 101-10-40). For CdSe core QDs, Emission spectra were acquired using an IHR-320 spectrofluorometer (Horiba) coupled with an SR-830 lock-in amplifier (Stanford Research System). The samples were excited at 365 nm, and the fluorescence was collected at 90° geometry.

The XPS experiments were conducted with a SSX 100/206 spectrometer from Surface Science Instruments (USA) using a monochromatized and micro focused Al-Kα X-ray beam operated at 10 kV, a parking chamber, and an automatic sample analysis.

Caution: This work involves the use of heavy metals (cadmium) and chalcogens (sulfur, selenium, tellurium). These compounds should be handled under a fume hood and with appropriate personal protective equipment (PPE). All the effluents generated must be disposed in appropriate containers with special labels following the instruction of EH&S authorities. All glassware

must be cleaned with commercial bleach (aqueous sodium hypochlorite for chalcogen decontamination).

6.2.2 Reagent and solvent

The reagents and solvents were purchased from commercial sources; these compounds are used without purification (Table 6.5).

Table 6.5. Solvents, chemicals and suppliers

Solvent	Purity (%)	CAS number	Supplier
Deuterium Oxide	99.90	7789-20-0	Eurisotop
Ethanol (absolute)	99	64-17-5	VWR
^{18}Oxygen Water	98	14314-42-2	Huayi Isotopes
Water HiPerSolv CHROMANORM®	/	7732-18-5	VWR
Chemicals	**Purity (%)**	**CAS number**	**Supplier**
3-Mercaptopropionic acid	99	107-96-0	Alfa Aesar
Borax decahydrate	$\geq$ 99.5	1303-96-4	Sigma Aldrich
Cadmium acetate dihydrate	98	5743-04-4	Sigma Aldrich
Hydrochloric acid	37	7647-01-0	VWR
Fluorescein sodium salt	N.A.	518-47-8	Sigma Aldrich
Oxalic acid anhydrous	$\geq$ 97	144-62-7	Fluka Analytical
Rhodamine 6G	99	989-38-8	Sigma Aldrich
Rhodamine 101	99	116450-56-7	Sigma Aldrich
Selenium powder *200 mesh*	99.999	7782-49-2	Alfa Aesar
Sodium hydroxide	$\geq$ 97	1310-73-2	VWR
Sulfur	99.98	7704-34-9	Aldrich
Tellurium *-18+60 mesh*	99.999	13494-90-9	Alfa Aesar
Thiourea	98	62-56-6	UCB
Tris-(2-carboxyethyhl)phosphine .hydrochloride	99.5	51805-45-9	Chem-Impex
Zinc chloride	N.A.	7646-85-7	Federa

Cadmium acetate and sodium borohydride must be stored under anhydrous conditions and tris-(carboxyethyl)phosphine (TCEP).hydrochloride must be stored at 4 °C.

6.2.3 Continuous flow setups

6.2.3.1 Microfluidic setups and parts

All microfluidic setups were assembled with commercially available parts.

1. Pumps

   Knauer AZURA P 4.1S HPLC pumps were used to handle all the liquid streams for microfluidic experiments.

2. PFA tubing

   PFA coil reactors and collection lines were constructed from PFA tubing (high purity PFA; 1.58 mm outer diameter, 500 µm internal diameter).

3. SS tubing

   The stainless tubing reactors were built with 316 stainless steel tubing (1.58 mm outer diameter, 500 or 750 µm internal diameter).

4. Connectors, ferrules and mixers

   Sections of the reactor that were not subjected to high temperatures and pressures were equipped with coned PEEK fittings and micromixers. Sections of the reactor that were subjected to high temperatures and pressures were equipped with Valco SS fittings, ferrules and unions. Connectors, ferrules and unions were purchased from IDEX/Upchurch or from VICI.

5. Check valves

   Check valves were inserted before the cross junction to prevent cross-contamination of the chalcogen columns and were purchased from IDEX/Upchurch Scientific.

6. Back pressure regulators

   To control the pressure inside the reactor, back pressure regulators of 100, 250 and 500 psi were used (IDEX/Upchurch Scientific).

7. Thermoregulatory devices

   Thermoregulation of PFA coil reactors was performed with a Heidolph™MR Hei-Tec® equipped with a Pt-1000 temperature sensor. The stainless steel coil reactors were embedded in a GC oven (Thermo Finnigan Interscience GC trace).

8. Setup flow parts and vendors

   Continuous flow parts and vendors are gathered in Table 6.6.

Table 6.6. Connectors, mixers, tubing and BPR

Part	Details	Vendor	Reference
Connectors	One-Piece Fingertight, PEEK, 10-32 Coned, for 1/16" o.d.	IDEX/Upchurch Scientific	F-120X
	Super Flangeless Nuts, natural PEEK 1/4-28 thread for 1/16" o.d. tubing	IDEX/Upchurch Scientific	P-255X
	Super Flangeless Ferrule Tefzel (ETFE) and SS ring 1/4-28 thread for 1/16" o.d. tubing	IDEX/Upchurch Scientific	P-259X
	303SS 10-32 NUTS for 1/16" o.d.	VICI (Valco Ins. Co. Inc.)	Zn1-10
	303SS union for 1/16" o.d. tubing with 0.5 mm BORE	VICI (Valco Ins. Co. Inc.)	ZU1M
	316 SS column end fitting 1/4" 1/16" 4 mm 4.6 mm cone, removable 2 µm frit	VICI (Valco Ins. Co. Inc.)	CEF 414.6F
Mixers	T-mixer, natural PEEK 1/4-28 thread for 1/16" o.d. tubing, 0.02" through hole	IDEX/Upchurch Scientific	P-712
	Cross assembly, natural PEEK 1/4-28 thread for 1/16" o.d. tubing, 0.02" through hole	IDEX/Upchurch Scientific	P-722
Tubing	High-purity PFA tubing, 1.58 mm outer diameter, 500 µm internal diameter	VICI (Valco Ins. Co. Inc.)	JR-T-4002-M25
	316 Stainless steel tubing 1/16" o.d. tubing, 0.03" through hole	VICI (Valco Ins. Co. Inc.)	TSS-130
	High-purity 1/8" and 1/4" PFA tubing, including appropriate PFA connections	Swagelok	PFA-T2-030-100 PFA-T4-047-100
	316/316L Stainless Steel Seamless Tubing, 1/4 in. od x 0.035 in.	Swagelok	SS-T4-S-035
Check-valve	Check-valve *in-line* 3 psi	IDEX/Upchurch Scientific	CV-3315
Back pressure regulators	BPR Assembly 100, 250, 500 psi	IDEX/Upchurch Scientific	P-787, P-788, P-789, U- 610

6.2.3.2 Mesofluidic setups and parts

1. Pumps

   During the scalability trials at the pilot scale, a Knauer AZURA P 4.1S HPLC pump, an Isco Teledyne 5000D dual syringe pump and a Knauer BlueShadow 80P (with 100 mL pump head), equipped with a Bronkhorst flow meter were used to handle liquids.

2. PFA tubing

   PFA coil reactors and collection lines were constructed from PFA tubing (high purity PFA 1/8"; 3.175 mm outer diameter, 1.65 mm internal diameter or high purity PFA 1/4"; 6.35 mm outer diameter, 3.2 mm internal diameter), and purchased from Swagelok.

3. SS tubing

   The stainless tubing reactors are built with 316 stainless steel tubing (3.175 mm outer diameter, 1.14 mm internal diameter), and purchased from Swagelok.

4. Connectors, ferrules and mixers

   Sections of the reactor that were not subjected to high temperatures were equipped with PFA Swagelok connectors. Sections of the reactor that were subjected to high temperatures were equipped with Swagelok SS fittings, ferrules and unions. Connectors, ferrules and unions were purchased from IDEX/Upchurch and from Swagelok PFA fittings

5. Back pressure regulator

   The pressure was regulated by an Equilibar BPR (H3P) that was inserted downstream of the pilot scale mesofluidic setup. The cracking pressure setpoints were regulated by a Bronkhorst EL-PRESS (M23211621B) connected to a compressed nitrogen gas cylinder (AirLiquide).

6. Thermoregulatory devices

   The Corning® AFR™G1 SiC reactor was thermostated by a Lauda XT 280 thermostat (Lauda Therm 180 thermal fluid) and the heat exchanger was cooled down by a Lauda PRO thermostat (containing water).

7. Setup flow parts and vendors

   Continuous flow parts and vendors are gathered in Table 6.7.

Table 6.7. Connectors, mixers, tubing and BPR

Part	Details	Vendor	Reference
Connectors	One-Piece Fingertight, PEEK, 10-32 Coned, for 1/16" o.d.	IDEX/Upchurch Scientific	F-120X
	Super Flangeless Nuts, natural PEEK 1/4-28 thread for 1/16" o.d. tubing	IDEX/Upchurch Scientific	P-255X
	316 Stainless Steel Nut for 1/8 in. Tube Fitting	Swagelok	SS-202-1
	316 Stainless Steel Nut for 1/4 in. Tube Fitting	Swagelok	SS-402-1
	316 Stainless Steel Nut for 1/2 in. Tube Fitting	Swagelok	SS-812-6
	Tube Fitting, Bulkhead Union, 1/8 in. x 1/4 in. Tube o.d.	Swagelok	SS-200-61-4
	Stainless Steel Tube Fitting, Reducing Union, 1/2 in. x 1/4 in. Tube o.d.	Swagelok	SS-810-6-4
	PFA Tube Fitting, 1/4 in. Nut	Swagelok	PFA-422-1
T-junction	Stainless Steel Tube Fitting, Union Tee, 1/8 in. Tube od	Swagelok	SS-200-3
	Stainless Steel Swagelok Tube Fitting, Reducing Union Tee, 1/2 in. x 1/4 in. x 1/2 in. Tube o.d.	Swagelok	SS-810-3-4-8
Tubing	High-purity PFA tubing, 1.58 mm outer diameter, 500 µm internal diameter	VICI (Valco Ins. Co. Inc.)	JR-T-4002-M25
	High-purity 1/8" and 1/4" PFA tubing, including appropriate PFA connections	Swagelok	PFA-T2-030-100 PFA-T4-047-100
	316 Stainless Steel Tubing, 1/8 in. o.d. x 0.040 in. Wall	VICI (Valco Ins. Co. Inc.)	TSS240
	316 Stainless Steel Tubing, 1/4 in. o.d. x 0.049 in. Wall	Swagelok	SS-T4-S-049-6ME
	316 Stainless Steel Tubing, 1/2 in. o.d. x 0.065 in. Wall	Swagelok	SS-T8-S-065-6ME
Check-valve	Stainless Steel Poppet Check Valve, Fixed Pressure, 1/8 in. Swagelok Tube Fitting, 1 psig (0.07 bar)	Swagelok	SS-2C-1
Back pressure regulators	High-pressure BPR	Equilibar	H3P1SNN8

6.2.4 Setups and protocols

6.2.4.1 Preparation of CdS QDs

1. Preparation of the feed solutions

   A 0.02 M aqueous solution of TCEP was prepared by dissolving TCEP · HCl (0.2866 g, 1 mmol, 1 equiv.) with milliQ water. The pH was adjusted to 10.7 with 2 M aqueous NaOH then the solution was filled up to 50 mL with milliQ water in a volumetric flask. The solution was then transferred into a round-bottom flask and degassed with a flow of argon for 15 min.

   The cadmium precursor feed solution was prepared by dissolving $Cd(OAc)_2$ (0.1333 g, 0.5 mmol, 1 equiv.) and 3-MPA (0.1327 g, 1.25 mmol, 1 equiv.) with milliQ water. The pH was adjusted to 11 by the addition of 2 M aqueous NaOH, then the solution was filled up to 100 mL with milliQ water in a volumetric flask.

2. Modus operandi

   The TCEP feed solution was infused (flow rates of 0.1, 0.2, 0.267 and 0.4 mL min^{-1}) through a column filled with elemental sulfur (1.991 g, 62.2 mmol). The resulting stream of TCEP=S was mixed through a T-mixer with the cadmium precursor that which was infused at a flow rate of 0.4, 0.8, 1.067 and 1.6 mL.min^{-1}, respectively. The SS reactor coil (1 mL, 1/16" SS tubing) was heated up to 170 °C, 180 °C, 190 °C, 200 °C and 210 °C under a downstream pressure of 500 psi. Residence times were fixed at 30 s, 45 s, 60 s and 120 s, respectively. The setup is detailed in Figure 6.38. The reactor effluent was thermally quenched and analyzed by *off-line* UV/Vis and emission spectroscopy (10x5 mm light path).

6.2.4.2 Preparation of CdSe QDs

1. Preparation of the feed solutions

   A 0.02 M aqueous solution of TCEP was prepared by dissolving TCEP · HCl (0.2866 g, 1 mmol, 1 equiv.) with milliQ water. The pH was adjusted to 10.7 with 2 M aqueous NaOH then the solution was filled up to 50 mL with milliQ water in a volumetric flask. The solution was then transferred into a round-bottom flask and degassed with a flow of argon for 15 min.

   The cadmium precursor feed solution was prepared by dissolving $Cd(OAc)_2$ (0.1333 g, 0.5 mmol, 1 equiv.) and 3-MPA (0.1327 g, 1.25 mmol, 1 equiv.) with milliQ water. The pH was adjusted to 11 by the addition of 2 M aqueous NaOH, then the solution was filled up to 100 mL with milliQ water in a volumetric flask.

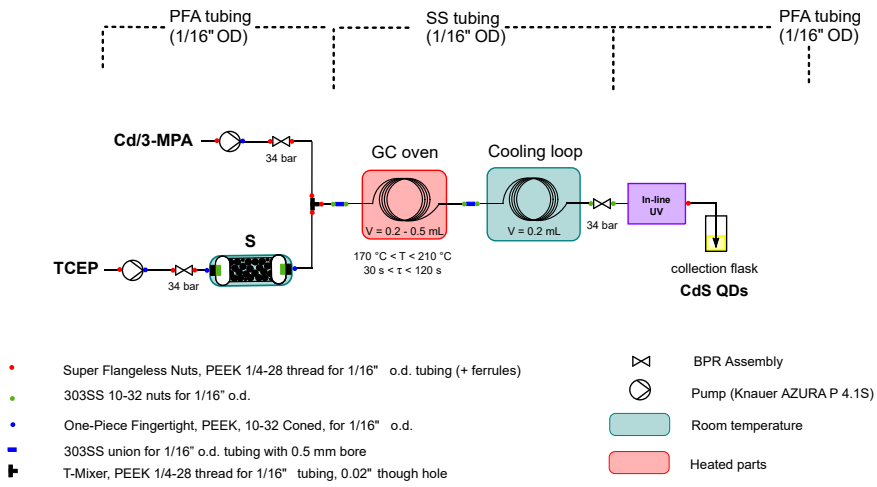

Figure 6.38. Setup for the preparation of CdS QDs

2. Modus operandi

   The TCEP feed solution was infused (under various flow rates, see Table 6.8 through a column filled with elemental selenium (3.743 g, 47.4 mmol). The resulting stream of TCEP=Se was mixed through a T-mixer with the cadmium precursor that which was infused at various flow rates, see Table 6.8. The SS reactor coil (1/16" SS tubing) was heated up to temperature ranging from 160 °C to 235 °C (*e.g.* 170 °C, 180 °C, 190 °C, 200 °C, 210 °C, 215 °C, 220 °C, 225 °C, 230 °C, 235 °C) under a downstream pressure of 500 psi. Residence times were fixed at between 4 s to 60 s, see Table 6.8. The setup is detailed in Figure 6.39. The reactor effluent was thermally quenched and analyzed by *off-line* UV/Vis and emission spectroscopy (10x5 mm light path).

6.2.4.3 Preparation of type I CdSe/ZnS core shell QDs

A solution was sought to improve the emissivity properties of CdSe QDs obtained through our TCEP-based concatenated protocol (see Figure 6.32). A common way reported in the literature to improve QD emission consists of surface passivation. One of the most efficient methods for surface passivation relies on the addition of a ZnS shell. [5] It was therefore envisioned to concatenate CdSe core synthesis with ZnS shell enclosure. To achieve this goal, careful selection of the sulfur source was paramount. Indeed, to avoid competition with potential leftovers of TCEP=Se from the upstream CdSe synthesis, a sulfur source reacting at a lower temperature than TCEP=Se must be selected. Thiourea [6] emerged as a convenient and widely available sulfur source. A concatenated setup was built accordingly (Figure 6.40).

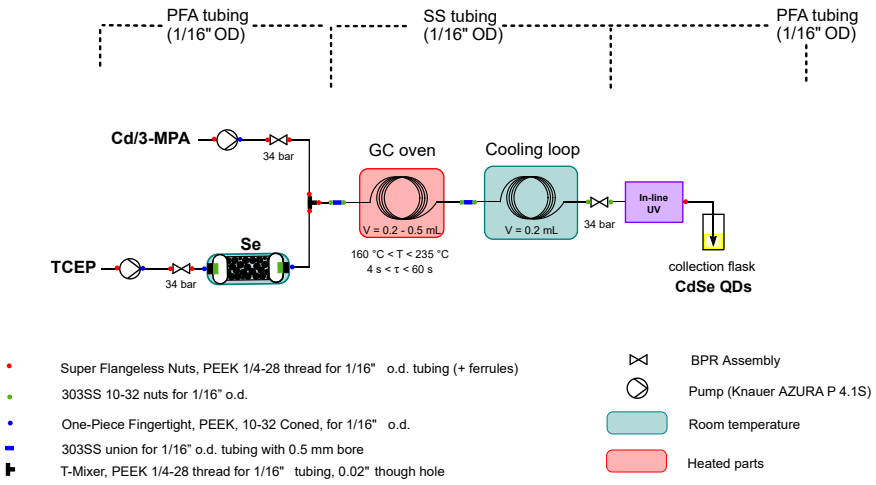

Figure 6.39. Setup for the preparation of CdSe QDs

Table 6.8. Correspondence residence time to flow rates, based on reactor's volume.

Time (s)	V_{reac} (mL)	$F_{Cd(3\text{-}MPA)_2}$ ($mL.min^{-1}$)	$F_{TCEP=Se}$ ($mL.min^{-1}$)
4	0.2	2.4	0.6
5	0.2	1.920	0.48
6	0.2	1.6	0.4
7	0.2	1.371	0.343
8	0.2	1.2	0.3
9	0.2	1.067	0.267
10	0.2	0.960	0.240
15	0.2	0.640	0.160
20	0.2	0.480	0.120
24	0.2	0.400	0.100
15	0.5	1.600	0.400
30	0.5	0.800	0.200
45	0.5	0.533	0.133
60	0.5	0.400	0.100

1. Setup

   A freshly prepared solution of TCEP=Se was infused with a Knauer Azura P4.1S pump (10 mL stainless steel head) and mixed through a T-mixer with the feed aqueous solution of $Cd(3\text{-MPA})_2$ (handled through a Knauer Azura P4.1S pump, 10 mL stainless steel head). Note that to ensure a stable flow rate, both the Knauer pumps were equipped with a 250 psi BPR. Both feeds reacted in a microfluidic SS coil reactor (1 mL internal volume) thermoregulated with a Thermo Finnigan Interscience GC oven operated at 190 °C under 250 psi.

   The reactor effluent was thermally quenched through an air-cooled SS coil (0.2 mL, id = 500 µm), before being blended with an aqueous feed of $ZnCl_2$/3-MPA through a T-mixer. The $ZnCl_2$/3-MPA feed solution was handled through a Knauer Azura P4.1S pump, equipped with a 10 mL stainless steel head. The setup is detailed in Figure 6.40. The reaction medium reacted next in a microfluidic PFA coil reactor (6 mL internal volume) operated at 120 °C < T < 160 °C (heating with a silicone oil bath) under 100 psi of counter-pressure. The reactor effluent was collected and analysed by UV/Vis and emission spectroscopy.

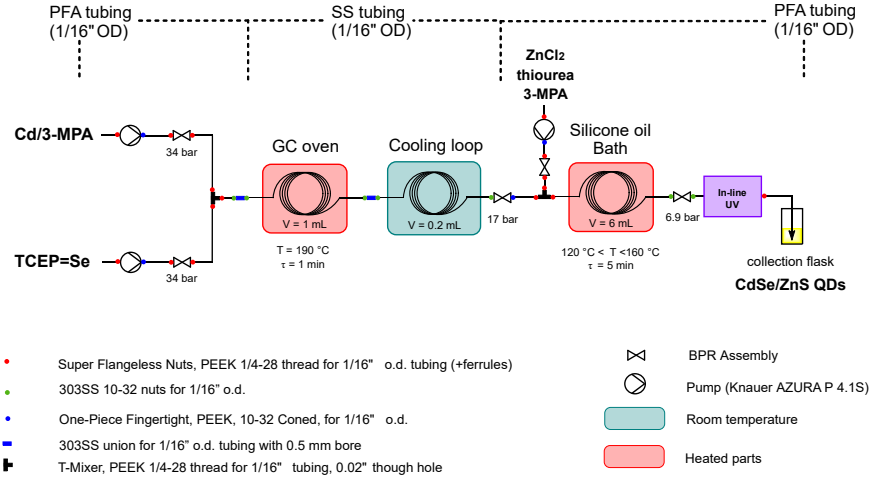

Figure 6.40. Concatenated setup for the preparation of CdSe/ZnS.

2. Preparation of the feed solutions

   The cadmium precursor $Cd(3\text{-MPA})_2$ feed solution was prepared by dissolving $Cd(OAc)_2$ (0.1333 g, 5 mmol, 5 equiv. vs TCEP) and 3-MPA (0.1327 g, 12.5 mmol, 2.5 equiv.) with milliQ water. The pH was adjusted to 11 by the addition of 1 M aqueous NaOH, then the solution was filled up to 100 mL with milliQ water in a volumetric flask.

   The feed solution of TCEP=Se (0.02 M) was prepared according to the procedure described in Section 6.1.4.7 and involved the reaction of

elemental selenium (0.1579 g, 2 mmol, 2 mmol, 2 equiv.) with an aqueous solution of TCEP (0.2866 g, 1 mmol, 1 equiv.), prepared in a 50 mL volumetric flask (pH increased to 11 with NaOH 1 M).

The zinc shell precursor feed solution was prepared by dissolving $ZnCl_2$ (0.1363 g, 1 mmol, 1 equiv.), thiourea (0.0761 g, 1 mmol, 1 equiv.) and 3-MPA (0.3184 g, 3 mmol, 3 equiv.) in milliQ water. The pH was then adjusted to 11 with the addition of 3.6 mL 1 M aqueous NaOH, then the solution was filled up to 50 mL with milliQ water in a volumetric flask.

3. Modus operandi

   The 0.02 M TCEP=Se feed solution and the 0.05 M $Cd(3\text{-MPA})_2$ feed solution were infused at 200 and 800 $\mu L.min^{-1}$, respectively, through a PEEK T-mixer and reacted at 190 °C for 1 min of residence time under 250 psi of counterpressure. After cooling down to room temperature, the reactor effluent containing CdSe QDs was then mixed through a PEEK T-mixer with the zinc shell precursor feed solution, infused at 200 $\mu L.min^{-1}$. CdSe/ZnS core-shell QDs occurred at 160 °C (100 psi) within 5 min of residence time.

6.2.4.4 Preparation of CdTe QDs

1. Preparation of the feed solutions

   A 0.003 M aqueous solution of TCEP was prepared by dissolving TCEP · HCl (0.2150 g, 0.75 mmol, 1 equiv.) with milliQ water. The pH was adjusted to 10.7 with 2 M aqueous NaOH, then the solution was filled up to 250 mL with milliQ water in a volumetric flask. The solution was then transferred into a round-bottom flask and degassed with an argon flow for 15 min.

   - Cd:Te ratio 5

     The cadmium precursor feed solution was prepared by dissolving $Cd(OAc)_2$ (0.9995 g, 3.75 mmol, 5 eq) and 3-MPA (0.9951 g, 9.375 mmol, 12.5 equiv.) with milliQ water. The pH was adjusted to 10.7 by the addition of 2 M aqueous NaOH, then the solution was filled up to 250 mL with milliQ water in a volumetric flask.

   - Cd:Te ratio 7.5

     The cadmium precursor feed solution was prepared by dissolving $Cd(OAc)_2$ (1.4992 g, 5.625 mmol, 7.5 eq) and 3-MPA (1.4926 g, 14.063 mmol, 18.75 equiv.) with milliQ water. The pH was adjusted to 10.7 by the addition of 2 M aqueous NaOH, then the solution was filled up to 250 mL with milliQ water in a volumetric flask.

   - Cd:Te ratio 10

     The cadmium precursor feed solution was prepared by dissolving $Cd(OAc)_2$ (1.9990 g, 7.5 mmol, 10 eq) and 3-mpa (1.9901 g, 18.75

mmol, 25 equiv.) with milliQ water. The pH was adjusted to 10.7 by the addition of 2 M aqueous NaOH, then the solution was filled up to 250 mL with milliQ water in a volumetric flask.

2. Modus operandi

   The TCEP feed solution was infused (flow rates of 0.625 mL.min^{-1} and 0.833 mL.min^{-1}) through a column filled with elemental tellurium (7.290 g, 57.4 mmol). The resulting stream of TCEP=Te was mixed through a T-mixer with the cadmium precursor that which was infused at a flow rate of 0.625 mL.min^{-1} or 0.833 mL.min^{-1}, respectively. The SS reactor coil (1.25 mL, 1/16" SS tubing) was heated up to 130 °C to 200 °C (*i.e.*, by step of 5 °C) under a downstream pressure of 250 psi. Residence times were fixed at 45 s and 60 s, respectively. The setup is detailed in Figure 6.41. The reactor effluent was thermally quenched and analyzed by *off-line* UV/Vis and emission spectroscopy (10 mm light path).

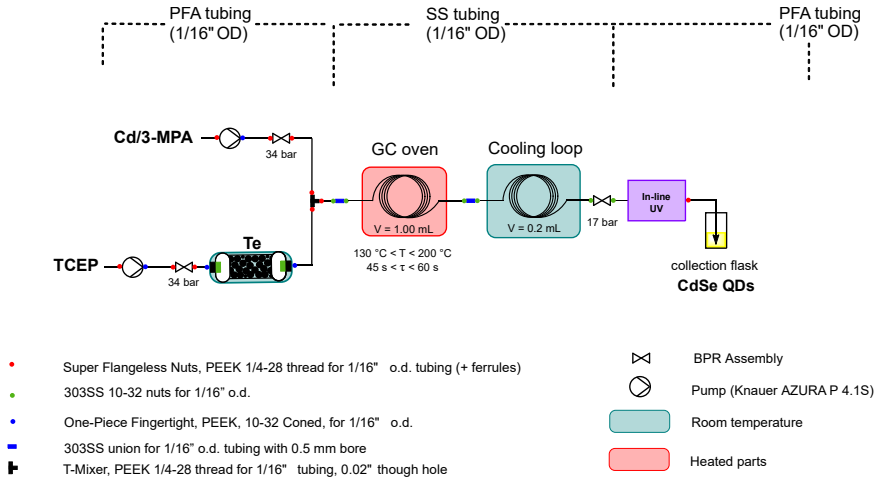

Figure 6.41. Setup for the preparation of CdTe QDs

3. Sample analysis Each sample produced was treated as follows:

   - Dilution: crude sample 100 µL + 1000 µL milliQ water
   - Absorbance measurement: between 350 nm to 1000 nm
   - Recording of 3D emission spectra: excitation (460 nm to 560 nm, 5 nm step), emission (470 nm to 900 nm, step 0.5 nm)

6.2.4.5 Pilot scale flow synthesis of CdTe

The scalability of our protocol was validated to produce of CdTe QDs. The pilot scale setup featured the upstream preparation of TCEP=Te, its dilution with a 0.05 M aqueous NaOH stream and tellurium transfer with a $Cd(3\text{-MPA})_2$ aqueous feed. The transfer of tellurium to cadmium occurred at temperatures ranging from 135 °C to 145 °C in a commercial mesofluidic Corning® AFR™G1 SiC reactor operated under 7 bar of counterpressure. The reactor effluent was thermally quenched through a cooling loop prior to *in-line* UV/Vis spectroscopy. A detailed flow chart is depicted in Figure

1. Detailed setup for the pilot scale production of CdTe

   The aqueous feed solution of TCEP was pumped with a Knauer Azura P4.1S HPLC pump (10 mL stainless steel head) through a thermostated packed-bed column filled with tellurium . The aqueous effluent containing TCEP=Te was then diluted with a stream of water through a SS T-mixer (Swagelok). The water feed was dosed with a Knauer BlueShadow equipped with a Bronkhorst flow meter. Both devices were connected to LabVision, which provided a PID feedback loop to ensure a constant flow rate. After dilution, the stream of TCEP=Te was then mixed with the aqueous cadmium feed, which was pumped by an Isco Teledyne 5000D dual syringe pump

   Both solutions then reacted in a mesolfuidic Corning® AFR™G1 SiC reactor equipped with 6 Silicon Carbide fluidic modules (10 mL internal volume each) connected in series. The temperature of the reactor was controlled by a Lauda XT 280 thermostat (using HL 60 thermal fluid) at temperatures ranging from 130 °C to 190 °C. The entire pilot scale setup was operated under 15.5 bar (225 psi) of counterpressure (Equilibar H3P) regulated by a Bronkhorst EL-PRESS. The reactor effluent was thermally quenched through a tube-in-tube heat exchanger (15 mL internal volume, operated at 4 °C) prior to *in-line* UV/Vis analysis (Avantes Flow cell-1/4", 5 mm pathlength). The detailled setup is shown in Figure 6.42

2. Heat exchanger

   Downstream of the mesofluidic reactor, a thermal quench is performed through a heat exchanger, which consists of a tube-in-tube exchanger. To maximize heat dissipation, the system is entirely made of stainless steel. The exchanger itself consists of 1 m of 1/4" tube surrounded, over 83 cm, by a 1/2" tube. Cooled water (set-point at 4 °C) circulates in the volume around the 1/4" pipe. A scheme of this system is provided in Figure 6.43. The heat exchange efficiency is assessed downstream by a thermocouple. The measured temperature remained between 20 °C and 30 °C throughout the experiments.

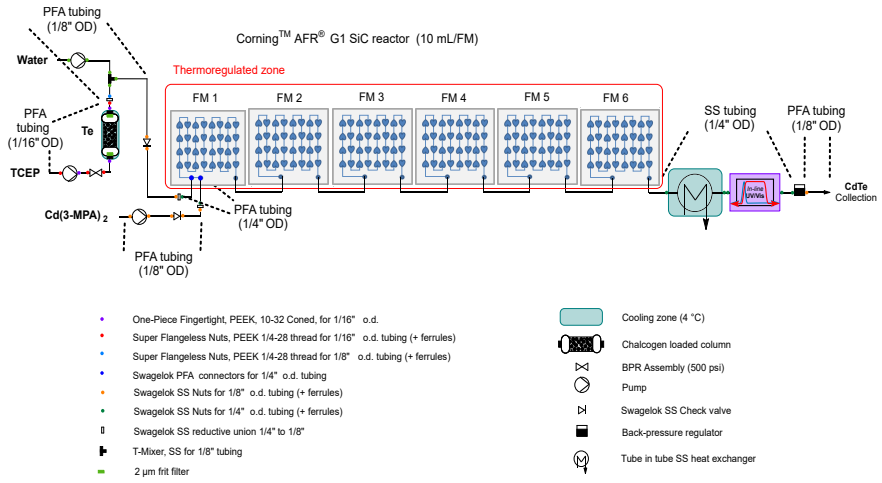

Figure 6.42. Detailed setup for the scalability trials toward CdTe

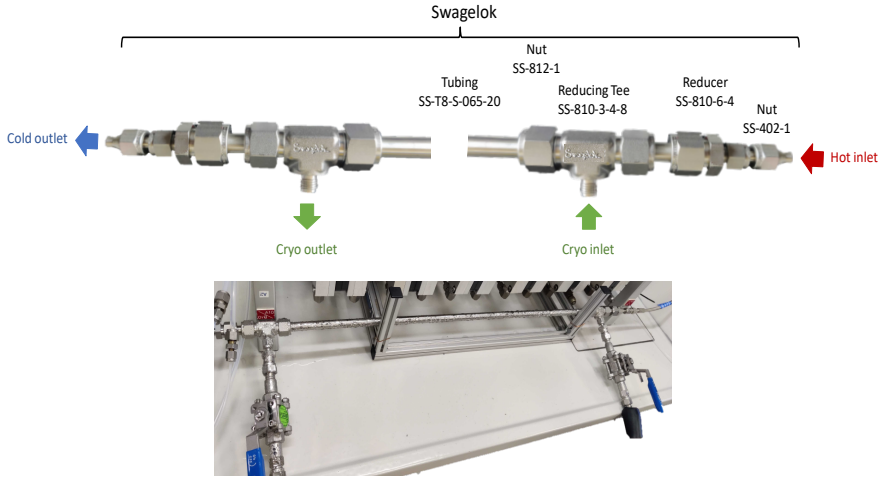

Figure 6.43. Detailed setup of the tube-in-tube heat exchanger.

3. Feed preparation

   A 2 M aqueous stock solution (300 mL) of NaOH was prepared by dissolving 24.00 g (0.6 mol) of NaOH in miliQ water in a volumetric flask.

   A 0.2 M aqueous solution of TCEP was prepared by dissolving TCEP.HCl (5.732 g, 20 mmol, 1 equiv.) with miliQ water. The solution was prepared by adding 54 mL with NaOH 2 M and then filling up to 100 mL with water in a volumetric flask. The solution was then transferred into a round-bottom flask and degassed with an argon flow for 15 min.

   The cadmium precursor feed solution was prepared by dissolving $Cd(OAc)_2$ (29.9846 g, 0.112 mol, 7.5 equiv.) and 3-MPA (29.85 g, 0.281 mol, 18.75 equiv.) in milliQ water. The pH was then adjusted with the addition of 220 mL 2 M aqueous NaOH, then the solution was filled up to 5000 mL with milliQ water in a volumetric flask.

4. Modus operandi

   The 0.2 M TCEP feed solution was infused at a flow rate of 0.45 or 0.6 $mL.min^{-1}$ through a column filled with elemental tellurium (7.34 g, 57.8 mmol). The resulting stream of TCEP=Te was diluted with a stream of milliQ water in a T-mixer (flow rate of 29.6 $mLmL.min^{-1}$ or 39.4 $mL.min^{-1}$). After dilution, the stream of TCEP=Te was then mixed with the aqueous cadmium feed, which was injected at a flow rate of 30 or 40$mL.min^{-1}$. CdTe QDs were obtained at process temperatures ranging from 130 °C to 190 °C (15.5 bar, 225 psi, of counter-pressure), with a residence time of 45 s or 60 s.

6.2.4.6 pH Titration

1) NaOH calibration using oxalic acid in the presence of phenolphthalein

First, a sodium hydroxide solution (NaOH, 2 $mol.L^{-1}$, V = 100 mL) was prepared . This stock solution was subsequently used to prepare the titration solution: 10 mL of the stock NaOH solution were transferred into a 250 mL volumetric flask, diluted with approximately 200 mL of Milli-Q water, and filled to the mark.

An oxalic acid solution (0.06 $mol.L^{-1}$) was prepared by dissolving 0.5443 g (6 mmol) of borax in Milli-Q water, followed by quantitative transfer into a 100 mL volumetric flask and dilution to volume.

Samples of 20 mL of the oxalic acid solution were titrated with the diluted NaOH solution in the presence of two drops of phenolphthalein as indicator. This procedure was repeated four times. The results of the calibration are summarized in Table 6.9.

Table 6.9. Calibration results for the titration of 20 mL of oxalic acid solution with NaOH in the presence of phenolphthalein.

Sample	Equivalent volume (mL)	$[NaOH]_{dil}$ ($mol.L^{-1}$)	$[NaOH]_{conc}$ ($mol.L^{-1}$)
1	28.5	0.0833	2.082
2	28.5	0.0833	2.082
3	28.5	0.8333	2.082
4	28.5	0.8333	2.082

The standardized NaOH concentration was determined to be 2.08 $mol\,L^{-1}$ and was used for all subsequent titration.

2) pH titration of 3-MPA

The 3-MPA solutions (C ≈ 0.056 and 0.075 $mol.L^{-1}$, V = 250 mL) were prepared by dissolving 3-MPA (1.4992 g, n = 14 mmol or 1.99 g, n = 18.7 mmol) with Milli-Q water, in a 250 mL volumetric flask.

For pH titration, the solution was transferred into a beaker (≈500 mL) equipped with a magnetic stir bar. The pH electrode was immersed in the solution, and the titration was performed by incremental addition of standardized NaOH (2 $mol.L^{-1}$) from a 25 mL burette.

3) pH titration of $Cd(3\text{-}MPA)_2$ systems

The $Cd(3\text{-}MPA)_2$ solutions (C ≈ 0.0225 and 0.03 $mol.L^{-1}$, V = 250 mL) were prepared by dissolving $Cd(OAc)_2 \cdot 2\,H_2O$ (1.4973 g, n = 5.61 mmol or 1.995 g, n = 7.48 mmol) and 2.5 eq of 3-MPA (1.4992 g, n = 14 mmol or 1.99 g, n = 18.7 mmol) with Milli-Q water, in a 250 mL volumetric flask.

For pH titration, the solution was transferred into a beaker (≈500 mL) equipped with a magnetic stir bar. The pH electrode was immersed in the solution, and the titration was performed by incremental addition of standardized NaOH (2 $mol.L^{-1}$) from a 25 mL burette.

4) HCl calibration using borax in the presence of methyl orange

First, a hydrochloric acid solution (HCl, 2 $mol.L^{-1}$) was prepared from a 37% stock solution by diluting 83.33 mL of concentrated acid with 416.67 mL of Milli-Q water. This stock solution was subsequently used to prepare the titration solution: 40 mL of the stock HCl solution were transferred into a 250 mL volumetric flask, diluted with approximately 200 mL of Milli-Q water, and filled to the mark.

A borax solution (0.12 mol.L^{-1}) was prepared by dissolving 4.5765 g (12 mmol) of borax in Milli-Q water, followed by quantitative transfer into a 100 mL volumetric flask and dilution to volume.

Samples of 20 mL of the borax solution were titrated with the diluted HCl solution in the presence of two drops of methyl orange as indicator. This procedure was repeated four times. The results of the calibration are summarized in Table 6.10.

Table 6.10. Calibration results for the titration of 20 mL of borax solution with HCl in the presence of methyl orange.

Sample	Equivalent volume (mL)	$[HCl]_{dil}$ (mol.L^{-1})	$[HCl]_{conc}$ (mol.L^{-1})
1	32.3	0.1486	1.858
2	32.2	0.1491	1.863
3	32.2	0.1491	1.863
4	32.3	0.1486	1.858

The standardized HCl concentration was determined to be 1.86 mol L^{-1} and was used for all subsequent titrations.

5) pH titration of TCEP=S systems

a) TCEP=S

A TCEP=S solution (C ≈ 0.02 mol.L^{-1}, V = 100 mL) was prepared by dissolving TCEP · HCl (0.5732 g, n = 2 mmol) in Milli-Q water in a 100 mL volumetric flask. The pH was adjusted to 11 using NaOH (2 mol.L^{-1}), and the solution was diluted to volume with Milli-Q water. The solution was transferred into a 100 mL round-bottom flask, sealed with a septum, and purged with argon for at least 15 min. Elemental sulfur (0.1283 g, n = 4 mmol) was then added, and the mixture was stirred vigorously under argon for 30 min.

For pH titration, the solution was transferred into a beaker (>100 mL) equipped with a magnetic stir bar. The pH electrode was immersed in the solution, and the titration was performed by incremental addition of standardized HCl (2 mol.L^{-1}) from a 10 mL burette.

b) TCEP=S with Cd(3-MPA)$_2$

A TCEP=S solution (C ≈ 0.04 mol.L^{-1}, V = 50 mL) was prepared following the same procedure as described above, using TCEP · HCl (0.5732 g, n = 2 mmol) and adjusting the pH to 11 with NaOH

(2 mol.L^{-1}). After dilution to volume, the solution was transferred into a septum-sealed flask, purged with argon, reacted with elemental sulfur (0.1283 g, 4 mmol), and stirred for 30 min under inert atmosphere.

A Cd(3-MPA)$_2$ solution (C ≈ 0.04 mol.L^{-1}, V = 50 mL) was prepared by dissolving Cd(OAc)$_2 \cdot 2\,H_2O$ (0.5331 g, n = 2 mmol) and 3-MPA (0.5307 g, 435 μL, 5 mmol) in Milli-Q water in a 50 mL volumetric flask. The ionic strength and pH were adjusted using NaOH (2 mol.L^{-1}), and the solution was diluted to volume.

For titration, equal volumes of the TCEP=S and Cd(3-MPA)$_2$ solutions were combined in a beaker (>100 mL) under stirring. The pH electrode was immersed in the mixture, and the solution was titrated with standardized HCl (2 mol.L^{-1}) using a 10 mL burette.

6) pH titration of TCEP=Se systems

a) TCEP=Se

A TCEP=Se solution (C ≈ 0.02 mol.L^{-1}, V = 100 mL) was prepared by dissolving TCEP · HCl (0.5732 g, n = 2 mmol) in Milli-Q water in a 100 mL volumetric flask. The pH was adjusted to 11 using NaOH (2 mol.L^{-1}), and the solution was diluted to volume with Milli-Q water. The solution was transferred into a 100 mL round-bottom flask, sealed with a septum, and purged with argon for at least 15 min. Elemental selenium (0.3158 g, n = 4 mmol) was then added, and the mixture was stirred vigorously under argon for 30 min.

For pH titration, the solution was transferred into a beaker (>100 mL) equipped with a magnetic stir bar. The pH electrode was immersed in the solution, and the titration was performed by incremental addition of standardized HCl (2 mol.L^{-1}) from a 10 mL burette.

b) TCEP=Se with Cd(3-MPA)$_2$

A TCEP=Se solution (C ≈ 0.04 mol.L^{-1}, V = 50 mL) was prepared following the same procedure as described above, using TCEP · HCl (0.5732 g, n = 2 mmol) and adjusting the pH to 11 with NaOH (2 mol.L^{-1}). After dilution to volume, the solution was transferred into a septum-sealed flask, purged with argon, reacted with elemental selenium (0.3158 g, 4 mmol), and stirred for 30 min under inert atmosphere.

A Cd(3-MPA)$_2$ solution (C ≈ 0.04 mol.L^{-1}, V = 50 mL) was prepared by dissolving Cd(OAc)$_2 \cdot 2\,H_2O$ (0.5331 g, n = 2 mmol) and 3-MPA (0.5307 g, 435 μL, 5 mmol) in Milli-Q water in a 50 mL volumetric flask. The ionic strength and pH were adjusted using NaOH (2 mol.L^{-1}), and the solution was diluted to volume.

For titration, equal volumes of the TCEP=Se and Cd(3-MPA)$_2$ solutions were combined in a beaker (>100 mL) under stirring. The pH electrode was immersed in the mixture, and the solution was titrated with standardized HCl (2 mol.L^{-1}) using a 10 mL burette.

7) pH titration of TCEP=Te systems

a) TCEP=Te

A TCEP=Te solution (C ≈ 0.02 mol.L^{-1}, V = 100 mL) was prepared by dissolving TCEP · HCl (0.5732 g, n = 2 mmol) in Milli-Q water in a 100 mL volumetric flask. The pH was adjusted to 11 using NaOH (2 mol.L^{-1}), and the solution was diluted to volume with Milli-Q water. The solution was transferred into a 100 mL round-bottom flask, sealed with a septum, and purged with argon for at least 15 min. Elemental tellurium (0.5104 g, n = 4 mmol) was then added, and the mixture was stirred vigorously under argon for 30 min.

For pH titration, the solution was transferred into a beaker (>100 mL) equipped with a magnetic stir bar. The pH electrode was immersed in the solution, and the titration was performed by incremental addition of standardized HCl (2 mol.L^{-1}) from a 10 mL burette.

b) TCEP=Te with Cd(3-MPA)$_2$

A TCEP=Te solution (C ≈ 0.04 mol.L^{-1}, V = 50 mL) was prepared following the same procedure as described above, using TCEP · HCl (0.5732 g, n = 2 mmol) and adjusting the pH to 11 with NaOH (2 mol.L^{-1}). After dilution to volume, the solution was transferred into a septum-sealed flask, purged with argon, reacted with elemental selenium (0.5104 g, 4 mmol), and stirred for 30 min under inert atmosphere.

A Cd(3-MPA)$_2$ solution (C ≈ 0.04 mol.L^{-1}, V = 50 mL) was prepared by dissolving Cd(OAc)$_2$ · 2 H$_2$O (0.5331 g, n = 2 mmol) and 3-MPA (0.5307 g, 435 μL, 5 mmol) in Milli-Q water in a 50 mL volumetric flask. The ionic strength and pH were adjusted using NaOH (2 mol.L^{-1}), and the solution was diluted to volume.

For titration, equal volumes of the TCEP=Te and Cd(3-MPA)$_2$ solutions were combined in a beaker (>100 mL) under stirring. The pH electrode was immersed in the mixture, and the solution was titrated with standardized HCl (2 mol.L^{-1}) using a 10 mL burette.

8) pH titration of Cd(3-MPA)$_2$ system

A Cd(3-MPA)$_2$ solution (C ≈ 0.04 mol.L^{-1}, V = 50 mL) was prepared by dissolving Cd(OAc)$_2$ · 2 H$_2$O (0.5331 g, n = 2 mmol) and 3-MPA

(0.5307 g, 435 μL, 5 mmol) in Milli-Q water in a 50 mL volumetric flask. The ionic strength and pH were adjusted using NaOH (2 mol.L^{-1}), and the solution was diluted to volume.

For titration, equal volumes of the Cd(3-MPA)$_2$ solution and milliQ water were combined in a beaker (>100 mL) under stirring. The pH electrode was immersed in the mixture, and the solution was titrated with standardized HCl (2 mol.L^{-1}) using a 10 mL burette.

6.2.5 Additional experimental details

6.2.5.1 Peak position derivation (for FW mechanism)

The expression developed in Equation 3.12 can be differentiated to identify changes in concavity and, consequently, the dominant phase of the FW mechanism. The first derivative was calculated and is presented in Equation 6.1.

$$\frac{dE_{\text{peak}}}{d\theta_{\text{norm}}} = (E_\infty - E_0) \cdot \exp\left(-\frac{\alpha}{\theta_{\text{norm}}}\right) \cdot \frac{\alpha}{\theta_{\text{norm}}^2} \tag{6.1}$$

The first derivative allows the identification of θ_{norm} corresponding to Burst Nucleation (*i.e.*, slope values significantly different from 0) and the maximum growth rate (*i.e.*, derivative returning to 0 after the induction period).

6.2.5.2 Model selection for CdS

The model selection was performed by fitting the parametrized form $\theta(t, T)$ to the experimental evolution of $E(\theta)$. The statistical criteria used to compare the one-parameter and three-parameter formulations are summarized in Figure 6.44 and Table 6.11.

Table 6.11. Statistical comparison of the one- and three-parameter models for the CdS QDs first excitonic peak.

Criterion	1 parameter	3 parameters
r^2	0.87418	0.87450
RSS	887.921	885.657
AIC	65.21	65.17
BIC	66.63	66.59

While the three-parameter model yields slightly improved RSS, r^2, AIC, and BIC values compared to the simpler one-parameter model, the improvement is marginal. Importantly, the three-parameter model modifies the weight of the temperature dependence through the γ exponent, reflecting a slightly stronger role of temperature in the effective time. This adjustment does not fundamentally change the shape or interpretation of the reaction kinetics since the α counterbalance the γ effect.

Consequently, the one-parameter model was retained: it captures already the kinetic trends and remains far more simple.

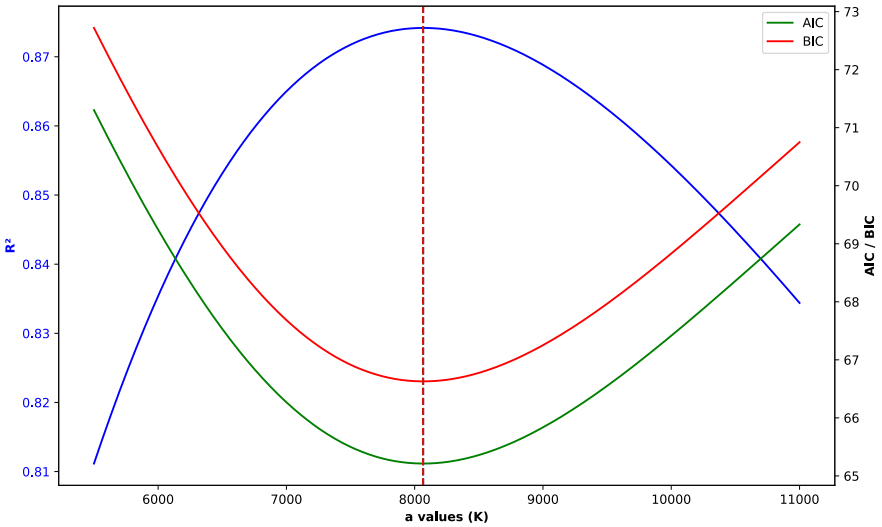

Figure 6.44. Statistical metrics for the CdS QDs ERT modelisation, screening a values, optimum $a = 8067.3$ K.

The corresponding expression for $\theta(t, T)$ becomes:

$$\theta(t, T) = t \cdot \exp\left(-\frac{8067.313}{T}\right) \tag{6.2}$$

6.2.5.3 Control experiment for the preparation of CdS with 3-MPA

The model selection was performed by fitting the parametrized form $\theta(t, T)$ to the experimental evolution of $E(\theta(t, T))$. The statistical criteria used to compare the one parameter and three parameters formulations are summarized in Table 6.12.

Table 6.12. Statistical comparison of the one- and three-parameter models for the CdS QDs, with 3-MPA, first excitonic peak.

Criterion	1 parameter	3 parameters
r^2	0.9999	0.9999
RSS	0.226	0.226
AIC	-11.49	-11.49
BIC	-12.28	-12.28

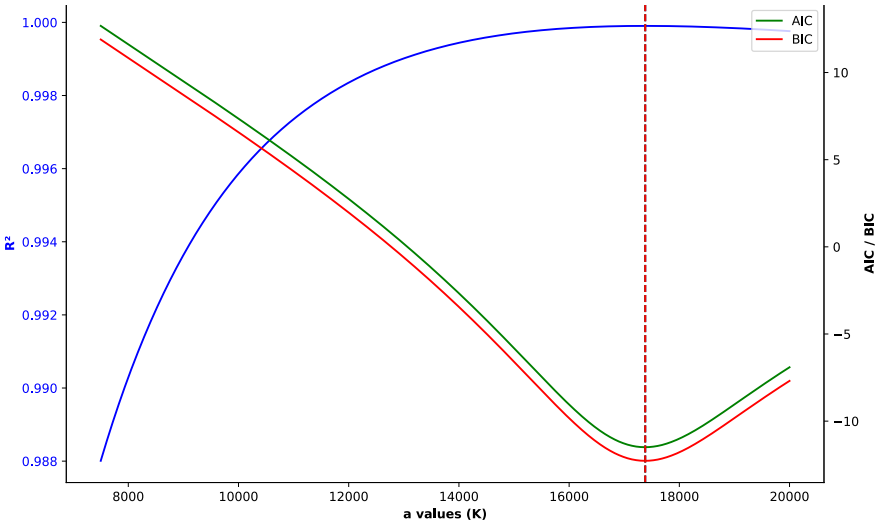

Figure 6.45. Statistical metrics for the CdS QDs, with 3-MPA, ERT modelisation, screening a values, optimum $a = 17381.18$ K.

The statistical analysis indicates that the three-parameter formulation provides a marginally better description of the experimental data, based on r^2, RSS, AIC, and BIC values. The corresponding expression for $\theta(t, T)$ is:

$$\theta(t, T) = t \cdot \exp\left(-\frac{17381.2}{T}\right) \tag{6.3}$$

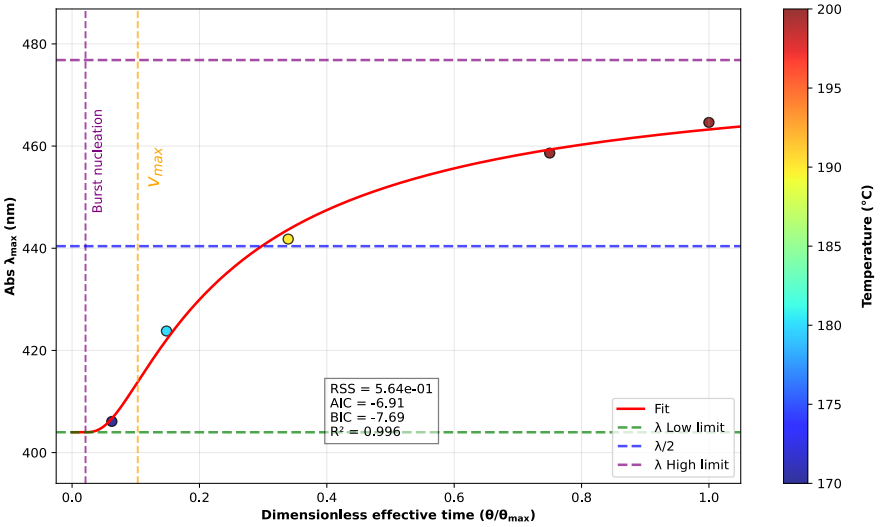

Figure 6.46. Modelling of the CdS QDs, formed with 3-MPA as sulfur source, peak absorbance position as a function of the dimensionless effective time. $E_0 = 403$ nm, $E_\infty = 477$ nm, $\alpha = 0.206$.

Table 6.13. Association of dimensionless effective time θ_{norm} with the dominant FW mechanism phases.

Reaction Phase	θ_{norm} **range**
Induction phase	0 to 0.0006
Burst nucleation	0.0006
Growth acceleration	0.0006 to 0.103
v_{max}	0.103
Growth slow down	0.103 to 1 and beyond

6.2.5.4 Model selection for CdSe

The model selection was performed by fitting the parameterized form $\theta(t, T)$ to the experimental evolution of $E(\theta)$. The statistical criteria used to compare

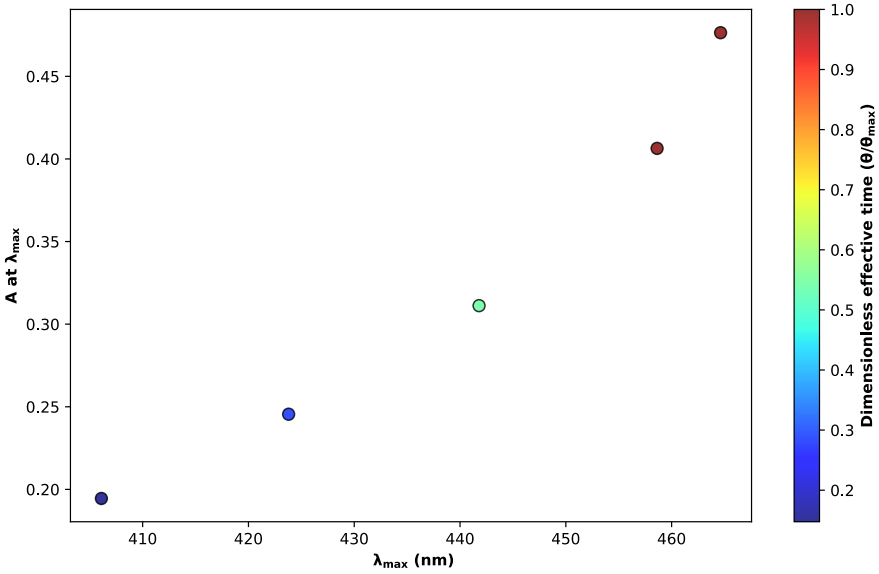

Figure 6.47. Absorbance values of CdS QDs, formed with 3-MPA as sulfur source, as a function of the first excitonic peak position, each point being associated with its DET value.

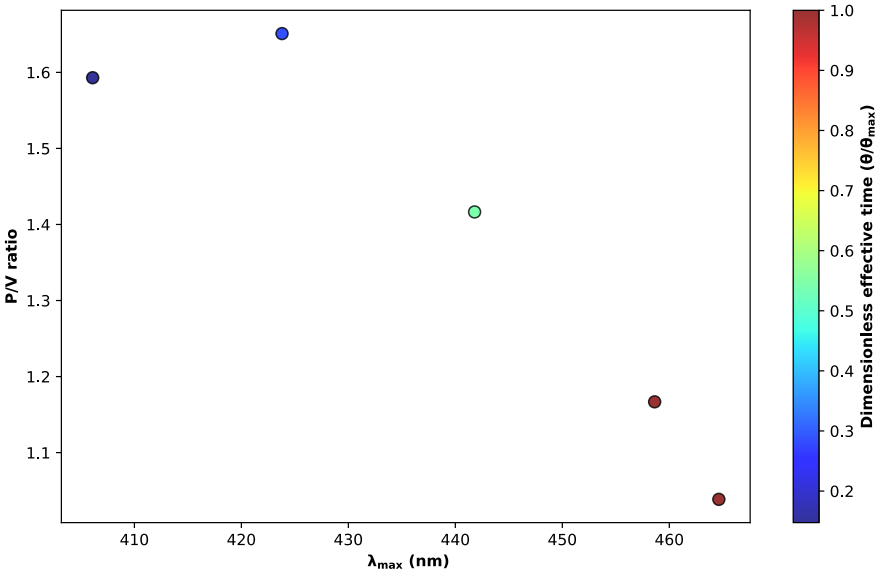

Figure 6.48. P/V ratio values of CdS QDs, formed with 3-MPA as sulfur source, as a function of the first excitonic peak position, each point being associated with its DET value.

the one-parameter and three-parameters formulations are summarized in Table 6.14.

Table 6.14. Model selection for CdSe QDs first excitonic peak

Criteria	1 parameter	3 parameters
r^2	0.87763	0.87838
RSS	4976.206	4945.575
AIC	185.36	185.13
BIC	188.58	188.35

As for CdS fit case, three-parameter model yields slightly improved RSS, r^2, AIC, and BIC values compared to the simpler one-parameter model but the improvement is marginal. Consequently, the one-parameter model was retained: it captures already the kinetic trends and remains far more simple.

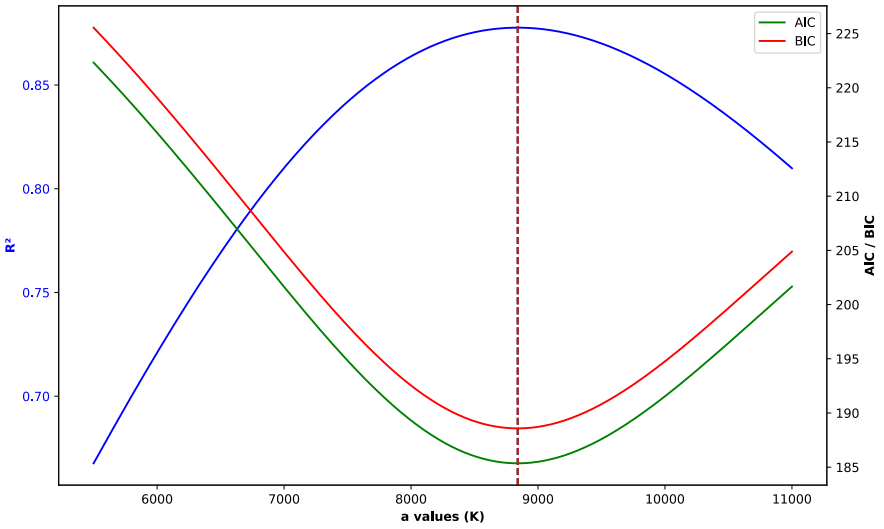

Figure 6.49. Statistical metrics for the CdSe QDs ERT modelisation, screening a values, optimum $a = 8839.9$ K.

The statistical analysis indicates that the one parameter formulation provides an adequate description of the data. The corresponding expression for $\theta(t, T)$ is:

$$\theta(t, T) = t \cdot \exp\left(-\frac{8839.884}{T}\right) \tag{6.4}$$

6.2.5.5 Model selection for CdTe

Firstly, a multivariate Partial Least Squares (PLS) analysis was performed on the data to estimate the relative influence on E_{peak} of temperature (T), 0.0823 for species concentration (C), 0.049 for reaction time (t), -0.108 for chalcogen excess (Eq), and 0.0310 for final pH. Based on their absolute values, temperature is by far the dominant factor, while the other parameters have comparatively minor effects.

To further illustrate the influence of each variable, a 2D PLS analysis was performed. The loadings vectors in the PLS latent space, indicate how strongly a variable contributes to the principal latent dimensions. By weighting these vectors with the Variable Importance in Projection (VIP) scores, the variables that most strongly influence the model, a plot containing the data and the vectors with the direction of their weight and intensity provide a lot of informations. A higher VIP-weighted vector corresponds to a greater contribution to the variation in E_{peak}.

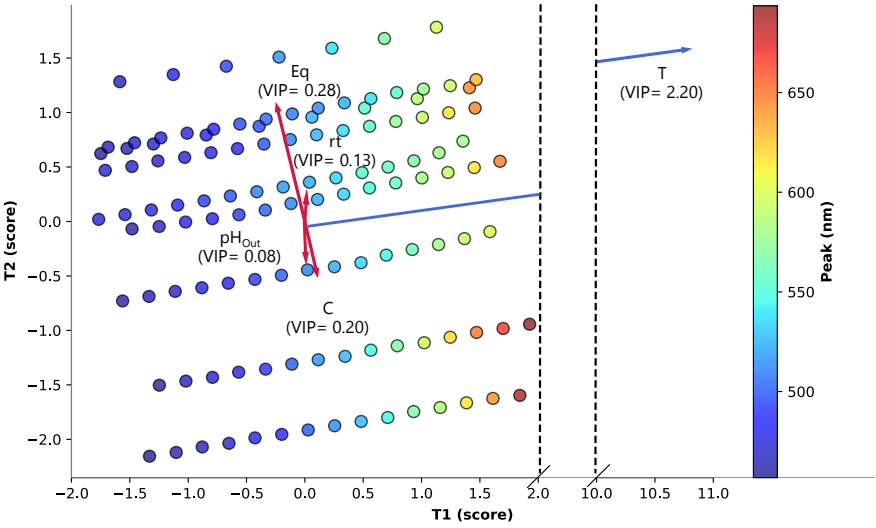

Figure 6.50. 2D PLS representation of loadings vectors multiplied by VIP scores for temperature, time, species concentration, chalcogen excess, and final pH on the T-1 and T-2 scores from PLS regression of E_{peak}.

In this representation (Figure 6.50), the length and orientation of the vectors allow a quick visual assessment of which parameters are most influential. Temperature, with both the highest standardized coefficient and a strong VIP-weighted loading, clearly dominates. The other parameters, although contributing to a lesser extent, can still be identified and interpreted within this framework.

This approach not only confirms the predominance of temperature but also provides a clear, interpretable visual tool for understanding the relative impact

of all experimental variables. It motivates the introduction of the reduced parameter $\theta(t, T)$, which combines the effects of time and temperature, simplifying the model without losing predictive power.

Table 6.15. Model merits for the CdTe QDs first excitonic peak, showing the effect of concentration (C), chalcogen excess (Eq) and initial pH (pH_0) on the fitted parameter a and the corresponding statistical metrics (R^2, AIC, BIC).

Conditions			**Fit constants**	**Merits**		
C	Eq	pH_0	a (K)	R^2	AIC	BIC
1.5	7.5	7.52	7311.16	0.9435	174.80	187.03
3.0	5.0	9.08	7007.54	0.9790	145.43	148.23
3.0	7.5	7.85	6203.52	0.9840	114.27	117.08
3.0	10.0	8.23	7128.14	0.9970	39.40	38.96
3.0	10.0	7.57	6364.32	0.9983	20.35	19.05

6.2.5.6 Determination of reaction yield

The protocol developed to estimate the reaction yield was executed as follows:

- Extended production of a given QD type (CdS, CdSe, or CdTe) to obtain more or less 150 mL of crude QDs.
- Purification of 20 mL of the crude mix (volumetric pipette) by selectively precipitating the QDs through the addition of 25 mL of ethanol (antisolvent) followed by centrifugation (10 min at 5000 rpm).
- Removal of the supernatant.
- Drying of the solid residue under vacuum.
- Weighting of the container with the dried powder.
- Removal of the QDs from the container.
- Weighting of the empty container.

This operation is repeated at least 4 times. The tare executed allows to calculate the QD mass. It is hypothesized that the weight so obtained is only composed of the crystal material (CdS, CdSe, or CdTe). The theoretical yield is calculated as follows:

$$Weight_{th} = \frac{n'_{limiting}}{V'_{tot}} \cdot V_{sample} \cdot MM_{crystal} \tag{6.5}$$

Where:

- $\mathbf{n'}$: Molar flow of the limiting reagent [mol.min^{-1}],
- $\mathbf{V'_{tot}}$: Total flow rate in the reactor [mL.min^{-1}],
- $\mathbf{V_{sample}}$: Sample volume [mL],
- $\mathbf{MM_{crystal}}$: Molar weight of the considered crystal [g.mol^{-1}].

The yield results are presented in Table 6.16

Table 6.16. Summary of the yield results and key values

Crystal type	ρ (g.cm^{-3})	MM (g.mol^{-1})	Experimental conditions	Yield (%)
CdS	4.826	144.48	rt = 45 s, T = 190 °C	40.3±8.8
CdSe	5.816	191.37	rt = 45 s, T = 180 °C	74.5±6.5
CdTe	5.850	240.01	rt = 45 s, T = 155 °C	64.6±4.0

6.2.5.7 Sample preparation for XPS QDs characterization

The QDs to be analyzed by XPS were purified using the process described in Section 6.2.5.6. The obtained powders were finally deposited on a square piece of double-sided tape and placed on an autosampler. The samples were analysed after staying three days in a high vacuum chamber (>10^{-9} torr).

6.2.5.8 Isotopic labeling

Before isotopic labeling, a TCEP=^{16}O reference was synthesized.

1. TCEP^{16}O reference synthesis

   The synthesis of TCEP16O was performed by oxidating TCEP.HCl with 30 % H_2O_2. A 0.2 M aqueous solution of TCEP was prepared by dissolving TCEP.HCl (0.0573 g, 0.2 mmol, 1 equiv.) in milliQ water. Then, 30 % H_2O_2 (25.5 µL, 0.25 mmol, 1.25 eq) was added to the mixture to oxidize the phosphine and generate TCEP^{16}O. Finally, 20 µL of this solution was added to 1000 µL of milliQ water before the analysis by HPLC-MS. The results of this analysis are provided in Figure S32. It shows two peaks centred at 2 min and 2.3 min. The mass analysis of these peaks matches the expected structure.

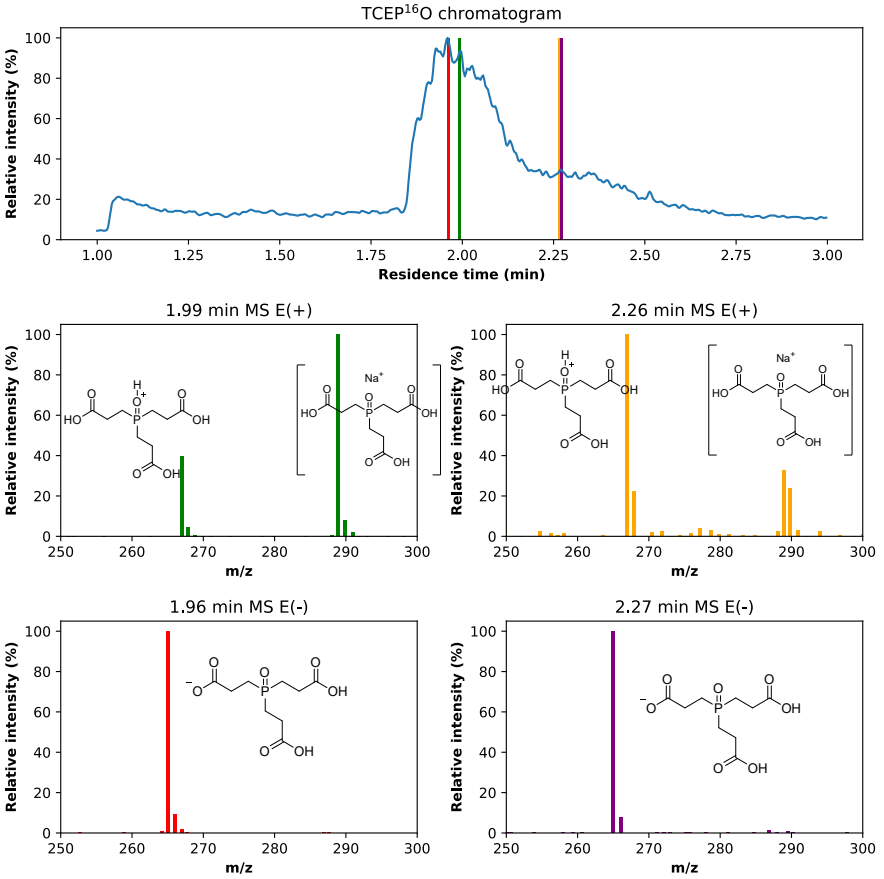

Figure 6.51. Reference chromatogram of TCEP=O with the representative mass spectra (positive and negative modes) of the two signals (1.97 min and 2.26 min)

2. Isotopic labeling for CdTe QDs synthesis

   The isotopic labeling experiment aimed to determine whether water serves as the oxygen source for the TCEP=O formation, a side product detected during the CdTe synthesis. The reaction was therefore conducted in $H_2^{18}O$, with all solutions saturated with argon and kept under an inert atmosphere.

   A 0.2 M aqueous solution of TCEP was prepared by dissolving TCEP.HCl (0.0573 g, 0.2 mmol, 1 equiv.) and NaOH (0.03 g, 0.75 mmol, 3.75 equiv.) with 1 g of $H_2^{18}O$. The solution was prepared in a 10 mL flask under argon. Then, Te was added (0.0510 g, 0.4 mmol, 2 equiv.) and the solution was stirred for 30 min. The product of the reaction (TCEP=Te) was extracted, filtered through a 0.2 µm membrane, and then added to the cadmium precursor solution.

   The cadmium precursor solution was prepared by dissolving $Cd(OAc)_2$ (0.0533 g, 0.2 mmol, 1 equiv.), 3-MPA (0.0531 g, 0.5 mol, 2.5 equiv.), and NaOH (0.05 g, 1.25 mmol, 6.25 equiv.) with 1 g of $H_2^{18}O$. The solution was purged with argon in a 10 mL flask for 15 min before adding TCEP=Te.

   The resulting mixture is heated up to 85 °C overnight. The product obtained is a dark viscous liquid that is filtered through a 0.2 µm membrane, leading to a yellowish liquid. 350 µL of this crude is mixed with 350 µL of ethanol, mixed, and centrifugated at 10 000 rpm for 5 min. 50 µL of the supernatant is diluted with 1000 µL of milliQ water and then analysed by HPLC-MS. The results are shown in Figure . The signal at 1.92 min was analysed and exhibited the same molecular ions but shifted by 2 units compared to Figure .

3. HPLC-MS method

   HPLC-MS analysis were performed with a Shimadzu LCMS-2020 Single Quadrupole MS equipped with a column C18 (100 x 4.6 mm, 3 µm) at 40 °C. A gradient of eluent A (0.1% formic acid in H_2O, v:v) and B (acetonitrile) was performed.

   - Eluent: A: 0.1% formic acid in H_2O; B: Acetonitrile.
   - Total flow rate: 1 $mL.min^{-1}$.
   - Gradient of the eluents:

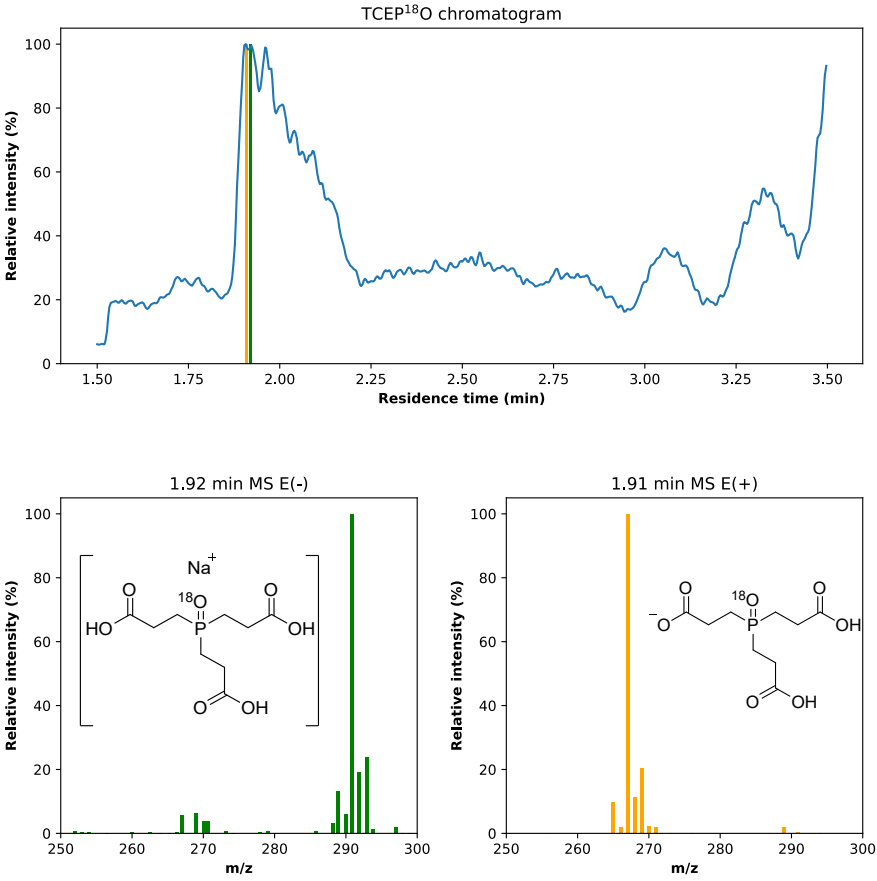

Figure 6.52. Chromatogram of the CdTe QDs crude supernatant with the representative mass spectra (positive and negative modes) of the signal at 1.91 min.

Table 6.17. HPLC-MS gradient over time with relative proportion 0.1% formic acid in H_2O/acetonitrile

Time (min)	A (%)	B %
0.00	100	0
10.00	30	70
30.00	20	80
33.00	0	100

6.3 Chapter 5: Supplemental Materials and Analysis

6.3.1 Purified CdTe QDs stabilization

1) Preparation of the PBS feed

The PBS solutions were prepared by weighting the salt amounts indicated in Tables from 6.18 to 6.20.

The PBS 1 feed is prepared with:

Table 6.18. Full PBS solution, V = 50 mL

Metric	NaCl	KCl	$NaHPO_4$	KH_2PO_4
C ($mol.L^{-1}$)	0.137	0.027	0.01	0.0018
n (mmol)	6.85	1.35	0.5	0.09
MM ($g.mol^{-1}$)	58.44	74.55	358.1	136.09
w (g)	0.4	0.1	0.179	0.0122

The PBS 2 feed is prepared with:

Table 6.19. Reduced saline PBS solution, V = 50 mL

Metric	NaCl	K_2HPO_4	KH_2PO_4
C ($mol.L^{-1}$)	0.05	0.005	0.005
n (mmol)	2.5	0.25	0.25
MM ($g.mol^{-1}$)	58.44	174.18	136.09
w (g)	0.146	0.044	0.034

The PB feed is prepared with:

2) 3-MPA surface saturation

To achieve the surface saturation, the mixture is purified by sedimentation according to protocols described in Section 6.2.5.6. The crude solution is then solubilized in a 0.0125 $mol.L^{-1}$ solution of 3-MPA at pH 11 and mixed for 24 hours at room temperature.

The QDs solution is then purified by ultrafiltration. The first step is carried out using a 10 kDa filter, at 5000 rpm for 15 minutes at

Table 6.20. Phosphate buffer without neutral salt solution, V = 50 mL

Metric	K_2HPO_4	KH_2PO_4
C (mol.L^{-1})	0.005	0.005
n (mmol)	0.25	0.25
MM (g.mol^{-1})	174.18	136.09
w (g)	0.044	0.034

room temperature, to remove unreacted 3-MPA. A 500 μL aliquot of the crude QDs solution is filtered. The QDs are then washed three times with 10 mmol.L^{-1} PBS (pH 7.4). The upper phase is collected, dissolved in PBS, and subjected to a second ultrafiltration step using a 30 kDa filter. After the second ultrafiltration, the lower phase is collected.

6.3.2 Biofunctionalization with Biotin

1) Cysteamine Thiol Protection

To enhance the regioselectivity of cysteamine coupling, the thiol group is initially protected by a trityl group in pure trifluoroacetic acid (TFA) with trityl chloride (Figure 6.53).

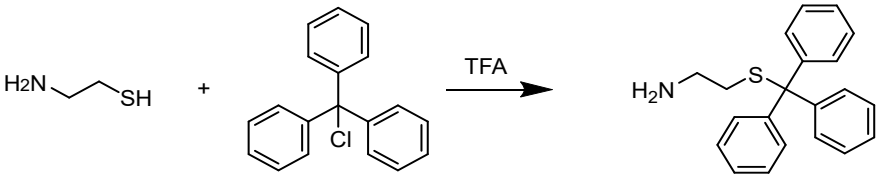

Figure 6.53. Cysteamine protection of the thiol function by trityl in TFA.

a) Protocol:

50 mmol of cysteamine · HCl (5.76 g, 1 equiv.) are dissolved in 36 mL of TFA. Then, 50 mmol of trityl chloride (14.1 g, 1 equiv.) are added, and the solution is stirred for 3 hours at 40 °C and 900 rpm. The TFA is removed by vacuum distillation (480 mbar), and the residue is recovered in 50 mL of EtOAc, washed sequentially with NaOH 1M, water, $NaHCO_3$, and brine. The organic phase is dried over $MgSO_4$ and evaporated to yield a solid product, which is purified by recrystallization from CH_2Cl_2/hexane.

b) Observations:

During the addition of trityl chloride, the solution changes from transparent to yellowish, and then finally brown. After the evaporation of TFA, a viscous brownish solid remains. This mixture is solubilized in 10 mL of CH_2Cl_2, and 34 mL of hexane is added, leading to significant recrystallization. After filtration, the solid is dried under vacuum at 30 °C, resulting in a white powder. The yield was estimated based on the recovered product's weight, which was 70.1%. This result is disappointing compared to the 95% yield reported in the publication used to develop this protocol. [7]

2) Biotin/Trityl-Cysteamine Coupling

The coupling reaction between biotin and trityl-cysteamine is carried out using the coupling reagent HBTU (hexafluorophosphate benzotriazole tetramethyl uranium) in the presence of DIPEA (diisopropylamine) inside DMF (dimethylformamide), as shown in Figure 6.54.

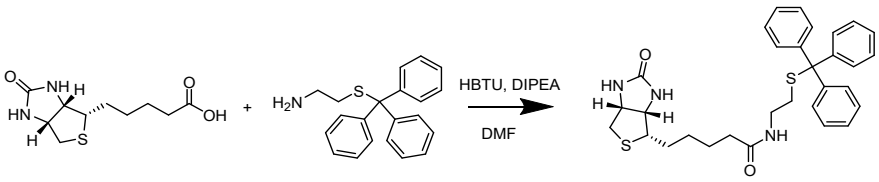

Figure 6.54. Biotin/Trityl-cysteamine coupling in DMF in the presence of HBTU and DIPEA.

a) Protocol:

0.4 mmol of trityl-cysteamine (0.127 g, 4 equiv.), 0.1 mmol of biotin (0.025 g, 1 equiv.), and 0.16 mmol of HBTU (0.607 g, 16 equiv.) are dissolved in a minimum volume of DMF (peptide grade). Then, 6.4 equiv. of DIPEA (0.827 g) are added to the mixture, which is stirred overnight at room temperature. Most of the DMF and DIPEA are removed from the crude mixture using a rotary evaporator (rotavapor) at 40 °C and 75 mbar. The mixture is then dissolved in 10 mL of ethyl acetate and washed with 0.1 M HCl (2 × 10 mL) and brine (1 × 15 mL). After drying over $MgSO_4$ and filtration, the solvent is removed (40 °C under 200 mbar). The product is finally dried under high vacuum, yielding a brownish slurry.

b) Observations:

Biotin, trityl-cysteamine, and HBTU are weighed directly in the reactor. Then, DMF is added slowly to dissolve the solid in a minimal amount of solvent (around 22.5 mL). DIPEA is added using a micropipette. During the reaction, the mixture transitions

from transparent yellowish to brownish. The reaction is stopped after 15 hours. Subsequently, DMF and DIPEA are removed with the rotavapor, followed by liquid-liquid extraction. Ethyl acetate is then evaporated under vacuum. The reaction yield is 54.6%, and the product purity is 98.3%.

3) Biotin-Cysteamine-Trityl Deprotection

After the production and purification of the coupling product, Biotin-Cysteamine-Trityl, the final step in the biotin modification process is the thiol deprotection. This reaction is performed using trifluoroacetic acid (TFA) and triisopropylsilane (TIPS), the latter acting as a scavenger, inside dichloromethane (DCM). The reaction scheme is presented in Figure 6.55.

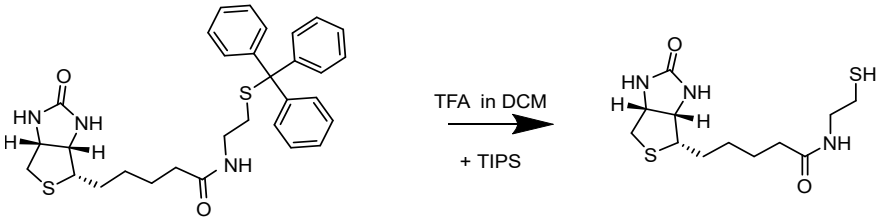

Figure 6.55. Biotin-Cysteamine-Trityl deprotection with TFA and TIPS in DCM.

a) Protocol:

To a magnetically stirred solution of BIO-CYS-TRT (0.546 mmol, 297 mg, 1 equiv.) dissolved in CH_2Cl_2 (10 mL), 10 mL of TFA was added, followed by 2 equiv. of triisopropylsilane (1.1 mmol, 173 mg, 224 µL). The reaction mixture was stirred at room temperature for four hours. Afterward, the crude mixture was concentrated under reduced pressure, and the residue was dissolved in 25 mL of ethyl acetate, followed by extraction with H_2O (3×10 mL). The aqueous extracts were combined and lyophilized. [7, 8]

b) Observations:

The Bio-Cys-Trt was dissolved in CH_2Cl_2, after which TFA was added, followed by TIPS. The reaction was performed under stirring (450 rpm) for 2.5 hours. After the reaction, the volatile compounds were removed under vacuum (40 °C, 200 mbar). The residue was dried under high vacuum and dissolved in 25 mL of ethyl acetate. The product was then extracted with milliQ water and purified by lyophilization for three days at -47 °C under high vacuum. The final product, a fine white powder (0.1594 g), corresponds to a yield of 96.5%.

4) Biofunctionalization on CdTe QDs

In order to functionalize the CdTe quantum dots (QDs) with biotin, a modified biotin molecule with a thiol group was used. This method allows for the binding of biotin to the surface of the quantum dots, which is crucial for subsequent biological applications. The process involves purified 590 nm CdTe QDs and ensuring that the surface chemistry remains stable throughout the reaction. A scheme of the reaction is provided in Figure 6.56.

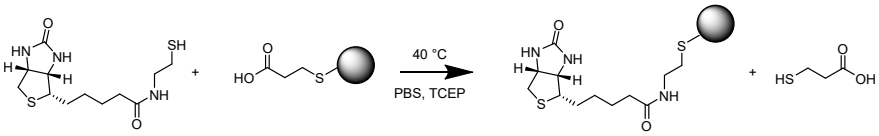

Figure 6.56. Biotin-Cysteamine-Trityl deprotection with TFA and TIPS in DCM.

a) Protocol:

For this biofunctionalization step, a modified biotin is used to bind to the CdTe quantum dots (QDs) via its thiol group. The reaction is carried out using purified 590 nm QDs to ensure consistent size and surface characteristics. To prevent the formation of unwanted disulfide bridges, 0.5 equiv. of TCEP are added to the reaction mixture. To promote ligand exchange and facilitate binding, the reaction mixture is heated to 40 °C and stirred at 650 rpm for one hour, allowing for the efficient attachment of the modified biotin to the surface of the quantum dots.

b) Observations:

The resulting mixture was a reddish liquid, which exhibited signs of instability. The modified biotin (5 mM) showed poor solubility in the PBS buffer, which complicated the purification process. This low solubility caused the biotin to become trapped in the centrifugation filter, requiring multiple washing steps to remove excess biotin from the system. Proton NMR analysis was performed to confirm the successful binding of the modified biotin to the QD surface. The results are presented in Figure 6.57.

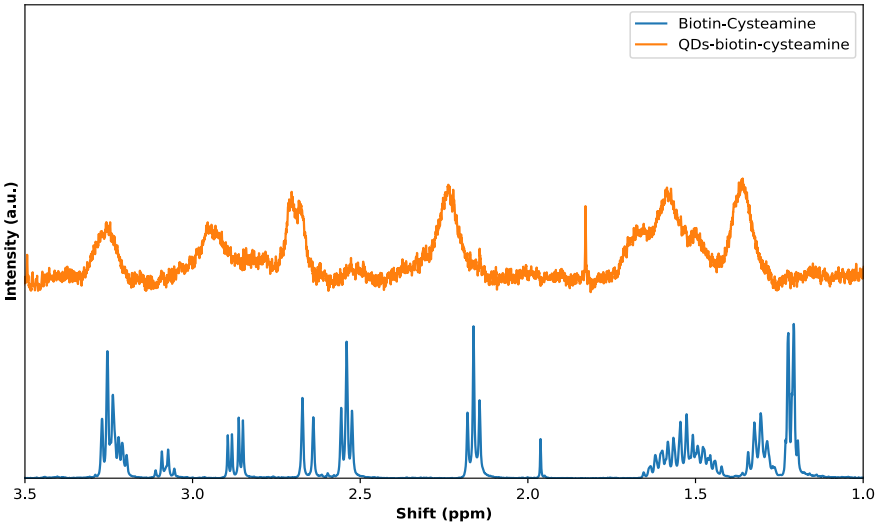

Figure 6.57. ^{1}H-NMR spectra of reference biotin-cysteamine (blue curve) and the assumed CdTe-cysteamine-biotin (orange).

The direct comparison between the reference biotin-cysteamine spectrum and the assumed CdTe-cysteamine-biotin spectrum provides two key observations: the main signals are broader, which suggests that the protons are attached to a larger molecule. Additionally, the primary peaks correspond to those observed in the reference spectrum, but they are slightly shifted or attenuated. This finding indicates the potential functionalization, but further confirmation is needed. One possible approach to confirm the binding would be through a DOSY experiment, although the results were inconclusive. An alternative solution could be to perform a FRET experiment. By mixing the sample with an organic dye functionalized with streptavidin, we could validate the FRET phenomenon, thereby confirming the functionalization of the QDs. [9]

References

[1] Avantes. *Fibre Optic Spectroscopy*. https://pro-lite.co.uk/products-services-index/spectroscopy/spectrometers/fibre-optic-spectroscopy/avantes-bundles/. Accessed: 2024-10-07. 2024.

[2] Wushuang Wan et al. "Room-temperature formation of CdS magic-size clusters in aqueous solutions assisted by primary amines". In: *Nature Communications* 11 (1 Aug. 2020), pp. 4–11. ISSN: 20411723. DOI: 10.1038/s41467-020-18014-6.

[3] Shahar Dery et al. "Insights into the deselenization of selenocysteine into alanine and serine". In: *Chemical Science* 6 (2015), pp. 6207–6212. DOI: 10.1039/c5sc02528a.

[4] M.J. Frisch et al. *Gaussian 16, Revision B.01*. Gaussian, Inc. Wallingford CT, 2016.

[5] Debasis Bera et al. "Quantum dots and their multimodal applications: A review". In: *Materials* 3.4 (2010), pp. 2260–2345. ISSN: 19961944. DOI: 10.3390/ma3042260.

[6] Huiguang Zhu et al. "Low temperature synthesis of ZnS and CdZnS shells on CdSe quantum dots." In: *Nanotechnology* 21 (25 June 2010), p. 255604. ISSN: 13616528. DOI: 10.1088/0957-4484/21/25/255604.

[7] Gregory R. Naumiec et al. "Synthesis of a CCT-lanthanide conjugate for binding the dopamine transporter". In: *Organic and Biomolecular Chemistry* 13 (9 Mar. 2015), pp. 2537–2540. ISSN: 14770520. DOI: 10.1039/c4ob02165g.

[8] André J. Van Der Vlies et al. "Synthesis of pyridyl disulfide-functionalized nanoparticles for conjugating thiol-containing small molecules, peptides, and proteins". In: *Bioconjugate Chemistry* 21 (4 Apr. 2010), pp. 653–662. ISSN: 15204812. DOI: 10.1021/bc9004443.

[9] Eduard Zenkevich et al. "Self-assembly of semiconductor quantum dots with porphyrin chromophores: Energy relaxation processes and biomedical applications". In: *Journal of Molecular Structure* 1244 (2021), p. 131239. ISSN: 00222860. DOI: 10.1016/j.molstruc.2021.131239.

List of Figures

List of Tables

Personal Quote Interpretation

"We shall all get dreamy to reach meaningful innovation."

David Lynch *(1946–2025)*